N-Heteroacenes in Organic Field-Effect Transistors

von

Fabian Paulus

Inaugural-Dissertation

Heidelberg 2016

Inaugural-Dissertation

zur

Erlangung der Doktorwürde

der

Naturwissenschaftlich-Mathematischen Gesamtfakultät

der

Ruprecht-Karls Universität Heidelberg

vorgelegt von

Diplom-Chemiker Fabian Paulus

aus Heidelberg

März 2016

Tag der mündlichen Prüfung: 13.Mai 2016

N-Heteroacenes in Organic Field-Effect Transistors

Gutachter: Prof. Dr. Uwe H. F. Bunz

                  Prof. Dr. Michael Mastalerz

Meinen Großeltern gewidmet

Teile dieser Arbeit wurden bereits in Fachzeitschriften veröffentlicht:

TIPS-Tetracene- and TIPS-Pentacene-Annulated Poly(norbornadiene)s: Synthesis and Properties
Porz, M.; Paulus, F.; Höfle, S.; Lutz, T.; Lemmer, U.; Colsmann, A.; Bunz, U. H. F.
Macromol. Rapid Commun. **2013**, *34* (20), 1611–1617.

Acceleration of Singlet Fission in an Aza-Derivative of TIPS-Pentacene
Herz, J.; Buckup, T.; Paulus, F.; Engelhart, J.; Bunz, U. H. F.; Motzkus, M.
J. Phys. Chem. Lett. **2014**, *5* (14), 2425–2430.

Electron-transporting Phenazinothiadiazoles with Engineered Microstructure
Lindner, B. D.[#]; Paulus, F.[#]; Appleton, A. L.; Schaffroth, M.; Engelhart, J. U.; Schelkle, K. M.; Tverskoy, O.; Rominger, F.; Hamburger, M.; Bunz, U. H. F.
J. Mater. Chem. C **2014**, *2* (45), 9609–9612.

N,N'-Dihydrotetraazapentacenes (DHTA) in Thin Film Transistors
Paulus, F.; Lindner, B. D.; Reiß, H.; Rominger, F.; Leineweber, A.; Vaynzof, Y.; Sirringhaus, H.; Bunz, U. H. F.
J. Mater. Chem. C **2015**, *3* (7), 1604–1609.

Unveiling Singlet Fission Mediating States in TIPS-pentacene and its Aza Derivatives
Herz, J.; Buckup, T.; Paulus, F.; Engelhart, J. U.; Bunz, U. H. F.; Motzkus, M. *J. Phys. Chem. A* **2015**, *119* (25), 6602–6610.

The Effect of Tuning the Microstructure of TIPS-tetraazapentacene on the Performance of Solution Processed Thin Film Transistors
Paulus, F.; Engelhart, J. U.; Hopkinson, P. E.; Schimpf, C.; Leineweber, A.; Sirringhaus, H.; Vaynzof, Y.; Bunz, U. H. F.
J. Mater. Chem. C **2016**, *4* (6), 1194–1200.

Side-Group Engineering: The Influence of Norbornadienyl Substituents on the Properties of Ethynylated Pentacene and Tetraazapentacene
Paulus, F.; Porz, M.; Schaffroth, M.; Rominger, F.; Leineweber, A.; Vaynzof, Y.; Bunz, U. H. F.
Org. Electron. **2016**, *accepted manuscript*

[#] beide Autoren haben in gleichem Maße zu dieser Veröffentlichung beigetragen

Poster:

Large N-Heteroacenes
Engelhart, J. U.; Lindner, B. D.; Paulus, F.; Bunz, U. H. F. International Symposium on Electronic/Optic Functional Molecules (ISEOFM), 11.3.-16.3.**2012**, *Shanghai*, China

A non-conjugated pentacene based polymer
Paulus, F.; Porz, M.; Bunz, U. H. F. The 11th International Symposium on Functional π-electron systems (Fπ-11), 2.6.-7.6.**2013**, *Arcachon*, Frankreich

Structure-Property Relationship for Charge Transport: Can Herringbone Packing give Superior Properties for *N,N'*-Dihydrotetraazacenes
Paulus, F.; Lindner, B. D.; Reiß, H.; Rominger, F.; Vaynzof, Y.; Sirringhaus, H.; Bunz, U. H. F., Gordon Research Conference 'Electronic Processes in Organic Materials', 4.5.-9.5.**2014**, *Lucca*, Italy

Weitere Veröffentlichungen an denen während der Dissertation mitgewirkt wurde.

Reverse Engineering Of Conjugated Microporous Polymers: Defect Structures Of Tetrakis(4-ethynyl-phenyl)stannane Networks
Uptmoor, A. C.; Freudenberg, J.; Schwäbel, S. T.; Paulus, F.; Rominger, F.; Hinkel, F.; Bunz, U. H. F.
Angew. Chemie Int. Ed. **2015**, *54* (49), 14673–14676.

Coronene-Containing N-Heteroarenes: 13 Rings In A Row
Endres, A. H.; Schaffroth, M.; Paulus, F.; Reiss, H.; Wadepohl, H.; Rominger, F.; Krämer, R.; Bunz, U. H. F.
J. Am. Chem. Soc. **2016**, *138* (6), 1792–1795.

Halogenated Symmetrical Tetraazapentacenes: Synthesis, Structures and Properties
Engelhart, J. U.; Paulus, F.; Schaffroth, M.; Vasilenko, V.; Tverskoy, O.; Rominger, F.; Bunz, U. H. F.
J. Org. Chem. **2016**, *81* (3), 1198–1205.

Linear acenes are a widely studied class of materials in the field of Organic Electronics. Their aromatic system and the strong interaction of the π-electrons of neighbouring molecules in the solid state allow an efficient charge transport in these materials. The defined molecular structure of these small molecules and the possibility to tune their optical and electronic properties as well as the solid state packing through careful chemical design and synthesis have resulted in numerous applications of acenes in organic transistors and optoelectronic devices.

This work focuses on the application of N-Heteroacenes and non-conjugated pentacene-based polymers as semiconductors in solution-processed organic field-effect transistors. These devices are used to evaluate the charge transport properties of the materials and derive structure-function relationships for the various compounds. To draw structure-function relationships from the studies described in this thesis, a myriad of characterisation techniques was employed to obtain an insight into the optical, electronic, electrical and morphological properties of each material. The effects of order, energetics and processing of the semiconductor on the transistor performance are all investigated.

While non-conjugated pentacene-based polymers offer an ease of processability, their amorphous nature inhibits efficient hole transport, resulting in a relatively poor transistor performance. The fashion in which the pentacene systems are connected to the polymer backbone changes their flexibility and therefore affecting the injection behaviour and charge transport properties.

The nitrogen substitution in N-Heteroacenes results in an energetic stabilisation of the frontier molecular orbitals, allowing for an enhanced electron injection into these materials. For the symmetrical tetraazapentacene and two halogenated phenazine derivatives relatively high electron mobilities were achieved demonstrating their potential for future application as n-type semiconductors in organic field-effect transistors.

The use of N-heteroacenes is not limited to electron transport only. Their *N,N'*-dihydro forms are electron rich compounds that exhibit good hole transport. This is demonstrated for differently substituted tetraazapentacenes as well as for a *N,N'*-dihydro diazahexacene and -heptacene. For these materials it is shown that the processing conditions not only affect the macroscopic transistor performance, but also influence the formation of polymorphs in thin films.

The solid state packing of functionalised acenes is typically determined by their solubilising side chains. A norbornadienyl substitution at the side chain of the well-known 6,13-bis(triisopropylsiliylethynyl)pentacene and its tetraaza derivative was shown to result in an enhancement of the charge transport properties for the p-type derivatives and deterioration of the performance of the n-type transistors. These observations are related to changes in the charge transfer integrals, the film microstructure and the solid state packing.

In conclusion, this work contributes to the development of guidelines for the design and synthesis of next generation N-heteroacenes to be applied in the future in state of the art organic electronic devices.

Kurzzusammenfassung

Lineare Acene sind eine gut untersuchte Klasse von Materialien im Bereich der Organischen Elektronik. Ihr aromatisches System und die starken Wechselwirkungen der π-Elektronen zwischen benachbarten Molekülen im festen Zustand ermöglichen einen effizienten Ladungstransport. Die definierte Molekülstruktur und die Möglichkeit, die optischen und elektronischen Eigenschaften, sowie das Packungsverhalten im Festkörper durch ein rationales Design und die chemische Synthese genau einzustellen, haben zu einer Vielzahl an Verbindungen und Anwendungen dieser kleinen Moleküle in organisch elektronischen Bauteilen geführt. Die vorliegende Arbeit beschreibt die Anwendung von N-Heteroacenen und nicht-konjugierten Polymeren auf Pentacen-Basis in flüssig-prozessierten organischen Feldeffekttransistoren. Diese Bauteile wurden genutzt um den Ladungstransport der verwendeten Materialien zu untersuchen und um Struktur-Eigenschaftsbeziehungen abzuleiten. Eine Vielzahl von Charakterisierungsmöglichkeiten wurde angewendet um Einsicht in die optischen, elektronischen, elektrischen und morphologischen Eigenschaften der eingesetzten Materialien zu erhalten. Für die Leistungsfähigkeit der Transistoren wurden die Einflüsse von Ordnung, der Position der Energielevel und der Prozessierung des untersuchten Halbleiters untersucht.

Die nicht-konjugierten Pentacen-Polymere überzeugen durch eine gute Filmbildung, allerdings sind aufgrund ihrer amorphen Struktur keine hohen Lochmobilitäten möglich. Es konnte aber gezeigt werden, dass die Art der Anbindung des Pentacen-Grundkörpers an die Polymerkette entscheidenden Einfluss auf die Ladungsträgerinjektion und den Ladungstransport hat.

Die Einführung von Stickstoffatomen in das aromatische Acenrückgrat im Falle der N-Heteroacene führt zu einer energetischen Absenkung der Grenzorbitale und ermöglicht eine verbesserte Injektion von Elektronen. Der Elektronentransport mit relativ hohen Ladungsträgermobilitäten konnte für das symmetrische Tetraazapentacen und zwei halogenierte Phenazin Derivate demonstriert werden und zeigt, welches Potential diese Stoffklasse für zukünftige Anwendung in organischen Feldeffekt Transistoren besitzt.

Die Anwendung von N-Heteroacenen ist nicht auf n-Kanal Bauteile beschränkt. In ihrer elektronenreichen *N,N′*-Dihydro-Form sind Azaacene Materialien, die einen Lochtransport aufweisen können, wie am Beispiel der drei unterschiedlich substituierten *N,N′*-Dihydrotetraazapentacene und den größeren *N,N′*-Dihydrodiazahexacen und -heptacen gezeigt wurde. Für die Pentacene wurde gezeigt, dass die Bedingungen der Prozessierung nicht nur die Transistoreigenschaften beeinflussen, sondern auch zu einer Ausbildung eines anderen Polymorphs im Film führen können.

Die Festkörperstruktur der funktionalisierten Acene wird typischerweise durch die löslichkeitsvermittelnden Seitengruppen beeinflusst. Eine Substitution mit Norbornadien an der Seitengruppe des 6,13-Bis(triisopropyl-silylethinyl)pentacens und des entsprechenden Tetraazaacenes führt zu einer Verbesserung der Lochtransporteigenschaften im Falle von Pentacen und verschlechtert den Elektronentransport des Tetraaza Derivats. Der beobachtete Effekt ist auf eine leicht modifizierte Kristallpackung, den daraus veränderten Transferintegralen für den Ladungstransport und eine andere Mikrostruktur der Filme zurückzuführen.

Die gewonnenen Erkenntnisse dieser Arbeit werden helfen, neue Konzepte für das Design und die Synthese zukünftiger N-Heteroacene, optimiert für den Einsatz in elektronischen Bauteilen, zu entwickeln.

Table of Contents

Abbreviations

μ	charge carrier mobility
1-D	one-dimensional
2-D	two-dimensional
a.u.	arbitrary units
AFM	atomic force microscopy
AMOLED	active matrix organic light emitting diode
BC	bottom-contact
BCB	benzocyclobutane
BG	bottom-gate
BJT	bipolar junction transistor
bp	boiling point
C	capacitance per area
CB	chlorobenzene
Cy	cyclohexyl
D	drain
d	layer thickness or layer distance
dba	dibenzylideneacetone
dec	decade
DHTA	*N,N'*-dihydrotetraazapentacene
e	electron
E	energy
ε	dielectric constant of the vacuum
ε_r	dielectric constant
FET	field-effect transistor
G	gate
GIWAXS	gracing incidence wide angle X-ray scattering
h	hole
h	Plank's constant
HMDS	Hexamethyldisilazane
HOMO	highest occupied molecular orbital
HPLC	high-performance liquid chromatography
I_D or I_d	drain or channel current
I_G or I_g	gate current
*i*Pr	isopropyl
ITO	indium tin oxide
I-V	current-voltage
$K_{\alpha 1}$	K-alpha emission line from $2p_{3/2}$
$K_{\alpha 2}$	K-alpha emission line from $2p_{1/2}$
k_B	Boltzmann constant
k_{ET}	electron transfer rate
L	channel length of a transistor
λ_{reorg}	reorganisation energy
λ	wavelength

LUMO	lowest unoccupied molecular orbital
m	meta
Mes	mesitylene
NMP	N-methyl-2-pyrrolidone
o	ortho
ODTS	Trichloro(octadecyl)silane
OFET	organic field-effect transistor
OLED	organic light-emitting diode
OPV	organic photovoltaic diode
OTS	Trichloro(octyl)silane
P3HT	Poly(3-hexylthiophene)
PCBM	[6,6]-Phenyl-C61-butyric acid methyl ester
PCE	power conversion efficiency
PDI	polydispersity index
PFBT	Pentafluorobenzenethiol
ϕ	injection barrier
PMMA	Poly(methyl methacrylate)
POM	polarised optical microscopy
PTFE	Polytetrafluoroethylene
PVA	Polyvinyl alcohol
Q	charges per area
q_{xy} and q_z	xy and z component of the scattering vector q
Ref	reference
rms	root mean square
ROMP	ring-opening metathesis polymerisation
RuPhos	2-Dicyclohexylphosphino-2',6'-diisopropoxybiphenyl
S	source
S	substhreshold swing
*s*Bu	1-methylpropyl
SHE	standard hydrogen electrode
t	transfer integral
T	temperature
TC	top-contact
TG	top-gate
θ	diffraction angle
TIPS	triisopropylsilyl
UPS	ultraviolet photoemission spectroscopy
UV	ultraviolet
V	voltage
ν	wavenumber
Vac	vacuum
V_D or V_d	drain voltage
V_G or V_g	gate voltage
vis	visible
vs.	versus
V_S or V_s	source voltage

W	channel width of a transistor
w.r.t.	with respect to
XRD	X-ray diffraction

Units

°	degrees
°C	degrees Celsius
μm	micrometre
A	ampere
Å	angstrom
C	coulomb
cm	centimetre
eV	electronvolt
F	farad
g	gramme
h	hours
kV	kilovolt
m	metre
mA	milliampere
mbar	millibar
mg	milligramme
min	minutes
mL	millilitre
mm	millimetre
mM	millimole per litre
mol	mole
nm	nanometre
ppm	parts per million
ppmV	parts per million by volume
s	second
V	volt
W	watt

Molecular structures discussed in this work are labelled with numbers. The compounds investigated in this study are abbreviated with an acronym. While the molecular structure and acronym for each material are given in the corresponding chapter, the reader should also refer to the Appendix for their systematic names.

This thesis was written using Microsoft Word 2013 and OriginLab Corporation OriginPro 2015G. All molecular structures and schemes were drawn in Cambridgesoft ChemDraw Professional 15.0. Crystal structures were analysed with CCDC Mercury 3.5.1 and visualised with Mercury or The PyMOL Molecular Graphics System 1.5. Atomic force microscopy images were visualised using Gywiddion 2.41. References were added using Mendeley Desktop 1.16.

Chapter 1

Introduction

One of the greatest achievements in the 20th century was the wide-scale introduction of plastic materials into countless applications that have revolutionised our daily life. It is generally considered that plastic materials are insulators, as the vast majority of their application is in a non-electric context. In the 1970s it was discovered that certain carbon-based plastic materials can be made conductive by doping. This discovery has been recognized in the award of a Nobel Prize in Chemistry to A. Heeger, A. G. MacDarmid and H. Shirakawa in 2000 and resulted in the birth of a new field of science, involving the application of organic materials in electronic devices, commonly known as *Organic Electronics*.[1–3]

The synthesis of organic compounds offers limitless possibilities of new materials to be applied in organic electronic devices. Consequently, the focus of research has, for the most part, been on the development of the device organic active layer, namely the synthesis of new organic compounds with tailored optical and electronic properties, development of structure-property relationships, effects of processing on solid state structure and morphology and more. The macroscopic performance of the organic material in electronic devices is strongly affected by its molecular structure and the organisation in thin films, allowing a bottom-up approach of designing new functionalities and applications.
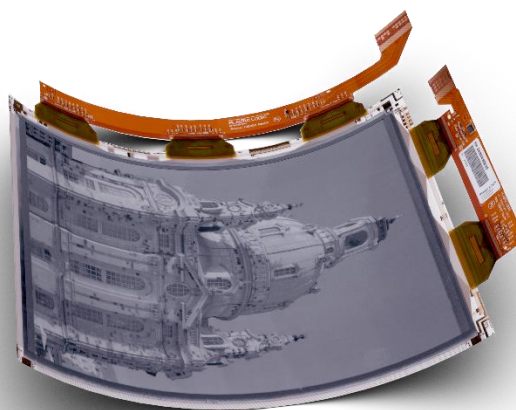
Figure 1. Glass-free flexible plastic display based on the recent advantages of organic electronics.
(Reproduced from Plastic Logic Ltd., copyright 2016, Photography courtesy of Plastic Logic Germany)

One of the biggest advantages of organic electronic devices is the ease of processability on a variety of substrates which allows, in contrast to their inorganic counterparts, an inexpensive, facile fabrication of large-area and mechanically flexible electronics. Other advantageous properties of organic materials include high extinction coefficients, the potential for integration in biological applications and most importantly the feasibility of creating rationally designed structures custom-made to the desired application. Despite these promising properties, many unanswered questions remain and further research is required to release the full potential of these materials. Numerous concepts have emerged to tackle the challenging problems of this field

of research and the work in the field of organic electronics is highly interdisciplinary, involving physicists, material scientists, engineers and chemists.[4]

There are mainly three device categories in research today in the context of organic electronics. These are organic light-emitting diodes (OLEDs), organic field-effect transistors (OFETs), and organic photovoltaic cells (OPVs). While the functionality and the underlying operational mechanisms of these devices are very different, charge transport plays an important role in determining the performance of all organic electronic devices. Among the variety of methods to probe the charge transport properties of organic electronic devices, organic field-effect transistors offer the unique possibility to characterise charge transport in organic materials in a fully functional device and is the focus of this work.

The first field-effect transistor (FET) with an organic semiconductor as an active layer was reported 1986.[5] While the performance of the device was rather poor, it launched the pursuit for new organic materials with better charge transport and higher charge carrier mobilities. To date, many thousands of organic compounds were investigated in field-effect transistors and the mobilities reported for state of the art devices often exceed 1 cm^2/Vs, comparable to that of amorphous silicon and many orders of magnitude higher than that of the first OFET. This remarkable advance in performance resulted in the integration of organic FETs in AMOLED displays and other industrial applications.

Further progress in the field of organic field-effect transistors can only be made by introducing new materials with an optimal set of properties – a task that can only be achieved through the powerful tools of synthetic chemistry.

Chapter 2

Theoretical Background

This chapter describes the working principle, architectures and components of organic field-effect transistors and derives the current-voltage (I-V) characteristics for these devices and commonly used methods for charge carrier extraction. Charge transport in organic semiconductor is discussed and the influence of the molecular design and charge transport on the charge carrier mobility is described. The second part of this chapter focuses on the recent developments of organic semiconductors and their application in devices and provides an overview over linear acenes, pentacene-based polymers and heteroacenes as hole and electron transporting materials and their performance in OFETs.

2.1.   Field-effect transistors

2.1.1. Working principle and architectures

A transistor is an electrical switch and is considered to be the most fundamental component of almost every electronic circuit.[6] A transistor allows to control the flow of current through the channel between two electrodes by applying a voltage to a third electrode. There are generally two types of transistors – a bipolar junction transistor (BJT) and the field-effect transistor (FET) – while both commonly used in modern electronics, their working principles are fundamentally different. A BJT controls the flow of current between a collector and emitter by the current that runs through the base, a field-effect transistor controls the channel current through the applied voltage at the gate.[7] The concept of a field-effect transistor was developed by J. Lilienfeld in the 1920s and first realised and patented by B. Schockley and co-workers at the Bell Laboratories in the late 1940s.[8,9] For the discovery of the transistor effect B. Shockley, J. Bardeen and W. Brattain were awarded the Nobel Prize in Physics in 1956.[10] The first organic field-effect transistor (OFET) with polythiophene as organic semiconductor was demonstrated by Ando *et al.* in 1986.[5] Since then, the field of OFETs has gained significant attention and nowadays organic semiconductors reach charge carrier mobilities >1 cm^2/Vs for solution processed devices, comparable to amorphous silicon.[11–13] The key advantage of organic field-effect transistors is that they can be implemented as fundamental matrix elements in inexpensive, flexible and transparent displays, fabricated through printing or other solution-based, low-temperature deposition techniques.[6,14] Scientifically, organic field-effect transistors are a powerful tool to evaluate the charge transport properties, performance and stability of newly synthesised organic semiconductors.[15,16] However, the extracted performance and in particular the charge carrier mobility measured in a field-effect transistor configuration should not be understood as the intrinsic material property, as this parameter is affected by among others, the device architecture, the fabrication process and the resulting film morphology.

Field-effect transistors are typically vertically stacked devices that consist of different layers, in which charge transport occurs in lateral direction within the channel of the active layer. An organic field-effect transistor requires, similarly to its inorganic counterpart, three main electrodes to operate the device. The current between the source and the drain electrodes is controlled by the applied voltage at the gate electrode. The organic semiconductor (active layer) is contacted by the source drain electrodes separated by the channel length L and a width W. This active layer is typically deposited through various deposition methods including spin-coating, thermal evaporation, drop-casting, spray-coating, printing or other techniques.[17] The active layer is separated through a dielectric layer from the gate electrode which controls the channel current (**Figure 2**).
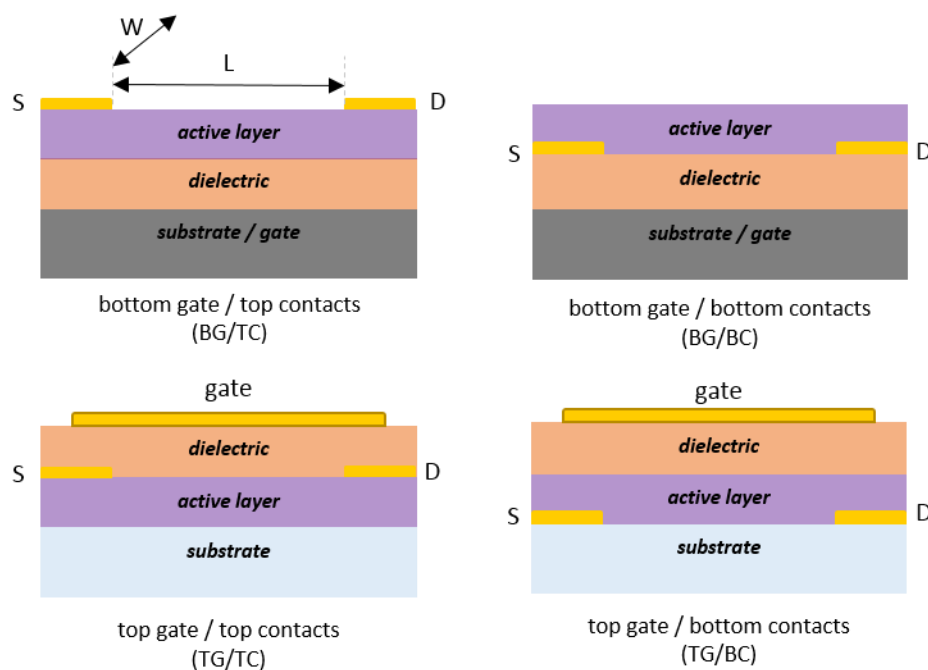
Figure 2. Schematic cross-section of field-effect transistors in four different geometries.

The simplest way to fabricate an organic field-effect transistor is the use of highly doped silicon wafer, acting as gate electrode and substrate, coated with thermally grown silicon dioxide as dielectric. Alternatively, non-conductive substrates such as glass or plastic are utilised for field-effect transistors and all three electrodes have to be subsequently structured. There are mainly four distinct configurations in which an FET can be structured: bottom-gate/ bottom-contact (BG/BC), bottom-gate/ top-contact (BG/TC), bottom-contact/ top-gate (BC/TG) and top-contact/ top-gate (TC/TG) architecture. Each device architecture provides certain advantages and disadvantages for the fabrication process. Studies of organic materials presented in this work utilised the BG/BC, BG/TC and BC/TG architectures to evaluate the performance in thin film transistors.

The intrinsic free charge carrier concentration in commonly used organic materials is not sufficiently high to allow for significant current to flow between source and drain electrodes. Only upon an application of a voltage between the source and gate electrodes, charges are injected into the material. Conventionally, the source electrode is grounded and the potential at this electrode is 0 V. A positive gate voltage results in the injection of electrons (n-channel FET or n-type), while a negative gate voltages will result in the accumulation of holes (p-channel FET or p-type). If then a small voltage between source and drain is applied, the charge carriers will travel through the channel to the drain electrode. Based on this simple working principle the current voltage (I-V) characteristics of a field-effect transistor can be derived.[15,16,18]

2.1.2. Current-Voltage Characteristics of a Field-Effect Transistor

The amount of accumulated charges as a function of the applied voltage V_G between source and gate is proportional to the capacitance of the device, similar to a plate capacitor. If no voltage between source and drain is applied, the density of charges in the channel is uniform in lateral direction. The amount of charges per area Q [C/m²] in the cannel can then be expressed as:

$$Q = C \cdot V_G \tag{1}$$

whereas C is the capacitance per area. Not all induced charges will contribute to a current and the amount of effective mobile charges can be expressed by correcting the gate voltage in equation (1) to an effective voltage V_G-V_{th} resulting in equation (2):

$$Q_{mobile} = C \cdot (V_G - V_{th}) \tag{2}$$

One can understand the introduction of the threshold voltage V_{th} as a voltage that has to be compensated to fill existing trap states before mobile carriers are present in the material. Impurities or a doping of the material can result in mobile carriers present already at $V_G = 0$ V. In this case an opposite voltage has to be applied to deplete the channel.

The charge carrier density between source and drain electrode turns into a function of the position x in the channel when a small voltage V_D (<< V_G) between source and drain is applied. Hereby is $V_{(x=0)} = V_S = 0$ V and $V_{(x=L)} = V_D$, resulting in a linear gradient for the charge distribution in the transistor channel, assuming Ohm's law. For a given position x in the channel one can write the amount of mobile charges therefore as:

$$Q_{mobile}(x) = C \cdot \left(V_G - V_{th} - V(x)\right) \tag{3}$$

These mobile charges are located between the electrodes and occupy a volume $W \cdot L \cdot h$, where h is the thickness of the accumulation layer, occupied by the injected and mobile charges. For the current that can be measured at the drain electrode one can write:

$$I_d = W \cdot h \cdot \sigma \cdot E(x) \tag{4}$$

with $E(x)$ being the electric field between source and drain electrode at a given position x. Using the relationship between conductivity and mobility equation (4) turns into equation (5):

$$I_d = W \cdot \mu \cdot Q_{mobile}(x) \cdot E(x) \tag{5}$$

or alternatively:

$$I_d = W \cdot \mu \cdot Q_{mobile}(x) \cdot \frac{dV(x)}{dx} \tag{6}$$

This equation can be integrated with the conditions mentioned above for $V(x)$:

$$\int_0^L I_d \, dx = \int_0^{V_D} W \cdot \mu \cdot C \cdot \left(V_G - V_{th} - V(x)\right) \, dV(x) \tag{7}$$

and finally results in equation (8)

$$I_d = \frac{W}{L} \cdot \mu \cdot C \cdot \left((V_G - V_{th}) \cdot V_D - \frac{V_D^2}{2}\right) \tag{8}$$

when a constant (field independent) charge carrier mobility is assumed. Furthermore, equation (8) is only valid for the gradual channel approximation, meaning that the electric field created by the gate electrode is perpendicular to the flow of charges and much larger than the field generated by the drain potential. This assumption is correct as long as the channel length L is significantly larger than the separation between active layer and gate electrode. For short channels or thick dielectric layers it is therefore no longer valid.

For a small drain potential ($V_D \ll V_G$) equation (8) can be simplified to equation (9):

$$I_d = \frac{W}{L} \cdot \mu \cdot C \cdot \left((V_G - V_{th}) \cdot V_D\right) \tag{9}$$

In this linear regime the channel current is directly proportional to the drain potential. If the gate voltage is kept constant the measured current increases linearly with increasing drain voltage. The charge carrier mobility in the linear regime can be extracted from the measured channel current using equation (10):

$$\mu_{lin} = \frac{\partial I_d}{\partial V_G} \cdot \frac{L}{W \cdot C \cdot V_D} \tag{10}$$

If the drain voltage is increased further and reaches $V_D = V_G - V_{th}$ the density of mobile charges reaches zero at the drain voltage and upon further increase of the drain voltage a depletion zone forms (pinch-off). This depletion zone increases with increasing drain voltage, but remains small compared to the channel length L.[15] Due to the relatively high electric field in the depletion region a space charge limited current can flow across the narrow depletion zone and the channel current cannot be further increased (saturation regime). This is expressed in equation (11) which no longer depends on V_D:

$$I_d = \frac{W}{2L} \cdot \mu \cdot C \cdot (V_G - V_{th})^2 \tag{11}$$

In the saturation regime the square root of the saturation current is directly proportional to the gate voltage and a linear fit allows the extraction of the threshold voltage as the intercept with the V_G axis. The mobility in the saturation regime can be obtained from the slope of this fit following equation (12):

$$\mu_{sat} = \frac{2L}{W \cdot C} \cdot \left(\frac{\partial \sqrt{I_d}}{\partial V_G}\right)^2 \tag{12}$$

There are typically two ways to represent the I-V characteristics of a field-effect transistor. In an 'output characteristic' the channel current is measured at different gate voltages which are kept constant and the drain voltage is varied (**Figure 3a**). The channel current exhibits for small drain voltages a linear behaviour and saturates when the source drain voltage exceeds V_G-V_{th}. Alternatively, the channel current is measured as a function of V_G at a constant drain voltage, named a 'transfer characteristic' (**Figure 3b**). Depending on the drain voltage, the channel current is proportional to V_G (linear regime) or its square root increases linearly with increasing gate voltage (saturation regime).
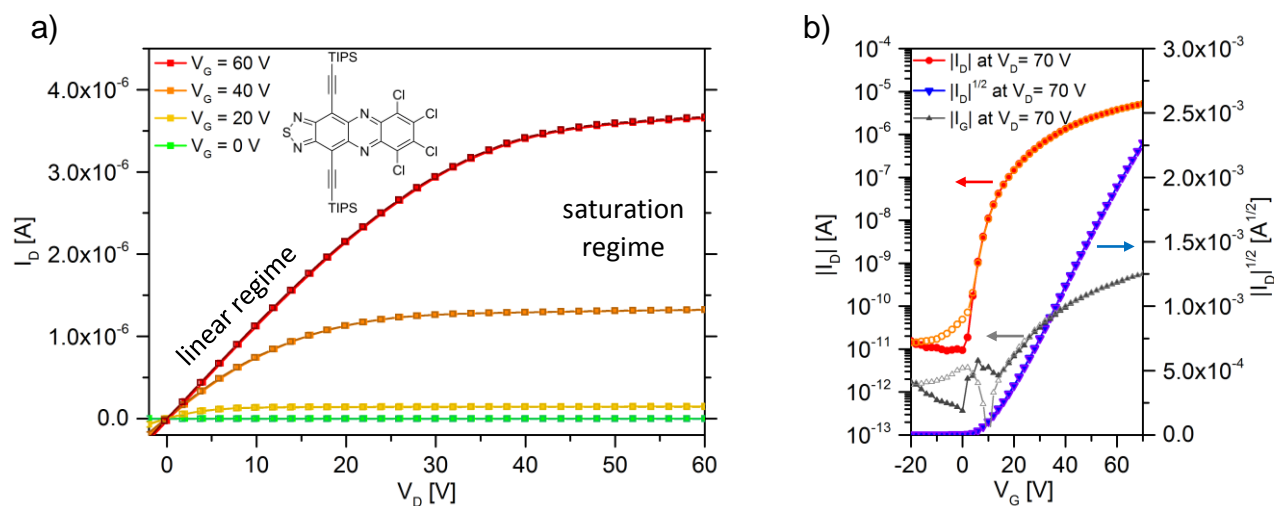
Figure 3. I-V characteristics of a field-effect transistor with an organic material (**Cl₄-Phen**, see inset or **Chapter 7**) investigated in this work. The device is measured from the off to the on state (forward sweep is depicted as filled symbols; backward sweep open symbols). (a) Output-characteristic for various gate voltages. (b) Transfer characteristics in the saturation regime (V_D = 70 V); (both W = 1,000 µm, L = 50 µm).

The on/off-ratio is another important parameter of a field-effect transistor that can be easily extracted from a semi logarithmic plot of the channel current versus gate voltage and represents the ratio between the channel current in the on-state an the channel current in the off-sate. A high on/off-ratio is desired as it represents a good switching behaviour of the device. The transistion between off and on state can be characterised by the subthreshold swing S which is definded as:

$$S = \frac{\partial V_G}{\partial (log I_d)} \tag{13}$$

and is typically given in [V/dec]. A fast transiston from the off to the on state is represented in a small subthreshold swing and is not only determined by the semiconductor used in the transistor but also affected by the device architecture, capacitance of the dielectric and denisty of trap states at the interface.

It has to be noted that the equations derived above for the I-V characteristics of a field-effect transistor and the equations (10) and (12) for mobility extraction include several assumptions and represent an ideal transistor behaviour. Extracting FET parameters can be difficult if a non-ideal transistor behaviour is observed.[6,19] Nevertheless, the hunt for ever higher mobility values for organic semiconductors results

sometimes in a questionable data interpretation, for example, linearly fitting a non-linear square root plot of the channel current to obtain the highest carrier mobility possible.[20,21] In addition, it is essential to present both the forward and backward sweeps of the I-V characteristics to judge if the channel current changes upon measurement due to possible instabilities of the organic material or the population of trap states in the material or at the dielectric interface. There is no way to judge the reliability of charge carrier mobility extraction if the sweep rate is used to mask these internal device processes or only one sweep is given. A non-equilibrium charge carrier distribution in such scenarios might lead to a gross overestimation of the charge carrier mobility.[6,22] Furthermore, the applied model for equation (8) assumes that the entire voltage between source and drain drops along the channel and neglects any contribution of the contacts at the metal/organic interface. Contact resistance can be a major problem in organic field-effect transistors and might affect the I-V characteristics. Often a non-linear behaviour of the square root plot of the channel current is observed in such devices, based on the varying effects of the contact resistance with increasing gate voltage. Extracting a charge carrier mobility from a linear fit of a non-linear I-V characteristic but at the point of maximum slope as can be seen by the examples in **Figure 4** might result in a gross overestimation of the real charge carrier mobility.
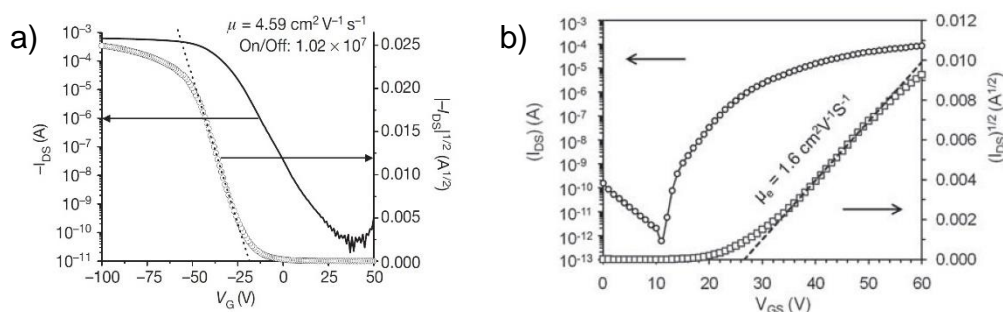
Figure 4. Common examples of a linear fit to a non-linear square root plot of the channel current for (a) a OFET with 6,13-bis(triisopropylsilylethynyl)pentacene (**TIPS-PEN**) from Giri *et al.*[20] (Reproduced with permission, copyright 2011, Nature Publishing Group) and (b) OFET with 6,13-bis(triisopropylsilylethynyl)-5,7,12,14-tetraazapentacene (**TIPS-TAP**) from Liang *et al.*[21] (Reproduced with permission, copyright 2011, John Wiley and Sons).

It is important to note that the equations above treat the charge carrier mobility as a constant and intrinsic property of the material and the integration of equation (7) assumes the mobility is field-independent, which does not necessarily represent the reality accurately enough. Many models have been proposed to describe charge transport processes in organic materials more accurately, including the introduction of electric field dependence. Some of these models are briefly described next. [6,14,23,24]

2.1.3. Charge Transport in Organic Materials

An efficient charge transport through organic semiconductors requires that the charges can travel from one electrode to the other and are not trapped or scattered along their way. Numerous parameters will affect the mobility of the charge carriers through the material, such as temperature, concentration of impurities,

molecular structure and molecular packing, degree of order/disorder, the charge carrier density and many more.[14,16,23] Organic materials exhibit a broad range of mobilities ranging from 10^{-6} cm^2/Vs to over 30 cm^2/Vs depending on the material, its purity and deposition method.[14,25] Several transport mechanisms and models have been proposed for organic semiconductors to describe this wide range of observed mobilities and were controversially discussed.[6,23,26,27] High mobilities in highly purified and well-ordered materials like single crystal rubrene or tetracene >1 cm^2/Vs have been reported and correlated with a band-like transport in organic materials similar to inorganic materials such as silicon.[28] The indication for this type of transport is an increasing charge carrier mobility with decreasing temperature as lattice vibrations become less dominant and the charge transport is no longer affected by phonon-scattering.[28,29] Other theories assume a more localised charge transport and take into account that the intermolecular interactions between organic molecules in the solid state are significantly weaker than in inorganic materials.[14,18,30] These weak interaction result in the electronic wave functions being localised on a finite number of molecules rather than being delocalised over the entire bulk of the material. The charge transport is characterised by the promotion of the charge carriers out of these localised states, resulting in an increasing mobility with increasing temperature as this process is thermally activated. Several models exist to describe the transport based on the energies of the localised states, their distribution and the transfer processes and are not discussed here.[24,26]

Assuming charges are localised on the single molecules of an organic semiconductor, the electronic interactions to neighbouring molecules determine the efficiencies of the charge transfer process. When considering a semiconductor composed of small molecules with conjugated π-systems, the electronic coupling of the frontier molecular orbitals in the solid state is strongly affected by the molecular orientation in the bulk. Brédas and co-workers have demonstrated that the transfer integrals of neighbouring molecules are very sensitive towards the relative orientation of the π-systems and affect the transfer of holes and electrons differently.[23] This is depicted in **Figure 5** were the transfer integral t is given for a different orientation of two cofacially oriented tetracene molecules. The relative orientation of the acene cores towards each other determines if a transfer of a hole or an electron is more efficient.
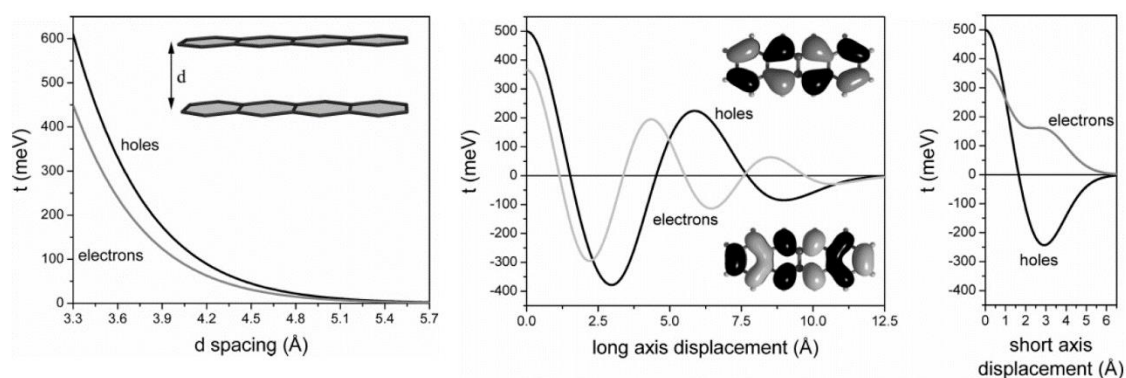

Figure 5. Evolution of the transfer integrals for holes an electrons for different orientations in a co-facial tetracene dimer. (Reproduced with permission from Ref. [23]; Copyright 2007, American Chemical Society.)

The charge transfer process is described by the classical approaches of Marcus theory, defining rate of the charge transfer k_{et}. In this approach, it is proposed that the charge carrier mobility is proportional to the charge transfer rate.[31] A large transfer integral and a low reorganisation energy λ_{reorg} will therefore enhance the resulting charge carrier mobility (equation (14)).

$$\mu \propto k_{et} \propto \frac{1}{T} \cdot t^2 \cdot e^{\left(-\frac{\lambda_{reorg}}{4k_B T}\right)} \tag{14}$$

The molecular overlap of the conjugated π-systems can be effectively tuned by the molecular structure that governs the solid state packing. The steric of side-chains or the incorporation of functional groups that order the semiconductor based on donor-acceptor interactions are typical examples how a rational chemical design can affect the solid state packing and therefore impact the charge transport properties.[32–34]

The charge transport also critically depends on the degree of order of the organic semiconductor and the density of structural or chemical defects in the solid state. This includes variations of the molecular weight in polymers or the isomeric purity of small molecules. The microstructure and morphology of an organic semiconductor influence the charge transport properties of the film and are affected by the properties described above as well as the processing conditions used for film fabrication. One of the first examples of a correlation between microstructure and charge transport was shown for field-effect transistors utilizing poly(3-hexyl)thiophene (**P3HT**).[35] The polymer exhibited higher mobilities if the solubilising side-chains are regioregularly attached to the polymer backbone compared to regiorandom **P3HT**. The alkyl chains in regioregular **P3HT** allow a larger conjugation length of the polymer and the material forms self-organised lamellar structures that allow a better charge transfer due to a better π-system interaction.[36] Furthermore, the deposition method of the organic semiconductor determined if the thiophene systems were oriented face-on or edge-on towards the substrate. The lateral charge carrier mobilities within the film parallel to the substrate's surface were two orders of magnitude higher in the lamellar edge-on orientation.[35]
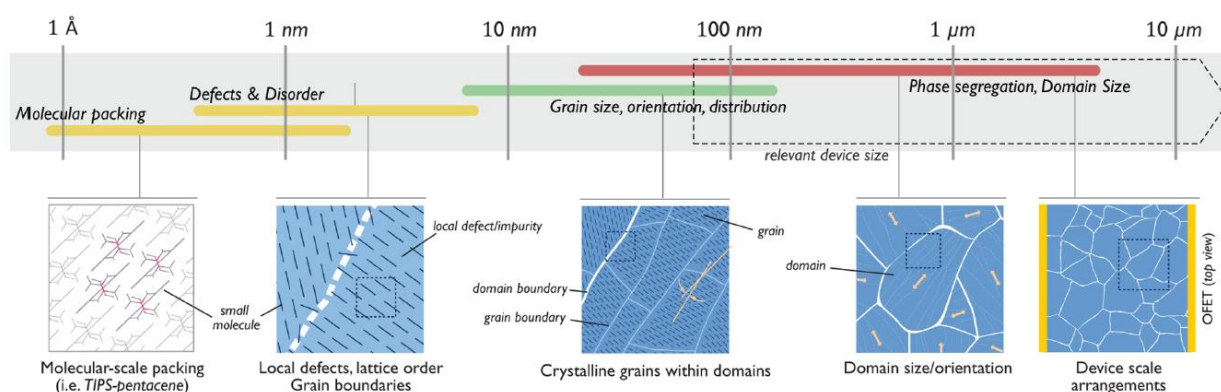

Figure 6. Illustration of the morphological features of a small molecule applied in a thin film transistor and differentiation of order and microsturcture based on its length scale. (Adopted with permisson from Ref. [37], Copyright 2012, American Chemical Society)

Similarly, not only the molecular structure of small molecule semiconductors, but also the processing of the active layer and its microstructure will determine the device performance. The precise control of the film formation process over various length scales, ranging from the molecular packing on an angstrom level up to domain sizes of several 10-100 micrometres, will affect the macroscopic charge transport properties of this film (**Figure 6**). Small molecules often exhibit polycrystalline films and grain boundaries and differently oriented domains can perturb the charge transport. However, due to the defined molecular structure and distinct molecular packing in the solid state the inherent order of small molecules is typically higher than in polymers, resulting in overall higher mobilities.[13] Nonetheless, charge transport over grain boundaries or between differently oriented domains might be difficult and typically result in low charge carrier mobilities, demonstrating the need for careful process optimisation for each material.

2.1.4. Electrodes

Charge injection into the organic material in a transistor occurs typically from metal electrodes. For a p-type transistor holes must be injected into the highest occupied molecular orbital (HOMO) of the semiconducting materials, while for n-type transistors electrons have to be injected into the lowest unoccupied molecular orbital (LUMO) of the semiconductor. The choice of metal and the interface to the organic material affects the efficacy of charge injection. To understand the differences of charge injection a simplistic energy diagram in the case of vacuum level alignment (Schottky-Mott limit) is given in **Figure 7**. The contact between the metal and organic is typically defined by an injection barrier ($\phi_{electron}$ or ϕ_{hole}), which can be understood as difference between work function of the metal ϕ_{metal} and the energetic position of the HOMO or LUMO level of the semiconductor.[38] In absence of interfacial dipole formation, the contact metal's work function determines therefore the height of the charge injection barrier for electrons and holes. An ohmic contact between a metal and an organic is achieved when the injection barrier is small. A high non-ohmic contact is represented in a non-linear behaviour of the channel current in the output characteristic of a field-effect transistor.
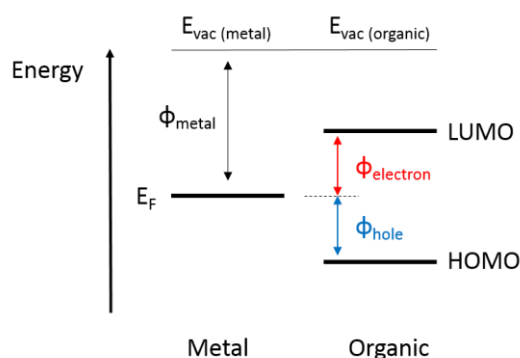
Figure 7. Schematic energy level diagram and injection barriers for hole and electron injection of a metal/organic contact.

The energy level diagram above does not account for interfacial dipoles at the metal/organic interface that can alter the charge injection barriers. The application of self-assembled monolayers is a possibility to tune

the work function of metals in order to lower the injection barrier for the desired charge carrier. Commonly, thiols are utilised to modify the work function of gold and silver electrodes due to formation of dense and well-defined monolayers.[39] Based on the dipole formed at the interface the work function of the electrode can be increased or lowered upon modification with a self-assembled monolayer, boosting hole or electron injection, respectively.[39,40]

Typically gold electrodes are used in organic field-effect transistors due to their excellent chemical stability and simple deposition through thermal evaporation. Silver electrodes attracted a significant interest over the last years as they allow a solution-based fabrication from silver inks.[41] The commonly accepted differentiation into p- and n-type materials does not represent an intrinsic property of the organic semiconductor, but originates from the observation of a hole or electron transport while gold or silver act as the metal contact. The typical work function of 4.9-5.2 eV for gold electrodes requires a deep LUMO level of the organic materials to act as n-type semiconductors.[42,43]

2.1.5. Gate Dielectrics

The transport of accumulated charges in a field-effect transistors occurs in close proximity (1-2 nm) to the interface between active layer and gate dielectric layer.[15,44] The properties of the interface therefore heavily determine the I-V characteristic and performance of the device. The thickness of the accumulation layer in which the charge transport occurs is in the range of the thickness of a monolayer for a small molecule. The interface between the organic semiconductor and the dielectric has to be therefore very smooth, flat and free of trap states to allow an efficient charge transport. The gate dielectric must also exhibit a high breakdown voltage to allow the operation of the device at high gate voltage and high charge carrier densities. Typically values of >1 MV/cm are desired.[45] This high electric stability can only be achieved if the dielectric material is free of impurities.

The amount of charges for a given gate voltage that can contribute to the channel current is proportional to the capacitance of the dielectric layer (see equation (2)). To enhance the channel current the thickness of the dielectric layer could be reduced or a dielectric material with a high dielectric constant need to be chosen. However, Veres *et al.* demonstrated that the mobility of an organic semiconductor depends on the dielectric constant ε_r of the dielectric material. According to the transport model from Bässler in disordered systems, an additional energetic disorder at the interface between the active layer and the dielectric is introduced with increasing ε_r, resulting in a broadening of the density of states close to the interface and therefore lowering of the mobility.[46,47]

Thermally grown silicon dioxide (ε_r = 3.9) on doped silicon wafers is often used as an inorganic dielectric due to its smoothness, reliable quality and commercial availability.[44] The surface of this oxide exhibits hydroxyl
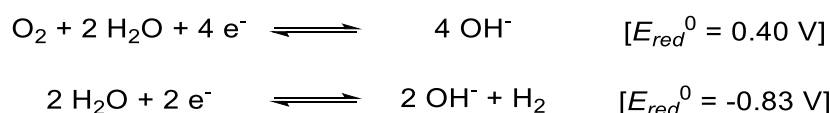
groups that can act as trap states for charge transport.[18] For several years it was commonly believed that electron transport in organic materials was much more difficult to achieve than the transport of holes. Chua *et al.* demonstrated that electron transport in a variety of organic materials, which were known to exhibit good hole transport mobilities, could be observed simply through changing the interface between dielectric and active layer by passivating the surface of silicon dioxide through introduction of a benzocyclobutane (BCB) interlayer.[45] The passivation of the hydroxyl groups of the silicon dioxide surface is mandatory to observe an efficient transport of electrons and to study and evaluate materials such as N-Heteroacenes as electron transporting compounds in organic field-effect transistors. It is also possible to utilize self-assembled monolayers such as alkyl chloro silanes to chemically passivate the hydroxyl groups.[48] However, the introduction of alky chains lowers the surface energy and influences the wettability with organic solvents and as a result affect adversely the film formation. Depositing the dielectric material on top of the active layer requires the choice of an orthogonal solvent to avoid mixing of both materials and dissolving of the underlying organic layer.[49]

2.1.6. Stability and Stress

For an application of organic semiconductors in modern electronics high mobility values are desired, as this parameter determines, for example, the effective switching times an active matrix displays.[14] But the charge carrier mobility is not the only key parameter to be considered, as future applications of organic semiconductors require a stable and reliable device performance with a large uniformity of the fabricated devices.[6] It has been observed for many organic semiconductors that the channel current and device performance vary as a function of time during operation and depend on the previously applied voltages and the history of the device. One of the most common observation is the shift of the threshold voltage upon gate bias stressing.[11,22,50–52] It has been reported that an applied gate voltage in the same order of magnitude used for operation of the transistor results in a shift of the threshold voltage in the same direction. This has been attributed to trapped charge carriers in localised states in the channel region, which still contribute to the overall electrostatic charge balance, but are immobile so that higher gate voltages are required to achieve the same charge carrier density and channel currents [22] Often a thermal treatment or illumination with light of wavelengths above the bandgap can help to release trapped charge carriers and results in a partly recovery of the original performance.[53] The nature of the trap states is often unknown, however defects and impurities in the organic semiconductor or/ and at the interfaces may serve as cause.[22] Additionally, the organic material may degrade upon electrical stressing introducing by-products that can form new trap states. Results from Kalb *et al.* demonstrated that rubrene transistor of single crystals with a very low density of defects exhibited a stable transistor performance over hours, while polycrystalline pentacene transistors suffered from significantly larger threshold voltage shifts.[54] The bias-stress behaviour also strongly depends on the

employed electrode and dielectric materials. Transistors with CYTOP[TM] as dielectric showed a small shift in threshold voltage upon bias stressing as compared to other dielectric materials.[55,56]

One of the biggest challenges for a wide application of organic materials in organic electronic devices is their stability against oxygen and water. Especially n-type transistors with a high density of electrons in the operating regime exhibit radical anions of the organic semiconductor which tend to degrade in ambient conditions depending on the oxygen and humidity levels. This degradation is related to the electron affinity of the organic material. The reduction of oxygen and water are described in **Scheme 1** and their electrochemical standard potential for pH = 7 against the standard hydrogen electrode (SHE) is given.[57]

$$O_2 + 2\ H_2O + 4\ e^- \rightleftharpoons 4\ OH^- \qquad [E_{red}^0 = 0.40\ V]$$

$$2\ H_2O + 2\ e^- \rightleftharpoons 2\ OH^- + H_2 \qquad [E_{red}^0 = -0.83\ V]$$

Scheme 1. Reduction of oxygen (top) and water (bottom) and their standard potential vs. SHE.

While neglecting any intermolecular interaction, polarisation, reorganisation of the charged molecule and overpotentials the organic semiconductor should exhibit a LUMO level deeper than that given in equation (15) to exhibit a stability against oxidation from water or air, based on the Gibbs free energy $\Delta G^0 > 0$: [57]

$$E_{LUMO} < -4.44\ eV - e \cdot E_{red}^0 \qquad\qquad (15)$$

These basic consideration require the position of the LUMO of the organic semiconductor to be below -4.84 eV to exhibit a stability against air and humidity. However, several studies have shown, that the reduction of oxygen exhibits a high overpotential and therefore LUMO energies of approximately -4.6 eV can result in semiconductors stable to ambient conditions.[22,58,59]

2.2.   Materials

Academic and industrial research in the field of organic semiconductors resulted in numerous organic compounds investigated over the last decades. The vast majority of organic semiconductors can be split into two categories – conjugated polymers and small molecular compounds.[11,13] Synthetic chemistry allows to finely control the molecular structure of the material and therefore its optical, electronic and solid state properties. A high transistor performance requires materials with efficient charge transport properties. The strong electronic coupling of molecules such as the interaction of π-systems in the solid state allows an efficient charge transport of charge carriers in the semiconducting layer. Linear acenes are a class of materials that exhibit this desired feature in their solid state and are used in a large variety of electronic and optoelectronic devices.[60]

2.2.1. Linear Acenes

The large aromatic π-systems of linear acenes can be easily synthesised and purified even in high amounts resulting in defined molecular structures. Modern organic chemistry (especially palladium mediated cross coupling reaction or C-H activation) allows efficient modifications of the molecular design and introduction of solubilising side-chains or the annulation and substitution of the core structure, resulting in a wide variety of organic semiconductors. The molecular structure of the acene molecule defines not only the optical and electronic properties of the material, but also affects other important parameters such as aggregation (or separation) of the single molecules in the solid state, the solubility and other film forming properties that all play a role in determining the final device performance. Acenes typically exhibit two different motifs of solid state interaction. In the so-called herringbone motif the acenes are oriented face to-edge towards each other, while the other motif consists of cofacially oriented acenes.[60] The π-π-interaction in the latter case is typically stronger than in a 'herringbone' packing and is characterised by a relative displacement of the acenes along the short and long axis of the aromatic system within the stack. In some materials the columns of stacked acenes exhibit strong interaction to an adjacent stack, resulting in a 2-dimensional (2-D) packing of the π-system. This so-called 'brickwork' arrangement has been proven to result in about two orders of magnitude higher charge carrier mobilities than those observed for one-dimensional stacked acenes (1-D) (compare **Figure 9**).[6,61,62]
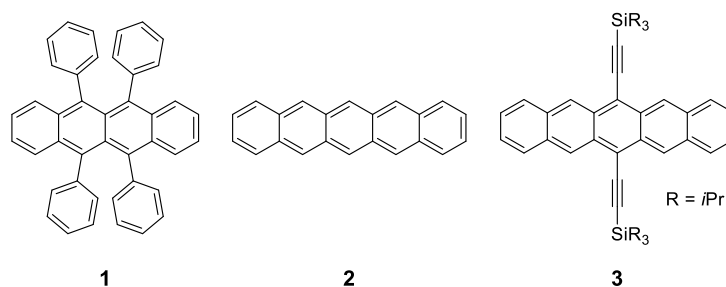
Figure 8. Molecular structure of rubrene (**1**), pentacene (**2**) and 6,13-bis(triisopropylsilylethynyl)pentacene (**3**).

One of the most studied acene derivatives for charge transport in OFET is the tetracene derivative rubrene (**1**) (**Figure 8**). It exhibits a strong π-π-interaction in the solid state and was one of the first materials for which hole transport in organic materials was studied. In highly purified single crystals rubrene exhibits high charge carrier mobilities >20 cm^2/Vs and Hall measurements revealed a band-like transport.[63,64] Rubrene cannot be reliably deposited by thermal evaporation due to the formation of different polymorphous phases and an irregular film, resulting in low quality and polycrystalline layers with significantly lower transistor performance.[65,66]

Pentacene (**2**) on the other hand is typically thermally evaporated due to its very poor solubility in common organic solvents. Pentacene exhibits a herringbone packing motif in its solid state, but also other different polymorphous phases were reported.[67] Every polymorph exhibits different charge transport properties depending on the molecular interaction in the solid state.[67,68] Due to its HOMO position (4.85 eV), pentacene is typically used as hole transporting material, but electron transport has also been demonstrated when the interface with the dielectric layer is quasi trap free and low work-function electrodes were chosen.[69–71] Polyvinyl alcohol (PVA) and calcium /gold electrodes were utilised to demonstrate electron and ambipolar transport in pentacene.[72] In single crystals pentacene exhibits hole mobilities of up to 35 cm^2/Vs while evaporated polycrystalline films typically show hole mobilities of 0.1-1 cm^2/Vs.[25,61,73] The charge carrier mobility in pentacene and its transistor performance critically depend on its purity. One of the major impurities of pentacene and main degradation product by exposure to oxygen is 6,13-pentacenequinone.[74] Studies from Reddy *et al.* showed that oxygen forms an endo peroxide with pentacene at the middle ring, which then further reacts to the pentacenequinone.[75]
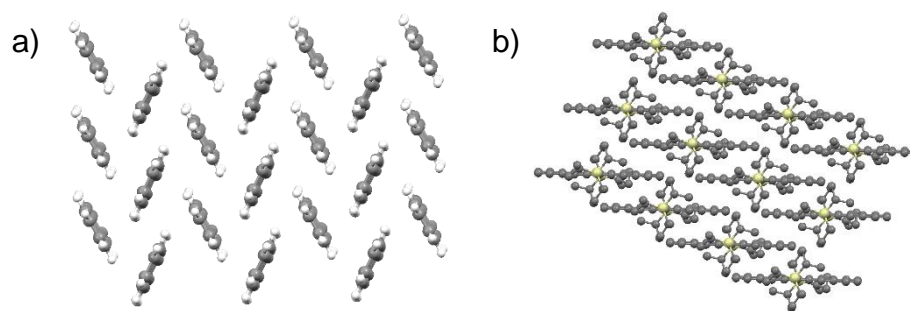
Figure 9. Solid state packing of (a) pentacene (**2**) and (b) **TIPS-PEN** (**3**). Structures based on single crystal data from Campbell *et al.*[76] and Anthony *et al.*[77]; view almost along c-axis, hydrogen atoms removed in (b).

The introduction of ethynyl side chains at the middle ring of the pentacene core was first reported by Anthony *et al.* with the most popular representative of this approach being the triisopropylsilylethynyl pentacene derivative (**TIPS-PEN**) (molecular structure **3** in **Figure 8**), several major advances for the application of pentacene in organic electronic devices were consequently achieved.[77] First, the side chains increased dramatically the solubility of the material and films of this functionalised pentacene could be deposited through solution-based techniques such as spin-coating, drop-casting, spray coating, printing and more.[17] Secondly, the position of the substituents at the middle ring prevented the oxidation in air, resulting in an air-stable performance in field-effect transistors. Last but not least, the molecular packing was modified based on the trialkyl silyl group.[78,79] All 6,13-bis(trialkylsilylethynyl)pentacenes show a co-facial orientation of the aromatic systems in the solid state. Based on the spherical size of the alkyl silyl group the long axis displacement varies in these pentacene derivatives.[32] A diameter of roughly the half of the acene length results in a 2-D packing motif, while larger or smaller groups favour a 1-D column like stacking of the acenes.[78] The charge carrier mobilities are strongly impacted and are highest for the 2-D case, reaching up to 1.5 cm^2/Vs for solution deposited films.[62,80–82] Also, the anisotropy of the charge transport is dramatically reduced for the 2-D packed derivative as theoretical calculations and experiments demonstrated.[83] Not only the charge transport properties of **TIPS-PEN** are superior compared to that of 1-D stacked pentacenes, the 2-D packing motif in the solid state and its layered structure is predominantly the cause of the excellent film formation and transistor performance. Due to a strong preferred (00*l*)-orientation of this functionalised acene, the aromatic core is ideally oriented for lateral charge transport between the electrodes of a transistor.[6,60,82] Spin-coating of **TIPS-PEN** often results in polycrystalline films with spherulitic domains (spherulites). The domain size increases with increasing boiling point of the solvent as the molecules have more time to organise and less nucleation sites are formed upon precipitation due to a slower evaporation rate of the solvent.[84,85] Films that consist out of such spherulites exhibit high mobilities (>1 cm^2/Vs), a low anisotropy of charge transport and the gradual change of the molecular orientation within the spherulites seems not to significantly affect the overall charge carrier mobility as compared to sharp grain boundaries.[29,86,87]

Further enhancement of the thin film transistor performance of pentacene and **TIPS-PEN** has been achieved by utilising the zone-casting deposition technique to improve the microstructure of the active layer.[83,88–90] This controlled deposition of an organic solution of the semiconductor results in highly ordered, crystalline films and was first used for a hexabenzocoronene derivative by Müllen and co-workers.[91,92] The slow evaporation of the solvent and the precise control over the deposition temperatures results in the formation of uniaxially aligned crystalline strands of the organic semiconductors, which exhibit a large anisotropy in their charge transport behaviour.[4] Such film morphologies were also obtained from other slow deposition techniques like dip-coating or modified drop-casting methods.[93,94] Other groups have adopted this approach and modified the deposition process in the recent years, resulting in impressive enhancement of the charge carrier mobilities. The group of Bao has demonstrated that depending on the speed of deposition metastable polymorphous phases can be formed that exhibit significantly different charge transport properties.[20,95,96]

Several structural variations of **TIPS-PEN** have been synthesised over the last decade and have been investigated in thin film transistors. Two soluble acene derivative (**diF-TES-ADT** and **TMTES-PEN**) with outstanding transistor performance are shown in **Figure 10**.[97,98] Kim *et al.* showed, that a careful engineering of the side groups of **diF-TES-ADT** can results in a large enhancement of the charge carrier mobility. This was achieved by substitution of the silyl atom with germanium (**diF-TEG-ADT**), which strengthened the van der Waals' interaction in the solid state and lower as the π-π-stacking distance, resulting in an increase of the hole mobility by a factor of 4, reaching 5.4 cm^2/Vs.[99,100]
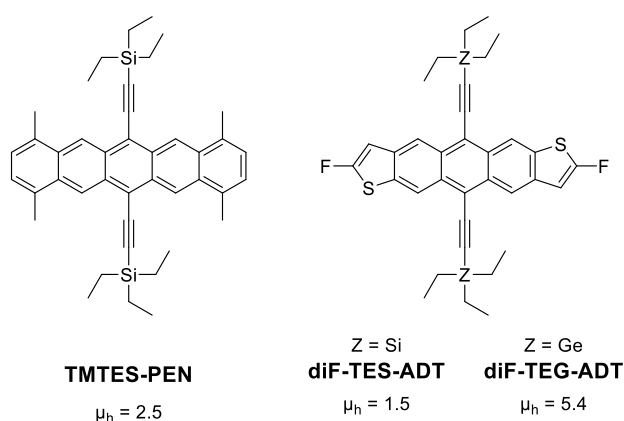
Figure 10. Molecular structure of high-performance **TIPS-PEN** derivatives: 1,4,8,11-tetramethyl-6,13-triethylsilylethynylpentace (**TMTES-PEN**); 2,8-difluoro-5,11-bis(triethylsilylethynyl)anthradithiophene(**diF-TES-ADT**) and 2,8-difluoro-5,11-bis(triethylgermanyl-ethynyl)anthradithiophene(**diF-TEG-ADT**) their hole mobilities (in [cm^2/Vs]).[97,98]

2.2.2. Pentacene-based polymers

Pentacene and **TIPS-PEN** have been also used as building blocks of semiconducting polymers (**Figure 11**).[101] One of the first polymers **4** was synthesised and employed in OLEDs by Tokito *et al.* in 2001.[102] The TIPS-ethynyl substituted pentacene polymers **5**-**7** were synthesised and investigated in the group of Bao. All three polymers exhibited an ambipolar transport in bottom-gate top contact transistors. The 2,10-connected

polymer **5** exhibited electron mobilities of up to $3 \cdot 10^{-5}$ cm^2/Vs and hole mobilities of $8 \cdot 10^{-6}$ cm^2/Vs, while the 2,9-polymer **6** exhibited a mobility of $1 \cdot 10^{-4}$ cm^2/Vs and $5 \cdot 10^{-5}$ cm^2/Vs for electron and holes, respectively. The random polymer **7** exhibited only an electron transport in the range of 10^{-7} cm^2/Vs.[103,104] Polymer **8** and **9** were also synthesised in the group of Bao and applied in thin film transistors and photovoltaic devices. The performance strongly varied based on the regioregularity of the polymer. Polymer **9** exhibited hole mobilities based on its structure between $4.6 \cdot 10^{-4}$ to $1.3 \cdot 10^{-3}$ cm^2/Vs and **8** showed hole and electron mobilities in the range of 10^{-2} cm^2/Vs when correctly modified dielectric and deposition method are chosen. The power conversion efficiency (PCE) of solar cells in standard architecture and [6,6]-Phenyl-C61-butyric acid methyl ester (PCBM) as acceptor reached 0.13% and 0.33% for **8** and **9**, respectively. The solid state interaction of all pentacene based polymers are weak and especially the regiorandom polymers **7**-**9** do not exhibit a high degree of order and form rather amorphous films. To compensate this effect a new synthetic route was employed by Kumarasamy *et al.* to build up discrete oligomers and polymers **10** and **11**.[105] So far no device performance for these new compounds has been reported.

Figure 11. Examples for pentacene containing polymers.
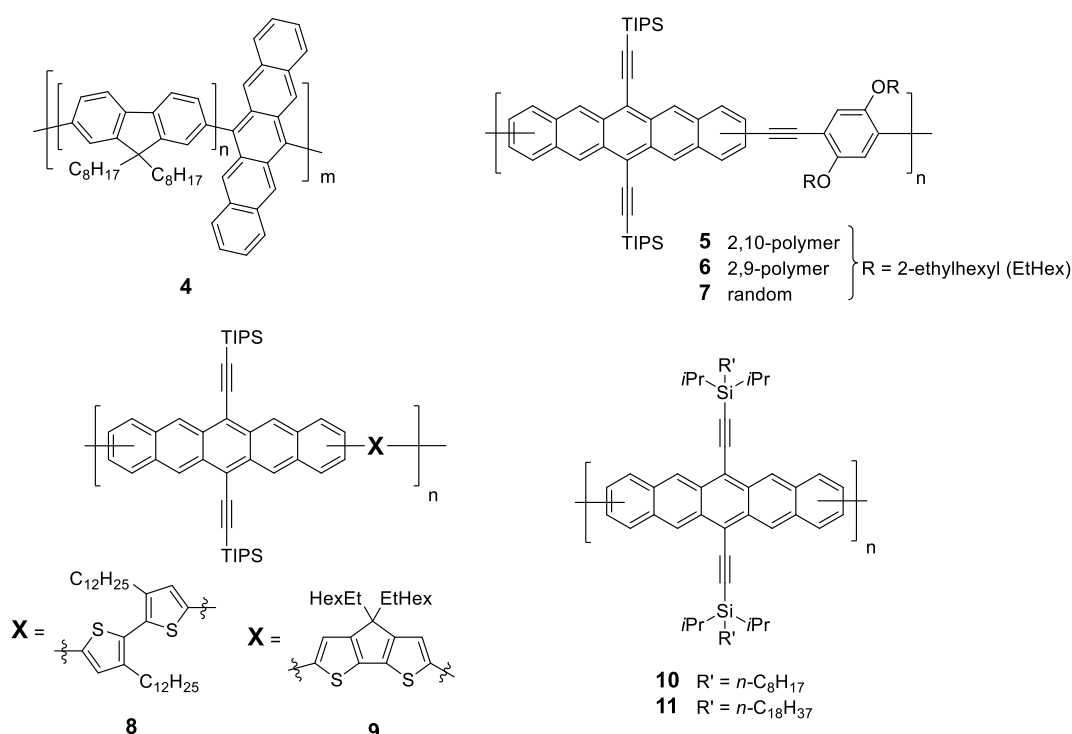
2.2.3. N-type Semiconductors based on Pentacene

Ever since the electron transport in pentacene was demonstrated (see above), several attempts focused on the modification of the molecular structure of pentacene to enhance the charge carrier mobility for electrons and to increase the stability against environmental influences. The motivation for these studies is related to

the desired application of organic semiconductors in integrated circuits, which require the fabrication of inverters that consist of p-type and n-type field-effect transistors.[15] To 'turn' an acene into a good electron transporting material is chemically straightforward: chemical modification should lower the frontier molecular orbitals so that injection of electrons becomes more efficient. The solid state packing can be finely tuned, for example, by varying the side chains, to result an optimised transfer integral for electron transfer (see **Figure 5**). A per-fluorinated pentacene derivative **12** was first reported by Suzuki and co-workers. The material exhibits a herringbone packing and thermally evaporated films showed an electron mobility of 0.2 cm^2/Vs.[106,107] Similar modifications have been reported for **TIPS-PEN** resulting in tetra- and octafluorinated TIPS-ethynyl pentacene derivatives **13** and **14** (**Figure 12**). The packing motif was not altered as compared to **TIPS-PEN** but the π-π-stacking distance was lowered upon fluorination.[108] As intended the electron mobility of the vacuum deposited semiconductors on passivated silicon dioxide increased significantly reaching 0.11 cm^2/Vs and 0.41 cm^2/Vs for **13** and **14**, respectively.[109]

| **12** | **13** X = H | **15** |
| | **14** X = F | **TIPS-TAP** |
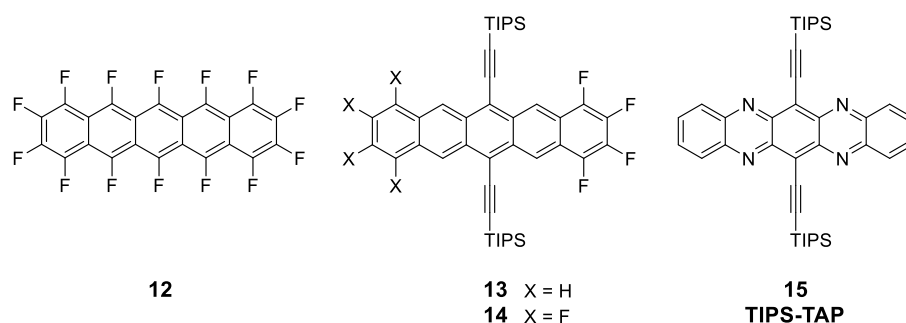
Figure 12. Molecular structure of fluorinated pentacene derivatives: (**12**) from Suzuki and co-workers, (**13-14**) from Anthony *et al.* and tetraazapentacene (**15**) from Bunz *et al.* first reported in 2009.

An alternative route to lowering the LUMO position in order to obtain electron transporting materials is the incorporation of nitrogen atoms into the aromatic backbone of pentacene. This route was first realised in 2009 by Bunz and co-workers for **TIPS-TAP**, the tetraaza derivative of **TIPS-PEN**. Theoretical calculations have shown, that the substitution with nitrogen based on the position and number of incorporated nitrogen atoms results in large shift of the LUMO level to lower energies for these N-heteroacenes, making electron injection more favourable from electrodes of noble metals.[110,111] N-heteroacenes based on smaller acenes like anthracene and tetracene exist and were already employed in organic devices, for example as emitters in OLEDs, however, the main focus of the following section is on N-heteropentacenes and larger azaacenes.[112–117]

2.2.4. N-Heteroacenes

Although nitrogen containing pentacene derivatives are known for more than 120 years, their first application as semiconductors in OFETs was reported just 14 years ago.[116,118] Fischer and Hepp reported in 1890 the synthesis of the *N,N'*-dihydro derivative **16** and in 1901 Hinsberg demonstrated the synthesis of the

symmetrical dihydro compound **17**.[119,120] Nuckolls and co-workers successfully demonstrated in 2003 with the *N,N'*-dihydro compounds **17** and **18** that the nitrogen containing acenes can exhibit hole mobilites in the range of 10^{-6}-$5 \cdot 10^{-5}$ cm²/Vs in thermally evaporated thin films on unmodified silicon dioxide as dielectric (**Figure 13**).[121] Dihydro-tetraazapentacene **16** showed hole mobilities of up to 0.02 cm²/Vs, but with very low on/off ratios of only 10^2.[122] The derivative **17** is isostructural to pentacene and exhibits a similar herringbone packing motif in the solid state. When the fabrication of thin film transistors with **17** was optimised utilising a silicon dioxide dielectric, modified with trichlorooctadecylsilyl self-assembled monolayer (ODTS), the hole mobilities reached up to 0.45 cm²/Vs for films evaporated onto 100°C heated substrates, when the correct polymorph of **17** was obtained.[123] The electron rich and formally anti-aromatic (24 π electron containing) heterocycles are stable compounds and withstand oxidation by oxygen or air in solution as well as in the solid state. These observations in stability were supported by computational studies.[124] Further nitrogen containing pentacene derivatives **18**-**20** were synthesised and investigated in field-effect transistors, with varying charge carrier mobilities based on the film morphology and modification of the silicon dioxide surface (**Figure 13**). The oxidation of **17** resulted in diazapentacene **20** which exhibited only a poor FET performance.[125] The n-type transport in these N-heteroacenes was achieved for azaacene **21** by Isoda *et al.* in 2012 reaching an electron mobility of 10^{-4} cm²/Vs.[126] Derivatives **20** and **21** exhibited a 1-D packing motif with acenes stacked in isolated columns, while for **19** hydrogen bonds determined the solid state packing.[125–127]
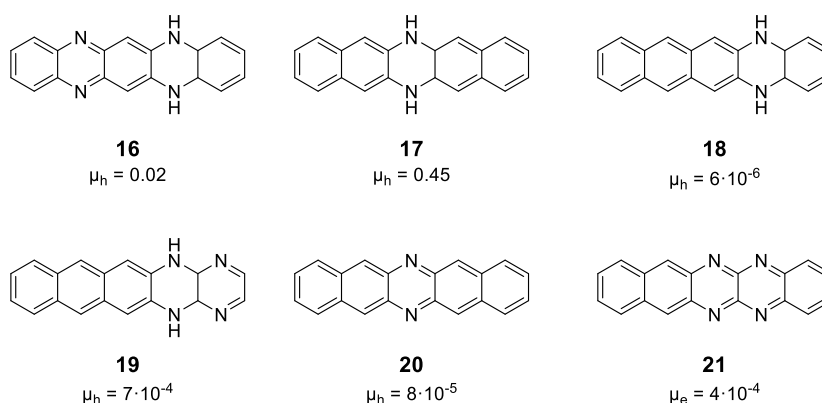
Figure 13. Molecular structure of the first N-heteropentacene semiconductors and highest reported charge carrier mobilities [in cm²/Vs] are given. For references refer to the text.

All of these materials **16**-**21** do not exhibit a high solubility in organic solvents and can basically only be deposited through thermal evaporation. The introduction of solubilising side chains tackled this problem and opened a way for solution-processed films by adopting the structural design of **TIPS-PEN**. This approach is synthetically easily realised by attaching the ethynyl groups in 6,13-position to the aromatic system, resulting in a large variety of aza derivatives of **TIPS-PEN** (**Figure 14**).
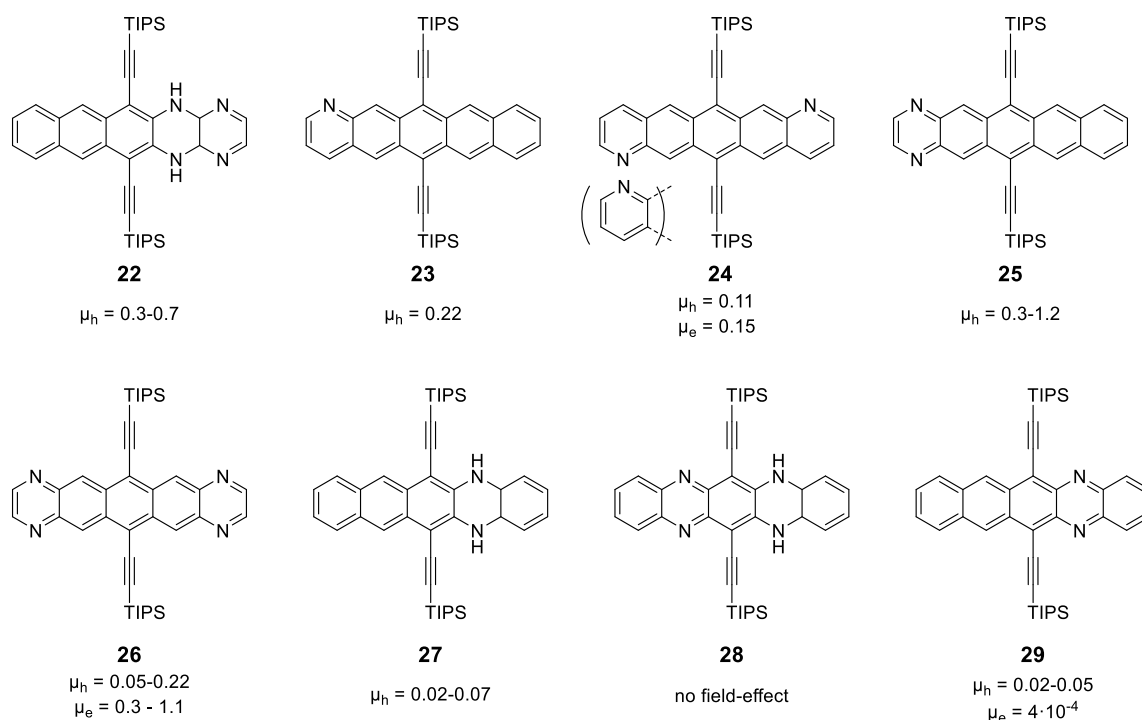
Figure 14. Nitrogen containing 6,13-bis(triisopropylsilylethynyl)pentacene derivatives and their charge carrier mobilities from field-effect transistor application (best reported mobility or range given, in [cm^2/Vs]).[116]

The tetraaza derivative **22** is the solubilised version of **19** and was synthesised and investigated by Miao and co-workers in 2012. The hole mobility could be increased by three orders of magnitude as compared to **19** due to the favourable change in the molecular structure and modified solid state packing. Furthermore, the use of modified silicon dioxide surfaces enhanced the charge transport further.[127] The azaacenes **23** and **24** were synthesised by the group of Zhang and investigated in bottom-gate/ top-contact transistors on ODTS modified silicon dioxide.[128] The hole mobilities were in the range of polycrystalline pentacene films, while the diaza derivative **24** exhibited also a contribution of electrons to the charge transport due to its lower LUMO level as compared to **23**. For **23** halogenated derivatives have been reported that exhibited a deeper LUMO level and as a result an ambipolar charge transport.[128,129] The derivatives **25**-**29** were investigated by Miao and co-workers.[21,111] Despite the solubilising side groups, all functionalised azaacenes **22**-**29** were thermally evaporated for application in field-effect transistors and the benefit of the solubilising side groups has not been utilised. This situation might be attributed to the fact, that solution-deposition of these materials from organic solvents is difficult as the ODTS modified surfaces do not provide a proper wettability. From **Figure 14** it is obvious that electron transport is only achieved in fully oxidised azaacenes with two or more nitrogen atoms in the aromatic backbone. This led to the assumption that **TIPS-TAP** would provide a good electron transport due to its crystal packing, which is very similar to **TIPS-PEN** and its low LUMO, predicted by DFT calculations to be 3.43 eV.[130]

The synthesis of **TIPS-TAP** was first reported by Bunz and co-workers and was modified by Miao in 2011 using Grignard precursors, resulting in more than ten times higher yields and a higher purity of the material (**Figure**

15).[21,130,131] The final step is the oxidation of **28** to **TIPS-TAP** which is easily achieved for all azapentacene derivatives with manganese dioxide.[113] Miao claimed 2014 that the originally employed route results in a material that would exhibit a poorer FET performance (with an electron mobility of maximal 0.1 cm^2/Vs), however, references and data to support this statement are still missing.[116]
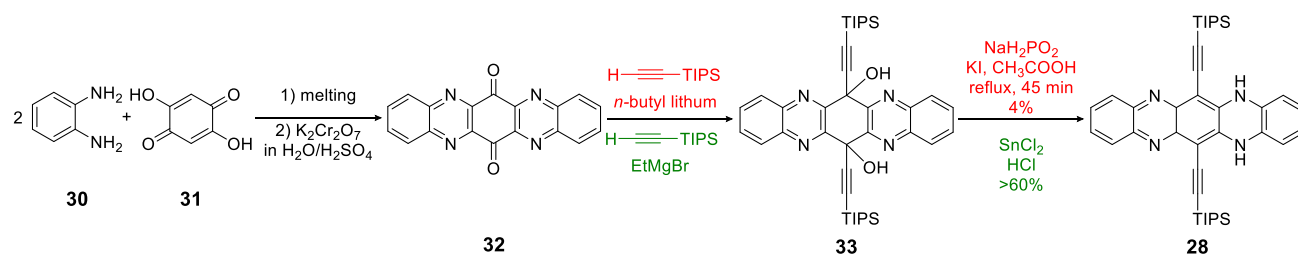
Figure 15. Synthesis of the reduced precursor of **TIPS-TAP 28** by the synthetic route from Bunz *et al.* (red) and modified version by Q. Miao (green) resulting in higher yields.[131]

The investigation of solution-processed transistors of **TIPS-TAP** was a major part of this work. Early results of Miao and co-workers demonstrated in 2011 that **TIPS-TAP** exhibited a high electron mobility of up to 3.3 cm^2/Vs for vacuum-deposited films in identical transistor architectures as used for the derivatives **22**, **25**-**29**.[21] Deposition from solution was only possible on untreated silicon dielectrics which resulted in an incredibly poor transistor performance and low mobilities. Only drop-casting from a mixture of toluene/ethanol or toluene/acetonitrile on ODTS modified substrates resulted in the formation of 'single'-crystals that were employed in field-effect transistors. Surprisingly, the extracted average charge carrier mobility was only 0.81 cm^2/Vs, significantly lower than those, observed for polycrystalline thermally evaporated films.[132] A better OFET performance for **TIPS-TAP** was achieved when the material was drop-cast on a mixed dielectric of AlO$_y$/TiO$_x$, passivated by a self-assembled monolayer of different phosphonic acids, which allowed, due to a polar tail group, a better wettability with the organic solvent.[133] Electron mobilities of up to 2.5 cm^2/Vs were reported. The mobilities could be further boosted utilising a cyclohexyl terminated phosphonic acid, reaching a maximum of 5.0 cm^2/Vs.[134] Despite the use of a novel self-assembled monolayers and bottom-gate architectures with an oxide dielectric the influence of charge trapping as well as the hysteresis and stability of these devices were not discussed, making it difficult to judge the reliability of these results. A very recent study from 2016 with slowly grown **TIPS-TAP** crystals on cross-linked BCB layers (as investigated in parallel in this work) claimed electron mobilities of up to 13.3 cm^2/Vs for **TIPS-TAP** transistors, using the non-linear square root of the channel current in the transfer characteristic to be fitted with a linear plot for the extraction of the charge carrier mobility.[135] Despite the promising charge transport properties and the high molecular absorption coefficient of **TIPS-TAP**, no photovoltaic devices have been reported until today, even though it has been demonstrated that **TIPS-TAP** exhibits efficient singlet fission in polycrystalline films, similar to the parent **TIPS-PEN**.[136,137]

The classic synthesis, as shown in **Figure 15** for N-heteropentacenes, is a condensation reaction of *ortho*-diamines with *o*-dihydroquinones, *o*-quinones or activated *o*-dihalides, typically in a melt reaction or under harsh reaction conditions.[117,131,138] The introduction of trialkylsilylethynyl side chains to the acene core can be achieved through a nucleophilic reaction of the corresponding alkyne or though Sonogashira coupling.[116] An introduction prior to the condensation reaction is also possible, however, the side chains often do not tolerate the required conditions of the condensation reaction and decompose. This issue was resolved by Bunz in 2010 when palladium catalysis was utilized for the synthesis of larger N-heteroacenes, adapting ligands known from the Buchwald-Hartwig amination.[139,140] Since then, numerous N-heteroacenes have been synthesised and investigated in their optical, electronic and charge transport properties.[141,142] Even larger functionalised acenes like azahexacenes and azaheptacenes are accessible through this synthetic method.[143,144] The variety of N-heteroacenes is not only limited to linear acenes as it might be unintentionally suggested here. Especially through the palladium catalysis unlimited possibilities are given for the design of novel semiconducting N-heteroacenes and also hybrid molecular structures with other heterocyclic compounds and/or perylene diimide derivatives were developed.[117,145]

2.3.   Scope of this thesis

This thesis focuses mainly on the application of small molecule N-heteroacenes in solution-processed organic thin film transistors. The promising electronic and solid state properties of these materials and their high solubility in organic solvents allowed the fabrication of organic field-effect transistors through different deposition methods. The materials are employed as mainly polycrystalline films in these devices and the impact of the processing conditions and the resulting film morphologies are correlated to the device performance. The charge carrier mobility is extracted from the I-V characteristics of the fabricated transistors and used as indicator for the efficiency of the charge transport in thin films of each material, while also hysteresis, threshold voltage, subthreshold swing and on/off-ratio of the field-effect transistors are evaluated. Not only the fabrication and characterisation of thin film transistors was the challenge of this thesis, also the entire device fabrication and characterisation facilities at the Institute for Organic Chemistry of the University of Heidelberg, had to be set up as part of this work.

Chapter 4 focuses on the application of non-conjugated pentacene-based polymers that exhibit a superior film formation behaviour compared to **TIPS-PEN** on pre-patterned substrates with silicon dioxide as dielectric. The electron conducting tetraaza derivative **TIPS-TAP** of the well-known **TIPS-PEN**, is studied in **Chapter 5** in various field-effect transistors and its performance in spin-coated and zone-cast transistors is evaluated. The behaviour of **TIPS-TAP** towards environmental and bias stress highlights the potential of this material. The performance of *N,N'*-dihydrotetraazapentacenes as valuable hole-transporting small molecules is described in **Chapter 6**, where the concept of hole conduction is also demonstrated for a *N,N'*-dihydroazahexacene

and -heptacene. The supramolecular interaction in phenazinothiadiazoles lead to a brickwork arrangement in the solid state and excellent electron transporting properties in polycrystalline films as described in **Chapter 7**. **Chapter 8** contains a detailed study of the substitution with norbornadienyl on the hole conducting **TIPS-PEN** and corresponding electron transporting **TIPS-TAP**, that does not affect the electronic properties of these materials but has a strong impact on the charge transport properties.

<div align="right">

Chapter 3

Materials and Experimental Methods

</div>

This chapter describes the materials and processes used in this work to fabricate thin films and field-effect transistors based on N-heteroacenes and related acene materials. The myriad of methods for characterisation of the optical, morphological, electronic and electrical properties are also described. The fabrication and characterisation facilities at the Institute for Organic Chemistry of the University of Heidelberg for organic field-effect transistors were set up as part of this work.
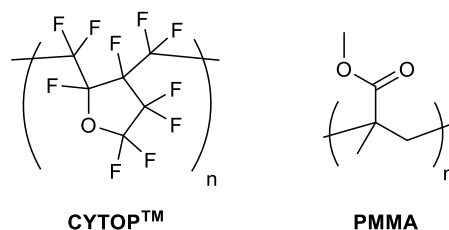
3.1.   Materials

3.1.1. Semiconducting materials

The semiconducting materials used in this study were mainly synthesised in the Bunz group (Institute for Organic Chemistry, University of Heidelberg, Germany) if not stated differently. Nitrogen containing small molecular semiconductors were synthesised in the heteroacene lab of the Bunz group by Dr B. Lindner (**Cl$_4$-Phen**, **F$_4$-Phen** and **DHTA-F$_2$**), Dr J. Engelhart (**TIPS-TAP**, **NH-Hex** and **NH-Hep**) and O. Tverskoy (**TIPS-TAP**, **DHTA-Cl$_2$**, **DHTA-H$_2$**, **Cl$_4$-Phen** and **F$_4$-Phen**) and purified multiple times by flash column chromatography and recrystallized subsequently at least twice from hexane and ethanol and stored under vacuum or argon gas at 5 °C until use.[131,146] Norbornadienyl substituted derivatives (**Nor-PEN**, **Nor-TAP**) and non-conjugated pentacene containing polymers (**P1**-**P5**) were synthesised by Dr M. Porz and purified either by flash chromatography, recrystallization or precipitation and preparative gel permeation chromatography.[147] 6,13-Bis(triisopropylsilylethynyl)pentacene (**TIPS-PEN**) was obtained from Sigma-Aldrich (München, Germany) and used without any further purification. Solvents (anhydrous, HPLC grade) used for this work were obtained from Sigma-Aldrich or Rotil (Cambridge, United Kingdom) and used without purification. Molecular structures for each compound are given in the corresponding chapter. Systematic names can be found in the Appendix.

The materials were weighed under ambient conditions in glass vials with polytetrafluoroethylene (PTFE)-liner cap and then brought open into a nitrogen filled glovebox where the anhydrous solvent was added. The materials were dissolved at 40°C for active layer deposition *via* spin-coating or zone-casting in anhydrous organic solvents including chloroform, toluene, chlorobenzene, xylene (isomers), mesitylene and tetralin (all Sigma Aldrich or Romil). Polymers were dissolved overnight under mild stirring at 60 °C. All solutions were filtered (pore size 0.45 μm, Merz Brothers, Haid, Austria) shortly before deposition. Mixtures of different materials were prepared by mixing the corresponding volumes of separately prepared solutions prior to deposition using microliter pipettes (Gilson Microman, Middleton, USA).

3.1.2. Dielectric Materials

CYTOP™   **PMMA**

Figure 16. Dielectric materials for solution-processed top-gate transistors: (left) per-fluorinated CYTOP™ Polymer, (right) Poly(methyl methacrylate) (PMMA).

As dielectric materials in top-gate transistors commercially available non-conjugated insulating polymers were used (**Figure 16**). Perflourinated CYTOP™ polymer (CTL-809M, Asahi Glass AGC, Chiyoda, Japan) and

Poly(methyl methacrylate) PMMA (MW = 125,000 g/mol, Polymer Source, Dorval Québec, Canada) were used without any further purification. The major challenge for device fabrication was to find an orthogonal solvent that does not affect the underlying active layer of N-heteroacenes, which typically exhibited due to their TIPS-ethynyl side chains a high solubility in many organic solvents. Devices with a PMMA dielectric were processed from a 40 mg/mL acetonitrile solution and dried at 90°C. The resulting PMMA layer thicknesses were between 600-800 nm. CYTOP^{TM} polymer was diluted using the corresponding CYTOP^{TM}-solvent (CT-180, Asahi Glass AGC) and spin-coated under inert atmosphere on the active layer of the transistors. The fluoropolymer was then baked at 90 °C for at least ten minutes resulting in film thickness of 400-450 nm. The actual dielectric layer thickness of each material was determined individually for each device using profilometry (see below). The geometric capacitance was calculated using the dielectric constants of 2.1 and 3.6 for CYTOP^{TM} and PMMA, respectively.[148]

3.2.   General Procedures

3.2.1. Substrates and Sample preparation

The field-effect transistors in bottom-contact/ top-gate architecture and thin organic films for morphological and optical measurements were fabricated on almost zero alkali alumino-silicate 1337F glass (Präzisions Glas & Optik PGO, Iserlohn, Germany). Bottom gate transistors were fabricated on silicon wafers (<100>; p-doped, boron, single side polished, 675 μm thick) with a thermal silicon dioxide layer of (250±12.5) nm thickness, purchased from ABC GmbH, (Brunnthal, Germany). Bottom-gate/ bottom-contact with pre-patterned transistor layout were fabricated using substrates (end-of-line OFET layout) from Fraunhofer IPMS (Dresden, Germany).

Cleaning and handling of substrates and samples took place in a standard chemical laboratory environment and not under cleanroom conditions. Active layer and dielectric layer deposition, thermal evaporation of contacts, handling and electric characterisation of finished devices took place under inert nitrogen atmosphere in a glovebox (GS Glovebox Systemtechnik, Malsch, Germany or MBraun, Garching, Germany) with humidity and oxygen levels of below 1 ppm.

All substrates were cleaned subsequently in acetone (99.8%, Sigma Aldrich) and 2-propanol (99.8%, Sigma Aldrich) in home-built teflon holders in an open 250 mL beaker in an ultrasonic bath (Bandelin Sonorex DT 100H) for five minutes. Protective resists were previously dissolved in acetone or ethyl acetate (99.7%, Sigma Aldrich). Substrates were dried with compressed, clean and dry air and transported and handled in covered sample boxes to avoid any further contamination.

Oxygen plasma treatment for cleaning and activation of surfaces was performed in a glass-cylinder plasma generator (Flecto 10, Plasma Technology, Herrenberg, Germany) at 0.4 mbar pure oxygen at 100 W for 10 min, unless stated differently.

Samples for optical and morphology studies such as atomic force microscopy (AFM), X-ray diffraction measurements on films (XRD), polarised optical microscopy (POM) and others were always prepared in identical fashion to those for devices to keep the results of all samples comparable.

3.2.2. Processing of self-assembled monolayers

Self-assembled monolayers are commonly used in organic electronic devices to modify the interfaces of materials. Typically, self-assembled monolayers on electrodes tune the work function of the electrode materials and improve injection or extraction for charge carriers.[18,38,48,149,150] Gold that is handled in a normal lab environment is quickly contaminated with organic adsorbates, which lower the work function.[42] Self-assembled monolayers of pentafluorobenzenethiol (PFBT, 97%, Sigma Aldrich) were used in this study to modify the work function of gold electrodes to improve hole injection in organic semiconductors. The substrates with structured gold electrodes were cleaned as described above, followed by an oxygen plasma treatment (0.4 mbar, 100 W, 3 min). After that, the substrates were immediately immersed in a solution of PFBT (Sigma-Aldrich) in toluene (10 mM) under ambient conditions. After ten minutes, the substrates were rinsed in an ultrasonic bath for three minutes in toluene and 2-propanol, respectively, dried with compressed clean and dry air and brought into the glovebox for further processing steps.

To passivate the trap states of silicon dioxide in bottom-gate/ bottom-contact transistors in this work, trichloro silanes were used. Trichloro(octyl)silane (OTS), trichloro(octadecyl)silane (ODTS) and hexamethyldisilazane (HMDS) from Sigma Aldrich were used without purification. The substrates were cleaned as described above and treated with an oxygen plasma (100W) for 10 min after drying. The chlorosilanes were dissolved (10 mM) in anhydrous toluene and the substrates were immersed for 30 minutes, rinsed with toluene and 2-propanol and dried with compressed air for further use. The volatile OTS and HMDS were processed through the gas phase in a desiccator. The uncovered, cleaned and activated substrates were placed above a few droplets (2-3 mL) of OTS or HMDS. The desiccator was then evacuated down to 5-7 mbar and kept sealed. After 12 hours the samples were removed and rinsed in an ultrasonic bath successively with toluene and 2-propanol. Contact angle measurement determined the coverage and wetting properties of the modified surfaces. For silicon dioxide modified with ODTS, OTS and HMDS used for field-effect transistor fabrication an average contact angle (with deionised water) was determined to (108±1)°, (103±1)° and (74±1)°, respectively. These values agree well with those reported in literature (**Figure 17**).[151–153]
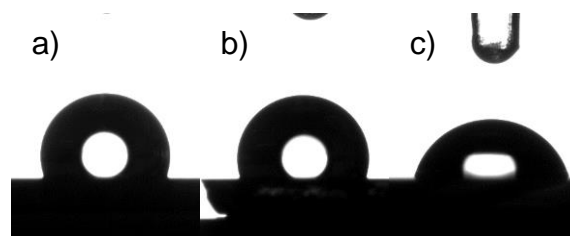
Figure 17. Water droplet on silicon dioxide modified with (a) ODTS, (b) OTS and (c) HMDS after rinsing.

3.2.3. Polyimide

To increase the wettability of the substrate with organic solvents during spin-coating and to ensure large domains of the crystalline semiconductors glass substrates coated with a cross-linked polyimide layer were used in this work for the investigations of small molecules in organic field-effect transistors and for studies of their optical and morphological properties, if not stated otherwise.[29,136,137] Glass substrates were cleaned and dried as described in 3.2.1. A dilute solution of a polyimide resist (PI2525, NMP, Hitachi Chemical DuPont MicroSystems GmbH, Neu-Isenburg, Germany) was spun over the substrate and, after drying, cross-linked under a nitrogen atmosphere for 1 h at 160 °C followed by 3 h at 300 °C. The thickness of the polyimide layer was chosen to be between 25 to 28 nm. Prior to their use, the polyimide coated substrates were rinsed in acetone and 2-propanol subsequently to remove any particles and residuals. The rms-roughness of these cross-linked interlayers was approximately 0.3 nm (**Figure 18**), representing the very smooth nature of these films.

3.2.4. BCB interlayer

An alternative for self-assembled monolayers as passivation of trap-states of silicon dioxide is the use of a benzocyclobutene (BCB) polymer interlayer, which is cross-linked and insoluble.[45] For BCB passivation a dilute solution of benzocyclobutene (CYLOTENE 3035-22, Dow Chemicals, kindly provided by M.Töpper, Fraunhofer IZM, Berlin, Germany) was spin-coated under nitrogen atmosphere on the cleaned substrates and cross-linked at 290°C resulting in a 55 nm thick passivation layer. These layers exhibited excellent wetting properties and the semiconducting materials could be spin-coated or zone-cast resulting in similar morphologies as compared to polyimide coated substrates. The roughness of cross-linked BCB coated substrates is below 0.6 nm (**Figure 18**) and similar to polyimide coated glass substrates.
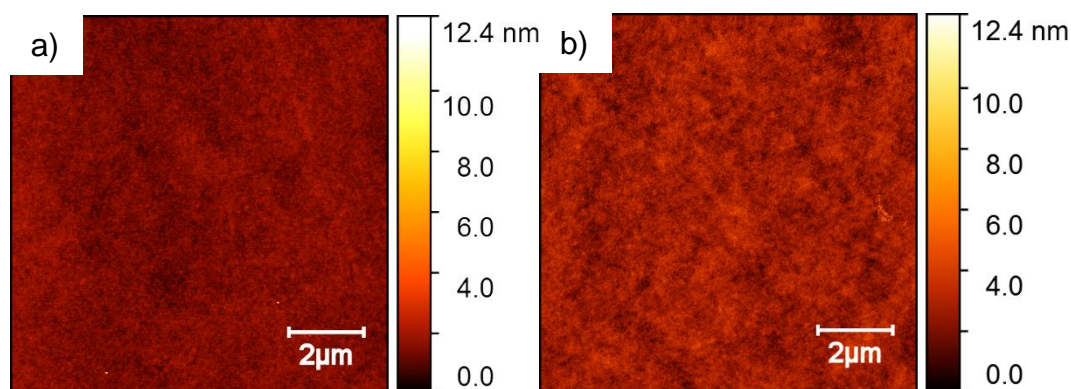
Figure 18. AFM height images of cross-linked interlayers used in this study (a) polyimide on 1737F glass and (b) BCB on a Si/SiO$_2$ wafer.

3.3.   Film-Preparation

3.3.1. Spin-Coating

To produce homogenous thin films of small molecules and polymers the spin-coating technique was used. All films and active layers investigated in this work were fabricated by spin-coating (Delta 6RC, Süss MicroTec, Garching, Germany) under inert conditions using anhydrous solvents, if not stated differently. To ensure a homogenous film only quadratic or round substrates were used. The substrates were placed centred on a vacuum chuck, the freshly prepared and filtered organic solutions were placed on the substrate to cover it fully and the spinning process was started immediately. During the fast rotation the liquid phase was thinned and formed a liquid film ideally covering the full substrate. While the organic solvent evaporated the solid film was formed on the substrate. The wettability of the substrate, the density of nucleation sites, the concentration and the organic solvent used for deposition determined the quality of the resulting film (**Figure 19**). After finishing the film formation step (typically 20-30 s) possible remaining droplets at the edges of the substrates were removed at high spin speeds (5 s). The spinning speeds during film formation were adjusted to obtain the desired film thicknesses from a few tens of nanometres to several hundreds of nanometres, depending on the material/ solvent/ substrate combination. Films used as active layer in organic field-effect transistors were typically 30-50 nm thick.
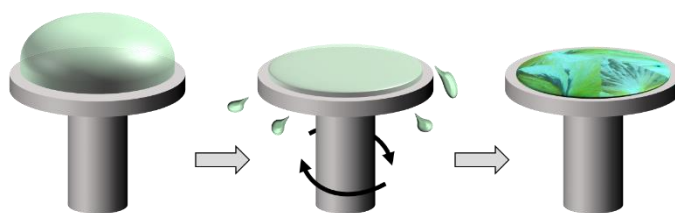

Figure 19. Schematic formation of polycrystalline films through spin-coating deposition.

All spin-coated films were directly annealed at 80 °C after the spin-coating process to remove excessive solvent for several minutes. Substrates that used tetralin solutions did not form solid films within the 20-30 seconds

of the spin-coating process, due to the high boiling point of the solvent. These films were placed directly after the spin-coating process on the hotplate (80 °C) to form the polycrystalline film upon drying.

3.3.2. Zone-Casting

To improve the alignment and ordering of small molecular semiconductors the zone-casting technique was employed to fabricate large oriented crystalline domains (**Figure 20a**). A zone-casting setup was home built during this studies and operated software controlled under inert atmosphere. The substrates for deposition are placed on a heatable sledge which can be moved at different speeds below a heated nozzle that supplies the dissolved organic semiconductor.
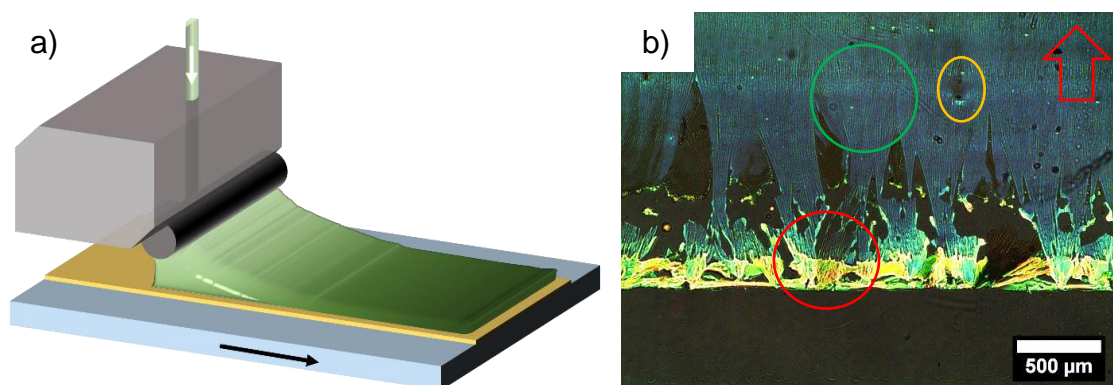
Figure 20. (a) Schematic drawing of the zone-casting deposition technique. (b) Front edge of a zone-cast sample under crossed-polarisers: the red circle highlights the randomised crystallisation at the beginning; upon zone-casting only few crystals can follow the casting direction (red arrow), resulting in an uniaxially aligned crystal growth (green circle). Particles or nucleation sites can interfere with the crystal growth and change locally the orientation of the crystallites (yellow circle).

The solution of the organic semiconductor was loaded in a glass syringe and supplied through a small pipe to the top of the metallic nozzle and running through it. A round bar in the width of the substrate at the bottom of the nozzle spread the organic solution over the entire substrate. While the solution was supplied, a meniscus formed between the substrate and the bar of the nozzle and the sledge was moved at a constant speed forward inducing the aligned crystallisation as the meniscus moves over the substrate. The temperature of the substrate and nozzle could be adjusted independently. Microscope images of zone-cast samples presented in this work are always oriented with the zone-casting direction from the bottom to the top of the image (compare **Figure 20**). During the casting process a large variety of parameters can be tuned to influence the crystallisation and the degree of alignment of the deposited material. The temperature of substrate and solution as well as the casting speed and supply rate of organic solution during this process play an important role for the formation of the organic film. Furthermore, the organic solvent itself, the concentration of the solution and the quality and properties of the substrates affect the casting process. Casting speeds did not exceed 250 µm/s to avoid the formation of metastable polymorphs in the crystalline materials through lattice strain, as it has been observed in literature for **TIPS-PEN**.[95] Nevertheless, to find an optimised film morphology with large, highly ordered domains required intensive optimisation.

If the optimised parameters for deposition were found, the zone-casting deposition resulted in oriented, uniaxially aligned crystalline films. The crystalline films of the organic semiconductor exhibited at the beginning an irregular randomised crystallisation (red circle in **Figure 20b**). As the zone-casting nozzle moved over the substrate (red arrow) the crystallisation process aligned to the zone-casting direction, resulting in oriented crystalline strands (green circle). Defect sites on the substrate or in the cross-linked interlayer perturbed the crystallisation process and resulted in differently oriented crystals, visualised under crossed-polarisers (yellow circle). The parameters used for obtaining the structures in this thesis are given in the appropriate chapters.

3.3.3. Thermal evaporation

Metal electrodes, if not already pre-structured on the substrates were thermally evaporated utilizing a MINI-Coater (Tectra, Frankfurt, Germany) or Edwards Coater E306 (Edwards Vacuum, Crawley, United Kingdom) at a base pressure of $<1\cdot10^{-5}$ mbar. Evaporation rates were measured constantly throughout the evaporation process using two independent quartz crystal monitors. The rate was adjusted after careful heating of the source, then the shutter was removed, starting the coverage of the samples. Gold (99.99 %, pellets or wire, Kurt J. Lesker Company, East Sussex, United Kingdom), silver (99.99 %, pellets, Kurt J. Lesker Company) were evaporated from tungsten boats (width 4'') at rates of 0.03-0.1 nm/s. Chromium for adhesion layers was evaporated from chromium coated tungsten rods (99.9 %, Kurt J. Lesker Company) at a rate of 0.03 nm/s. Aluminium (99.99 %, wire or pellets, Kurt J. Lesker Company) was evaporated from degassed boron nitride crucibles at rates of 0.08-0.3 nm/s. The samples were rotating and not heated during this procedure. Shadow-mask evaporation used self-designed 0.1 mm thick stainless steel masks (Becktronic, Derschen, Germany) in direct contact with the samples. The MINI-Coater allowed loading the samples from inert atmosphere.
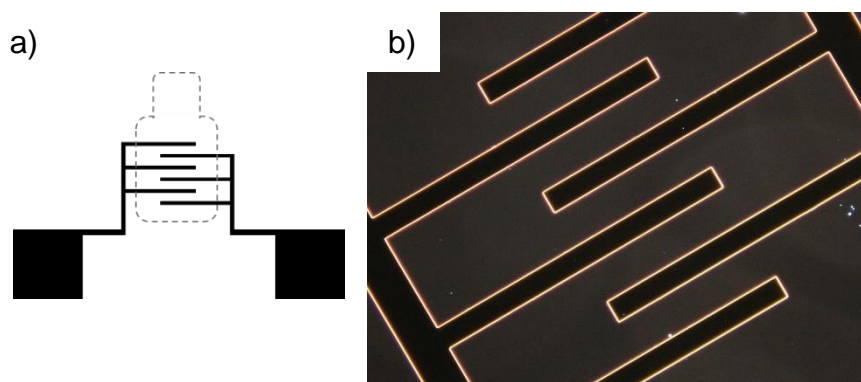
3.3.4. Photolithography and structuring of source drain contacts

Interdigitated source and drain electrodes for top-gate field-effect transistors were structured by photolithography using a two-layer resist and lift-off process. The cleaned polyimide coated substrates were coated with a 360 nm thick layer of LOR 5B (micro resist technology GmbH, Berlin, Germany) and baked at 290 °C for 5 min, followed by a 1.1 µm thick layer of Microposit S1813 photoresist (micro resist technology GmbH), baked at 120°C. The substrates were aligned towards the pattern of the photomask (Compugraphics, Jena, Germany) and exposed with UV-light using a Süss Mask Aligner MJB3 (Süss MicroTec) in soft contact mode. The pattern was developed using the MF-319 developer (micro resist technology GmbH) creating an undercut of a few micrometres by dissolving the underlying LOR 5B (**Figure 21**).

empty substrate
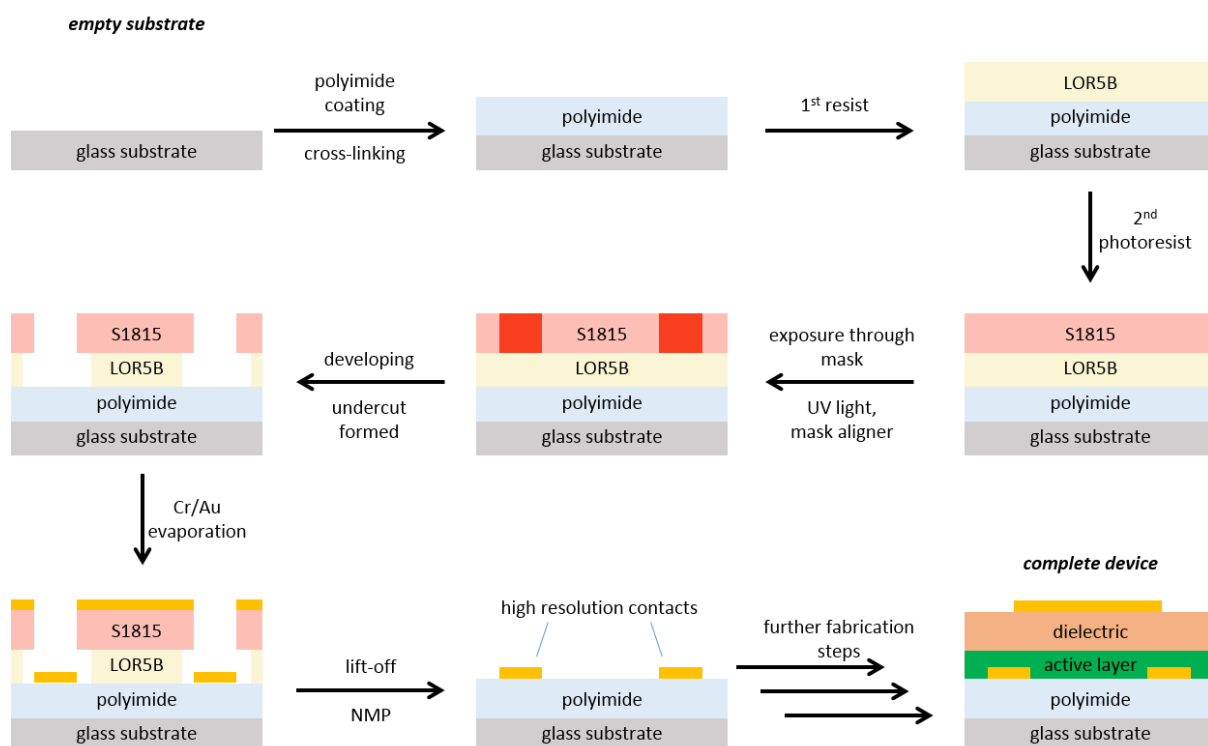
Figure 21. Schematic device fabrication for bottom-contacts for BC/TG field-effect transistors used in this work.

The substrates were dried with nitrogen and packed in a light-proof box for transportation to the thermal evaporator. After evaporating a few nanometres of chromium (1-2 nm) for adhesion and 20 nm of gold the metallised substrates were immersed fully for 18 to 24 h in *N*-methyl-2-pyrrolidone (NMP), rinsed in an ultrasonic bath for 3 min subsequently in NMP, acetone and 2-propanol, dried with clean and dry air and used directly for device fabrication or further treatments. The undercut of the LOR-5B allowed the fabrication of gold contacts with smooth and clearly defined edges that did not exhibit a high density of nucleation sites for small molecules (**Figure 22**).


Figure 22. (a) Schematic structure of the interdigitated source drain electrodes patterned by photolithography and dashed line for the position of the gate electrode. (b) Optical microscope image of the gold electrodes structured by double layer photoresist lithography under dark-field illumination (L = 50 μm).

3.4.   Transistor Fabrication

3.4.1. Bottom-gate/ bottom-contact

Bottom-gate/ bottom-contact organic field-effect transistors were fabricated using pre-patterned gold electrodes on pre-cut silicon/silicon dioxide wafers (15x15mm^2), purchased from Fraunhofer IPMS with a dielectric layer (thermal silicon dioxide) of (230±10) nm thickness (**Figure 23**). The highly n-doped silicon wafer acted as the main gate electrode and was contacted through a small scratch at the substrate's edge through the dioxide layer, sealed with a droplet of silver paste after finishing all processing steps prior to the measurement. The interdigitated 30 nm thick gold electrodes exhibit channel lengths of L = 2.5, 5, 10 and 20 μm and the channel width was 10,000 μm (4th generation) or 2,000 μm (5th generation). The substrates contain an adhesive layer of 10 nm indium tin oxide (ITO) for the electrodes that can be affected by the processing of trichloro silanes as self-assembled monolayers (see **Chapter 4**). The purchased substrates were subsequently cleaned twice in acetone (removal of the protective resist) and 2-propanol and dried with compressed clean air followed by the treatment for self-assembled monolayers (see 3.2.2). Spin-coating or drop-casting of the active layer under inert atmosphere followed the general procedures above (3.2.1). The FET structures were manually separated to limit charging effects and handled in nitrogen atmosphere only.
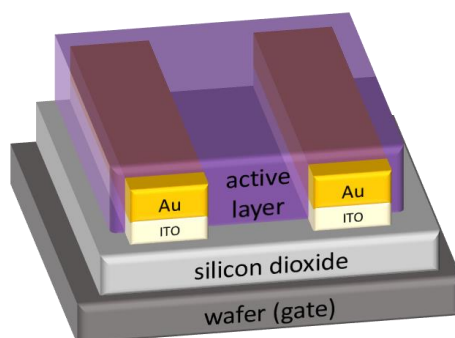

Figure 23. Schematic cross-section of a bottom-gate/ bottom-contact transistor.

3.4.2. Bottom-gate/ top-contact

Cut silicon wafers (p-doped, ca 20x20 mm^2, ABC GmbH) with a thermal silicon dioxide layer of (250±12.5) nm were cleaned successively in an ultrasonic bath with acetone and 2-propanol, dried with compressed clean air, followed by an oxygen plasma treatment for 10 min. For passivation of possible trap states at the dielectric semiconductor interface, a self-assembled monolayer was deposited (see 3.2.2) or a cross-linked benzocyclobutene (BCB) interlayer was used. The active layer was spin-coated or zone-cast (see 3.3) under nitrogen on the passivated wafer substrates. Source and drain electrodes (typically 50-60 nm thick) were thermally evaporated through a shadow mask in double T-shape resulting in transistors with channel length of L = 130, 180, 230 and 280 μm and channel widths of W = 1,500 μm (**Figure 24**). For devices with zone-cast materials the source and drain electrodes were oriented perpendicular to the zone-cast direction, allowing a

charge transport along the grown crystalline domains. The doped wafer substrate acted as the main gate electrode and was contacted with silver paste at the edge. Each field-effect transistor was manually separated from its neighbouring devices.
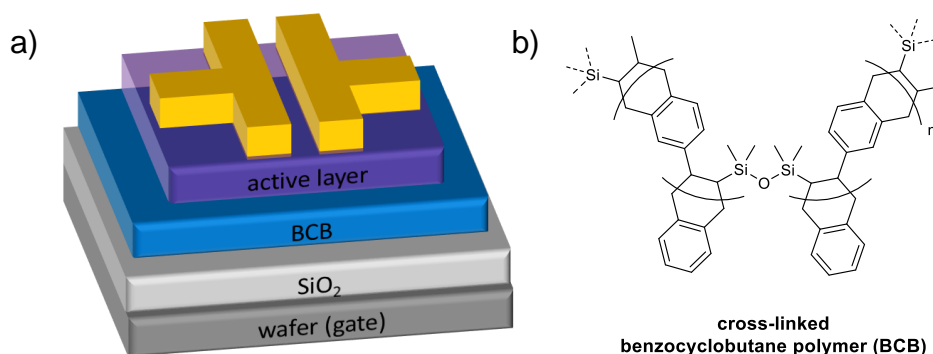

Figure 24. (a) Schematic device architecture of bottom-gate/ top-contact (BG/TC) transistors with BCB passivation layer. (b) Molecular structure of the cross-linked BCB interlayer.

Field-effect transistors for environmental and bias-stress experiments were fabricated on p-doped pre-cut 11.9x11.9 mm^2 wafers (ABC GmbH) with a silicon dioxide layer of (250±12.5) nm, cleaned by acetone, 2-Propanol and oxygen plasma (see 3.2.1). The interface was passivated with BCB and the active layer was spin-coated from anhydrous mesitylene (15 mg/mL) under inert atmosphere. The active layer was then manually patterned into a stripe by wiping of the organic semiconductor 5 mm from the sides with toluene. The source and drain electrodes in double L-shape for four transistors were evaporated parallel to the remaining stripe through a shadow mask resulting in channel length between 65-130 µm and a channel width of 1,500 µm. After evaporation the stripe of organic material was separated with a toothpick to isolate neighbouring transistor structures. The devices were mounted and contacted inside a sample holder under inert atmosphere. For each transistor the channel length was determined using an optical microscope.

3.4.3. Bottom-contact/ top-gate

Transistors with top gate were fabricated on pre-cut 1737F glass covered with cross-linked polyimide. The sample size was ca 17x17 mm^2 (manually aligned substrates for the gate evaporation) or 20x20 mm^2 (tolerance +0.00 mm/-0.25 mm) for fully aligned contact fabrication. The freshly prepared gold electrodes were structured through double-resist photolithography (see 3.3.4). Contacts were then optionally treated with self-assembled monolayers (see 3.2.2). The active layer was spin-coated or zone-cast on the source drain contacts and annealed at 80 °C under inert atmosphere. After the films cooled down to room temperature the devices were coated with a dielectric layer that was spun on top from an orthogonal solvent resulting in film thicknesses of the dielectric layer between 400-800 nm (see 2.1.5). The devices were completed by a thermal evaporation of small pads from gold, silver or aluminium as the ca 50-60 nm thick gate electrode above the interdigitated source drain electrode (**Figure 25**). The substrates were therefore aligned under a shadow mask

in direct contact to the mask. Prior to measurements, the source and drain electrodes were carefully freed mechanically from the overlying dielectric layer.
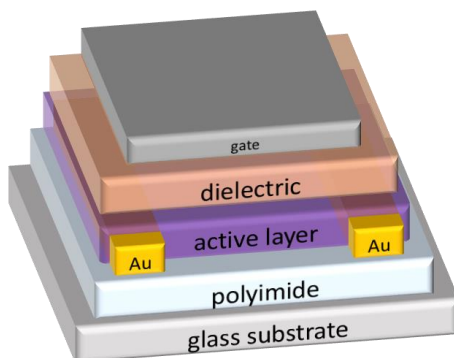
Figure 25. Cross-section of a schematic BC/ TG architecture with patterned gold-electrodes on polyimde coated glass.

3.5.   Optical, morphological and electronic characterisation

Films for optical and morphological studies were prepared in identical fashion to those used for field-effect transistors.

3.5.1. UV/vis

Absorption spectra were obtained using a Jasco V670 spectrometer under ambient conditions from either dilute solutions of hexane or DCM or as thin film on polyimide coated glass substrates or fused silica. A cuvette filled with pure solvent or the bare substrate without the organic film were used as reference samples and were directly subtracted from the measured spectra utilizing the Jasco Spectra Manager software. The onset of the low energy absorption of the film spectra was used to calculate the optical gap in thin films. The λ_{max} values were obtained from the position of the lowest local maxima of the absorbtion spectra.

3.5.2. AFM

Atomic force microscopy was performed in tapping mode either on a digital instruments Nanoscope IIIa in ambient conditions. The recorded height and phase images were processed (e.g. polynomial background removal) with Gywiddion 2.41.

3.5.3. Optical microscopy

Optical microscopy utilized a Nikon Eclipse LV100POL microscope equipped with objectives of 10x-100x magnification. Pictures were taken in bright- and dark-field illumination. Polarized images were taken under fully crossed polarisers. All images were processed (brightness, scale bar etc.) using the Nikon BR software 4.0. To determine the width correction in zone-cast transistors the picture was converted into a binary using either the brightness or hue as selective criteria.

3.5.4. Contact angle measurements

Contact angle measurements were performed on a Ramé-Hart 260 goniometer with an automatic dispensing system for water using the sessile drop method. The droplets were manually placed carefully on the substrate surface and were measured after 2.5 s. The obtained values from a set of measurements were averaged.

3.5.5. Profilometry

Film thicknesses of the fabricated layers and electrodes were measured on a Bruker Dektak XT stylus profilometer. The thicknesses were measured as step height of the film after scratching or dissolving part of it to form a measurable edge. The resulting height profile was levelled and then analysed. Thicknesses of dielectric layers were determined after full electronic characterisation on the actual devices. Several measurements were performed and the resulting film thicknesses represent the average values.

3.5.6. XRD

X-ray diffraction on thin films was performed in collaboration with Prof Dr Andreas Leineweber at the Technische Univeristät Bergakademie Freiberg, Germany, formerly at Max-Planck Institute for Intelligent Systems, Stuttgart, Germany. The diffraction patterns were recorded at room temperature on a Philips X'Pert diffractometer with a Ge Johannson-type incident beam monochromator or on a Seifert FPM URD6 diffractometer and a graphite monochromator. X-ray radiation was produced by a copper anode and the wavelength of only $K_{\alpha 1}$ or both $K_{\alpha 1}$ and $K_{\alpha 2}$ were used for Bragg diffraction (1.54056 Å, 1.54437 Å). The diffractometers worked in Bragg-Brentano geometry, keeping the diffraction vector parallel to the film normal. During the measurement the specimen was rotated around its normal. Also lattice planes with a divergence of ca. 1 ° of their normal contributed to the recorded pattern. The samples were carefully mounted on clay and the diffraction patterns were recorded from 2θ = 3-40 ° with different steps of resolution. Pseudo-Voigt function were fitted to all reflections obtained to extract the layer spacing d. In some cases height errors arising from a displacement of the position of reflection from the focal plane of the spectrometer were corrected using equation (16):

$$\Delta 2\theta = 2s \cdot cos\ \theta / R \tag{16}$$

with R being the distance between specimen and diffractometer aperture and s being the displacement of the specimen outward of the focusing circle. Mecury 3.5.1 was used to calculate the powder pattern of some materials under consideration of a preferred *(hkl)*-orientation. Two wavelength of 1.54056 Å and 1.54437 Å, a Marche-Dollase parameter of 0.01 and the single crystal structure were used as input for calculations.

3.5.7. UPS

The exact determination of the energy levels via ultra-violet photoemission spectroscopy (UPS) of organic materials investigated in this work was important for the choice of the correct contact materials in organic field-effect transistors. Measurement were performed on thin films, deposited from toluene on gold (50 nm) coated silicon wafers. Measurements and analysis were gratefully conducted by Prof Dr Yana Vaynzof at the Kirchhoff-Institut für Physik, Ruprecht-Karls Universität Heidelberg, formely at the Cavendish Laboratory, University of Cambridge, United Kingdom on a Escalab 250Xi (Thermo Fisher Scientific, Waltham, USA) at a pressure of approximately $2 \cdot 10^{-8}$ mbar in the analysis chamber during the measurement. The UPS measurements were performed using a double-differentially pumped He gas ($h\nu$ = 21.22 eV) with a pass energy of 2 eV. The onset of the low energy edge of the valence band was interpreted as the position of the HOMO in the organic material. The position of the LUMO was obtained by adding the optical gap, extracted from the long-wavelength onset of the absorbance spectra of similar prepared films.

3.5.8. GIWAXS

Gracing incidence wide angle x-ray scattering (GIWAXS) measurements were kindly performed by Dr Tomasz Marszalek and Dr W. Pisula, Max-Planck-Institut, Mainz using a Siemens Kristalloflex X-ray source (copper, $K_{\alpha 1}$) operated at 30 kV and 20 mA, Osmic confocal MaxFlux optics with a pinhole collimated beam and a Mar345 image plate detector. The incidence angle of the X-Ray beam on the sample was 0.12°. Zone-cast films of **TIPS-TAP** on BCB coated Si/SiO_2-wafers were investigated to determine the molecular order and growth direction. The samples were cast at 110°C from mesitylene at 150 µm/s sample displacement. The incidence direction of the X-ray beam was chosen to be parallel and perpendicular towards the zone-cast direction resulting in different diffraction patterns for **TIPS-TAP**.

3.5.9. Single Crystal analysis

Single Crystal structure analysis was conducted by Frank Rominger at the Institute for Organic Chemistry, University of Heidelberg, Germany on a Bruker Smart CCD, Bruker APEX or Bruker APEX II diffractometer. Single Crystals were grown either in solution from hexane/toluene mixtures or as described by drop-casting on polyimide. All crystals were free of solvent molecules.

3.6.   Electrical Characterisation

3.6.1. Transistors

The I-V characteristics of the fabricated field-effect transistors were recorded under inert atmosphere in a nitrogen filled glovebox (water & humidity <1 ppm). The devices were contacted with gold coated needles on micromanipulators (PH100 or PH110, Süss MicroTec) and double shielded coaxial connectors. A Keithley

SCS4200 (Keithley Instruments, Solon, USA) or Agilent 4155B Semiconductor Parameter Analyser (Agilent Technologies, Santa Clara, USA) with three source-meter unites was used to record the device characteristics, while the source electrode was grounded ($V_S = 0$ V). Hold and delay times of 0.25 s were chosen to reliable measure the channel current free of influences from charging or other internal device dynamic, while the typical step size for measurements was 0.5-2 V. Measurements typically occurred in the dark, avoiding influence of illumination on charge trapping and charge transport. OFETs were measured from the off to the on state. The charge carrier mobilities reported in this work represent the saturation mobility and were obtained from the slope of a linear fit of the square root of the channel current versus the applied voltage, using equation (17):

$$\mu = \left(\frac{\partial \, (I_D)^{\frac{1}{2}}}{\partial V_G} \right)^2 \frac{2L}{WC} \tag{17}$$

where I_D is the channel current, V_G the applied gate voltage, L the channel length, W the channel width and C the geometric capacitance [F/m^2], determined by the geometry of the transistor using equation (18).

$$C = \frac{\varepsilon_0 \varepsilon_r}{d} \tag{18}$$

The capacitance of transistors with a BCB interlayer was calculated under consideration of a series of two plate-like capacitors with different dielectric constants and individual dielectric thicknesses.

The threshold voltage of a transistor was obtained from the intercept of the square root plot of the channel current in the saturation regime with the gate voltage axis. Due to the ideal assumption resulting in equation (8), only devices with a linear fit with $R^2 > 0.98$ were used for analysis and interpretation, all other devices were considered as non-functioning. Furthermore, the observed gate current in the devices did not exceed 1% of the channel current in the on-state and was typically significantly lower. Analysis of the acquired data was conducted with OriginPro 8.6 to 9.2 or OriginPro 2015G.

3.6.2. Bias-stressing

For bias-stressing BG/TC transistors on BCB were used and fabricated following the procedure above. All single FETs on the substrate were connected through pins of a home build sample holder, allowing an accurate control over the environmental conditions. The devices were biased and measured after the environmental conditions were set up and gas was purged through the sample holder and passing the surface of the active layer. The bias-stress experiment was performed using two 2450 SMUs (Keithley) to measure I_D and I_G while Source was put on common. The devices were connected individually through a relay matrix and the entire measurement was controlled by a homebuilt LabVIEW routine. The hold and delay times were identical to the measurements reported above. Mobility and threshold voltages were obtained from a linear fit of the square

root plot of the channel current in the saturation regime. The relative hysteresis [%] in case of a lower back-sweep current is calculated as the relative difference of the area below the I-V curves of the forward and backward sweep.

Chapter 4

Pentacene-based Polymers

This chapter describes the investigation of various pentacene-based polymers as hole conductors in field-effect transistors. The main goal of the study was to investigate the feasibility of using non-conjugated pentacene containing polymers as active layers to resolve the wettability issues of small molecules such as **TIPS-PEN** on silicon dioxide modified with self-assembled monolayers. Despite the promising film formation properties, the polymers showed only mediocre charge transport with mobilities lower by many orders of magnitude than the small molecule **TIPS-PEN**. Some of the results presented in this chapter have been reported in Ref. [154]: M. Porz, F. Paulus, S. Höfle, T. Lutz, U. Lemmer, A. Colsmann, U. H. F. Bunz, „TIPS-Tetracene- and TIPS-Pentacene-Annulated Poly(norbornadiene)s: Synthesis and Properties", *Macromol. Rapid Commun.* **2013**, *34*, 1611–1617.

## 4.1.   Limitations of BG/BC Structures and Motivation

TIPS-pentacene (**TIPS-PEN**) has been extensively investigated for application in field effect transistors since it was first reported by Antony and co-workers in 2001.[6,77,85,95,155] The introduction of the TIPS-ethynyl groups at the middle ring of the pentacene system resulted in an improved stability against oxidation and altered the molecular packing of the acenes in the solid state (see **Chapter 2**). Furthermore, the substitution resulted in a tremendous enhancement of the solubility in organic solvents. This property opened the route to solution processed transistors deposited by various techniques such as spin-coating, drop casting, shear coating, spraying, and zone-casting.[20,29,82,90,156] The simplest method for solution processed field-effect transistor fabrication is the deposition of the organic layer on top of a pre-structured substrate (see **Chapter 3**). These substrates are commercially available and eliminate the need for structuring using lithography and thermal metal evaporation. A highly doped silicon wafer acts as the substrate and the main gate electrode in these devices (**Figure 26a and b**). Thermally grown silicon dioxide acts as the dielectric layer. The source drain contacts are pre-patterned from gold in form of interdigitated electrodes allowing high channel widths with different channel lengths. Since gold is known to have a poor adhesion to silicon or silicon dioxide a thin layer of indium tin oxide (ITO) is introduced between the dielectric and the electrodes.
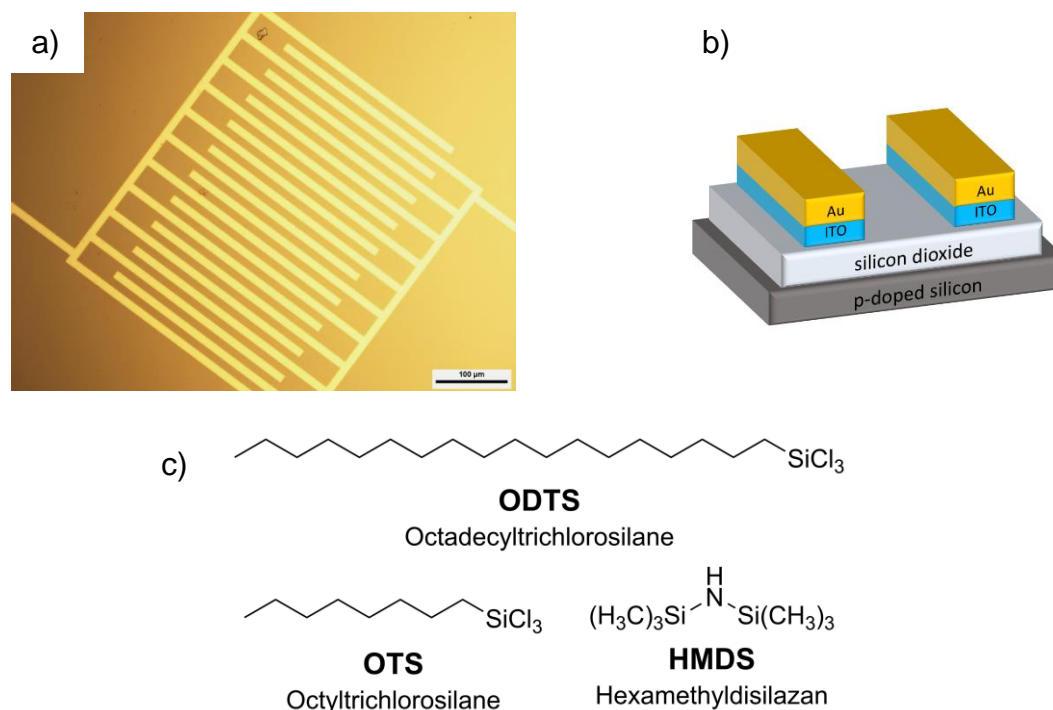
Figure 26. a) Pre-structured source and drain electrodes on an IPMS-substrate (W = 10.000 μm) b) Schematic cross-section of such a substrate. The doped silicon acts as gate electrode. c) Chemical structure of commonly used modifiers for silicon dioxide dielectric.

With the transistor architecture described above, it is necessary to modify the surface of the SiO_2 layer for the charge transport to occur in the transistor channel due to the large density of hydroxyl groups at the oxide/organic interface that act as trap states.[15,18,45] Among the myriad of possible modifiers, the three most

common ones are shown in **Figure 26c**. Trichloro silanes are of particular interest as they are highly reactive and efficiently covalently bind and passivate the hydroxyl groups of the silicon dioxide surface prior to spin-coating of the organic layer. Attempts to modify the pre-patterned substrates described above with trichloro silanes following well-established procedures from Angst *et al.* or Salleo *et al.* resulted in a significant damage to the patterned Au electrodes on the substrates (**Figure 27a**).[151,153] The substrates were immersed in a dilute solution of ODTS or OTS in anhydrous toluene, baked and rinsed prior to further use, but the corrosive character of the trichloro silanes etched the ITO adhesion layer. Altering the procedure to gas phase deposition of OTS lowered the degree of damage, but still resulted in partial etching of the gold electrodes edges. This is detrimental to the deposition of the organic layer as the rough edges serve as nucleation sites for molecules and prevent the formation of a compact layer. These rough edges and nucleation sites can be visualised by dark-field illumination at the contacts (compare these findings to the structure of electrodes patterned by double layer photo resist lithography in 3.3.4).
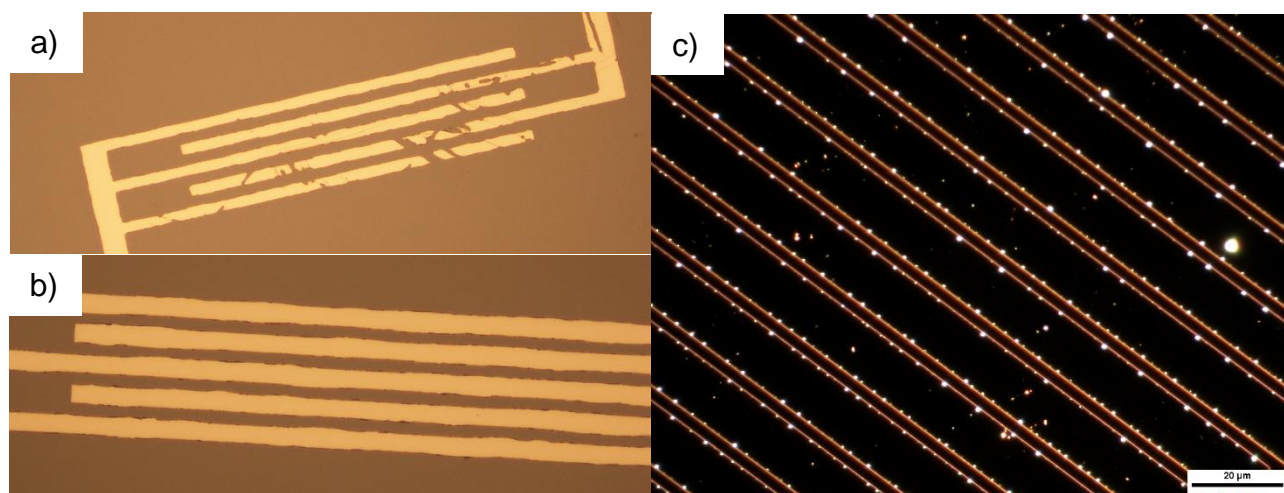

Figure 27. a) Damaged and destroyed pre-structured transistor electrodes after application of chlorosilanes and rinsing for multilayer removal. b) Partially etched gold electrodes after gas phase deposition of OTS and ultra-sonic rinse. c) Source-Drain contacts after short-time contact with OTS and rinse under dark-field illumination.

Since all attempts to modify the surface with trichloro silanes failed, the dielectric layer in the channel region of the pre-structured electrodes was modified with HDMS (see **Figure 26c**), which had no detrimental effect on the contacts or the adhesion layer. Despite this fact, the high surface energy and poor wettability of HMDS modified silicon dioxide layers with organic solvents prevented a successful and reliable deposition of **TIPS-PEN** or other small molecule semiconductors by neither spin-coating nor drop casting (**Figure 29**). A sufficient coverage of the substrate and channel region for a reproducible and reliable transistor fabrication could not be obtained.

4.2.   First Generation of Pentacene-based Polymers

The limitation of the surface modification with HDMS required an alternative route to promote film formation of **TIPS-PEN** upon spin-coating. A previously unexplored approach to achieve this was the application of TIPS-pentacene based polymers. This approach is investigated in depth in this chapter. The pentacene containing polymers were synthesised by M. Porz through ring opening-metathesis polymerisation (ROMP) in high yields.[147] Due to the use of the norbornadiene ring the resulting polymers are non-conjugated and randomised in their stereochemistry of the C=C double bond (E/Z-isomers) along the polymer backbone. The first generation of a pentacene containing polymer **P1** exhibited a typical molecular weight of ca. 21,000 g/mol and a PDI of 1.3 (**Figure 28**).[147]
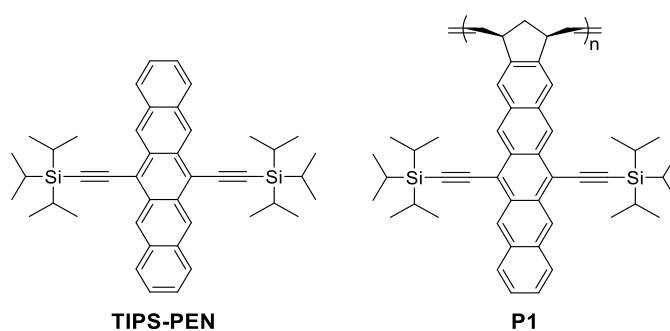
Figure 28. Molecular Structures of the non-conjugated pentacene-based polymer **P1** synthesised by ring-opening metathesis polymerisation (ROMP).

The stark difference between the results of spin coating **TIPS-PEN** and **P1** can be seen in **Figure 29**. Attempts to form a film of **TIPS-PEN** on the HDMS treated pre-structured substrates resulted in few specs of material to be deposited in random locations on the sample (**Figure 29a**). On the other hand, the deposition of the **P1** polymer resulted in the formation of a compact thin film suitable for transistor fabrication (**Figure 29b**).
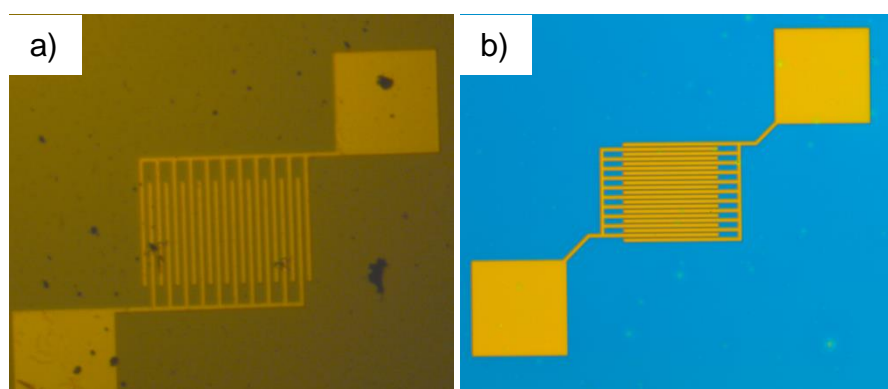
Figure 29. Optical microscopy images of a) attempt of spin-coating **TIPS-PEN** on HMDS treated substrates. b) Film of **P1** on HMDS treated substrates (pad size 0.5x0.5 mm²). [Fig. (b) adopted from Ref. [154] – with permission from John Wiley & Sons, Inc.]

4.2.1. Thin film Transistor Performance

Bottom-gate/ bottom-contact transistors with **P1** as an active layer showed several adverse properties. First, the transistors suffered from significant contact limitations suggesting poor injection from the gold contacts into **P1**. This resulted in a very large threshold voltage of around -55 V (**Table 1**). Secondly, the transistors exhibited significant hysteresis which could be observed in both the output and transfer characteristics. Finally, the obtained hole mobilities were disappointingly low with an average mobility in the saturation regime of only $(1.6\pm0.2)\cdot10^{-6}$ cm^2/Vs (**Table 1**). The extracted hole mobilities are six orders of magnitude below those, found for polycrystalline, spin-coated **TIPS-PEN** transistors.[82,155] In order to improve the performance of the transistors and especially minimise the non-ohmic injection effects, the gold contacts were modified with PFBT following the procedure of Park *et al.*[82] PFBT forms a self-assembled monolayer on the gold contacts and results in an increase in the contact work function (5.45 eV), and therefore a better hole injection into the HOMO of pentacene and its derivatives.[152] The output and transfer characteristics of a representative **P1** OFET with PFBT modified gold contacts is shown in **Figure 30**. Although some improvement was observed as compared to the unmodified Au contacts, the transistors still show non-ohmic injection effects. This suggests that the injection limitations are not purely energetic in nature, but that perhaps a poor contact is formed between the electrodes and **P1**. The PFBT treatment, however, did result in an overall improvement of the transistor performance, with the average threshold voltage dropping to -29 V and the mobility slightly increasing to $5\cdot10^{-6}$ cm^2/Vs. Due to these positive effects, the remaining studies on **P1** were performed with PFBT modified gold contacts only.
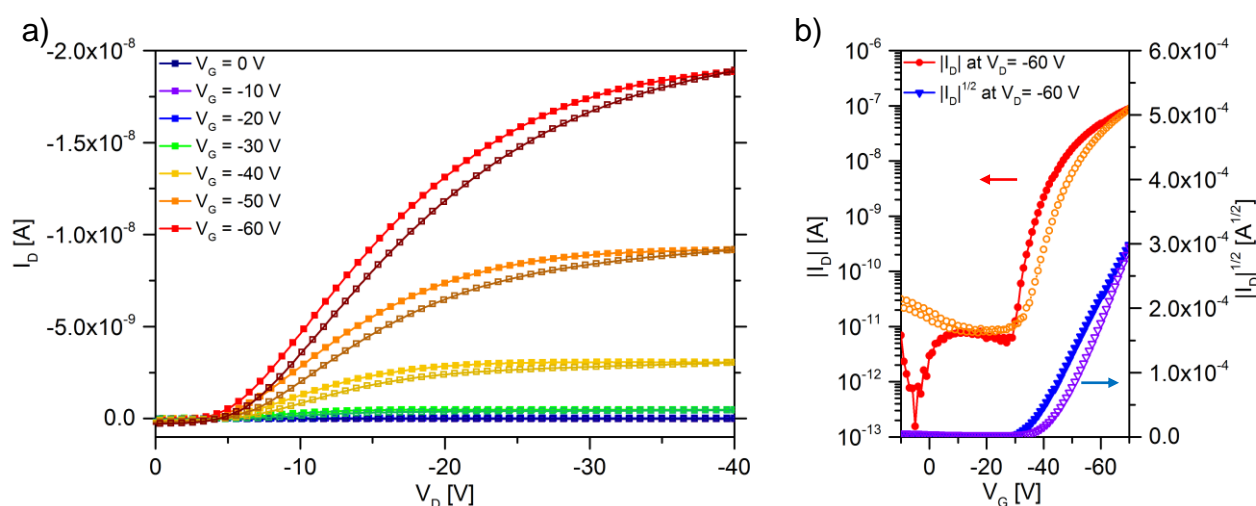
Figure 30. a) Output characteristics of a representative OFET with **P1** as active layer. Despite PFBT treatment of the gold contacts the transistors exhibited a non-ohmic contact behaviour (W = 10,000 μm / L = 5 μm, BG/BC). b) Transfer I-V curve of the same transistor. Transistors from **P1** exhibit a high threshold voltage and show hysteresis.

Table 1. Summarised FET parameters for bottom-gate/ bottom-contact transistors with **P1** as active layer. The average value and standard deviation for threshold voltage, hole mobility and on/off-ratio are given. [adopted from Ref. [154] – with permission from John Wiley & Sons, Inc.]

polymer	FET architecture	solvent	contact	average mobility [cm^2 V^{-1} s^{-1}]	average threshold voltage [V]	average On/off ratio
P1	BG/BC	toluene	Au	$(1.6\pm0.2)\cdot10^{-6}$	-55 ± 2	$8\cdot10^3$
P1	BG/BC	toluene	Au/ PFBT	$(5.0\pm0.4)\cdot10^{-6}$	-29 ± 4	$9\cdot10^3$
P1	BG/BC	chloroform	Au/ PFBT	$(4.6\pm0.7)\cdot10^{-6}$	-26 ± 4	$8\cdot10^3$
P1	BG/BC	tetralin	Au/ PFBT	$(2.2\pm0.2)\cdot10^{-6}$	-31 ± 3	$3\cdot10^3$

In order to investigate the effect of the polymer film morphology on the performance of the OFETs, three different solvents were utilized for **P1** active layer deposition. A higher boiling point solvent should affect the dynamics of drying during the spin-coating deposition and allow for larger, ordered domains, as has been observed for **TIPS-PEN** and derivatives.[84] The performance parameters of **P1** OFETs deposited from different solvents are summarised in **Table 1**. It can be seen that despite the change of solvent, the performance of the transistors remains largely unaltered, suggesting that **P1** forms a rather amorphous layer, which is not influenced by the changes in the drying dynamics. The amorphous nature of **P1** (that is also supported by optical microscopy, see Appendix) explains the rather poor charge transport properties of this pentacene polymer compared to **TIPS-PEN**. Similar transistor performances have been reported for other non-conjugated amorphous semiconductors.[157,158] The rather rigid nature of **P1** and the inflexible attachment of the pentacene units to the polymer backbone do not allow them to undergo a π-π-stacking or any other strong solid state interaction (see properties of **P1** in Ref. [147] and [154]) that is required for an efficient charge transport within this material. Additionally, annealing of these films for several hours under inert atmosphere did not result in a change of the transistor performance.[147,154]

4.2.2. Blending with TIPS-Pentacene

As mentioned above, all attempts to deposit **TIPS-PEN** on the pre-structured FET substrates were not successful. While the performance of **P1** in OFETs was disappointing, it offered an ease of processability, which could be taken advantage of in the case of blending **TIPS-PEN** and **P1**. With the hope to combine the advantageous charge transport properties of **TIPS-PEN** with the ease of processability of **P1**, a series of OFETs was fabricated with active layers consisting of blends of **P1:TIPS-PEN** in various blending ratios. The percentage of **TIPS-PEN** in the blend was varied from 5% to 50% in order to investigate the effect of crossing the percolation threshold (ca. 30%).[159,160] The performance of the transistors is summarised in **Table 2** and **Figure 31a**. Gradually increasing the **TIPS-PEN** percentage from 5% to 30% did not affect the transistor performance significantly. The threshold voltage of the transistors remained fairly constant at -25V and the hole mobility

did not improve as compared to that measured in **P1** on its own. The performance of the 1:1 blend of **P1:TIPS-PEN** was somewhat improved as compared to the other blending ratios. The mobility has increased by roughly an order of magnitude and the threshold voltage has been lowered to -6 V only. The transfer characteristics of a representative OFET with a 1:1 blend as its active layer is shown in **Figure 31b**.

Table 2. BG/BC-transistor parameters for **TIPS-PEN** and **P1** blends. Averaged values for threshold voltage, hole mobility and on/off-ratio obtained from a set of identically prepared transistors. The standard deviation is given for threshold voltages and hole mobilities.

P1:TIPS-PEN blend	FET architecture	solvent	contact	average mobility [cm^2 V^{-1} s^{-1}]	average threshold voltage [V]	average On/off ratio
95:5	BG/BC	tetralin	Au/ PFBT	$(5.2\pm0.7)\cdot10^{-6}$	-25±3	$6\cdot10^3$
90:10	BG/BC	tetralin	Au/ PFBT	$(6.2\pm0.6)\cdot10^{-6}$	-25±2	$5\cdot10^3$
80:20	BG/BC	tetralin	Au/ PFBT	$(7.7\pm3.3)\cdot10^{-6}$	-24±2	$7\cdot10^3$
70:30	BG/BC	tetralin	Au/ PFBT	$(4.2\pm3.9)\cdot10^{-6}$	-24±2	$3\cdot10^4$
50:50	BG/BC	tetralin	Au/ PFBT	$(3.5\pm0.1)\cdot10^{-5}$	-6±2	$6\cdot10^3$
50:50	BG/BC	toluene	Au/ PFBT	$(2.7\pm0.6)\cdot10^{-5}$	-9±1	$1\cdot10^4$
50:50	BG/BC	chlorobenzene	Au/ PFBT	$(2.6\pm0.1)\cdot10^{-5}$	-4±4	$3\cdot10^3$
50:50	BG/BC	1,2-dichloro-benzene	Au/ PFBT	$(2.9\pm0.3)\cdot10^{-5}$	-6±3	$6\cdot10^3$
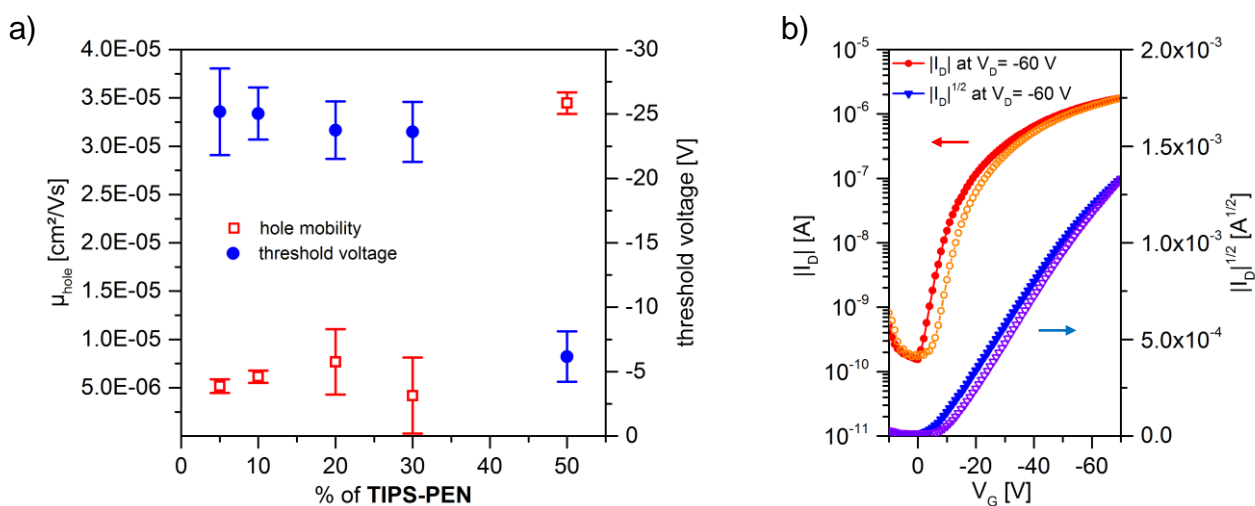
Figure 31. a) Threshold voltage and hole mobility values as a function of **TIPS-PEN** blending ratio with **P1**. b) Transfer characteristic of a **P1**:**TIPS-PEN** bottom-gate/ bottom contact transistor with a mixing ration 1:1 (W = 10,000 μm/ L = 5 μm).

While it is tempting to ascribe this improvement to crossing the percolation threshold, it is unlikely to be the case. Firstly, one would expect a significantly higher mobility to be measured as **TIPS-PEN** typically results in mobilities in the 10^{-2} – 1.0 cm^2/Vs range. Additionally, optical microscopy images showed that only isolated **TIPS-PEN** crystallites have been formed within the active layer, showing no continuous path for charge transport between the electrodes (**Figure 32**). This suggests that the transport in **P1** is the limiting factor to the performance of the blend transistors.
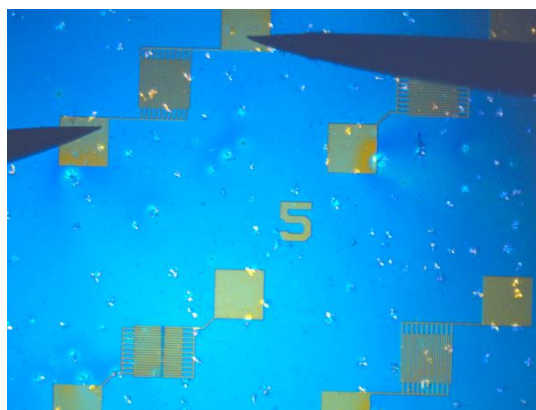
Figure 32. Film and transistors of the **P1**:**TIPS-PEN** blend with a mixing ratio of 1:1 (pad size 0.5x0.5 mm^2).

Further attempts to improve the blending and transistor performance of **TIPS-PEN** within the 1:1 blend active layer were made by changing the solvent used for deposition. Four different solvents have been investigated: toluene, chlorobenzene, 1,2-dichlorobenzene and tetralin, that exhibit increasing boiling points. The choice of solvent did not affect the measured OFET performance, similarly to what has been observed previously for **P1** (**Table 2**). This is in agreement with the observation that the performance of the **P1:TIPS-PEN** transistors is hindered by the poor charge transport properties and the amorphous nature of **P1**.

4.3.   Second Generation Pentacene-based Polymers

With the goal of improving the morphology and the charge transport properties of **P1**, a second generation of pentacene-based polymers was developed. While **P2** has a rather similar structure to **P1**, changing the manner in which the TIPS-pentacene units are connected to the polymer backbone should allow a larger degree of flexibility, which could be beneficial for a π-π-stacking and the charge transport properties (**Figure 33**). Polymers **P3**, **P4** and **P5** follow a different structural theme, in which one of the ethynyl side chains of the TIPS-pentacene unit is eliminated and in its stead the pentacene backbone is connected to the polymer backbone by various means (**Figure 33**). Due to the higher flexibility of these pentacene-based polymers, the synthesis yielded higher average molecular weights of 26,000, 34.000 to 38,000 g/mol for **P3**, **P2** and **P5**, respectively, while for **P4** 42,000 g/mol were achieved (refer to Ref. [147] for details). The absorption properties of thin films of **P2-P4** are comparable to the absorption spectra of these polymers in solution, indicating no strong solid state interactions of the pentacene chromophores.[147] Only **P5** exhibits a broadening and red shift in thin films as compared to measurements in solution and the purification after synthesis yielded a crystalline material.[147] However, films of **P5** deposited by spin-coating in thin film transistors did not show crystalline domains (for optical microscope images of **P2-P5** see Appendix.)
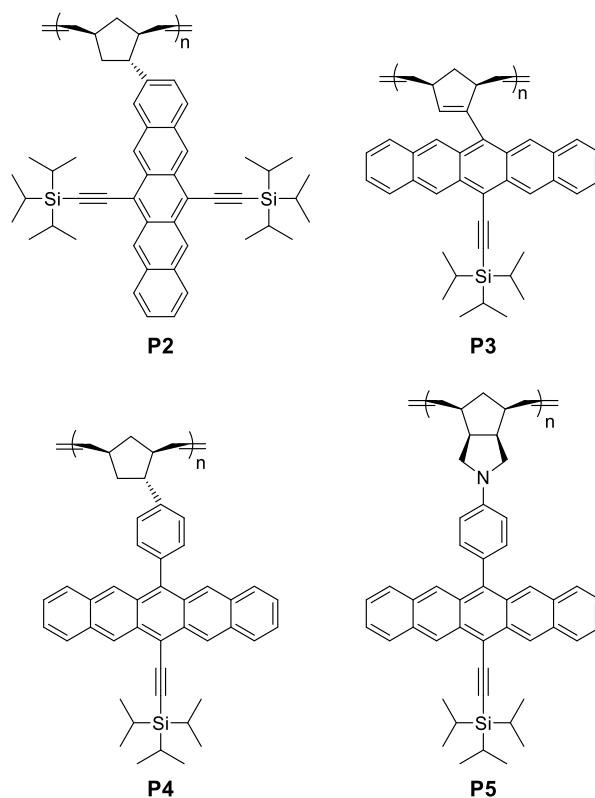
Figure 33. Second generation of non-conjugated pentacene polymers **P2**-**P5**.

4.3.1. Thin film transistor Performance

Due to the structural similarities, it is interesting to compare the OFET performance of **P1** and **P2**. For this purpose, transistors with and without PFBT modification were fabricated and characterised. While some improvement in mobility was observed for **P2** as compared to **P1**, the biggest difference was seen in the hole injection from the gold contacts (**Figure 34a and b**). Contrary to the significant limitations observed for **P1**, no non-ohmic effects were observed for **P2**. As a result, the threshold voltage was significantly lowered, -9 V for **P2** as compared to -55 V for **P1** for untreated gold electrodes.
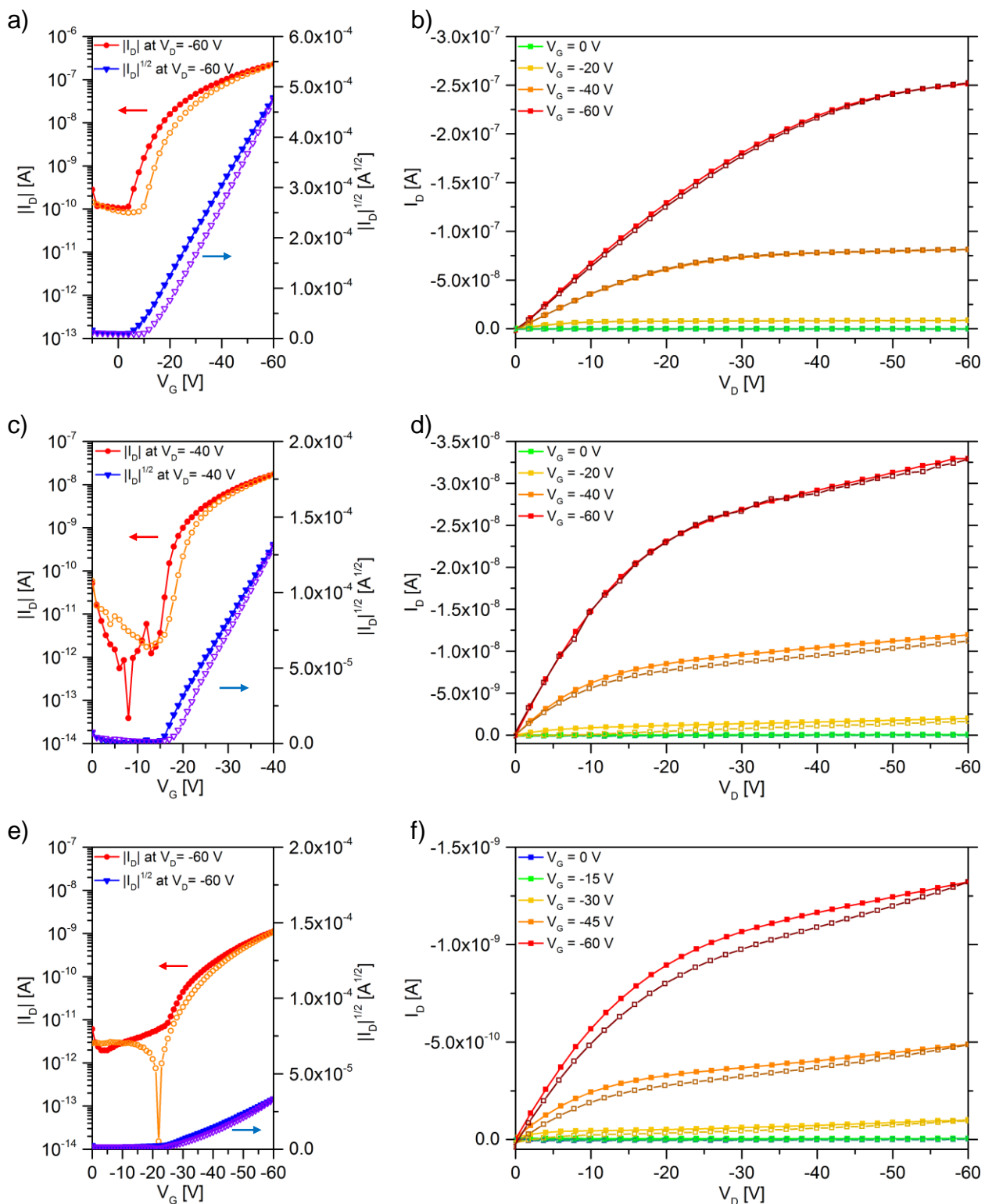
Figure 34. Transfer and output characteristics for representative OFETs (all W = 10,000 μm / L = 10 μm); (a) and (b) for **P2** (BG/BC), (c) and (d) for **P4** (BC/TG) and (d) and (e) for **P5** (BC/TG).

Table 3. Transistor performance of second generation pentacene polymers **P2-P5**. Average values and standard deviation for threshold and hole mobility.

polymer	FET architecture	solvent	contact	average mobility [cm^2 V^{-1} s^{-1}]	average threshold voltage [V]	on/off ratios
P2	BG/BC	toluene	Au	$(1.1\pm0.1)\cdot10^{-5}$	-9±3	$10^3 - 10^4$
P2	BG/BC	toluene	Au/PFBT	$(1.0\pm0.2)\cdot10^{-5}$	2±5	$10^3 - 10^4$
P3	solubility issues					
P4	BC/TG	toluene	Au/ PFBT	$(1.5\pm0.4)\cdot10^{-5}$	-14±3	10^3
P5	BC/TG	toluene	Au/ PFBT	$(6.5\pm0.8)\cdot10^{-7}$	-23±2	10^2-10^3

Attempts to fabricate OFETs from **P3-P5** gave mixed results. Polymer **P3** suffered from solubility issues and showed difficulties in forming a compact thin film suitable for FET fabrication. Consequently, no working transistors were demonstrated using **P3** as an active layer. Since the OFET performance was no longer limited by the injection from the gold contacts, their modification with PFBT made little to no difference to the performance of **P2** (**Table 3**), only the average threshold voltage dropped to about 2 V upon the use of PFBT. **P4** showed a very similar performance to that of **P2**, with an average hole mobility of $1.5\cdot10^{-5}$ cm^2/Vs. **P5**, on the other hand, exhibited a significantly poorer transistor performance with an average mobility nearly two orders of magnitude lower than that of **P2** or **P4** ($6.5\cdot10^{-7}$ cm^2/Vs). Such low mobilities are at the very limit of what can be reliably measured. The output characteristics exhibited also for **P4** and **P5** a linear injection behaviour (**Figure 34**). The transistor performance is summarised in **Table 3**.

4.4. Energetics and hole injection in Pentacene-based Polymers

Despite the variation in performance between **P2**, **P4** and **P5**, neither of the materials resulted in non-ohmic contact effects in transistors as has been previously observed for **P1**. This dissimilarity could be explained by a difference in the electronic energy levels of the different polymers, if for example, the hole injection barrier for **P1** is significantly larger than that of the other polymers. To investigate if a change of energetics is the reason for the observed effect, ultra-violet photoemission spectroscopy measurements were performed on **P1-P5** as well as **TIPS-PEN** thin films on gold. The valence band features of **P1-P4** are similar, only **P5** that contains an aniline moiety that contributes to the π-system[147] exhibits a slightly different valence band feature (**Figure 35**). The extracted ionisation potentials for **P1-P5** coincide within the experimental error with that of **TIPS-PEN**. As a reference, the ionisation potential of **TIPS-PEN** was found to be 5.1 eV in agreement with previous measurements.[161] The results from UPS measurements are in good agreement with those made by cyclic voltammetry.[147] The small difference for the HOMO level extracted from measurements in solution

to the ionisation potential of films represents again the weak solid state interaction and highlights the amorphous nature of these materials.
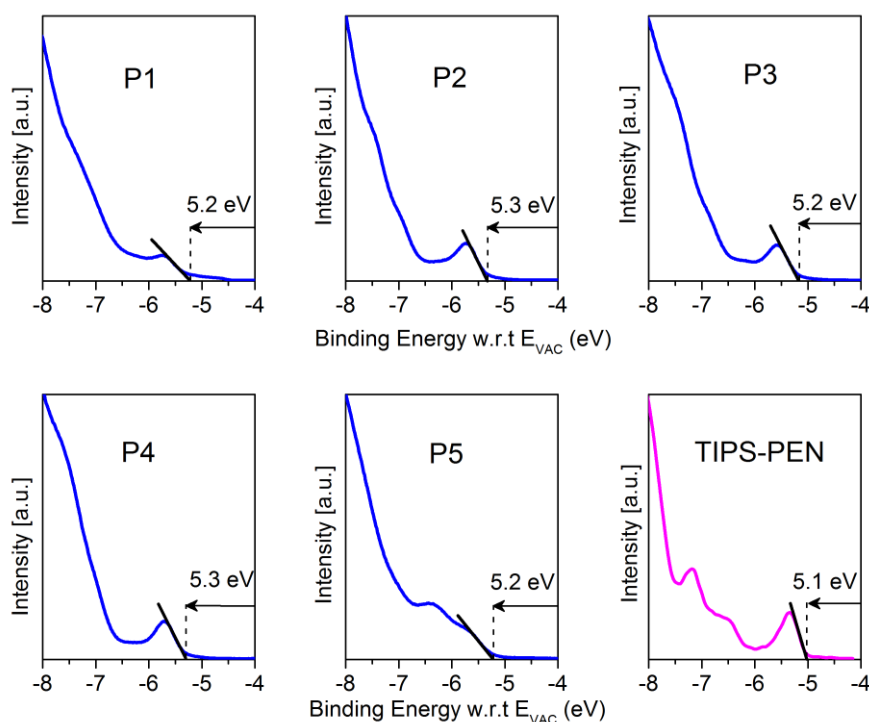
Figure 35. Ultra violet photoemission spectroscopy measurements of the valence band features of the pentacene polymers **P1-P5** and **TIPS-PEN** as reference.

The similarity in the valence band features of the different polymers to those of **TIPS-PEN** indicates that the electronic structure is mostly determined by the TIPS-pentacene group and is unaffected by the polymer backbone or the manner in which the pentacene units are connected to it. Since all the polymers showed a very similar HOMO position, it is likely that the higher degree of flexibility of the pentacene body at the polymer backbone of **P2-P5** allowed for a more favourable contact to be formed between the polymer and the gold electrode improving hole injection. However, despite these improvements the overall hole mobilities were still very low and are not competitive with those achieved for small molecules.

4.5. Conclusion

The various non-conjugated amorphous pentacene-based polymers could be successfully employed in organic field-effect transistors. Despite the fact that most of the polymers are well soluble in a range of solvents and formed uniform compact thin films suitable for field effect transistor fabrication, the performance of such transistors was poor. This is a result of the amorphous nature of the polymers and the absence of strong intra- and interchain interactions of the pentacene units, which considerably lowers the efficiency of charge transport. However, the extracted hole mobilities are in good agreement with values reported for other pentacene containing polymers.[104,162] Future pentacene containing polymers should mainly focus on the

interaction of the pentacene's π-system to promote a good charge transport within the material unlike those investigated in this study.

<div align="right">

Chapter 5

TIPS-Tetraazapentacene
in Spin-Coated and Zone-Cast Transistors

</div>

This chapter describes the studies of the morphological and electric properties of **TIPS-TAP** in solution-processed n-channel organic field-effect transistors. First, the solution for the wettability issues of **TIPS-TAP** deposition on glass or silicon dioxide modified surfaces by utilizing cross-linked interlayers like polyimide and benzocyclobutane (BCB) is presented. Changing the processing conditions for the deposition of the **TIPS-TAP** layers resulted in the formation of a variety of microstructures and film morphologies. X-ray diffraction experiments on these films revealed an excellent ordering of **TIPS-TAP** and the polycrystalline films of **TIPS-TAP** were successfully implemented in different transistor architectures to evaluate the charge transport properties. To enhance the ordering of **TIPS-TAP** and reduce the influence of grain boundaries on the extracted electron mobilities, the zone-casting deposition technique was utilized, resulting in highly aligned, ordered films of **TIPS-TAP** with improved charge transport properties. Finally, the bias-stress and environmental stability of **TIPS-TAP** transistors were evaluated. Some of the results presented in this chapter have been reported in Ref. [163]: F. Paulus, J. U. Engelhart, P. E. Hopkinson, C. Schimpf, A. Leineweber, H. Sirringhaus, Y. Vaynzof, U. H. F. Bunz, „The effect of tuning the microstructure of TIPS-tetraazapentacene on the performance of solution processed thin film transistors", *J. Mater. Chem. C* **2016**, *4*, 1194–1200.

5.1.   Motivation

In 2009 Bunz and coworkers reported the synthesis of the symmetrical tetraazapentacene (**TIPS-TAP**) that represents the aza congener to the well-known and broadly studied TIPS-pentacene (**TIPS-PEN**) (**Figure 36**).[61,77,130,138] The substitution of nitrogen resulted in a significant stabilisation of the frontier molecular orbitals so that **TIPS-TAP** was considered to be an excellent candidate for electron transport due to its low LUMO. The molecular packing of **TIPS-TAP** is very similar to **TIPS-PEN**. Both molecules exhibit a brickwork packing and a layered crystallite structure that is beneficial for lateral charge transport (**Figure 37**). As mentioned before (see **Chapter 2**), the group of Miao published the first thin film transistors utilizing **TIPS-TAP** in 2011.[21] Since then, parallel to this work, Miao and co-workers have demonstrated the superb electron transport properties of **TIPS-TAP** in various publications.[21,132–135,164] However, the deposition methods, obtained microstructures and device architectures used in this study are different to those reported by Miao and co-workers. Nevertheless, the device performance, extracted electron mobility values and device stability reported here do not coincide with the reported values and are discussed in this chapter.
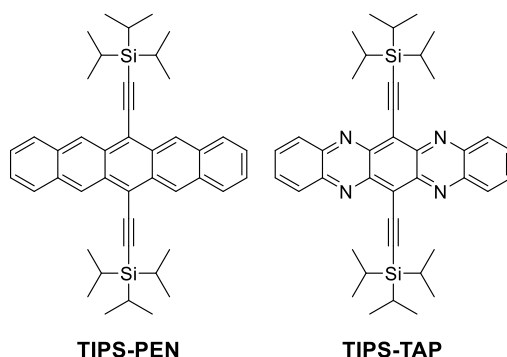
TIPS-PEN   **TIPS-TAP**

Figure 36. Molecular structures of **TIPS-PEN** (left) and **TIPS-TAP** (right).

TIPS-TAP crystallises in a brickwork pattern like the congener **TIPS-PEN**. In the solid state packing every acene molecule is surrounded by four neighbouring molecules, of which two are symmetrically equivalent (**Figure 36**). The geometrical overlap to these two neighbours exhibit an average π-π-stacking distance of 3.30 Å, which is slightly smaller than in the corresponding **TIPS-PEN** (3.41 Å).[77,130] The synthesis and crystallographic structure for **TIPS-TAP** was reported by S. Miao et al. in 2009, while Q. Miao and co-workers reported a different crystal structure for **TIPS-TAP** in 2011.[21,130] Even though the unit cell parameters of both structures are very similar, the effective cell volume differs significantly. Calculations have shown, that the effective transfer integrals for HOMO-HOMO and LUMO-LUMO interactions are different for both structures.[165] The HOMO-HOMO transfer integral almost entirely disappears for the structure of Q. Miao, while the LUMO-LUMO transfer integrals are rather similar for both structures.[165] The origin of the discrepancy in the single-crystal structure are unknown and it remains unclear if the differences are a result of a different crystal preparation, a thermal effect or are pointing to another polymorph of **TIPS-TAP**.
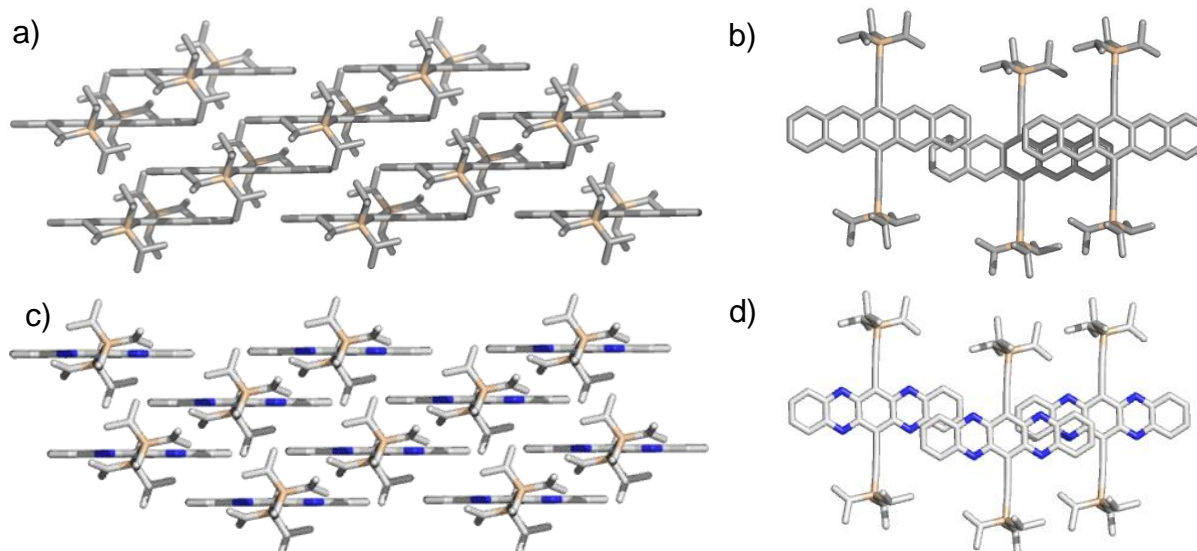
Figure 37. Solid state packing of (a)+(b) **TIPS-PEN** and (c)+(d) **TIPS-TAP**. Both materials exhibit a 2-dimensional brickwork pattern. View in (a) and (c) along the plane of the molecular π-systems; (b) and (d) view onto the molecular plane.

5.2.   Deposition of TIPS-TAP on BG/BC pre-structured substrates

Early attempts to fabricate thin film transistors with **TIPS-TAP** focused on the application of the pre-patterned bottom-gate/ bottom-contact substrates with thermally grown silicon dioxide as gate dielectric. To obtain an efficient transport of electrons at the interface, self-assembled monolayers had to be deposited on the silicon dioxide surface to passivate trap states.[15,18] As mentioned previously (see **Chapter 4**), a variety of surface modifiers were used in attempts to passivate the silicon dioxide surface. However, their deposition resulted in partially destroyed and etched contacts that acted as nucleation sites for **TIPS-TAP** and prevented uniform film formation. Furthermore, the high surface energy of the modified silicon dioxide layers did not allow a deposition of **TIPS-TAP** *via* spin-coating, as the solvent did not wet the substrate properly. Hence, only slow drop-casting process lead to a crystallisation of **TIPS-TAP** on the modified dielectric surface, but the process was driven by the affected gold contacts and the resulting films consisted of isolated crystallites and no homogenous and continuous layers of the organic material were observed (**Figure 38**).
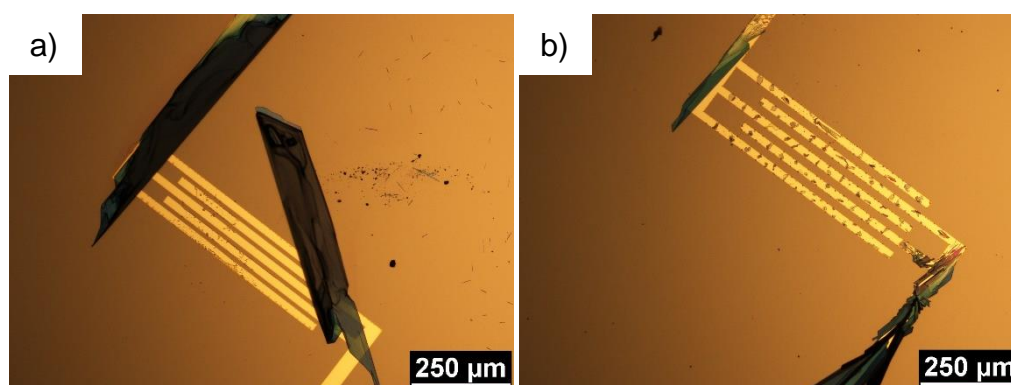
Figure 38. TIPS-TAP deposited on different FET substrates and surfaces; (a) drop-casting on OTDS/SiO$_2$ and (b) drop-casting on OTS/ SiO$_2$ did not result in proper films.

Reproducible fabrication of reliable **TIPS-TAP** transistors on these OTS, ODTS and HMDS modified surfaces proved to be impossible. Even spin-coating of **TIPS-TAP** on bare untreated cleaned glass substrates resulted in inhomogeneous and discontinuous films which could not be used for a reliable production of thin film transistors (**Figure 39a and b**).
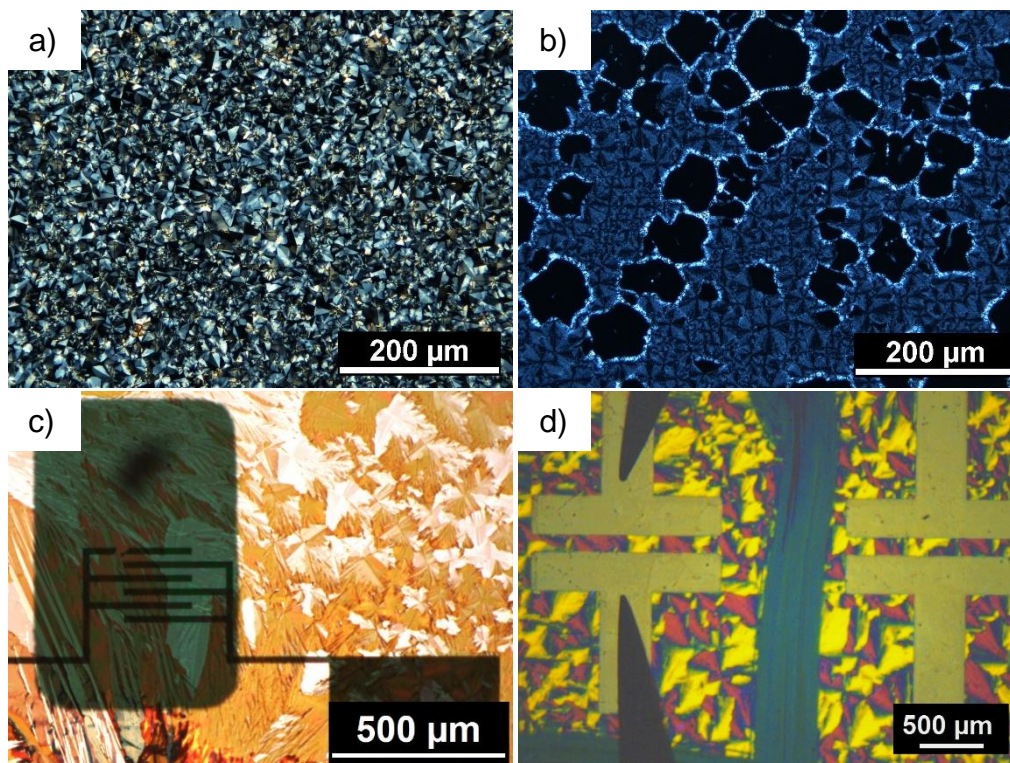

Figure 39. Polycrystalline films of **TIPS-TAP** on bare, untreated glass (a) spin-cast from toluene solution (20 mg/ml) and (b) spin-cast from *m*-xylene (10 mg/ml). Homogeneous films of **TIPS-TAP** deposited by spin-coating on (c) pre-patterned source/ drain electrodes on polyimide coated glass (with dielectric layer and gate electrode on top) and (d) on a cross-linked BCB layer on SiO$_2$ topped with shadow-mask structured source/ drain electrodes. [Images (a) and (b) adopted from Ref. [163] - Reproduced by permission of The Royal Society of Chemistry]

5.3.   Properties of thin films formed on polyimide and BCB interlayers by spin-coating

To overcome this problem, different interlayers between substrate and organic layer were used. It was previously reported, that deposition of **TIPS-PEN** on cross-linked and therefore insoluble polyimide interlayers by spin-coating, resulted in polycrystalline films with spherulitic domains that exhibited high mobilities of >1 cm^2/Vs.[29,87] This performance of **TIPS-PEN** transistors was successfully reproduced following the reported procedure from Sakanoue *et al.*. **TIPS-PEN** in this transistor architecture deposited by spin-coating from tetralin solution exhibited a high average hole mobility of (0.74±0.12) cm^2/Vs and a best mobility of 1.2 cm^2/Vs (see Appendix). The transistors showed small threshold voltages and low hysteresis for PFBT treated gold electrodes and CYTOP^{TM} dielectric. This fabrication method could be successfully adopted for **TIPS-TAP** and the polyimide coated glass substrates finally allowed the fabrication of thin film transistors with **TIPS-TAP** layers deposited by spin-coating (**Figure 39c**). Also the use of a cross-linked benzocyclobutane (BCB) interlayer

on thermally grown SiO_2 resulted in homogenous polycrystalline films of **TIPS-TAP** (**Figure 39d**) allowing for two device architectures to be successfully employed for this material.

Despite the numerous publications of **TIPS-TAP** OFETs during this work, discussing the good electron transport behaviour of **TIPS-TAP**, no accurate positions of the energy levels in the solid state have been reported for this material. Gas phase DFT calculations (B3LYP 6-31G**//B3LYP 6-31G**) of isolated molecules determined the HOMO and LUMO energies to be -5.29 eV and -3.43 eV, respectively.[130] In solution, cyclic voltammetry measurement interpreted the position of the LUMO level to be -4.01 eV.[21,130] Combined with the experimentally determined optical gap the HOMO level was found to be -5.75 eV. The energy levels of **TIPS-TAP** in the solid state are not represented by these measurements. Ultra-violet photoemission spectroscopy on thin films determined the HOMO to be 6.05 eV (**Figure 40b**). The absorption spectra of **TIPS-TAP** in thin film was red shifted by 11 nm and significantly broadened compared to the absorption in solution (**Figure 40a**). The onset of the long-wavelength absorption feature of the film is interpreted as the optical gap of **TIPS-TAP** in the solid state (λ_{onset} = 770 nm), resulting in a LUMO of (-4.45±0.1) eV for **TIPS-TAP**. These values indicate a strong stabilisation of the frontier molecular orbitals in the solid state and emphasise the importance of a correct energy level determination in the solid state prior to an application in organic devices. Compared to **TIPS-PEN** (HOMO: 5.04 eV)[161], the substitution with nitrogen in the aromatic backbone leads to a significant stabilisation of the frontier molecular orbitals and underline the potential for an efficient electron transport in **TIPS-TAP** due to the low electron injection barrier from gold electrodes (ϕ = 5.0-4.5 eV).[43]

a)

b)
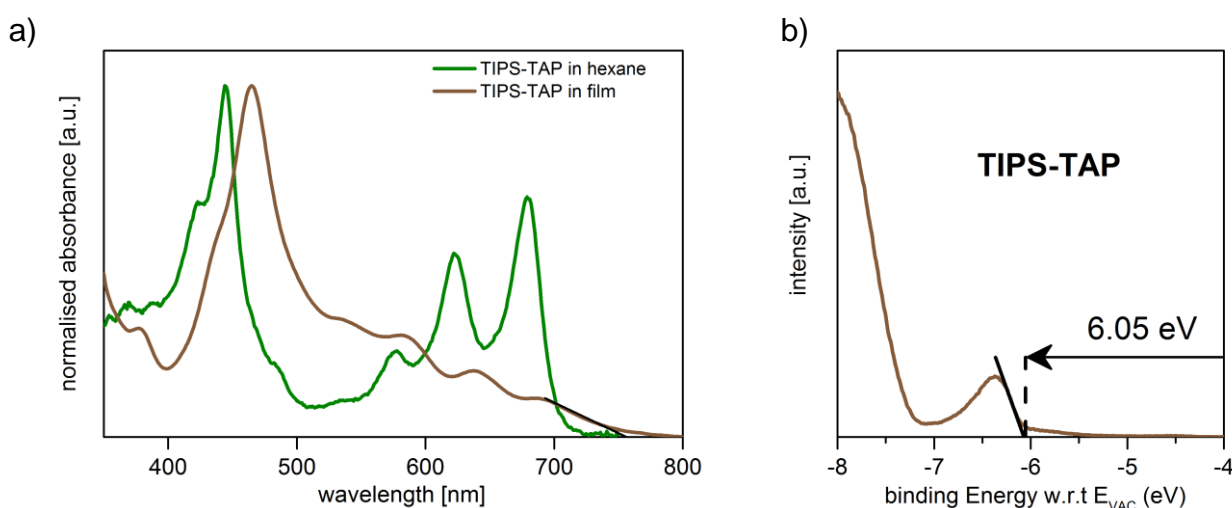
Figure 40. (a) Absorption spectra of **TIPS-TAP** in solution (hexane) and thin film (on polyimide). (b) UPS-spectra of the low-binding energy edge of a thin **TIPS-TAP** film. [Adopted from Ref. [163] - Reproduced by permission of The Royal Society of Chemistry]

Depending on the boiling point of the solvent used for deposition by spin-coating films of **TIPS-TAP** various morphologies could be obtained on polyimide coated substrates (**Figure 41**). Films spun from toluene, xylene and tetralin solution exhibited a spherultic growth that also has been reported for high-performance **TIPS-PEN** transistors.[29,87] The size of the spherultic superstructure increased with increasing boiling point as the slower

evaporation process of the organic solvent gave the material more time to organise. Films spun from chlorobenzene showed overall a small grain size. In case of tetralin the spherulites reached diameters of millimetre size. Domains of several hundred micrometre size appear in the same hue under crossed polarisers, indicating an identical orientation of the **TIPS-TAP** molecules in large areas of the film. The size of these areas are in the typical range of the interdigitated transistor electrodes, which led to the expectation of high-mobility in **TIPS-TAP** transistors in case of tetralin, due to the low density of grain boundaries in these films. The roughness of the cast films decreased consequently with the use of higher boiling point solvents, as determined by atomic force microscopy (**Figure 42**). The crystallites for films cast from tetralin were very smooth with an rms-roughness of below 3 nm.
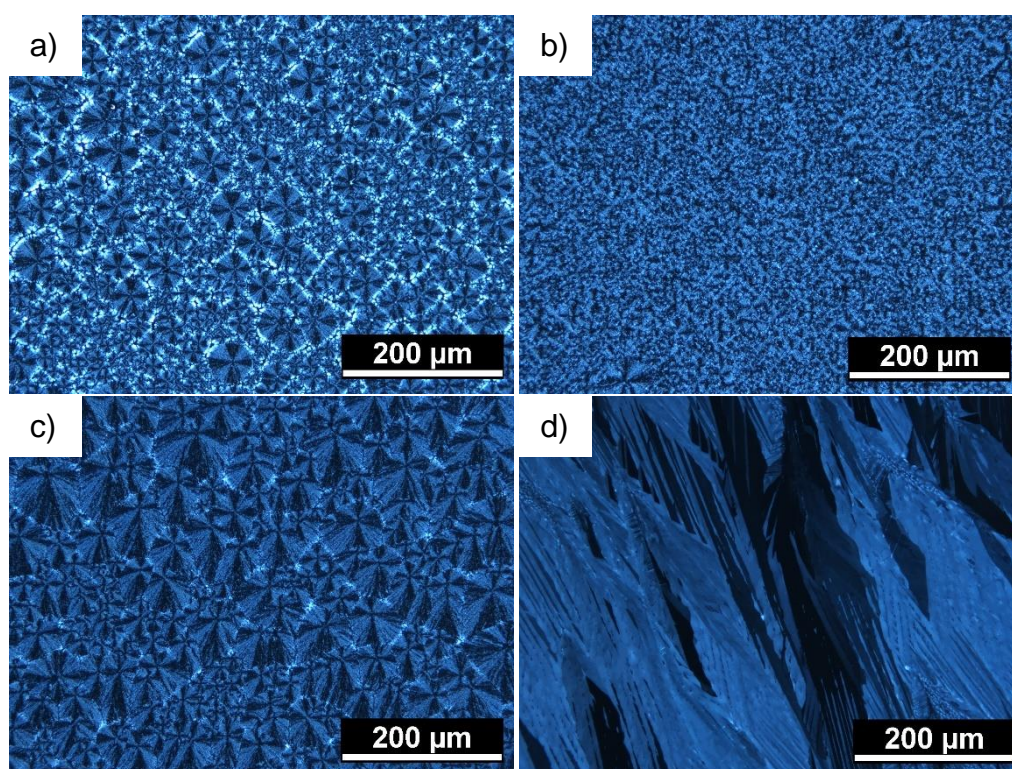
Figure 41. Optical microscope images of spin-cast **TIPS-TAP** films on polyimide coated glass substrates (a) cast from toluene, (b) from chlorobenzene, (c) from *m*-xylene and (d) from tetralin (all under crossed polarisers; 10 mg/mL). [Adopted from Ref. [163] - Reproduced by permission of The Royal Society of Chemistry]
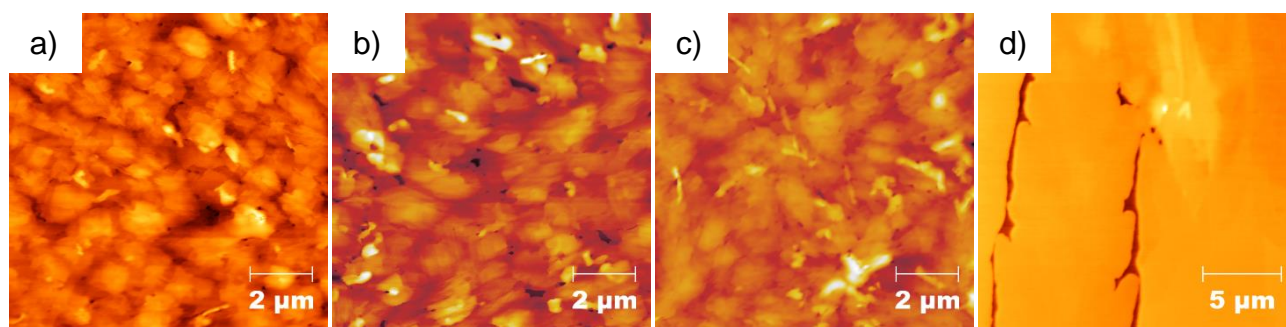
Figure 42. AFM height images of **TIPS-TAP** films on polyimide, spin-cast from (a) toluene (rms = 10.1 nm), (b) chlorobenzene (rms = 8.9 nm), (c) *m*-xylene (rms = 6.4 nm) and (d) tetralin (rms = 2.5 nm). [Adopted from Ref. [163] - Reproduced by permission of The Royal Society of Chemistry]

Films deposited on cross-linked BCB layers showed a very similar microstructure. The domain sizes of films on BCB interlayers exhibited a slightly reduced domain sizes as compared to those on polyimide, probably due to a higher concentration of nucleation sites. Due to a better wettability, mesitylene and tetralin were chosen as solvents for the deposition of **TIPS-TAP** on BCB (**Figure 43**). The use of mesitylene resulted in polycrystalline films with irregular shaped crystalline domains. Films cast from tetralin showed a spherultic growth with domains in the order of 100 µm - significantly smaller than on polyimide substrates.
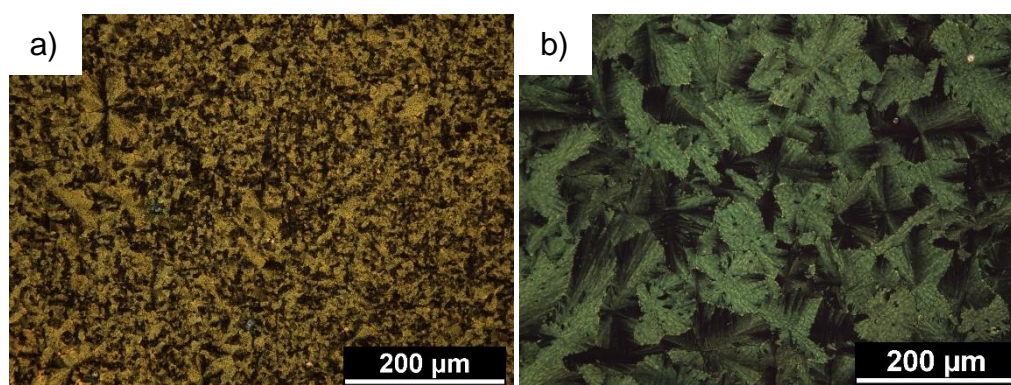
Figure 43. Spin-cast polycrystalline films of **TIPS-TAP** on BCB passivated Si/SiO$_2$ substrates (under crossed polarisers) (a) from mesitylene and (b) from tetralin.

The excellent charge transport properties of **TIPS-PEN** originate from the (00*l*)-orientation and therefore perfect positioning of the aromatic units towards the lateral charge transport direction. Miao and co-workers reported for vacuum deposited and drop-cast films X-ray diffraction data that corresponds due to the large d-spacing value of >16 Å to the same (00*l*)-orientation for **TIPS-TAP**.[21,133,134] To evaluate the molecular orientation in spin-coated films, X-ray diffraction of **TIPS-TAP** films on polyimide and BCB coated substrates was performed (**Figure 44**). The observed diffraction patterns showed a similar background intensity that can be ascribed to the glass/polyimide or the Si/SiO$_2$/BCB substrates. All samples exhibited a series of higher order Bragg reflections that coincides with a (00*l*)-orientation of **TIPS-TAP** in each sample. Reflections from tetralin on polyimide and BCB appeared sharper and were more intense compared to other samples, indicating the high degree of crystallinity and order in these samples. The extracted d-spacing values ranged from 16.48 Å to

16.51 Å, which is surprisingly accurately coinciding with the predicted value of 16.50 Å for the (001)-plane based on the analysis of the crystal structure by S. Miao *et al.* (**Table 4**).[130] The sharp reflexes and the occurrence of only these reflections lead to the conclusion that **TIPS-TAP** undergoes a strong preferred orientation with the (00*l*)-planes parallel to the substrate's surface. These results clearly show that spin-coating **TIPS-TAP** from various solutions on polyimide and BCB interlayers did not change the molecular orientation or resulted in the formation of a different polymorph. The reported d-values by Q. Miao and co-workers are in good agreement with these results, however the reported values of 16.53 Å and 16.56 Å for vacuum deposited and drop-cast films are marginally larger.[21,133,134]
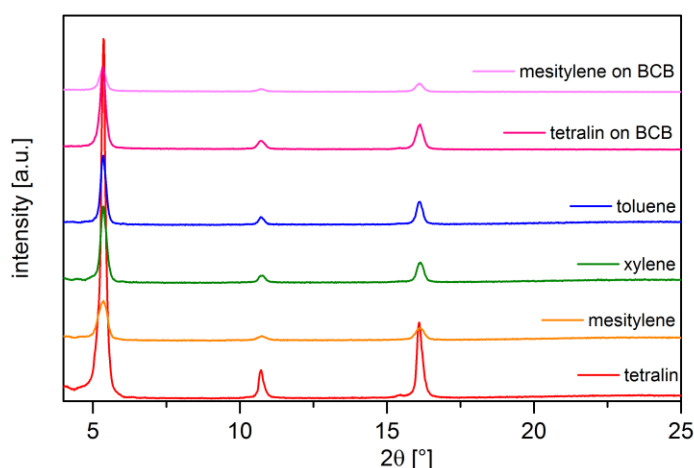
Figure 44. X-ray diffraction patterns of the thin **TIPS-TAP** films deposited by spin-coating from various solutions. If not stated otherwise the films were prepared on polyimide [partially adopted from Ref. [163] - Reproduced by permission of The Royal Society of Chemistry].

Table 4. Summarised peak positions and extracted d-values based on the Bragg equation for X-ray diffraction experiments on the polycrystalline **TIPS-TAP** films [Partially taken from Ref. [163] - Reproduced by permission of The Royal Society of Chemistry].

peak	toluene		chlorobenzene		xylene		mesitylene		tetralin		mesitylene on BCB		tetralin on BCB	
	2θ [°]	d_0 [Å]	2θ [°]	d_0 [Å]	2θ [°]	d_0 [Å]	2θ [°]	d_0 [Å]	2θ [°]	d_0 [Å]	2θ [°]	d_0 [Å]	2θ [°]	d_0 [Å]
1	5.36	16.49	5.36	16.49	5.34	16.55	5.36	16.49	5.36	16.49	5.34	16.55	5.36	16.49
2	10.72	16.51	10.70	16.54	10.74	16.47	10.74	16.47	10.72	16.51	10.72	16.51	10.72	16.51
3	16.12	16.49	16.14	16.47	16.10	16.52	16.14	16.47	16.10	16.52	16.12	16.49	16.12	16.49
4	-	-	-	-	-	-	-	-	27.06	16.48	-	-	-	-
		avg. **16.50**		avg. **16.50**		avg. **16.51**		avg. **16.48**		avg. **16.50**		avg. **16.52**		avg. **16.50**

5.3.1. FET performance of spin-coated TIPS-TAP

The first thin film transistors with spin-coated **TIPS-TAP** were fabricated in a bottom-contact/ top-gate architecture on polyimide coated glass. The double layer photoresist lithography process allowed the fabrication of interdigitated source drain electrodes with different channel lengths. This process resulted in smooth edges of the gold contacts which did not act as nucleation sites and did not affect the film formation

contrary to what has been observed previously for the pre-patterned bottom-gate/ bottom-contact substrates. The devices were completed with a dielectric layer of PMMA, spun from acetonitrile. Acetonitrile was chosen due to the fact that the deposition of the dielectric layer had to occur from an orthogonal solvent and the **TIPS-TAP** film should not be dissolved. Commonly used solvents for PMMA like *n*-butyl acetate, propylene carbonate, dimethyl sulfoxide or nitromethane either did not wet the film or dissolved it. Attempts to utilize CYTOP™ as dielectric resulted in nicely formed dielectric layers, however the observed leakage currents and the hysteresis of such devices were not satisfactory.
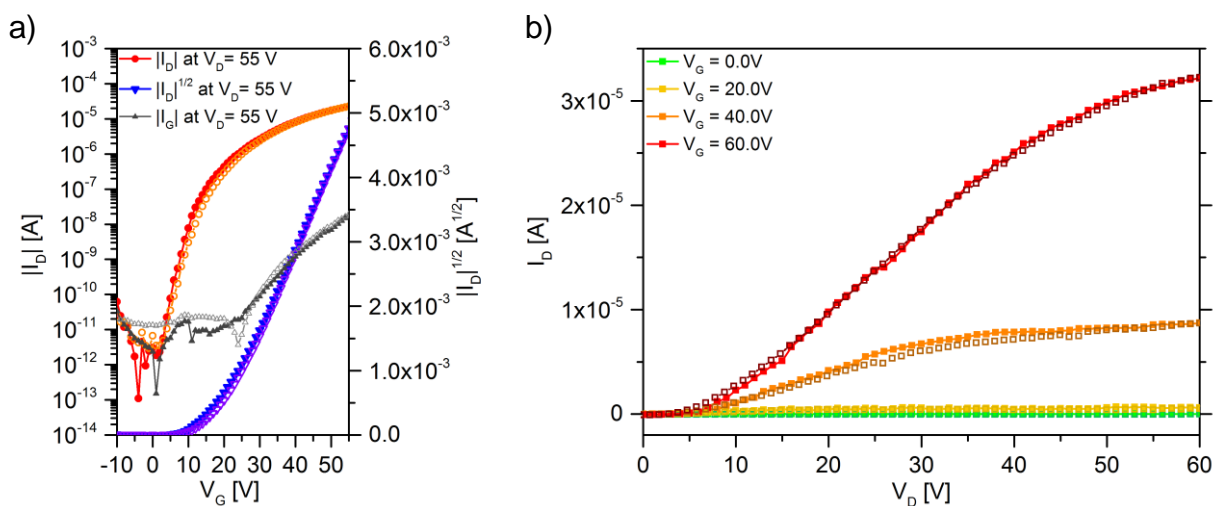
Figure 45. Thin-film transistor characteristic: (a) transfer and (b) output curves of a representative **TIPS-TAP** bottom-contact/ top-gate device deposited by spin-coating from tetralin solution in (W = 1,000 µm; L = 10 µm). [Modified from Ref [163] - Reproduced by permission of The Royal Society of Chemistry]

The average and best electron mobility of **TIPS-TAP** in bottom-contact/ top-gate transistors showed a clear trend of increase with the increasing boiling point of the solvent used for deposition, ranging from $(2.7\pm0.5)\cdot10^{-3}$ cm^2/Vs for devices from toluene to 0.10±0.03 cm^2/Vs in case of tetralin (**Figure 45**, **Table 5**). The increase in domain size and the decrease in the density of grain boundaries resulted in this enhancement of the charge carrier mobility. The subthreshold behaviour of these devices showed a mediocre subthreshold swing that improved for the devices with larger domain sizes. The fabricated transistors for all solvents exhibited almost no hysteresis, indicating no dynamic trapping processes within the **TIPS-TAP** layers and its interfaces. Unfortunately, all bottom-contact/ top-gate devices exhibited a non-linear injection behaviour, representing a large contact resistance (**Figure 45b**). This effect could explain the gradual increase of the threshold voltages extracted from the devices through a linear fit of the square root plot of the channel current. The observed non-linearity of the channel current in the output-characteristic could potentially originate from the strong (00*l*)-orientation of **TIPS-TAP** on the contact material, making it difficult to inject charge carriers into the aromatic systems. The poor non-ohmic injection behaviour and the method applied for charge carrier mobility extraction might result in an overestimation of the mobility of **TIPS-TAP** in these devices.[19] Therefore, bottom-gate/ top-gate transistors were fabricated and due to the evaporated gold on

the organic material a more intimate contact was achieved. These devices showed an improved injection behaviour, high on-off ratios, a better subthreshold swing and lower threshold voltages (**Figure 46**). However, the extracted electron mobilities of $(5.8\pm0.3)\cdot10^{-2}$ cm²/Vs were slightly lower, but in a similar range compared to the bottom-contact/ top-gate devices (**Table 5**).

Table 5. Summarised transistor parameters for **TIPS-TAP** thin film transistors. Average value and standard error are given for the electron mobility and threshold voltage. For the substhreshold swing and on/off ratio the range is given [Adopted from Ref. [163] - Reproduced by permission of The Royal Society of Chemistry].

architecture	solvent	$\mu_{electron}$ best [cm²/Vs]	μ_{hole} average [cm²/Vs]	threshold voltage average V_{th} [V]	range subthreshold swing [V/dec]	range on/off ratio
BC/TG	toluene	0.005	$(2.7\pm0.5)\cdot10^{-3}$	4.8±3.4	3.2-4.1	10^3-10^4
BC/TG	chlorobenzene	0.07	$(3.3\pm1.2)\cdot10^{-2}$	9.8±3.4	2.8-3.9	10^4
BC/TG	xylene	0.09	$(4.0\pm0.7)\cdot10^{-2}$	9.9±0.9	2.5-3.9	10^3
BC/TG	tetralin	0.31	$(1.0\pm0.3)\cdot10^{-1}$	25.4±1.6	2.5-3.4	10^5 -10^6
BG/TC	mesitylene	0.07	$(5.8\pm0.3)\cdot10^{-2}$	9.5±0.3	1.9-2.5	10^3-10^4
BG/TC	tetralin	0.05	$(3.4\pm0.2)\cdot10^{-2}$	6.6±0.3	1.8-2.6	10^4-10^5
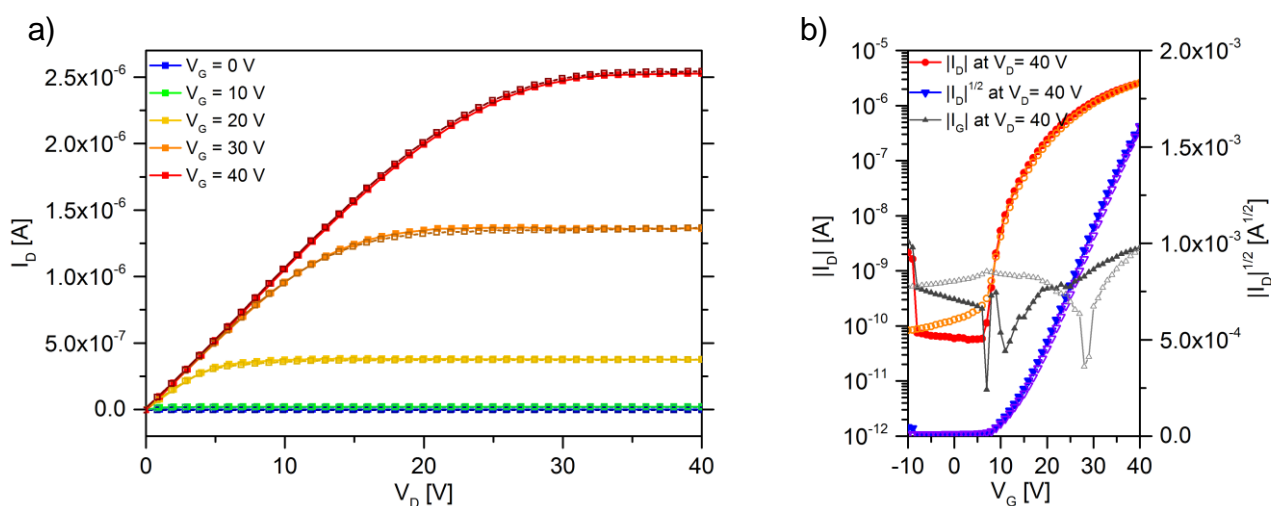
Figure 46. Top-contact device (W = 1,500 µm; L = 130 µm) with **TIPS-TAP** spin-coated from mesitylene on BCB coated Si/SiO₂ and improved injection behaviour; (a) output characteristic and (b) transfer characteristic [Modified from Ref. [163] - Reproduced by permission of The Royal Society of Chemistry].

The observed and extracted electron mobility values for bottom-contact and top-contact transistors differ significantly from the values reported in literature by Miao and co-workers during the time in which this work was carried out.[21,133,134] There might be several reasons for this discrepancy. The devices presented in this work require higher gate voltages due to the use of a thicker dielectric layer compared to literature, where thin aluminium-titanium oxide layers with passivating self-assembled monolayers were used.[133,134] The resulting charge charrier density in the transistors presented here is therefore lower, suggesting that the charge transport might occur in the low energy tail of the transport states, resulting in lower electron mobilities. Furthermore, transistor characteristics of **TIPS-TAP** presented in literature often show a non-

linearity (bending) of the square root plot of the channel current and a non-zero channel current for $V_D = 0$ V in the output characteristics. Both observations could indicate contact issues, charge trapping and gate leakage problems in those devices. The transistors fabricated by Miao and co-workers were normally characterised in vacuum and the presented I-V characteristics do not show a backward sweep. This practice makes it very difficult to judge the influence of environmental causes, such as even low humidity and oxygen concentrations on the device (like in an inert glovebox atmosphere) or untangle the contribution of dynamic trapping effects. Especially the use of inorganic oxides with self-designed monolayers as dielectric layers would normally require a careful analysis of the trapping processes at the organic/dielectric interface. The main difference in the **TIPS-TAP** transistors presented here is the use of polycrystalline **TIPS-TAP** films obtained through spin-coating deposition, while Miao and co-workers deposited **TIPS-TAP** by drop-cast deposition or sublimation in vacuum, resulting in different film structures and morphologies.[133–135]

5.4.   Properties of zone-cast TIPS-TAP films and field-effect transistor performance

To further improve the microstructure of **TIPS-TAP** the zone-casting technique was employed. The slow deposition process and precise control of the deposition temperatures and substrate speed using a zone-casting setup allowed the fabrication of highly aligned crystalline films, such as has been reported for **TIPS-PEN**.[88,90]

To investigate whether similar improvements in structure could be achieved for **TIPS-TAP**, solutions of chlorobenzene or mesitylene were zone-cast on polyimide coated substrates (3 mg/mL). The choice of these solvents allowed the study of a broad range of deposition temperatures, resulted in a good wettability and a reasonable film formation during the casting process. Once the deposition parameters were optimized the zone-casting deposition technique resulted in uniform films, which consist of uniaxially oriented crystalline ribbons of **TIPS-TAP** with a uniform thickness. Ribbons with identical molecular orientation and of uniform thickness appear in the same brightness and colour under the crossed polarisers. Films cast from chlorobenzene at a substrate temperature of 80°C did not result in long connected crystalline ribbons, but rather in V-shaped structures that were not connected with each other (**Figure 47a**). A higher substrate temperature resulted in inhomogeneous films with an intermixed growth of ribbon and plate like structures (**Figure 47b**). The **TIPS-TAP** crystallites obtained from chlorobenzene developed cracks during deposition and were therefore not used in transistors. Films cast from mesitylene appeared more regular and ordered (**Figure 47c-f**). The ribbon thickness increased slightly with increasing temperature. A substrate temperature of 80 °C resulted in crystal strands with a low degree of order. The ordering and uniaxial orientation of the **TIPS-TAP** ribbons was improved for higher temperatures of 100 °C, 120 °C and 130 °C.
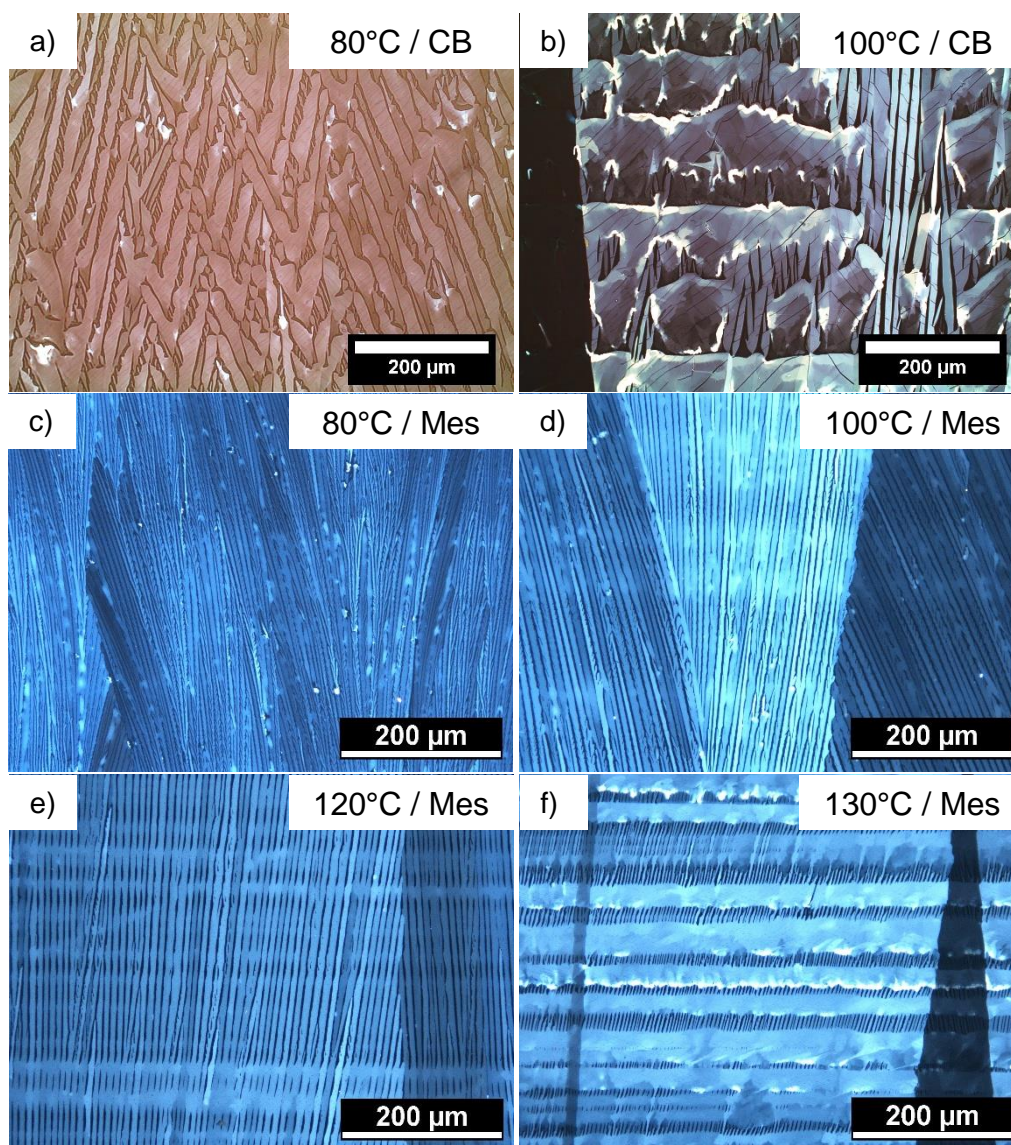
Figure 47. Optical microscope images (under crossed polarisers (c-f) or with λ/4-plate (a-b)) of zone-cast films of **TIPS-TAP** from chlorobenzene and mesitylene solutions, respectively. (a)+(b) cast from chlorobenzene at given substrate temperatures. (c)-(f) zone-cast from mesitylene at different temperatures. All samples were cast at a substrate velocity of 250 μm/s.

These ordered films of zone-cast **TIPS-TAP** were investigated in bottom-contact field-effect transistors. The source and drain electrodes were chosen to be perpendicular to the zone-casting direction. The average electron mobility and transistor performance varied strongly depending on the temperature chosen for deposition. A low substrate temperature and a poorly ordered film resulted in an average mobility of only $(4.3\pm1.0)\cdot10^{-3}$ cm^2/Vs, which is comparable to the performance of spin-cast films from toluene solution (**Table 6**). The highest electron mobilities values with an average of (0.22 ± 0.04) cm^2/Vs reaching up to 0.41 cm^2/Vs were measured for a substrate temperature of 120 °C. The bottom-contact/ top-gate devices exhibited the same injection issues as the ones fabricated through spin-coating and the output characteristics shows an S-shape for low V_D-voltages (see Appendix). The extracted threshold voltages for all zone-cast devices in this device geometry are significantly higher than those previously shown for spin-coated **TIPS-TAP** in this architecture (see **Table 5**).

Table 6. Average electric parameters for zone-cast **TIPS-TAP** transistors. For the electron mobility and threshold voltage average values and standard errors are given. For the on/off ratios the range per set of devices is represented.

architecture	solvent	temperature [°C]	$\mu_{electron}$ best [cm²/Vs]	μ_{hole} average [cm²/Vs]	threshold voltage average V_{th} [V]	range on/off ratio
BC/TG	mesitylene	80	0.01	$(4.3\pm1.0)\cdot10^{-3}$	50.5 ± 2.2	10^3-10^4
		100	0.05	$(2.2\pm0.9)\cdot10^{-2}$	48.4 ± 2.6	10^3-10^5
		120	0.41	(0.22 ± 0.04)	52.7 ± 1.8	10^4-10^5
BG/TC	mesitylene	100	0.02	$(7.5\pm2.5)\cdot10^{-3}$	8.4 ± 3.3	10^2-10^3
		110	0.16	$(9.9\pm1.2)\cdot10^{-2}$	8.5 ± 1.1	10^4-10^5
		120	0.13	$(8.6\pm0.6)\cdot10^{-2}$	15.4 ± 4.8	10^3-10^4

The fabrication of zone-cast **TIPS-TAP** transistors in bottom-gate/ top-contact architecture resulted also in this case in an improved injection behaviour. BCB coated substrates were used at different temperatures to form aligned **TIPS-TAP** films and gold electrodes were evaporated through a shadow mask onto these films. The best wettability and film formation was achieved for a slightly reduced casting speed of 150 µm/s.
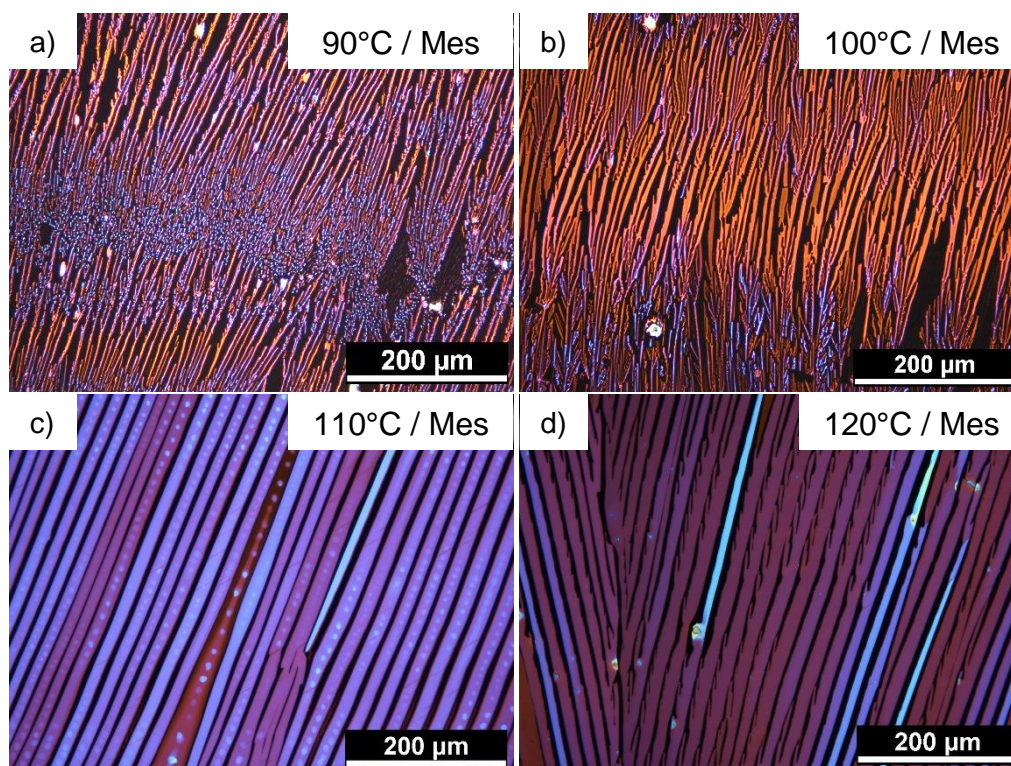
Figure 48. Polarised optical microscopy images (crossed polarisers) of zone-cast **TIPS-TAP** films from mesitylene solution on BCB at different substrate temperatures (casting speed 150 µm/s). [Adopted from Ref. [163] - Reproduced by permission of The Royal Society of Chemistry]

The substrate temperature affects the formed microstructure of **TIPS-TAP** on BCB in a more pronounced manner than on the polyimide substrates. Casting temperatures of 90 °C and 100 °C did not result in aligned crystalline ribbons and form irregular narrow **TIPS-TAP** crystallites with fringy edges (**Figure 48a and b**).

Despite the fact, that the length of these crystallites is increased for 100 °C the observed crystalline structures appear partially isolated, resulting in a low transistor performance (**Table 6**). Substrate temperatures of 110 °C or higher resulted in uniform, mainly parallel crystalline strands with clear edges, homogenous thickness and orientation. The average widths of the grown **TIPS-TAP** ribbons on BCB at 110 °C and 120 °C are much larger than those observed on polyimide which might be attributed to the slower casting speed and different wettability of the substrate (**Figure 48c and d**). Overall, the transistor performance of zone-cast **TIPS-TAP** on BCB substrates at 110 °C is comparable to the one on polyimide. The injection in all zone-cast devices on BCB is ohmic and the extracted threshold voltages are therefore comparable to those from spin-coated **TIPS-TAP** on BCB (**Figure 49**).
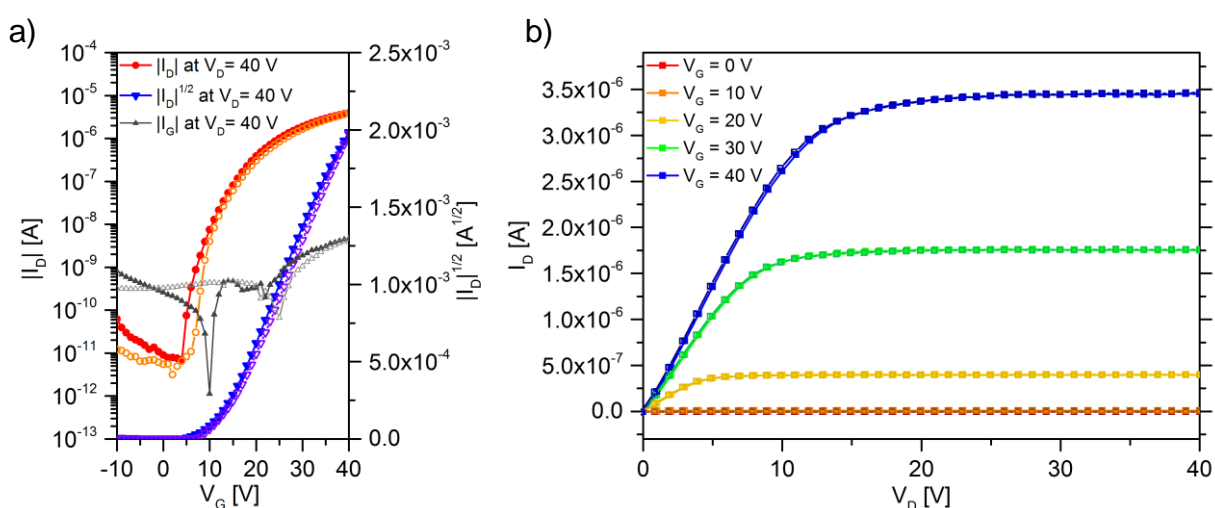
Figure 49. I-V-characteristics of a representative zone-cast **TIPS-TAP** transistor on Si/SiO$_2$/BCB (W = 1,500 μm; L = 250 μm); (a) transfer and (b) output measurements.

The best electron mobility of 0.16 cm^2/Vs and the highest average mobility (9.9±1.2)·10^{-2} cm^2/Vs were measured for a substrate temperature of 110 °C and are about one order of magnitude higher compared to transistors cast at 100 °C. A higher substrate temperature of 120 °C resulted in a slightly decreased electron mobility and higher average threshold voltage. Atomic force microscopy revealed that the crystalline strands zone-cast at 120 °C exhibit cracks along their growth direction which might be the origin of the lower performance (**Figure 50**).
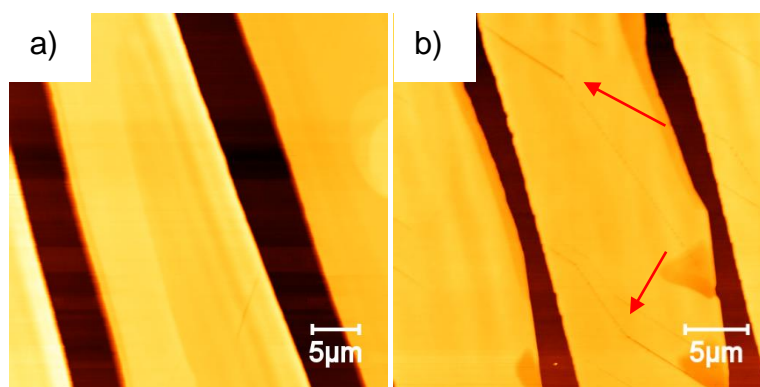
Figure 50. AFM height images of **TIPS-TAP** (a) 110°C zone cast films and (b) zone-cast films at 120°C.Red errors indicate the cracks formed during zone casting.

To probe the molecular orientation of **TIPS-TAP** towards the substrate and zone-cast direction, XRD measurements on zone-cast film of **TIPS-TAP** were performed (**Figure 51**). The highly ordered zone-cast films on BCB at 110 °C and 120 °C exhibit both very sharp and intense reflections, representing the highly crystalline nature of these films. The samples showed the identical diffraction pattern that was observed for **TIPS-TAP** on polyimide and BCB. The extracted d-spacing values of 16.49 Å and 16.51 Å for a deposition temperature of 110 °C and 120 °C, respectively were identical to the one observed for spin-coated **TIPS-TAP** films (**Figure 51**). The results clearly indicate that the chosen casting speed produces highly (00*l*)-oriented **TIPS-TAP** films.
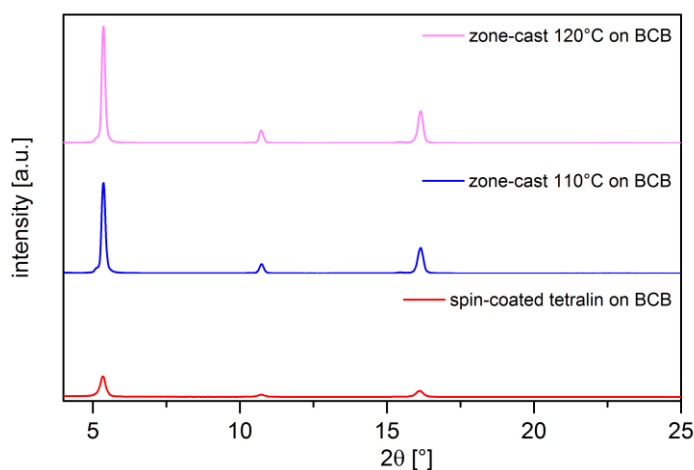
Figure 51. X-ray diffraction pattern of zone-cast **TIPS-TAP** films on BCB/SiO$_2$ substrates and comparison to the pattern of spin-coated **TIPS-TAP** on BCB/SiO$_2$.

The deposition process does not result in a tilt of the aromatic molecules upon casting or a reduced layer spacing, which makes the results of zone-cast transistors comparable to the ones fabricated through spin-coating. To evaluate the growth and charge transport direction of the crystalline ribbons during zone-casting and interpret the charge transport along these crystalline strands, grazing incidence wide angle X-ray scattering (GIWAXS) was performed on a zone-cast **TIPS-TAP** film (**Figure 52**). The measurement was taken parallel and perpendicular to the zone-casting direction to obtain information regarding the solid state

packing along the growth direction of the crystal strands. Both diffraction maps exhibited very sharp and defined diffraction peaks which indicate the high crystallinity of the zone-cast **TIPS-TAP** film. The observed differences in the GIWAXS pattern for parallel and perpendicular incident suggest that the **TIPS-TAP** crystallites are highly oriented towards the zone-cast direction. The staggered diffraction peaks for $q_{xy} = 0$ in the parallel and perpendicular measurement origin from scattering of the (00l)-Miller planes parallel to the substrate's surface and resemble the observations from the XRD-measurements with a d-spacing value of 16.5 Å. For the incident parallel to the zone-cast direction a series of reflections with a $q_{xy} = 0.853$ Å^{-1} were found, which correspond to Miller planes (01l). The length of the scattering vectors for the (011), (013) and (014) reflections were measured to be 6.74 Å, 4.35 Å and 3.54 Å, respectively, which coincides very well with the predicted values of 6.77 Å, 4.39 Å and 3.58 Å based on the single crystal structure of **TIPS-TAP**.[130] The reflection at $q_{xy} = 1.673$ Å^{-1} can be described by the diffraction vector from the (022) plane, lying in the same scattering direction as the corresponding (011) reflection (see Appendix). For measurements perpendicular to the zone-cast direction the scattering of (01l)-Miller planes was not visible which clearly highlights the strong anisotropic orientation of the **TIPS-TAP** crystals towards the zone-cast direction. The set of staggered reflections occurring at $q_{xy} = 0.826$ Å^{-1} could be ascribed to the (10l)-Miller planes of the crystalline sample (see Appendix). The comparison between the reflexes occurring from measurements parallel and perpendicular to the zone-casting direction emphasises that the b-axis of the unit cell is oriented perpendicular to the casting and growth direction, meaning, that the growth of **TIPS-TAP** ribbons occurs along the (100) crystal plane of **TIPS-TAP**. This results in a π-π-stacking, which does not coincide with the direction of zone-casting. As a result, charge transport in the chosen transistor configuration does not match the direction of π-π-stacking and might explain why only mild improvements were observed in the performance for zone-cast **TIPS-TAP** FETs.
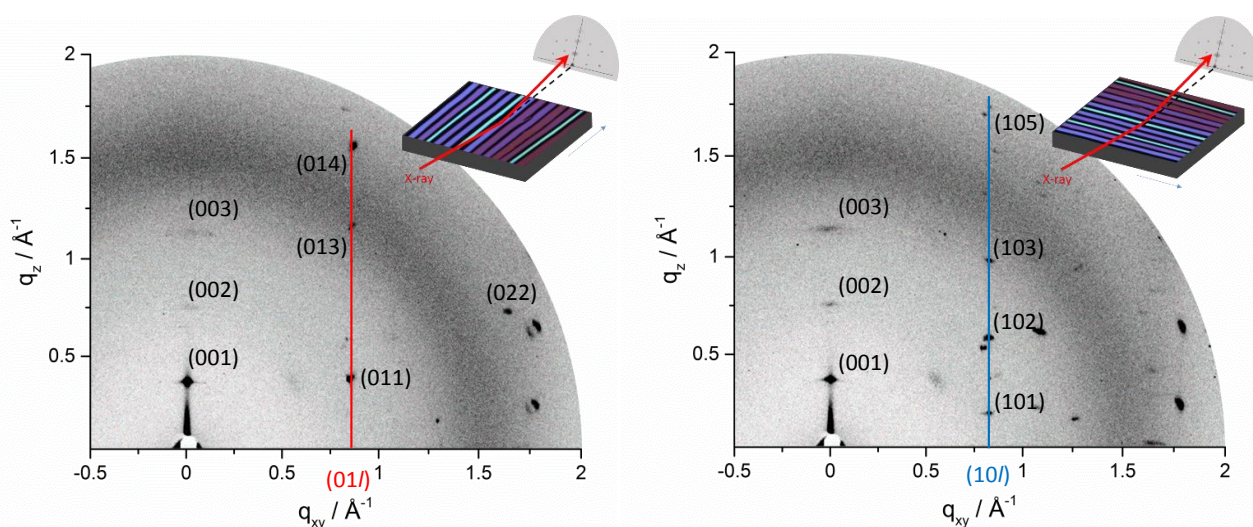
Figure 52. (left) 2-D GIWAXS diffraction map and schematic experimental setup (inset) for an beam incident parallel to the zone-cast direction of TIPS-TAP; (right) diffraction pattern of GIWAXS measurement perpendicular to the zone-cast direction of **TIPS-TAP**.

The observed orientation and growth of **TIPS-TAP** crystallites in the zone-cast films has been predicted by Wang *et al.* and is similar to that of drop-cast or shear-coated **TIPS-PEN**.[*] [20,96,132,166] In the case of **TIPS-PEN**, it has been shown that the highest charge carrier mobility can be obtained for a casting direction ~35° to the charge transport direction.[83] Since the transistor configuration investigated here did not include a tilted casting direction, it is possible that these results can be improved further.

Despite the fact that the zone-cast films of **TIPS-TAP** exhibit a large similarity to drop-cast structures reported by Miao and co-workers during the time of this work, the extracted electron mobilities reported in literature for **TIPS-TAP** could not be reproduced even with these highly ordered and aligned crystalline films. The molecular orientation in both cases is identical and cannot be the cause of the differences in the charge transport behaviour. The origin of the discrepancy between these results and the values published by Miao et al. remains further unclear.

5.5.   Bias stress and environmental stability of TIPS-TAP transistors

The **TIPS-TAP** transistors on BCB were investigated in bias stress experiments with different environmental conditions to evaluate the stability of **TIPS-TAP** in thin film transistors. The bottom-gate/ top-contact architecture was used for these studies, due to the fact that the active organic layer is directly exposed to the environment and is not encapsulated or buried under additional dielectric layers or gate electrodes. Mesitylene was used for deposition and the devices exhibited prior to the stability investigation an average performance similar to those reported above (see **Table 5**). The fabricated **TIPS-TAP** devices were placed and contacted in a home-built sample holder that allowed a precise control of the oxygen (ppm) and water (ppmV) concentration during the measurement (see Appendix). The source electrode was grounded while the gate and channel current and voltages were supplied from external source-meter units. The devices were switched on to saturation ($V_G = V_D = +40$ V) and left in this state for several minutes (electrical stressing), followed by transfer and output measurements to evaluate changes in the transistor performance. Optional resting times were included that allowed the devices to recover. The changes in electron mobility, threshold voltage and relative hysteresis (see **Chapter 3** for definition) were normalised to visualise the changes in transistor performance throughout the experiment. The detailed order of measurements and stressing conditions is indicated for each experiment individually as flow-diagram. I-V characteristics of each device at a particular time of the experiment are shown in the Appendix.

The performance of **TIPS-TAP** transistors did not remain constant when the device was electrically stressed for 30 min (**Figure 53**). The extraction of the electron mobility values and the threshold voltages from transfer

---

[*] The reader should note that the interpretation of the crystal growth direction and alignment of **TIPS-PEN** in the recent publications of Bao and co-workers is based on a unit cell in which the a and b axes are interchanged as compared to the original crystal structure reported by Anthony *et al.*[77]

measurements in the saturation regime after a bias-stress of 30 min showed that the threshold voltage increased constantly with the progress of the experiment reaching nearly twice its initial value after the first 2.5 hours, while the electron mobility increased in parallel. The relative hysteresis was reduced upon bias-stressing. This can be attributed to a population of the initial trap states in the **TIPS-TAP** devices during bias-stressing, as previously observed for **TIPS-PEN**.[167,168] These states remain populated during the transfer measurement that follows, resulting in a large shift of the threshold voltage. Injected charge carriers at gate voltages above the effective threshold voltage are therefore not affected by trap-states and the electron mobility increases. This filling of trap states occurs in the first four stressing cycles and afterwards almost no changes occur. An output characteristic at the beginning of bias stressing and after about 7 hours (see Appendix) indicate a linear injection behaviour throughout the experiment.
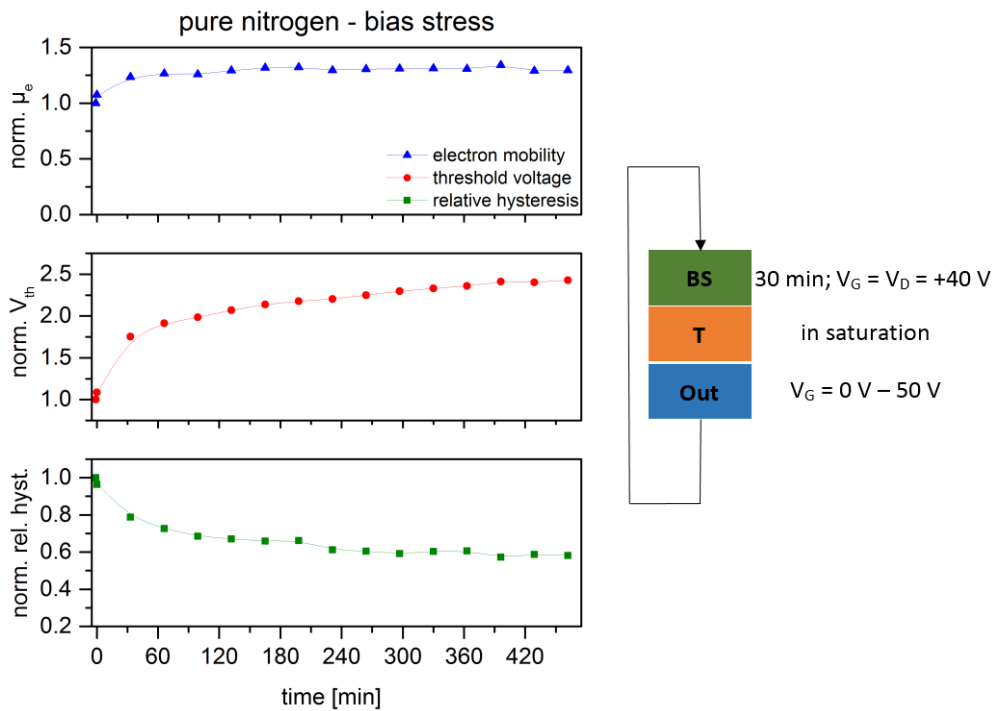
Figure 53. Development of electron mobility, threshold voltage and hysteresis (all normalised to value at 0 min) of a **TIPS-TAP** transistor under bias stress versus time in nitrogen (left) and schematic flow chart of the experiment (right).

To verify that trap filling is responsible for the observed performance changes, the experimental procedure was modified. The bias stressing times were shortened to 10 minutes and a transfer characteristic used for the extraction of the presented parameters was measured directly afterwards, before the device was allowed to rest for a short time. The output characteristic was only performed after every fifth stressing cycle to lower the impact of this measurement on the data, while still being able to monitor the injection properties (**Figure 54**). The observations made in this case are identical and the previous ones, only the magnitude of improvement in electron mobility and changes in threshold voltage are larger and achieved faster, resulting in an almost 350% improvement in the electron mobility after 40 hours after an initial three fold increase

within the first 5 hours. This effect confirms that the filling of trap states occurs within the first few hours of electrical stressing and afterwards the device performance remains stable for many tens of hours. Also in this case the injection remained linear with devices operational over 100 stressing cycles.
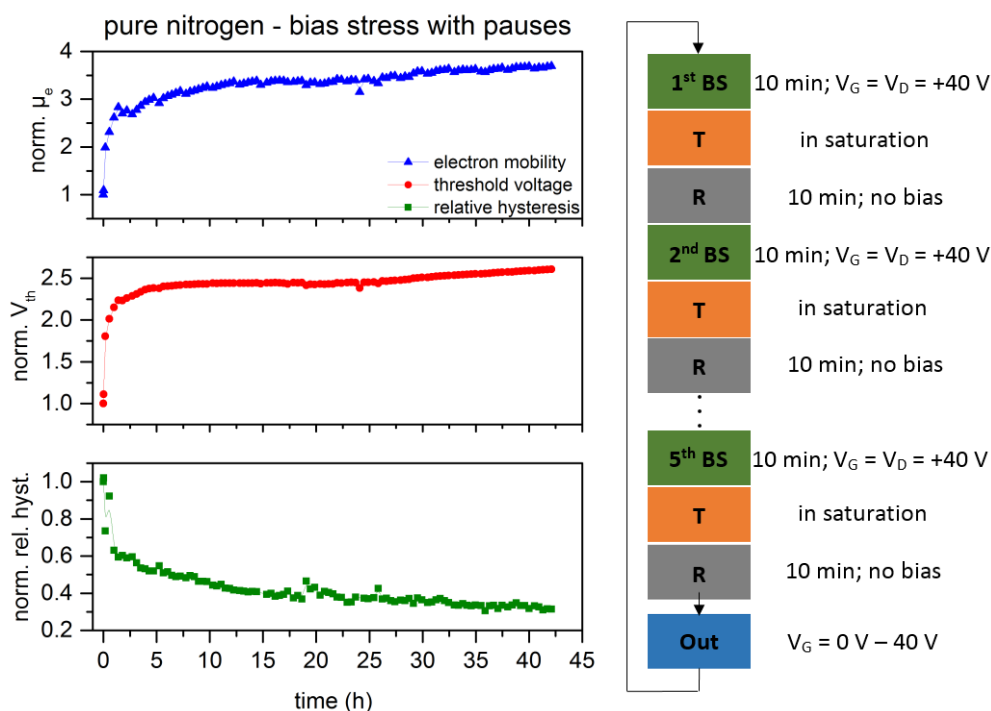
Figure 54. Behaviour of transistor parameters (mobility, threshold voltage and hysteresis; all normalised) versus time upon bias stressing with resting phases under inert atmosphere. (left) and overview of the programmed experiment.

After the initial filling of trap states, the constant performance of the transistor suggests a high electric stability of **TIPS-TAP** in the devices. No decomposition or degradation was observed that affects the **TIPS-TAP** active layer in the device in nitrogen. To probe the environmental stability of **TIPS-TAP** in top-contact transistors the environmental conditions of the bias-stressing experiment were changed. The experimental schedule remained unaltered. Devices tested in this way at 1.5% oxygen concentration and a background level of 200-300 ppmV water showed a different evolution of the normalised electron mobility, threshold voltage and hysteresis (**Figure 55a**). Both an increase and subsequent decrease of the mobility could be observed, suggesting that two competing processes are taking place. The dynamics after 25-30 hours indicates that an environmental degradation of **TIPS-TAP** took place as the mobility started to decrease monotonically, while the threshold voltage and hysteresis increased. This increase might be attributed to the continuous formation and filling of new trap states that origin from an environmental degradation of **TIPS-TAP** in the transistor channel. While the degradation process is present at earlier times it is not the dominant effect, but is still superimposed on the process of filling the initial trap states that was observed and described for nitrogen. As a result the initial increase of the mobility occurred on a longer time scale than that measured in pure nitrogen. The output measurements showed that the injection into **TIPS-TAP** remains linear throughout the experiment.
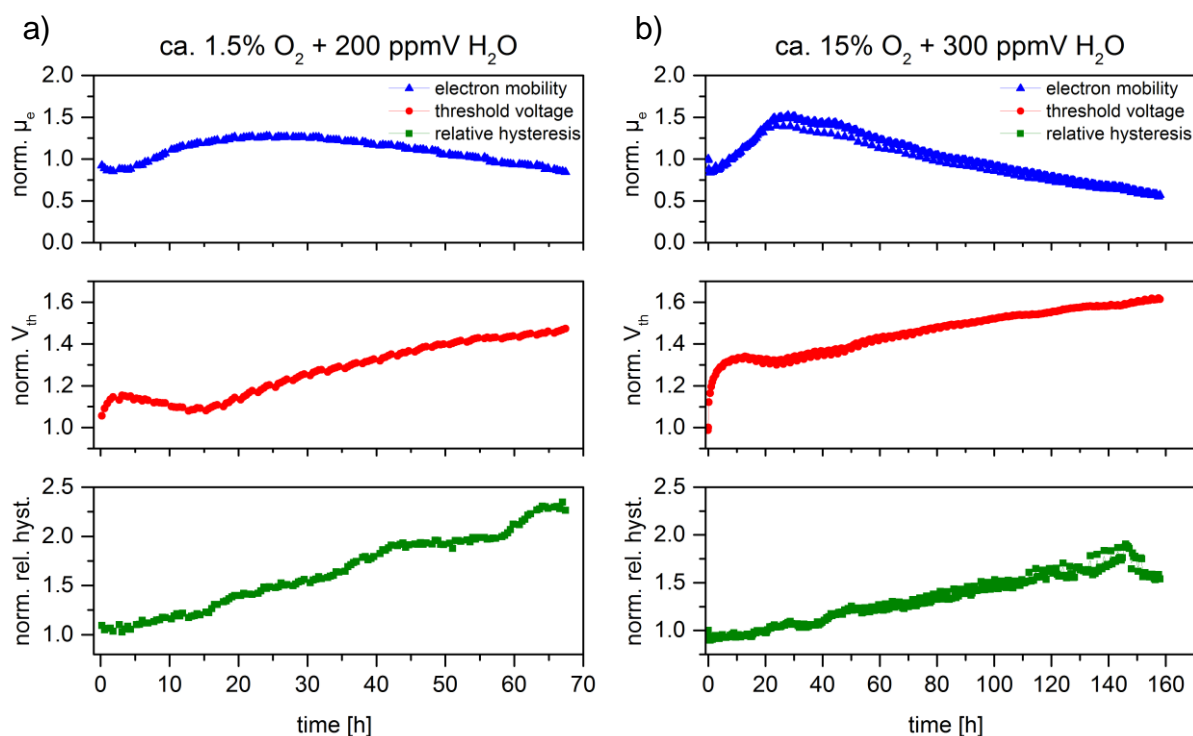
Figure 55. Time development of normalised electron mobility, threshold voltage and hysteresis of **TIPS-TAP** transistors upon bias-stressing in oxygen containing atmosphere (a) at 1.5% oxygen and (b) at 15% oxygen.

To untangle the contribution of oxygen from water on the degradation of **TIPS-TAP** transistors, an experiment at ten times higher (15%) oxygen concentration with a similar background humidity was performed. The dynamics and relative changes in electron mobility, threshold voltage and hysteresis remained almost unaltered. If oxygen was the main degradation factor an increase in its concentration would have expedited the effects of degradation (e.g. a faster decrease in mobility). Since no changes in dynamics were observed, the results suggest that it was water rather than oxygen that acted as a main cause of degradation of **TIPS-TAP** upon bias-stressing (**Figure 55b**). It should be mentioned that all **TIPS-TAP** transistors in 15 % oxygen atmosphere were till operational after more than 160 hours and over 330 stressing cycles.

To study the influence of water on the device performance and degradation, bias stressing at a higher water level of 500 ppmV water and no oxygen (background level of 5 ppm) was conducted (**Figure 56**). The dynamics of the electron mobility was similar to the one described above, however the increased concentration of water caused the degradation process to become dominant significantly earlier than before. As a result the mobility started to decrease already after 2h of the experiment.
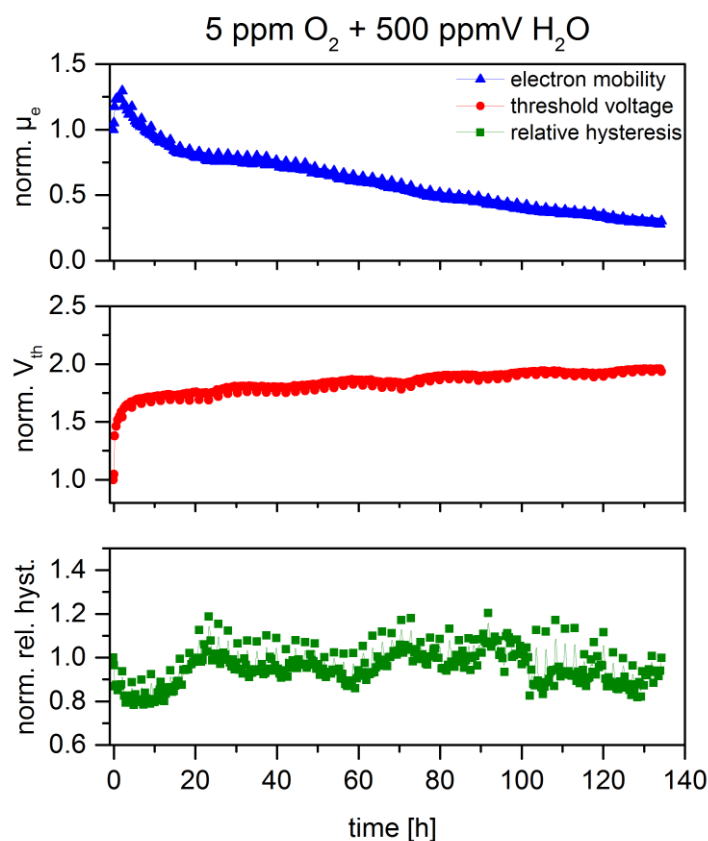
Figure 56. Decrease in electron mobility with time at quasi oxygen-free atmosphere and higher water concentration (blue curve) and correlation of normalised threshold voltage and normalised hysteresis with time.

Attempts to record the evolution of the transistor performance at higher water levels (>500 ppmV) or in ambient conditions failed, as the non-encapsulated **TIPS-TAP** devices were no longer operational after the first few hours (see Appendix). Due to the fact that the LUMO of **TIPS-TAP** is reasonably low (-4.45 eV), an oxidation by oxygen or water was not expected. However, the experimental results demonstrate only water induced degradation, suggesting that a more complex process is taking place. A possible effect of water on the N-heteroacene **TIPS-TAP** is described in **Scheme 2**. Throughout the exposure to water the azaacenes could be protonated. If this process results at the end in the formation of the reduced *N,N'*-dihydrotetraacenpentacene (**28**) cannot be elucidated, as the corresponding oxidation process remains unknown. In any case, a protonated compound has a significantly higher LUMO level than that of **TIPS-TAP**, potentially interfering with the electron transport and resulting in a decrease of the electron mobility. Further studies paired with spectroscopic investigations on degraded **TIPS-TAP** films are required to confirm this hypothesis and to reveal the true cause of the deteriorated device performance of **TIPS-TAP** in the presence of water.

$$H_2O \quad OH^-$$

$$\text{TIPS-TAP}^{\cdot-} \longrightarrow \text{TIPS-TAP}\text{-H} \xrightarrow{\;??\;} \text{TIPS-TAP}\text{-H}_2$$
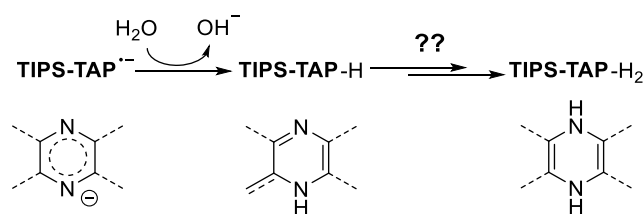
Scheme 2. Possible protonation and decomposition of **TIPS-TAP** in a field-effect transistor through ambient humidity.

5.6. Conclusion

The fabrication of thin film transistors of **TIPS-TAP** deposited by spin-coating could be successfully achieved utilizing cross-linked interlayers as **TIPS-TAP** did not form homogenous and continuous films on glass of passivated silicon dioxide surfaces. It was demonstrated that the incorporation of four nitrogen atoms in the aromatic backbone of **TIPS-PEN** lowered the LUMO level to -4.45 eV, so that an efficient electron injection from gold electrodes is possible. The polycrystalline **TIPS-TAP** films exhibited electron mobilities ranging from 10^{-3} cm^2/Vs up to 0.31 cm^2/Vs depending on the domain sizes and solvent used for deposition. However, gold bottom-contact FET architectures suffered from non-linear contact behaviour in the I-V characteristics while top-contact devices exhibited an ohmic contact with **TIPS-TAP**. XRD-measurements confirmed that the strong preferred (00*l*)-orientation of **TIPS-TAP** is also achieved in spin-coated films independent on the choice of substrate and is even present in zone-cast films of **TIPS-TAP**. The environmental and bias-stress experiments elucidated, that **TIPS-TAP** is fairly stable against oxygen, however, its stability towards humidity in organic field-effect transistors must be improved. This leaves room for a further design of stable and high-performing electron transporting N-heteroacenes.

Chapter 6

N,N'-Dihydroazaacenes as Hole Conductors in Organic Field-Effect Transistors

This chapter focuses on the application of the electron rich *N,N'*-dihydroazaacenes as hole conductors in organic field-effect transistors. The differently substituted *N,N'*-dihydrotetraazapentacene (**DHTA**) derivatives exhibited different solid state packing motifs based on their single crystal structure, suggesting large differences in their charge transport properties. The optical, electronic and morphological properties of polycrystalline **DHTA** films were investigated and the extracted hole mobilities reached up to 0.11 cm^2/Vs in the case of the chlorinated **DHTA-Cl$_2$**. X-ray diffraction on films revealed that that a new polymorph is formed for all **DHTA** compounds in thin films and in case of the unsubstituted **DHTA-H$_2$** the solid state packing of the film phase could be revealed. The concept of hole conduction in *N,N'*-dihydroazaacenes was successfully demonstrated for the corresponding hexacene and heptacene, reaching in average mobilities of 0.01 cm^2/Vs. The results of the study on DHTA derivatives has been reported in Ref. [169]: F. Paulus, B. D. Lindner, H. Reiß, F. Rominger, A. Leineweber, Y. Vaynzof, H. Sirringhaus, U. H. F. Bunz, „*N,N'*-Dihydrotetraazapentacenes (DHTA) in thin film transistors ", *J. Mater. Chem. C* **2015**, *3*, 1604–1609.

6.1.   Motivation and Synthesis *N,N'*-dihydroazaacenes

The use of palladium catalysis for the synthesis of azaacenes was first shown by Bunz and coworkers in 2011 using the Buchwald-Hartwig amination (**Scheme 3**).[139] Coupling of the diamine **34** with the chlorinated quinoxalines **35** using Bis(dibenzylideneacetone)palladium(0) (Pd(dba)$_2$), 2-Dicyclohexylphosphino-2',6'-diisopropoxybiphenyl (RuPhos) and Hünig's base resulted in the *N,N'*-dihydro compounds **DHTA,** which can be easily oxidised with manganese dioxide to the corresponding tetraazapentacenes. The synthesis for **DHTA-H$_2$** and **DHTA-Cl$_2$** was first described by Tverskoy *et al.* followed by the successful attempt of B. Lindner of synthesising the difluorinated azaacene **DHTA-F$_2$** and its corresponding oxidised azaacene.[139,146,169] The substitution with halogen atoms was chosen to lower the energy of the lowest unoccupied molecular orbital of the corresponding tetraaza derivative.
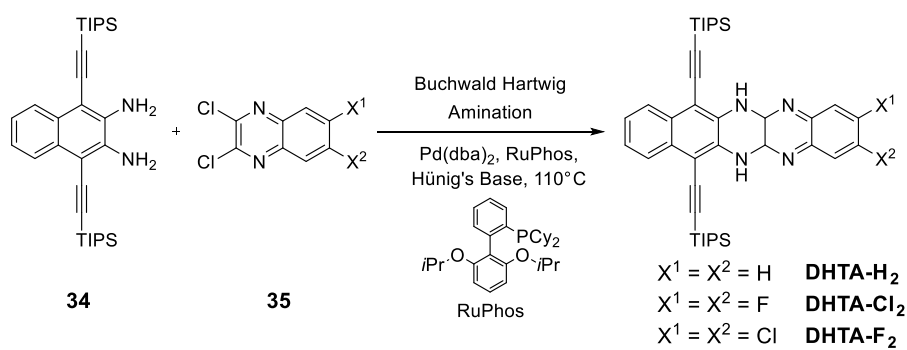
Scheme 3. Reaction scheme for the synthesis of *N,N'*-dihydrotetraazapentacenes DHTA *via* palladium catalysis.

The **DHTA** derivatives are electron rich components and their rigid molecular structure might allow for efficient hole transport. Nuckolls and coworkers demonstrated in 2003 that *N,N'*-dihydrodiazapentacenes can be used as p-channel semiconductors.[121] However, these materials were unsubstituted and did not allow for solution-based deposition techniques. The TIPS-ethynyl side chains of the presented **DHTA** compounds increase the solubility in organic solvents, making these azapentacenes interesting for an application in solution processed thin film transistors.

6.2.   Single Crystal X-Ray structures of the three DHTA derivatives

Interestingly, the three **DHTA** materials (depending on the substituent X = H; Cl or F), exhibit a different packing motif in the solid state for solution grown crystals (**Figure 57**).[139,169] Despite the similarity in the molecular structure, the packing patterns and interaction between the π-systems differ significantly. For **DHTA-H$_2$** a one dimensional pattern was observed. In the solid state the aromatic π-systems stack along isolated columns (**Figure 57a and b**) with a stacking distance of 3.44 Å. The TIPS-ethynyl side chains separate the stacked columns from each other. One would expect a rather needle like crystallite growth and a one dimensional charge transport for such a packing motif. **DHTA-Cl$_2$** forms a paired herringbone structure in the

solid state. Two chlorinated molecules are orientated head to tail to each other and form a dimer, possibly minimizing their effective dipole moment (**Figure 57c and d**). These dimers form the herringbone packing. This type of molecular packing has also been reported for the related 5,14-bis(triisopropylsilylethynyl)pentacene derivative in which the solubilising TIPS-ethynyl side groups are also attached to the second ring of the aromatic system.[77] The fluorinated **DHTA-F$_2$** exhibits a dimer brickwork pattern in its solid state (**Figure 57e and f**). Here, the dimer structure is also formed of two head to tail oriented molecules (black rectangular inset in **Figure 57e**) with a distance of 3.36 Å between the aromatic cores. Those dimers are arranged in the well-known brickwork pattern, like **TIPS-PEN** or **TIPS-TAP**. In all three **DHTA** compounds the TIPS-ethynyl side chains are bent out of the plane of the acene core, indicating an energetic strain in the crystallographic packing.
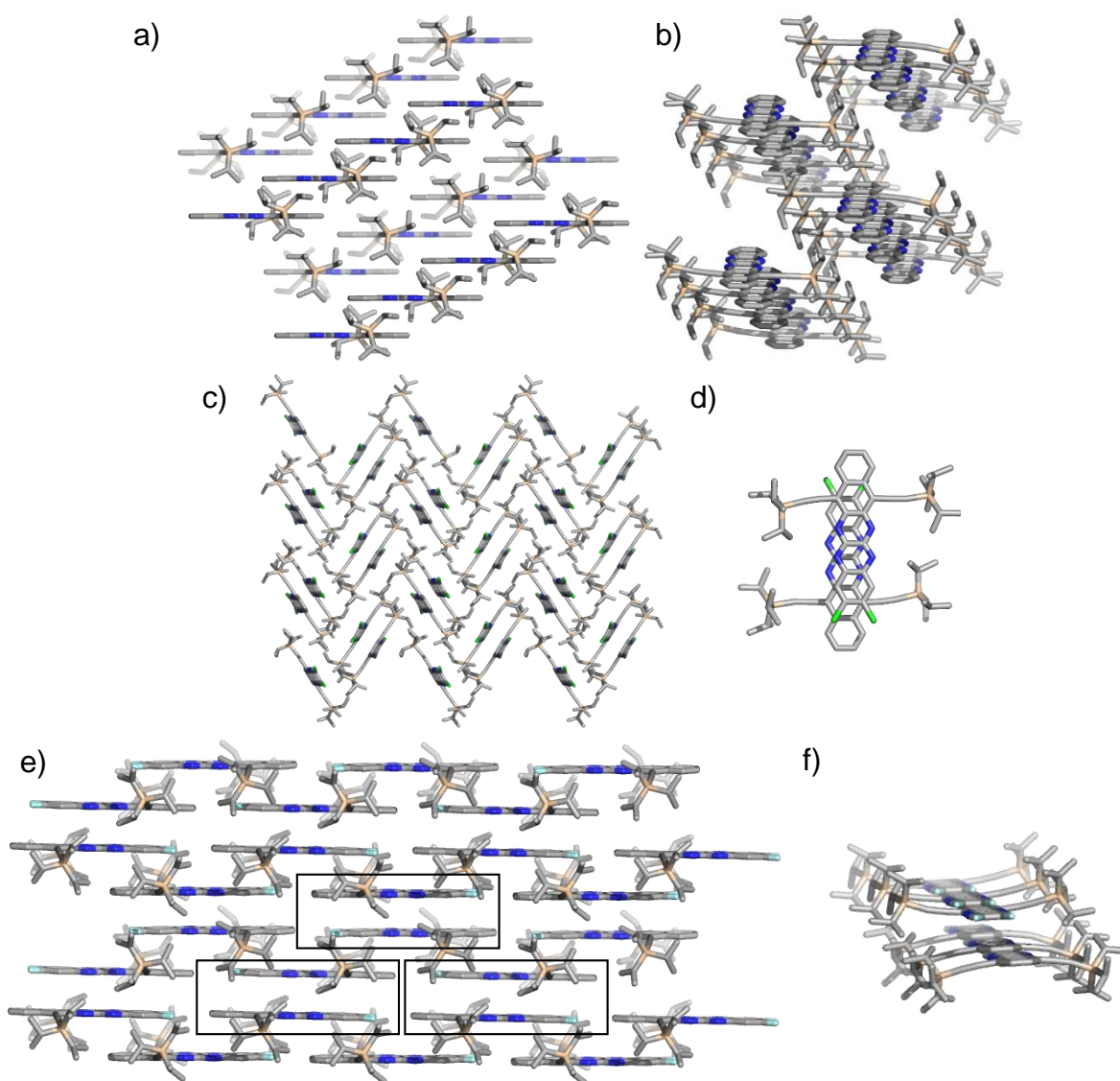
Figure 57. Solid state packing for crystals grown from hexane solution; (a)+(b) **DHTA-H$_2$**, (c)+(d) **DHTA-Cl$_2$** and (e)+(f) **DHTA-F$_2$**. The frames in (e) highlight the dimeric character of the brickwork packing. Single crystal structures for solution grown crystals obtained from Ref. [139] and Ref. [146,169]. [Adopted from Ref. [169] - Reproduced by permission of The Royal Society of Chemistry]

The charge transport properties of the **DHTA** compounds should be strongly affected by the different solid state packing motives of the substituted molecules. Also the electronic properties of the **DHTA** derivatives may have an effect on the charge transport, as they determine the charge injection barriers from the electrodes into the organic material. To investigate these and also the optical properties of the **DHTA** derivatives, ultra-violet photoemission spectroscopy and UV/vis absorption measurements were performed on thin films of each of the unsubstituted and halogenated molecules.

6.3.   Thin film properties of the DHTA compounds

The position of the long-wavelength absorption maximum of the **DHTA** molecules in solution was found to be 455 nm, 458 nm and 455 nm for **DHTA-H₂**, **DHTA-Cl₂** and **DHTA-F₂**, respectively (**Figure 58a, c and e**). This relatively large optical gap is typical for the dihydropyrazine motif.[124,170] All three **DHTA** components are fluorescent in solution with Stokes shifts of below 4 nm, representing the rigidity of the aromatic core (**Table 7**). Once applied in a thin film the fluorescence vanished due to the strong intermolecular interactions. The absorption spectra of the thin films is red shifted and broadened compared to the absorption in solution by about 10 nm for **DHTA-H₂** and 23 nm for **DHTA-Cl₂** and **DHTA-F₂** (**Table 7**).

Table 7. Summarised optical parameters for **DHTA-H₂**, **DHTA-Cl₂** and **DHTA-F₂** for solution and film. [based on Ref. [169] - Reproduced by Permission of The Royal Society of Chemistry]

compound	absorption sol. λ_{max} [nm]	emission sol. λ_{max} [nm]	Stokes-Shift [nm] ([cm^{-1}])	absorption film λ_{max} [nm]	red shift λ_{max} film [nm] ([cm^{-1}])
DHTA-H₂	455	459	4 (192)	465	10 (431)
DHTA-Cl₂	458	461	3 (142)	481	23 (1044)
DHTA-F₂	455	458	3 (144)	478	23 (1058)

The position of the highest occupied molecular orbital (HOMO) was determined utilizing ultraviolet photoemission spectroscopy on thin films of each material on gold. The onset of the valence band feature at the low binding energy edge was interpreted as the energetic position of the HOMO for each material (**Figure 58b, d and f**). The halogenation of the aromatic backbone leads to a significant stabilisation of the HOMO. The ionisation potentials of the halogenated derivatives are higher (5.5 eV and 5.8 eV for **DHTA-Cl₂** and **DHTA-F₂**, respectively) than that of the unsubstituted **DHTA-H₂** (5.1 eV). Despite the position of these HOMOs being rather low for classical p-type semiconductors in organic electronic applications, efficient injection of holes in those *N,N'*-dihydrotetraazapentacenes should still be possible from gold electrodes modified with PFBT (work function 5.4 eV).[152]

Prior to application of the DHTA components in thin film transistors, the microstructure and morphology of thin films prepared by spin-coating from solvents with different boiling points were examined. To obtain

homogenous and well-crystallised films of the *N,N'*-dihydrotetraazapentacenes, glass substrates coated with a thin cross-linked polyimide layer were used.
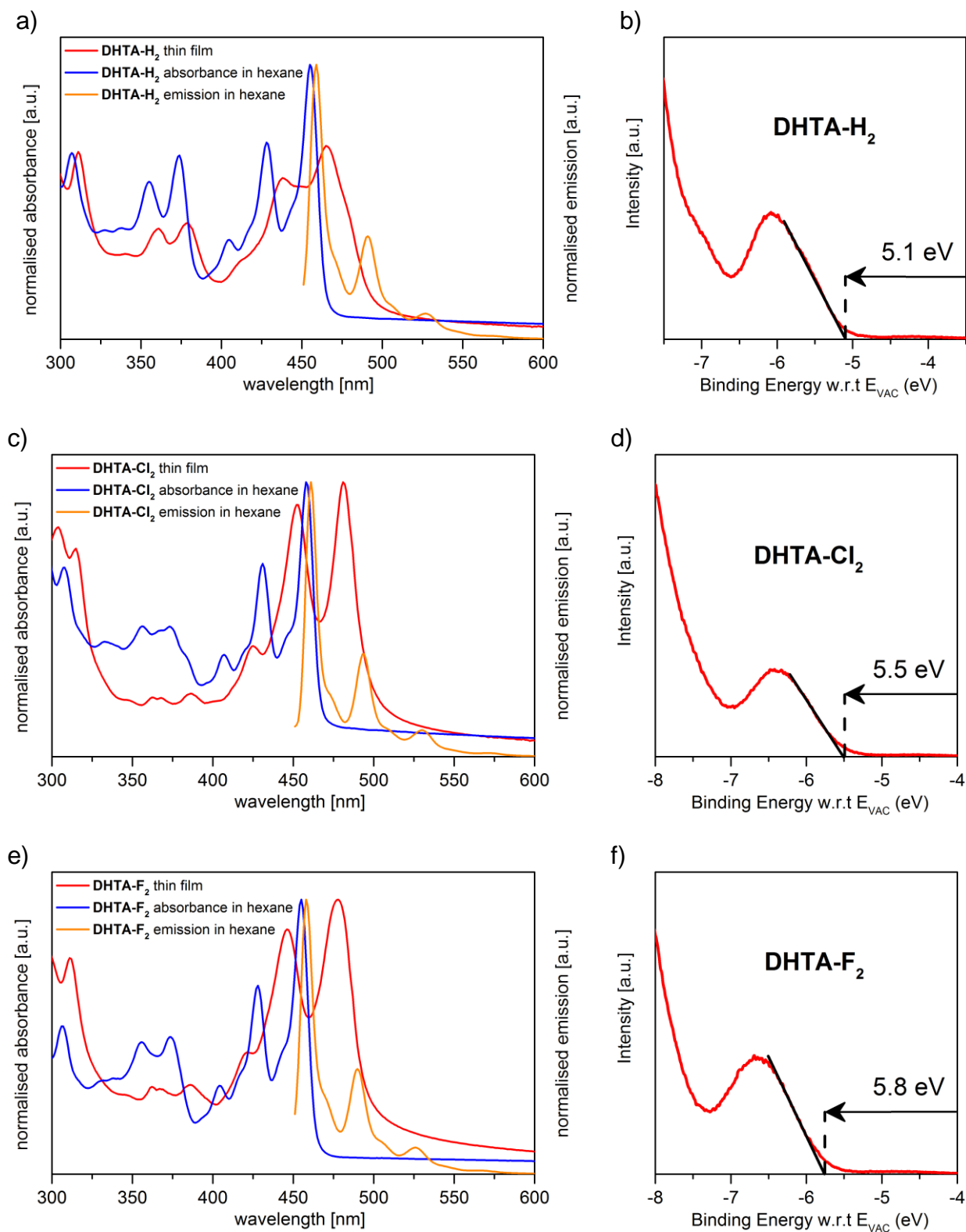

Figure 58. Absorption and emission spectra of **DHTA** compounds in hexane and absorption in thin film (left) and valence band feature of (a) +(b) **DHTA-H₂**, (c)+(d) **DHTA-CL₂** and (e)+(f) **DHTA-F₂**.

Films were prepared by spin-coating a 20 mg/mL solution from xylene (bp = 137-140°C), mesitylene (bp = 163-166°C) or tetralin (bp = 207°C). The microstructure of the films was characterised by optical microscopy under crossed-polarisers and by atomic force microscopy. All films deposited by spin-coating were polycrystalline and the domain sizes varied strongly based on the material/solvent combination (**Figure 59**). Films of **DHTA-H$_2$** showed an increase in domain size for an increasing boiling point of the solvent used for deposition. Films spun from tetralin solution exhibited a spherulitic growth with diameters of 35-200 µm of the spherulites. Films of **DHTA-Cl$_2$** showed very small grains and no spherulitic structure was observed. The boiling point of the solvent did not influence the grain or domain size. The morphology in thin films of **DHTA-Cl$_2$** seemed to be independent of the boiling point used for deposition. Films of **DHTA-F$_2$** showed a similar structure compared to films of the unsubstituted **DHTA** derivative. The use of tetralin also resulted in a spherultic growth, with diameters between 10-60 nm. These findings were supported by atomic force microscopy (**Figure 60**). Films of **DHTA-Cl$_2$** exhibited a flake like structure with flake sizes of 2-8 nm independent of the choice of solvent. Films deposited from a xylene solution exhibited slightly smaller grains and appeared denser. Interestingly, the crystallisation of **DHTA-H$_2$** does not appear to be needle-like as one would expect for the one-dimensional packing motif of the unsubstituted dihydroazaacene.
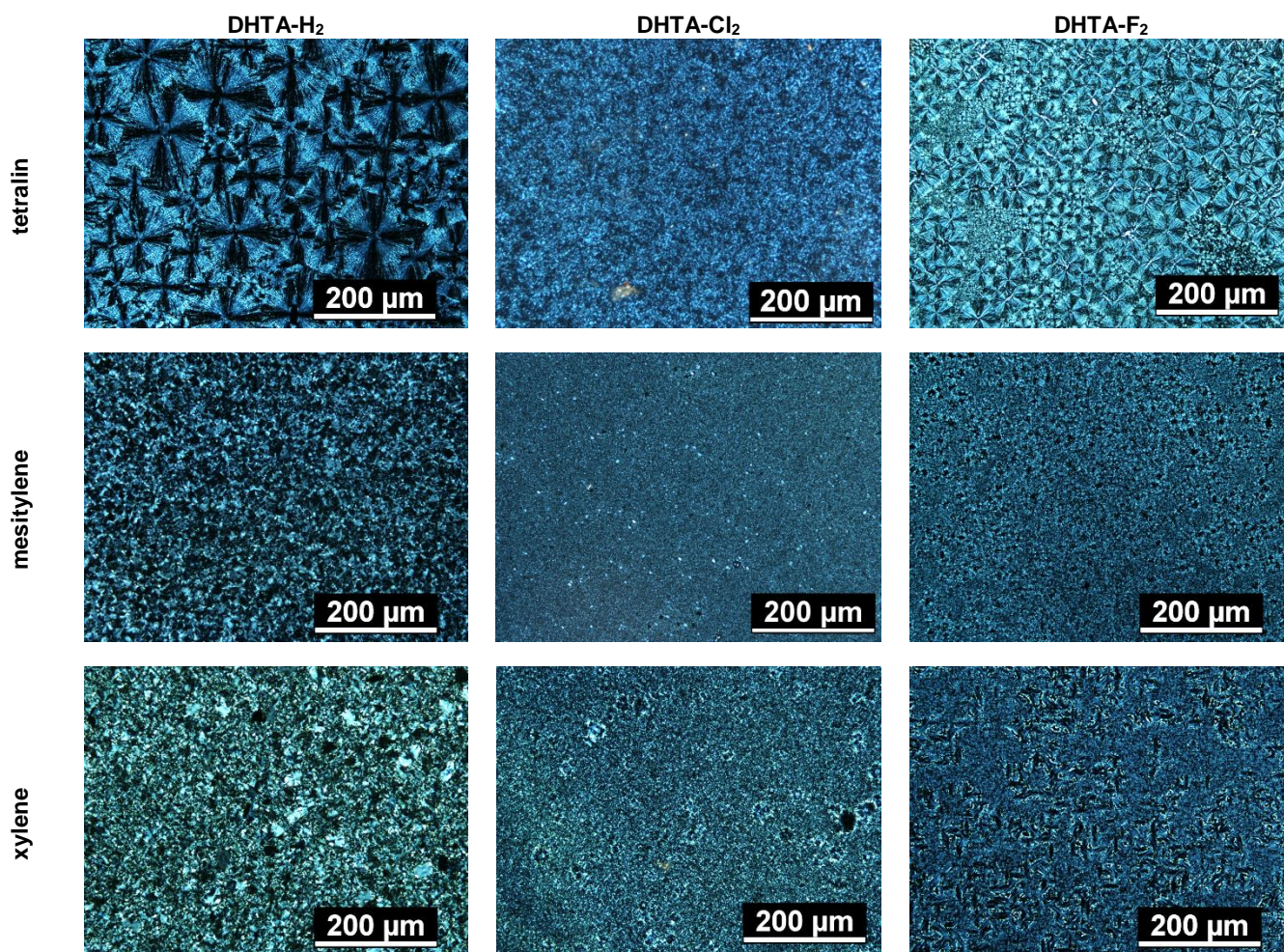
Figure 59. Micrographs of the polycrystalline films of **DHTA-X₂** spin-coated on polyimide under crossed polarisers. [Adopted from Ref. [169] - Reproduced by permission of The Royal Society of Chemistry]
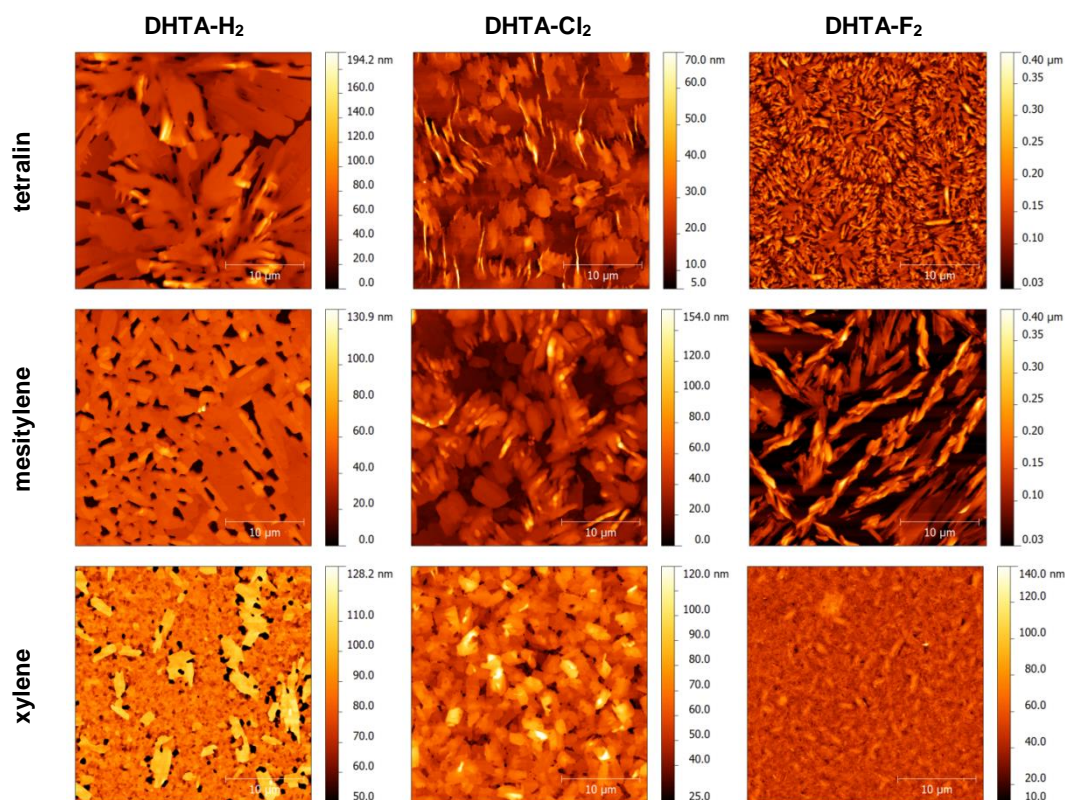
Figure 60. AFM height images of the polycrystalline **DHTA** films on polyimide. The films were deposited from different solvents with increasing boiling point. [Adopted from Ref. [169] - Reproduced by permission of The Royal Society of Chemistry]

6.4. Thin film transistor performance of DHTA compounds

The polycrystalline films of **DHTA-H$_2$**, **DHTA-Cl$_2$** and **DHTA-F$_2$** were used in bottom-contact/ top-gate field-effect transistors to evaluate the charge transport properties of these materials. All devices were prepared identically to compare the device performance. Perfluorinated Cytop^{TM} polymer was used as the gate dielectric and was spun on the organic films from an orthogonal solvent (CT-180). The gold bottom-contacts were modified with PFBT for better hole injection into the low lying HOMO of the materials. All fabricated devices showed a clear hole transport with good on/off ratios for which the off-currents were not dominated by the gate leakage except for devices with **DHTA-F$_2$** (**Figure 61**). In all devices the hysteresis between forward and backward sweep was very low, indicating a low concentration of trap states and a well-defined interface with the dielectric layer. All output characteristics showed a linear injection behaviour representing ohmic contact of the chosen electrode material and the organic layer. The threshold voltages of each material were in the range of 10-20 V and did not vary strongly upon the use of higher boiling point solvents. Only devices of **DHTA-H$_2$** deposited by xylene suffer from a lower threshold voltage that might be attributed to the relatively high off-currents in these devices (see Appendix). The hole mobility of **DHTA-H$_2$** transistors increased with the boiling point of the solvent used for deposition up to a maximum of 0.03 cm^2/Vs for active layers spun from tetralin (**Table 8**). This is in excellent agreement with the observed increased crystallite and domain size of the polycrystalline films (see **Figure 59** and **Figure 60**). **DHTA-Cl$_2$** showed among all **DHTA** compounds for all three

solvents the highest average mobilites of up to 0.11 cm^2/Vs (**Figure 61**). The average hole mobility was always higher compared to **DHTA-H$_2$** and was not affected by the choice of solvent. This can be attributed to the flake-like microstructure and almost processing independent size distribution of the crystallites in the **DHTA-Cl$_2$** films.

Table 8. Parameters of the thin film transistors with **DHTA** fabricated using different solvents. The average values and standard deviation were obtained from a set of identically prepared devices. [Adopted from Ref. [169] - Reproduced by permission of The Royal Society of Chemistry]

compound	solvent	μ_{hole} best [cm^2/Vs]	μ_{hole} average [cm^2/Vs]	threshold voltage average V_{th} [V]	on/off ratios range
DHTA-H$_2$	tetralin	0.03	$(1.8\pm0.9)\cdot10^{-2}$	-(13 ±6)	10^4-10^5
	mesitylene	0.01	$(5.9\pm2.4)\cdot10^{-3}$	-(20.5±5)	10^4-10^5
	xylenes	0.005	$(1.4\pm1.6)\cdot10^{-3}$	(8±6)	10^2-10^3
DHTA-Cl$_2$	tetralin	0.09	$(4.3\pm2.7)\cdot10^{-2}$	-(23±6)	10^3-10^4
	mesitylene	0.07	$(3.0\pm1.9)\cdot10^{-2}$	-(20.5±4)	10^4
	xylenes	0.11	$(3.7\pm2.9)\cdot10^{-2}$	-(18±4)	10^3-10^4
DHTA-F$_2$	tetralin	$2.2\cdot10^{-4}$	$(7.3\pm5.9)\cdot10^{-5}$	-(11±7)	10^2-10^3
	mesitylene	$9.3\cdot10^{-3}$	$(1.5\pm3.5)\cdot10^{-3}$	-(29±7)	10^3-10^4
	xylenes	$8.5\cdot10^{-4}$	$(3.6\pm3.3)\cdot10^{-4}$	-(22±13)	10^3-10^4

Transistors with **DHTA-F$_2$** showed significantly lower hole mobilities (in the range of 10^{-4} cm^2/Vs) as compared to **DHTA-H$_2$** and **DHTA-Cl$_2$** regardless of the choice of solvents. Even though this material exhibits a brickwork type packing, its transistor performance was inferior to the other two derivatives. Despite the fact that the three *N,N'*-dihydrotetraazapentacenes exhibit three different packing motives in the solid state, these differences seem to not be represented in the transistor data. One would expect the fluorinated derivate which exhibits a brickwork type packing to perform better than the other two derivatives, however, its performance is unexpectedly poor. The good performance of **DHTA-H$_2$** transistors cast from tetralin and the processing independent performance of **DHTA-Cl$_2$** required are more detailed investigation of the origin for this behaviour.
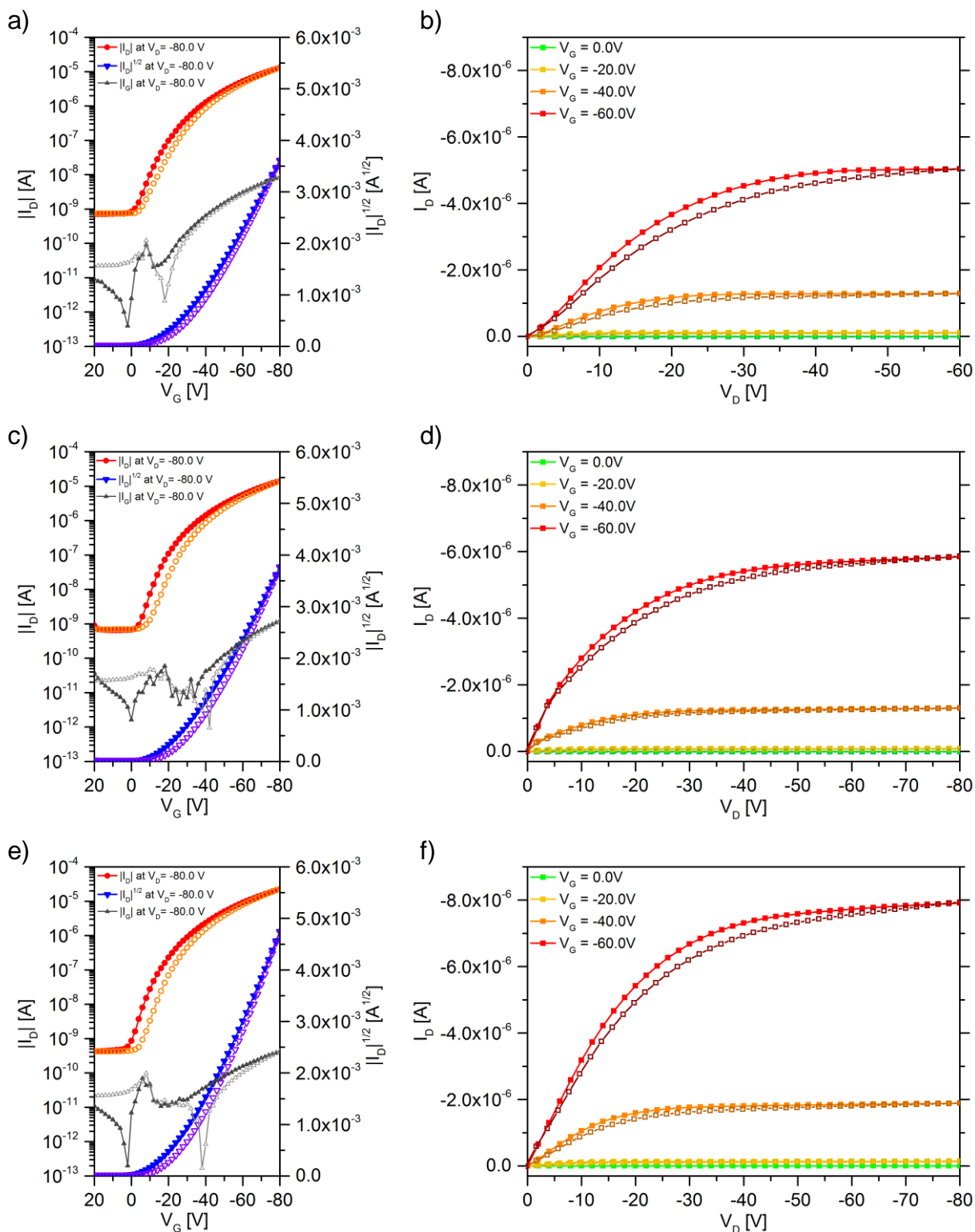
Figure 61. I-V-characteristics of the best performing transistors (W = 1,000 µm; L = 20 µm) with **DHTA-Cl₂** for different solvents (identically scales, transfer characteristics left, output right); (a)+(b) tetralin, (c)+(d) mesitylene and (e)+(f) xylenes (forward – filled symbols; backward sweep – open symbols).

6.5.   XRD measurements on DHTA films

The unexpected transistor performance of the three differently substituted **DHTA** derivatives could originate from different orientations of their aromatic systems towards the charge transport direction or even the formation of a new polymorphous phase in thin films. To investigate this further, X-ray diffraction measurements on the polycrystalline films were performed. The samples were identically prepared to those used for field-effect transistors. The X-ray diffraction of all material/solvent combination revealed a series of sharp Bragg reflexes, indicating a highly crystalline nature of all samples. In case of **DHTA-H$_2$** and **DHTA-Cl$_2$** Laue oscillation was observed, indicating a homogenous films thickness. However, the diffraction patterns of all three materials could not be described by the solid state structure obtained from single crystal analysis (**Figure 57**). The observed relative intensities and positions of the reflexes do not correlate with any Miller planes of the single crystal structure, showing that a different polymorph was present in these films for all three materials. Films of **DHTA-F$_2$** exhibited for each solvent two series of Bragg reflexes with two different d-spacing values (**Table 9**), possibly originating from two different polymorphs in the film. Furthermore, the relative contribution to the XRD-pattern varied based on the choice of solvent (**Figure 62c**). This observation might explain the poor performance of **DHTA-F$_2$** in thin film transistors as a mixture of two polymorphs might heavily affect the charge transport. The films of **DHTA-H$_2$** and **DHTA-Cl$_2$** exhibited only one series of Bragg-reflexes with a constant d-spacing value. The Bragg-Brentano geometry of the measurement implies that the observed diffraction peaks originated from lattice planes parallel to the substrate surface. The extracted d-spacing between these lattice planes, utilising the Bragg equation $n\lambda = 2d \cdot \sin d(\theta)$, was found to be 17.5-18.0 Å for all materials. Such a large d-spacing value can only be achieved when the molecules are orientated 'edge-on' to the substrate' surface, as the distance from TIPS to TIPS group is of similar length. However, apart from the molecular orientation the solid state packing in these films for all **DHTA** compounds remains unclear and cannot be identified by X-ray diffraction.
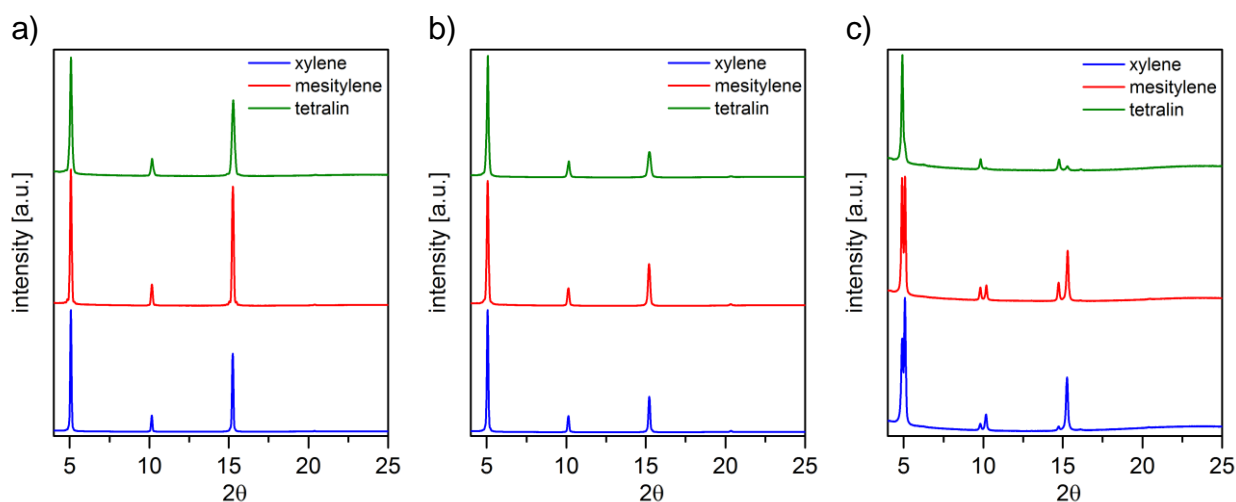

Figure 62. X-Ray diffraction patterns for (a) **DHTA-H$_2$**, (b) **DHTA-Cl$_2$** and (c) **DHTA-F$_2$** for films deposited from three different solvents.

Table 9. Summarised parameters for the higher order reflexion series of **DHTA** films observed in XRD measurements.

compound	d_0 [Å]; solvent: xylene	d_0 [Å]; solvent: mesitylene	d_0 [Å]; solvent: tetralin
DHTA-H₂	17.42	17.41	17.38
DHTA-Cl₂	17.45	17.46	17.44
DHTA-F₂	18.02 and 17.39	18.02 and 17.36	17.99 and 17.38

To reveal the true molecular packing of the **DHTA** compounds in thin films, crystallisation experiments on polyimide coated substrates under slow drying conditions were conducted to produce larger crystallites on the polyimide interlayer. In case of **DHTA-H₂** drop-casting of a xylene solution and drying in an enclosed atmosphere over 48 h resulted in crystallites large enough for single crystal X-ray analysis. After careful dissection from the surface the single crystal diffraction measurement revealed a new unit cell and a different molecular packing of **DHTA-H₂** (see Appendix). The cell parameters of the **DHTA-H₂** yield upon calculation of a (001)-orientation a d-spacing of 17.38 Å, which is in perfect agreement with the observed reflexes of the XRD measurement (d = 17.42 Å; only *l* = 2n, with n = 1, 2, 3… are visible due to the glide symmetry of the unit cell). In this polymorph **DHTA-H₂** adopts a distinct layered structure (**Figure 63a**) in which the layers are, based on the XRD results, parallel to the substrate's surface, ideal for lateral charge transport. Within each layer the molecules are zig-zag orientated and do not form a brickwork pattern, but exhibit a small π-π-distance of 3.34 Å (**Figure 63b**). Unfortunately, several attempts to similarly realise crystallites for **DHTA-Cl₂** and **DHTA-F₂** were not successful and the exact molecular packing and orientation of these compounds in thin films remain unknown. The single crystal analysis of **DHTA-F₂** showed a reversibly formed polymorph at a temperature of -73°C (see Appendix). From the crystallisation experiments of **DHTA-Cl₂**, a third polymorph was observed that exhibited 1-D stacked molecules (see Appendix), but the cell parameters of this polymorph do not coincide with the reflections of the XRD measurements. Due to the large similarity in d-spacing and charge carrier mobility of the chlorinated component one could assume that the molecular packing might be similar to **DHTA-H₂**.
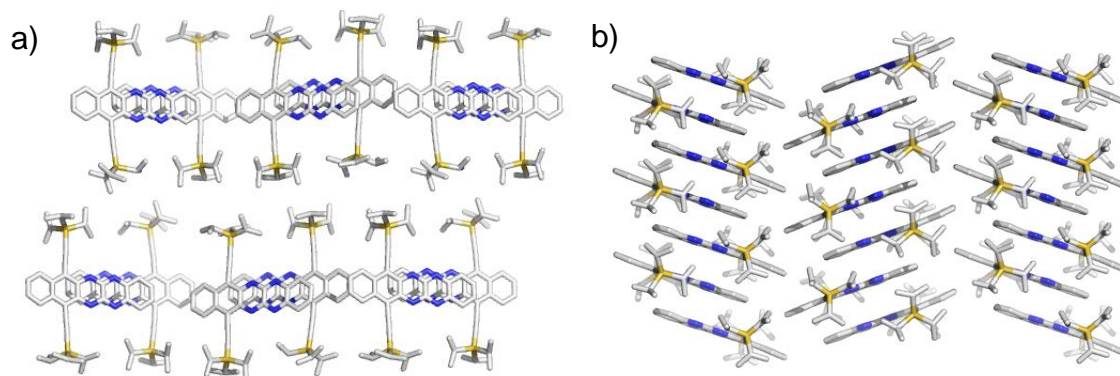
Figure 63. Solid state packing of **DHTA-H₂** in thin film (a) view along the substrate's surface (a,b-axes horizontal) and (b) top view on a **DHTA-H₂** layer (along c* axis).

6.6.   Hole transport in larger *N,N'*-dihydroazaacenes

To investigate whether the concept of using *N,N'*-dihydroazaacenes as hole transporting semiconductors is not limited to the pentacenene structure, the azahexacene and azaheptacene systems were studied next. The two dihydro compounds **NH-Hex** and **NH-Hep** were also synthesised by palladium coupling using dibromonaphthaline or dibromoanthracene, respectively (**Figure 64**).[131,140,171] The **NH-Hep** molecule carries bulkier side chains (*s*Bu) than the smaller **NH-Hex** molecule (*i*Pr), in an attempt to stabilise the corresponding azaacene, if oxidised. Despite these efforts, both molecules showed in their oxidised form a poor stability and dimerised in the solid state in a Diels-Alder reaction, making them unattractive for any electronic application.[171] The dihydropyrazine species, however, could be used as hole transporting materials in thin film transistors. Since both **NH-Hex** and **NH-Hep** exhibited a lower solubility in organic solvents and did not crystallise from solution, no single-crystal x-ray structures were obtained.[131]
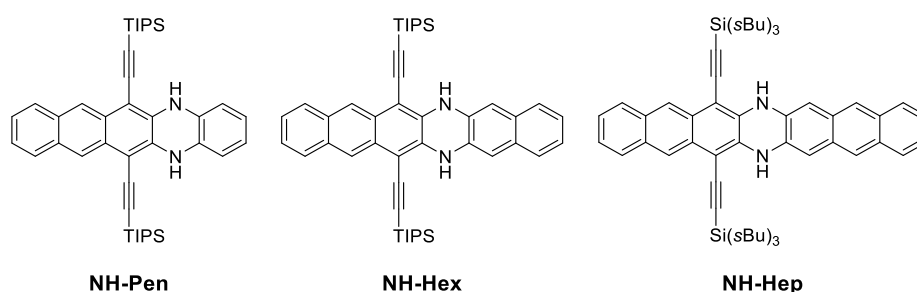
Figure 64. Molecular structures of the larger *N,N'*-dihydrodiazahexacene **NH-Hex** and -heptacene **NH-Hep** and **NH-Pen** for comparison.

The absorption and emission in solution were very similar for both materials and were comparable to the **DHTA** derivatives or other materials with the dihydropyrazine moiety (**Figure 65a and b**).[124,170] The small Stokes shift indicate very rigid aromatic systems. The film absorption spectra were broadened and red shifted as compared to those in solution, indicating a strong interaction of the aromatic systems of neighbouring molecules. The red shift was slightly stronger for the **NH-Hex** derivative, which could hint to a better molecular packing or better crystallisation. The energy levels of the larger *N,N'*-dihydroazaacenes were not determined previously as **NH-Hex** showed an irreversible oxidation during cyclic voltammetry measurements.[131] To investigate the position of the highest occupied molecular orbital ultraviolet photoemission spectroscopy on thin films of **NH-Hex** and **NH-Hep** was performed (**Figure 65c and d**).
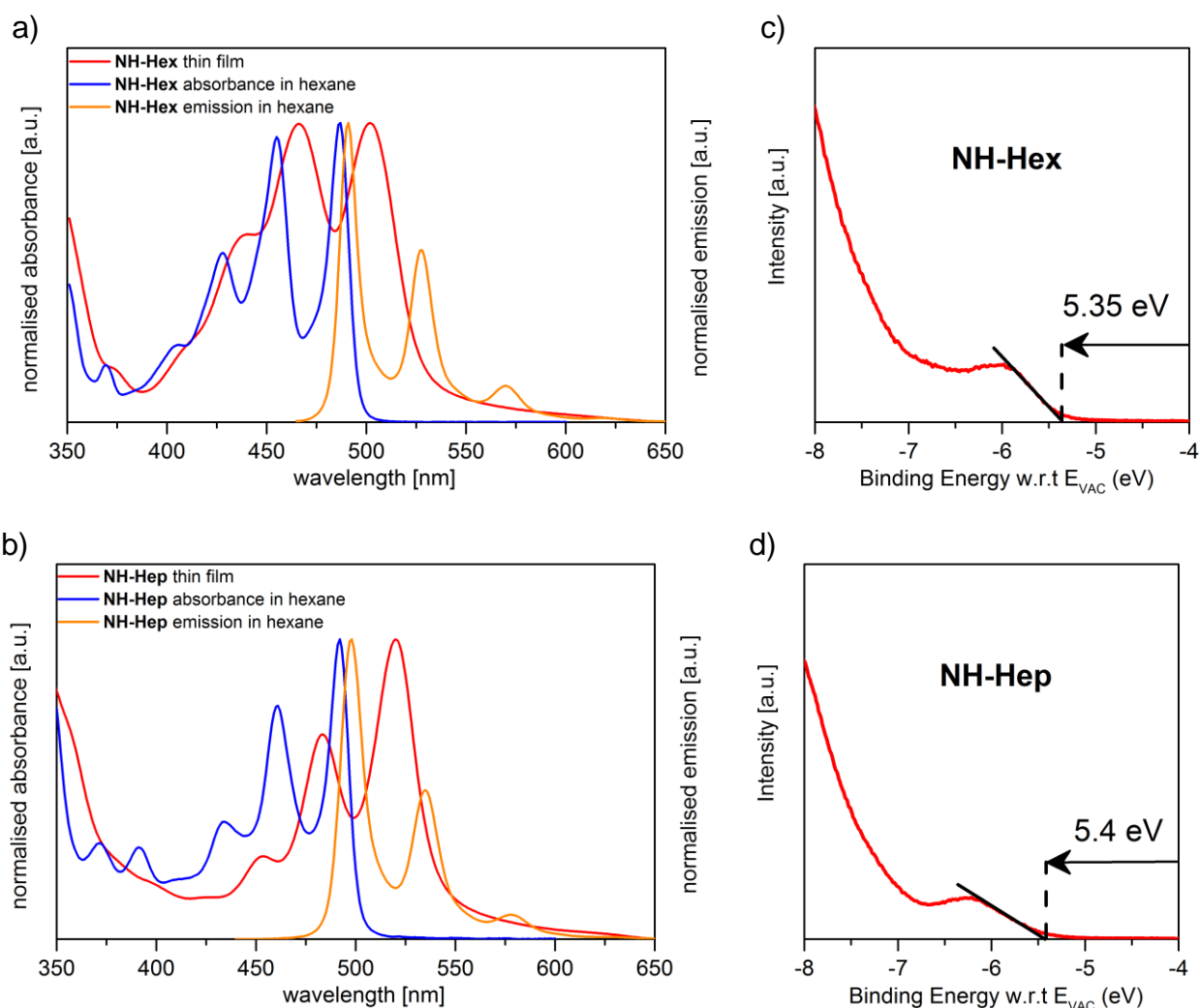
Figure 65. Absorption, emission in solution and film absorption spectra of (a) **NH-Hex** and (b) **NH-Hep**. Low binding energy edge of the ultraviolet photoemission spectra of (c) **NH-Hex** and (d) **NH-Hep**. [Absorption and emission in solution modified from Ref. [131]]

NH-Hex exhibited in thin film an ionisation potential of 5.35 eV and **NH-Hep** one of 5.4 eV. The frontier molecular orbitals of the dihydroazahexacene and dihydroazaheptacene are stabilised compared to the dihydrodiazapentacene **NH-Pen** (5.06 eV) or the tetraaza derivative **DHTA-H₂** (5.1 eV, see **Figure 58b**) due to the larger aromatic system.[21,169] PFBT modified gold electrodes should also allow in this case an efficient injection of holes into the material. Spin-coating of **NH-Hex** and **NH-Hep** on polyimide from toluene resulted in polycrystalline films with very small domain sizes of only a few micrometers, significantly smaller than the typical channel length of the fabricated transistors or the grain size observed for the **DHTA** compounds (**Figure 66a and c**).[169]
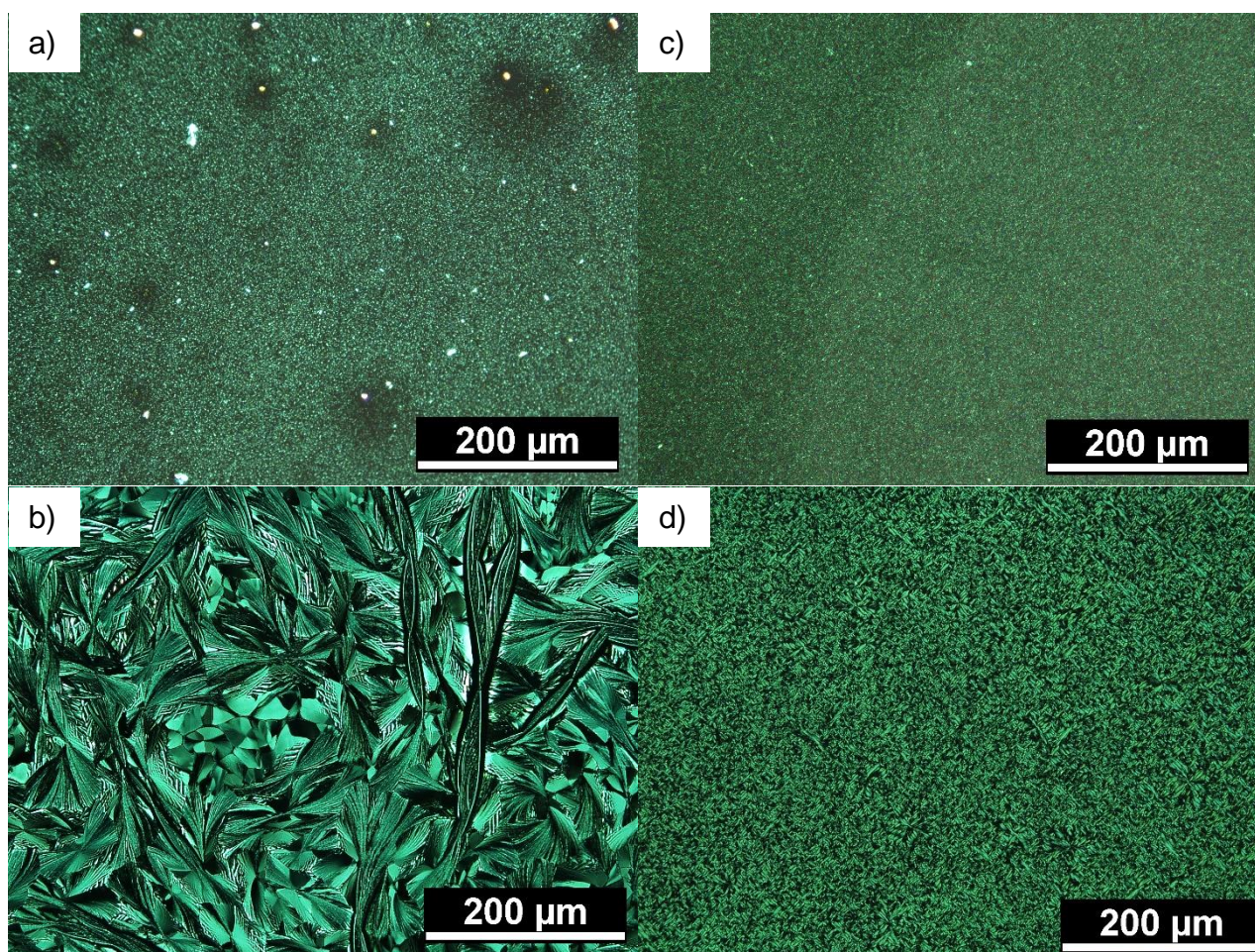
Figure 66. Spin-coated polycrystalline films of (a) **NH-Hex** from *m*-xylene, (b) **NH-Hex** from tetralin, (c) **NH-Hep** from *m*-xylene and (d) **NH-Hep** from tetralin. All under crossed polarisers on polyimide coated substrates.

To boost the size of the crystallites deposition from tetralin was chosen, resulting in case of **NH-Hex** in polycrystalline films with larger domains of several tens to hundred micrometres. The enhancement in domain size for **NH-Hep** is visible, but not as pronounced compared to the hexacene compound. Thin film transistors with **NH-Hex** and **NH-Hep** were fabricated in the bottom-contact/ top-gate architecture with a polyimide interlayer and CYTOP™ as dielectric material. All fabricated devices resulted in working p-type transistors. A contribution of electrons to the charge transport was not observed in any case.
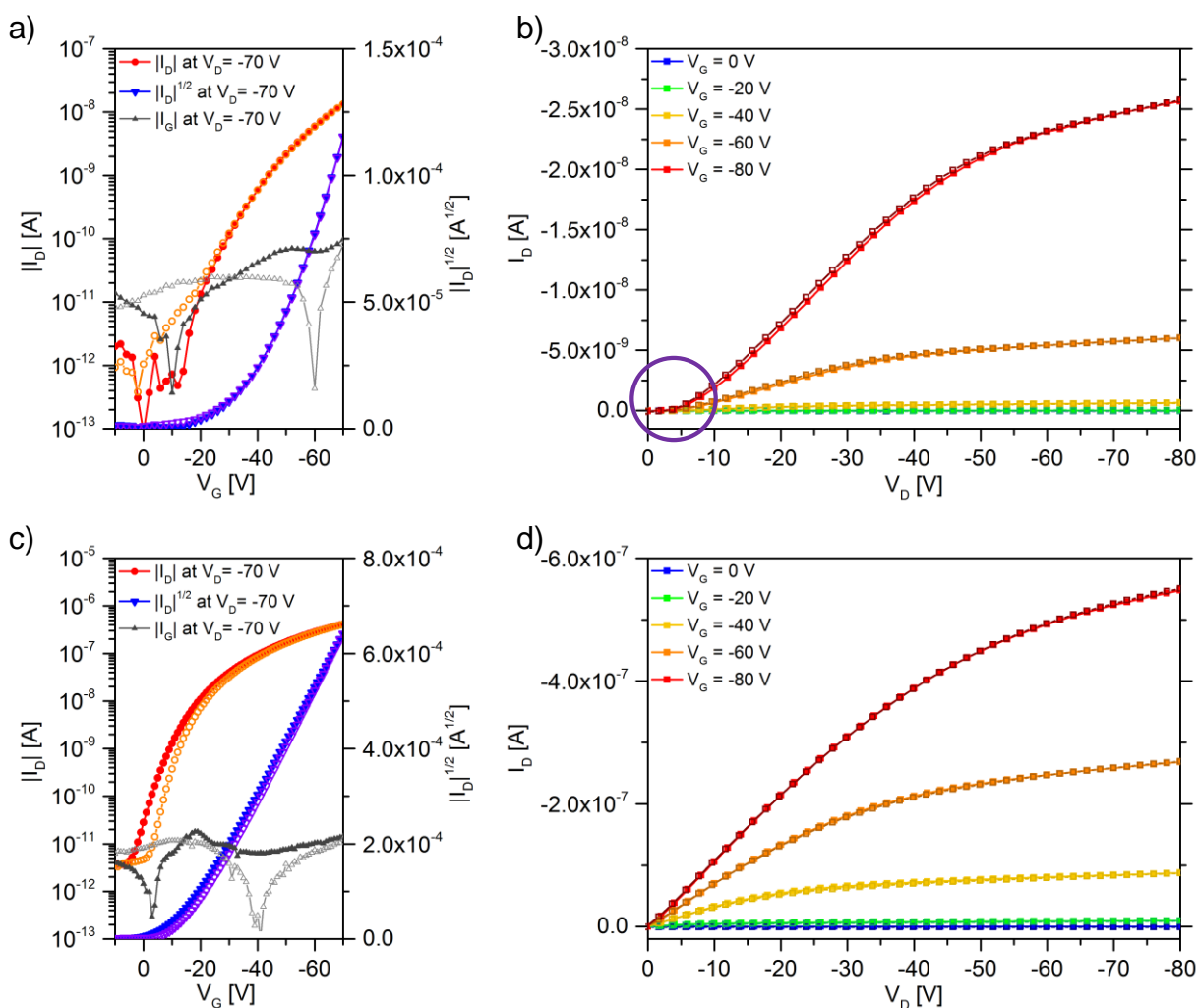
Figure 67. Field-effect transistor characteristics for devices with **NH-Hex**; (a) and (b) for bare gold-contacts cast from *m*-xylene and (c) and (d) for contacts treated with PFBT for a better hole injection and improved performance spun from tetralin (all W = 1,000 µm; L = 20 µm). The purple circle highlights the non-linear contact effects for untreated gold electrodes.

Table 10. Summarised electrical parameters for the bottom-contact/ top-contact field-effect transistors for the larger *N,N'*-dihydrodiazaacenes. The mean values and standard deviations were averaged from a set of similarly performing transistors. Transistors deposited by tetralin used PFBT treated gold electrodes.

Compound	Solvent	μ_{hole} best [cm²/Vs]	μ_{hole} average [cm²/Vs]	average threshold voltage V_{th} [V]	on/off ratios range	working FETs
NH-Hex	*m*-xylene	$7.7 \cdot 10^{-4}$	$(4.5 \pm 1.9) \cdot 10^{-4}$	$-(48 \pm 3)$	10^3-10^4	16
	tetralin	$2.7 \cdot 10^{-3}$	$(1.6 \pm 0.5) \cdot 10^{-3}$	$-(19 \pm 7)$	10^4	15
NH-Hep	*m*-xylene	$6.4 \cdot 10^{-3}$	$(2.3 \pm 1.5) \cdot 10^{-3}$	$-(34 \pm 6)$	10^3-10^4	21
	tetralin	0.024	$(1.1 \pm 0.7) \cdot 10^{-2}$	$-(22 \pm 4)$	10^3-10^4	18

The first fabricated transistors utilised an active layer deposited from xylene on top of untreated source-drain electrodes. Unfortunately, the devices with untreated gold-electrodes exhibited a non-linear contact behaviour (**Figure 67b**) and a rather poor performance. Not only the output-characteristics suffered from the poor injection of holes into **NH-Hex** and **NH-Hep**, but also the transfer characteristic were affected as the square root plot of the channel current showed a strong bending in the square root plot of the channel current

(**Figure 67a**). The extracted threshold voltages were therefore very high and the transistors showed a poor subthreshold behaviour. The extracted hole mobilities for untreated contacts are low and do not exceed the range of 10^{-4} cm^2/Vs for **NH-Hex** and 10^{-3} cm^2/Vs for **NH-Hep**. Consequently, the fabrication procedure was modified to include deposition from tetralin and PFBT treated gold contacts. Once the contacts were treated with PFBT, the injection became ohmic and the subthreshold behaviour was clearly improved (**Figure 67**). The average hole mobility for **NH-Hex** reached a maximum of $2.7 \cdot 10^{-3}$ cm^2/Vs with mediocre on-off-ratios (**Table 10**). Its transistor performance was comparable to the corresponding **NH-Pen** in solution processed transistors ($3 \cdot 10^{-4}$ cm^2/Vs).[21]
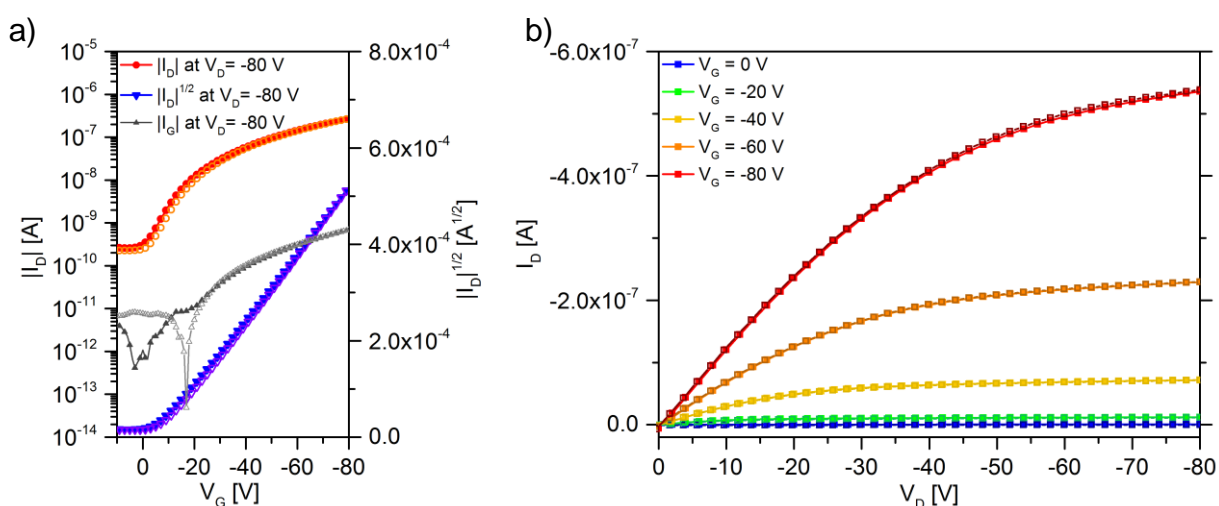
Figure 68. I-V characteristics for a bottom-contact/ top-gate field effect transistor with **NH-Hep** and PFBT modified gold contacts, spin-coated from tetralin. (a) Transfer and (b) output characteristic (both W = 1,000 μm; L = 50 μm).

The *N,N'*-dihydrodiazaheptacene **NH-Hep** showed a better transistor performance and reached hole mobilities of up to 0.024 cm^2/Vs even though its grain size was significantly smaller in spin-coated films (**Figure 68**). These results indicate that even the larger azaacenes in the *N,N'*dihydro form can act as useful hole transporting semiconductors. The extracted hole mobilities of the two derivative **NH-Hex** and **NH-Hep** were lower compared to the **DHTA** derivatives studied above, however, compared to the *N,N'*-dihydrodiazapentacene **NH-Pen** the transistor performance of **NH-Hep** and **NH-Hex** is comparable.[21]

6.7.   Conclusion

The soluble trialkylsilyl-ethynyl substituted *N,N'*-dihydroazaacenes based on a pentacene, hexacene and heptacene core were successfully implemented as hole transporting semiconductors in field-effect transistors. The three **DHTA** compounds exhibited among the studied *N,N'*-dihydroazaacenes the highest hole mobilites of up to 0.11 cm^2/Vs in case of the chlorinated **DHTA-Cl$_2$**. X-ray diffraction measurement on thin films revealed that these materials exhibit a different solid state packing in thin films deposited by spin-coating as compared to solution grown crystals. The polycrystalline films of **NH-Hex** and **NH-Hep** exhibited average hole mobilities

of 10^{-3} cm^2/Vs and 10^{-2} cm^2/Vs, respectively. This study shows that even the *N,N'*-dihydro precursors of the azaacene class can act as valuable semiconductors in solution-processed organic electronic applications.

Chapter 7

Halogenated Phenazinothiadiazoles as Electron Transporting Semiconductors

The focus of this chapter is the investigation of the charge transport properties of the halogenated phenazinothiadiazoles **Cl$_4$-Phen** and **F$_4$-Phen**. The supramolecular interaction of the thiadiazole moiety and formation of an almost planar dimer allows strong π-π-interactions between neighbouring molecules, necessary for an efficient charge transport. The substitution with halogen atoms at the outer periphery of the four-membered ring system resulted in very deep LUMO levels, suitable for electron transport. The polycrystalline films deposited through spin-coating were investigated an employed in thin film transistor reaching electron mobilities of up to 0.36 cm^2/Vs for **Cl$_4$-Phen**. Attempts to improve the morphology of **Cl$_4$-Phen** *via* zone-casting did not result in an improved transistor performance due to structural damage that occurred to the material in those films. The first results of this chapter have been reported in Ref. [172]: B. D. Lindner[#], F. Paulus[#], A. L. Appleton, M. Schaffroth, J. U. Engelhart, K. M. Schelkle, O. Tverskoy, F. Rominger, M. Hamburger, U. H. F. Bunz, „Electron-transporting phenazinothiadiazoles with engineered microstructure", *J. Mater. Chem. C* **2014**, *2*, 9609–9612. ([#] both authors contributed equally)

7.1.   Motivation

The high performance of **TIPS-PEN** in organic field-effect transistors originates from the 2-D brickwork packing of the aromatic units in the solid state. This solid state packing motif results in a layered growth of TIPS-Pentacene on the substrate and in an ideal orientation of the acene core for lateral charge transport within the film. The bulky character of the TIPS-ethynyl side chains arranges the π-systems in this desirable way and their size influences the geometric overlap and electronic coupling between two neighbouring pentacenes.[60,61,78,173] The beneficial brickwork arrangement is typical for **TIPS-PEN** or higher TIPS-functionalised acenes, while TIPS-tetracene does not exhibit a 2-D layered, but a herringbone solid state packing.[174] In thin film transistors TIPS-Tetracene acts as an insulator and does not exhibit significant charge transport due to the absence of strong π-π-interactions.

The molecular structures investigated here derive from the synthesis of N-heteroacenes with annulated thiadiazole moieties as precursors for diamine structures, which are typically used in classic condensation or palladium coupling reactions. The study of the solid state packing of such thiadiazole derivatives revealed an interesting feature of these compounds: two thiadiazole units of neighbouring molecules form a planar dimer structure due to the strong interaction of nitrogen and sulphur in two thiadiazole units.[146,172,175,176] This supramolecular interaction has dramatic consequences for the molecular packing and allows an efficient π-π-stacking of the adjacent acene core. Two phenazinothiadiazole derivatives with this structural motif were selected to conduct this study in which the substitution with halogens at the outer ring should lower the frontier molecular orbitals to allow the injection from electrons (**Figure 69**).
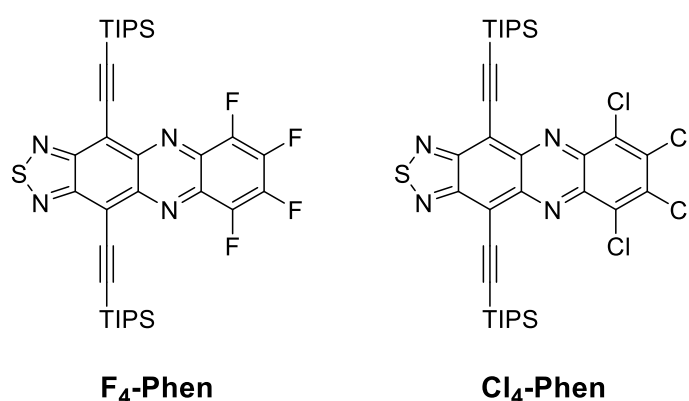
F₄-Phen   **Cl₄-Phen**

Figure 69. Molecular structure of the tetra-fluorinated (**F₄-Phen**) and tetra-chlorinated (**Cl₄-Phen**) phenazinothiadazoles.

7.2.   Molecular packing and solid state properties of the halogenated phenazinothiadiazoles

The solid state packing of these two compounds, **F₄-Phen** and **Cl₄-Phen** shows the expected supramolecular packing motif with a distinct layered growth and close π-π-stacking is observed in contrast to the herringbone

packing of TIPS-tetracene. The green circle in **Figure 70** highlights the interaction of the thiadiazole moiety that is responsible for the formation of a planar dimer. These dimers are packed in a 2-D-brickwork for both derivatives with two symmetrically different π-π-stacking distances (red and pink). In the case of **Cl$_4$-Phen** the two distances are very similar 3.38 Å and 3.35 Å (**Table 12**). However, the geometrical size of the overlap differs significantly (red and pink circle in **Figure 70**). The fluorinated compound **F$_4$-Phen** exhibits two very different π-π-stacking distances of 3.13 Å and 3.32 Å, the latter obtained from the overlap in which the two phenazine cores exhibit a large short axis offset (**Figure 70** and **Table 12**).
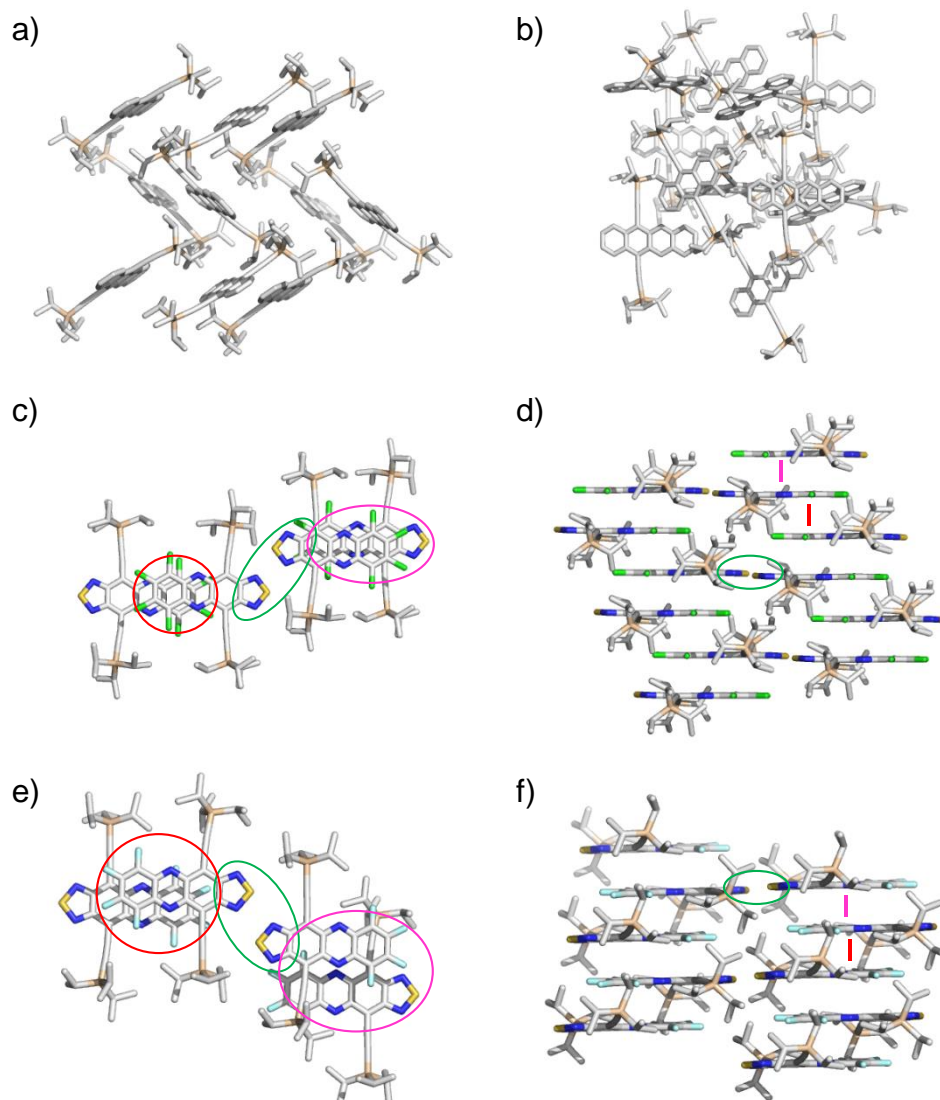
Figure 70. Solid State packing of (a)+(b) TIPS-tetracene[174]; (c)+(d) **Cl$_4$-Phen** and (e)+(f) of **F$_4$-Phen**. The geometrical large and small π-π-overlap of the phenazinothiadiazoles are highlighted pink and red, respectively. The strong interaction of the thiadiazole unit is marked with a green circle.

The theoretical calculations of the electronic coupling in these solid state structures were carried out by M. Schaffroth.[165] The calculations reveal that **Cl$_4$-Phen** exhibits a very balanced LUMO-LUMO overlap to its neighbouring molecules. These transfer integrals are larger than the corresponding HOMO-HOMO interaction,

suggesting that **Cl₄-Phen** might act as efficient electron transporting semiconductor in organic field-effect transistors. **F₄-Phen** shows two π-π-interactions of different size, depending on the overlap in the solid state structure. The LUMO-LUMO interaction is again the dominating coupling part and overpowers the HOMO-HOMO interaction. In both structures the contribution of the LUMO-LUMO coupling along the two thiadiazole units cannot be neglected, emphasising the strong interaction of these moieties. While the energetic position of the LUMO for each material was calculated by DFT theory, the effect of the solid state packing was not taken into account.

Table 11. Summarised parameters of the solid state packing of **Cl₄-Phen** and **F₄-Phen** and calculated transfer integrals.

compound	large π-π-overlap (pink)			small π-π-overlap (red)			along thiadiazole dimer (green)	
	π-π-distance[a] [Å]	transfer integral[b] [meV]		π-π-distance[a] [Å]	transfer integral[b] [meV]		transfer integral[b] [meV]	
		HOMO-HOMO	LUMO-LUMO		HOMO-HOMO	LUMO-LUMO	HOMO-HOMO	LUMO-LUMO
Cl₄-Phen	3.38	38.2	54.4	3.35	34.7	61.2	9.5	49.4
F₄-Phen	3.14	56.0	68.4	3.32	1.3	170.6	12.4	51.1

[a] π-π-distance of neighbouring molecules calculated as distance of two planes, each defined by the six atoms of the pyrazine ring
[b] values taken from Ref. [165,172]. [For Ref.[172] - Reproduced by permission of The Royal Society of Chemistry]

Reliable determination of the energetic positions of the frontier molecular orbitals was achieved by performing ultraviolet photoemission spectroscopy on thin films of **Cl₄-Phen** and **F₄-Phen**. The onset of the absorption spectra of the thin films was used to calculate the optical gap, determined to be 748 nm (1.66 eV) and 750 nm (1.65 eV) for **F₄-Phen** and **Cl₄-Phen**, respectively. These values are smaller than the observed optical gap for both materials in solution, representing the strong π-π-interaction in the solid state that is also expressed in the significant broadening and red-shift of the entire absorption spectrum.[172] UPS measurements determined the ionisation potential to be 6.45 eV and 6.30 eV for **F₄-Phen** and **Cl₄-Phen**, respectively. The chemical modification of the aromatic body through halogen substitution, incorporation of the diazole unit and the nitrogen substitution and the solid state packing result in a large stabilisation and a deep HOMO compared to materials like TIPS-pentacene (5.05 eV, see **Chapter 8**) or tetracene (5.1 eV).[71] The subtraction of the optical gap results in a positon of the LUMO of 4.79 eV and 4.65 eV for **F₄-Phen** and **Cl₄-Phen**, respectively. These values are remarkably low for an aromatic four ring system and allow easily injection of electrons from gold electrodes. Paired with the promising transfer integrals, the deep LUMO suggest that these compounds might act as excellent electron transport materials in thin film transistors.
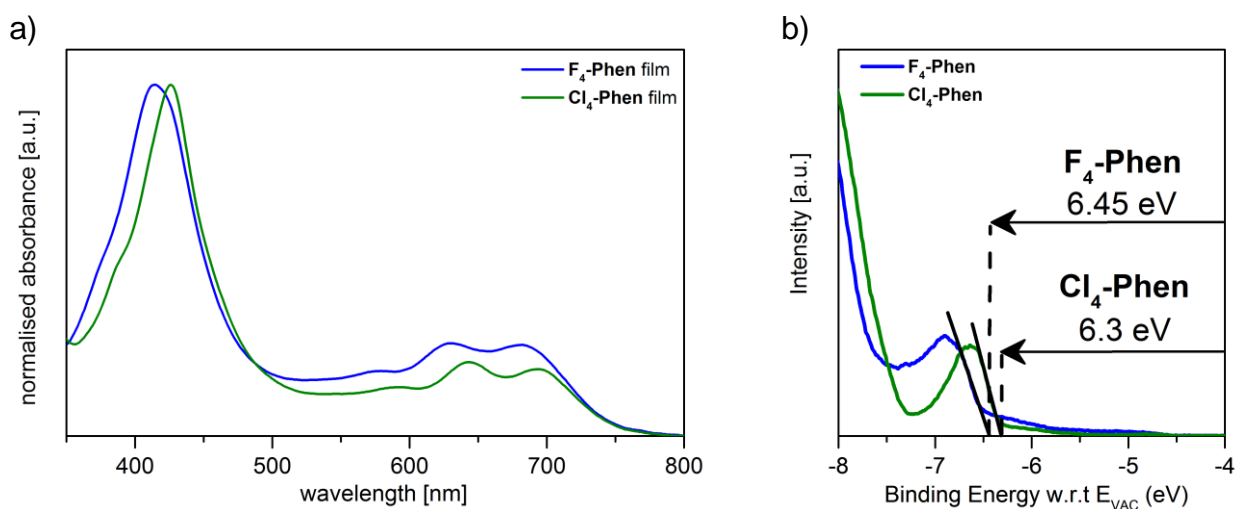
Figure 71. (a) Absorption spectra of the phenazinothiadiazole films. (b) Low-binding energy edge of **F₄-Phen** and **Cl₄-Phen**.

Films of **F₄-Phen** and **Cl₄-Phen** were spin-coated from toluene and chlorobenzene solution. The side chains make the materials well soluble in organic solvents and allow for solution processing techniques. Polyimide coated glass substrates allow homogenous film formation and provide a good wettability. **F₄-Phen** and **Cl₄-Phen** exhibited polycrystalline films on these substrates when spin-coated from toluene with crystalline domains of only a few micrometre size (**Figure 72**). Using chlorobenzene for deposition resulted in an increased size of the crystalline structure within in the film with an average size of 5-40 µm for these crystallites, whereas **F₄-Phen** exhibited slightly larger structures. Compared to films of **TIPS-TAP** or other N-heterocycles the exhibited domain sizes are rather small (see **Chapter 5**). However, the films are homogenous and dense with a uniform film thickness. Independent of the solvent used for deposition, films of **F₄-Phen** and **Cl₄-Phen** exhibited a relatively high rms-roughness of ca 10-12 nm. (**Figure 73**).
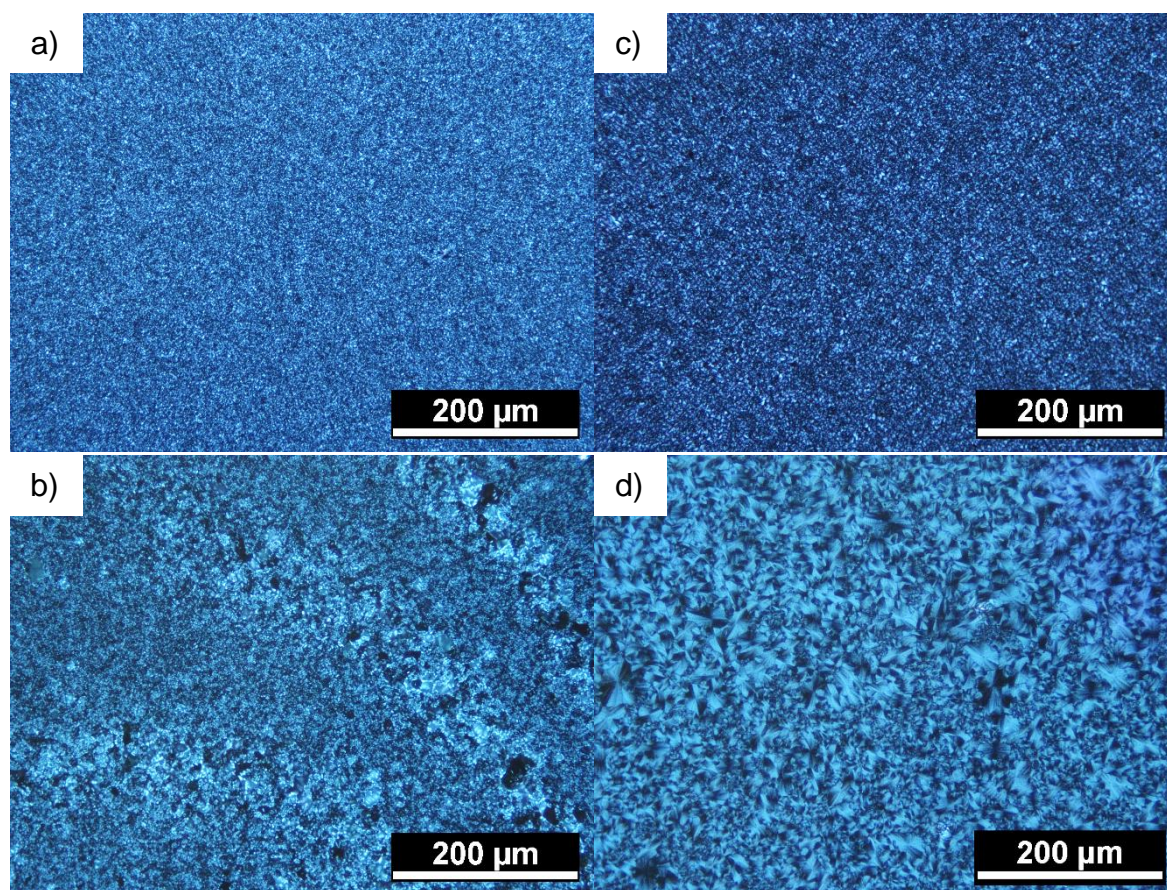
Figure 72. Optical microscopy images of the polycrystalline films of the phenazinothiadiazoles under crossed-polarisers on polyimide coated substrates; (a) **Cl₄-Phen** from toluene and (b) from chlorobenzene; (c) **F₄-Phen** from toluene and (d) from chlorobenzene.
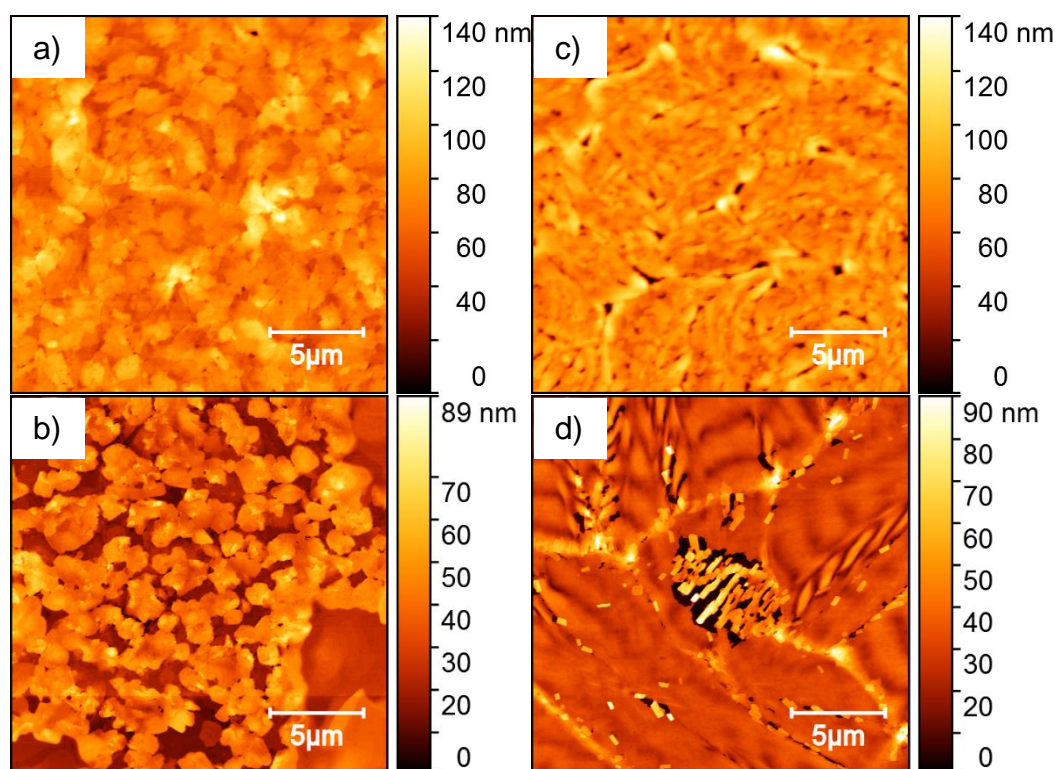
Figure 73. AFM height images (20 x20 μm^2) of polycrystalline films of **Cl₄-Phen** (left) and **F₄-Phen** (right); (a) **Cl₄-Phen** from toluene, (b) from chlorobenzene; (c) **F₄-Phen** from toluene and (d) from chlorobenzene.

XRD measurements were performed on these polycrystalline films to probe the molecular orientation of the phenazinothiadiazoles in thin films. Films of **F₄-Phen** and **Cl₄-Phen** exhibited a series of higher order Bragg-reflections in the X-ray diffraction measurements. Films spun from chlorobenzene showed more pronounced reflections of higher order at higher diffraction angles, indicating the larger domains and more crystalline nature of films cast from the higher boiling point solvent. The first reflection occured for both samples at a small diffraction angles of only 5.5°, representing a layer spacing of above 15-17 Å. This dimension suggests that the phenazinothiadiazoles are also oriented on the substrate with their TIPS-ethynl side groups aligned close to vertical. Analysis of the relative intensities and position of the reflections coincides with an (001)-orientation of **F₄-Phen** and **Cl₄-Phen** on the polyimide coated substrates. The extracted $d_{(001)}$-spacing values of the diffraction patterns match the predicted values of 16.8 Å and 15.5 Å for **Cl₄-Phen** and **F₄-Phen**, respectively. This molecular orientation results in a layered growth of the phenazinothiadiazoles in thin films and the observed brickwork arrangement and staggered nature of the aromatic units is ideal for a 2-D charge transport within each layer along the substrate's surface (**Figure 75**).
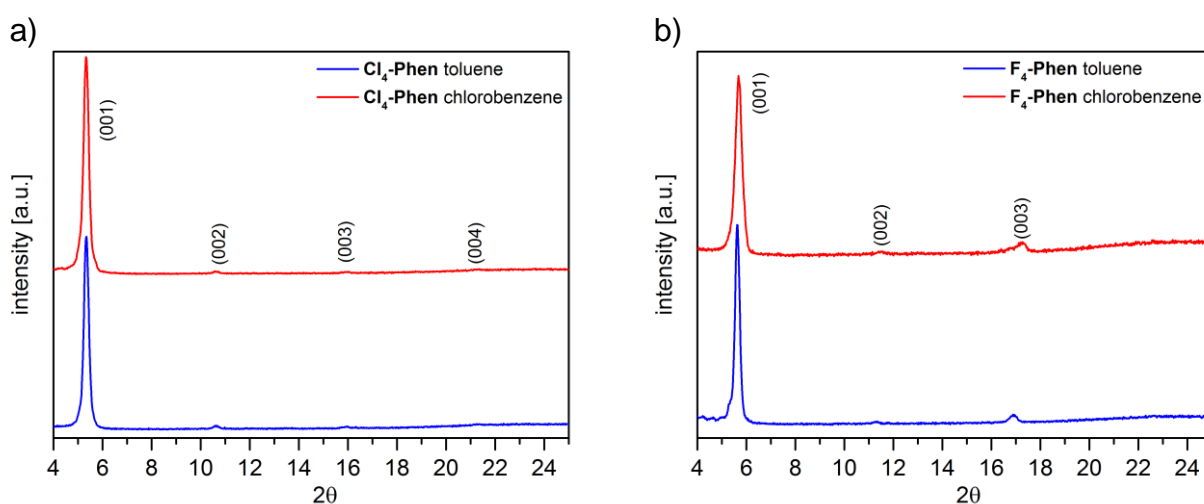
Figure 74. XRD diffraction pattern (with Cu Kα₁,₂) of thin films of (a) **Cl₄-Phen** and (b) **F₄-Phen** spin-cast from toluene and chlorobenzene.

Table 12. Extracted d-spacing values from the X-ray diffraction patterns for thin films of **Cl₄-Phen** and **F₄-Phen**.

compound	solvent	extracted $d_{(00l)}$-spacing value [Å]	calculated $d_{(00l)}$-spacing value [Å]	tilt angle of the molecule [°]
Cl₄-Phen	toluene	16.6	16.8[a]	19
	chlorobenzene	16.6		
F₄-Phen	toluene	15.5	15.5[b]	35
	chlorobenzene	15.6		

[a], [b] obtained from single crystal structure of **Cl₄-Phen** and **F₄-Phen**, respectively.[172]

The small differences in the unit cell and in the intermolecular packing distances of **Cl₄-Phen** and **F₄-Phen**, combined with the preferred orientation of the (001)-Miller plane parallel to the substrate's surface result in

a different vertical alignment of the aromatic π-system to the surface normal. The plane of the **Cl$_4$-Phen** molecule exhibits a more upright orientation on the surface compared to **F$_4$-Phen**, which is tilted about 35° away from the surface normal.
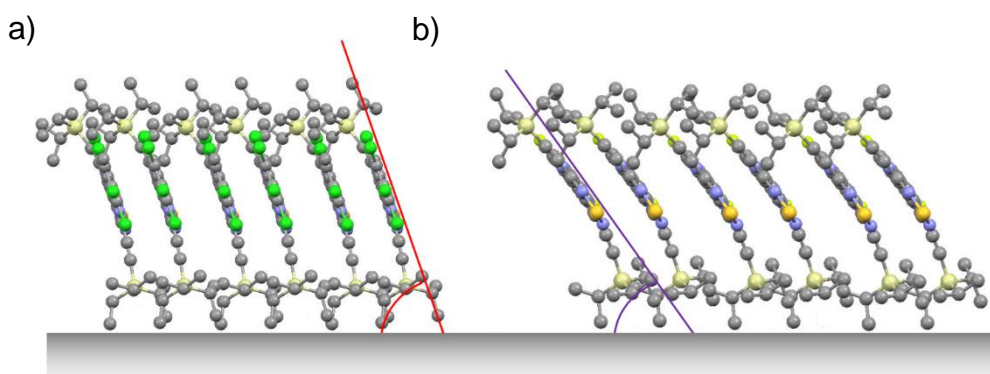
Figure 75. Schematic orientation of (a) **Cl$_4$-Phen** and (b) **F$_4$-Phen** molecules on a substrate's surface with the (001)-plane parallel to the substrate as obtained from XRD measurements. The coloured lines and angle represent the different tilt angles of the aromatic backbone towards the surface.

7.3.   Field-effect   transistor   performance   of   spin-coated phenazinothiadiazoles

To evaluate the charge transport properties of the phenazinothiadiazoles in thin films, bottom-contact/ top-gate transistors on polyimide were fabricated. After spin-coating the active layer on the pre-patterned gold electrodes, CYTOP^{TM} was used as a dielectric layer and a gate electrode was evaporated above the interdigitated electrode structure. The **Cl$_4$-Phen** and **F$_4$-Phen** transistors showed an n-channel behaviour with high on/off-ratios as expected from their deep LUMO and large transfer integrals (**Figure 76**).
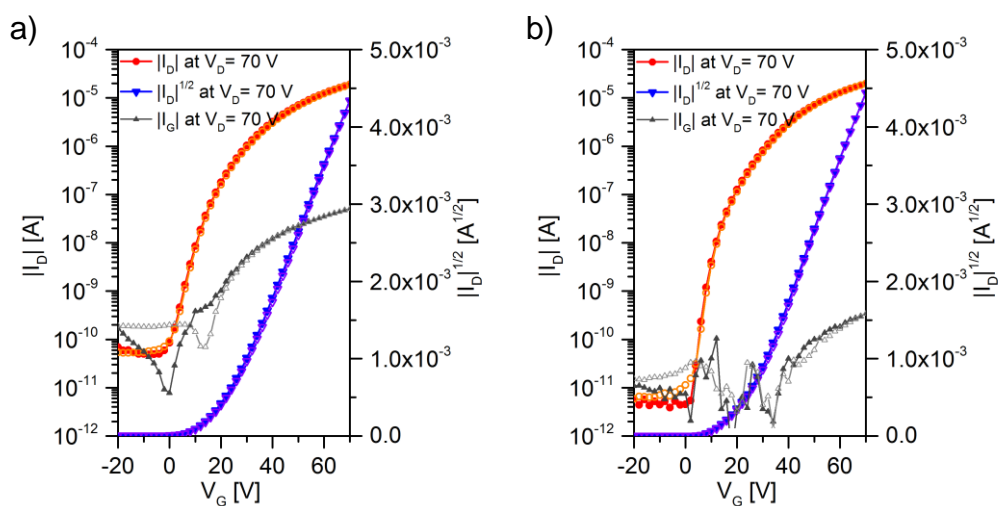
Figure 76. Transfer characteristics of the field-effect transistors (W = 1,000 µm; L = 20 µm) deposited from toluene for (a) **Cl$_4$-Phen** and (b) **F$_4$-Phen**.

The off-current of the devices were limited by the gate current and can potentially be improved if the organic were patterned to supress parasitic charging and leakage currents. The hysteresis of all the fabricated devices was negligible and the backward and forward sweep were basically identical in these transistors. The threshold voltages for **Cl₄-Phen** and **F₄-Phen** fabricated transistors were always in the range of 13-16 V for devices fabricated from toluene, and slightly increased with the use of chlorobenzene (**Figure 76** and **Table 13**). The extracted electron mobilities for both materials could be improved through the use of chlorobenzene and can be attributed to the improved microstructure of the polycrystalline films (**Figure 77**). **F₄-Phen** exhibited average electron mobilities of $5.9 \cdot 10^{-2}$ cm^2/Vs for devices spun from toluene. The average mobility increased by almost a factor of two for devices with chlorobenzene and a maximal mobility of 0.26 cm^2/Vs was found (**Table 13**). Upon the use of a higher boiling point solvent, not only the electron mobility improved, but also the subthreshold swing decreased to values of 2.7 and 3.0 V/dec for **Cl₄-Phen** and **F₄-Phen**, respectively.

Table 13. Summarised FET parameters for bottom-contact / top-gate transistors with phenazinothiadiazoles deposited by spin-coating. The average value and standard error of the mean are given and were obtained from a set of identically prepared devices.

| compound	solvent	$\mu_{electron}$ best [cm²/Vs]	μ_{hole} average [cm²/Vs]	threshold voltage average V_{th} [V]	subthreshold swing [V/dec]	on/off ratios range
F₄-Phen	toluene	0.07	0.059±0.005	13.1±0.6	3.6	10^5
	chlorobenzene	0.26	0.091±0.019	18.1±1.7	3.0	10^5-10^6
Cl₄-Phen	toluene	0.16	0.107±0.016	16.2±0.5	4.9	10^5
	chlorobenzene	0.36	0.111±0.018	18.9±1	2.7	10^5-10^6
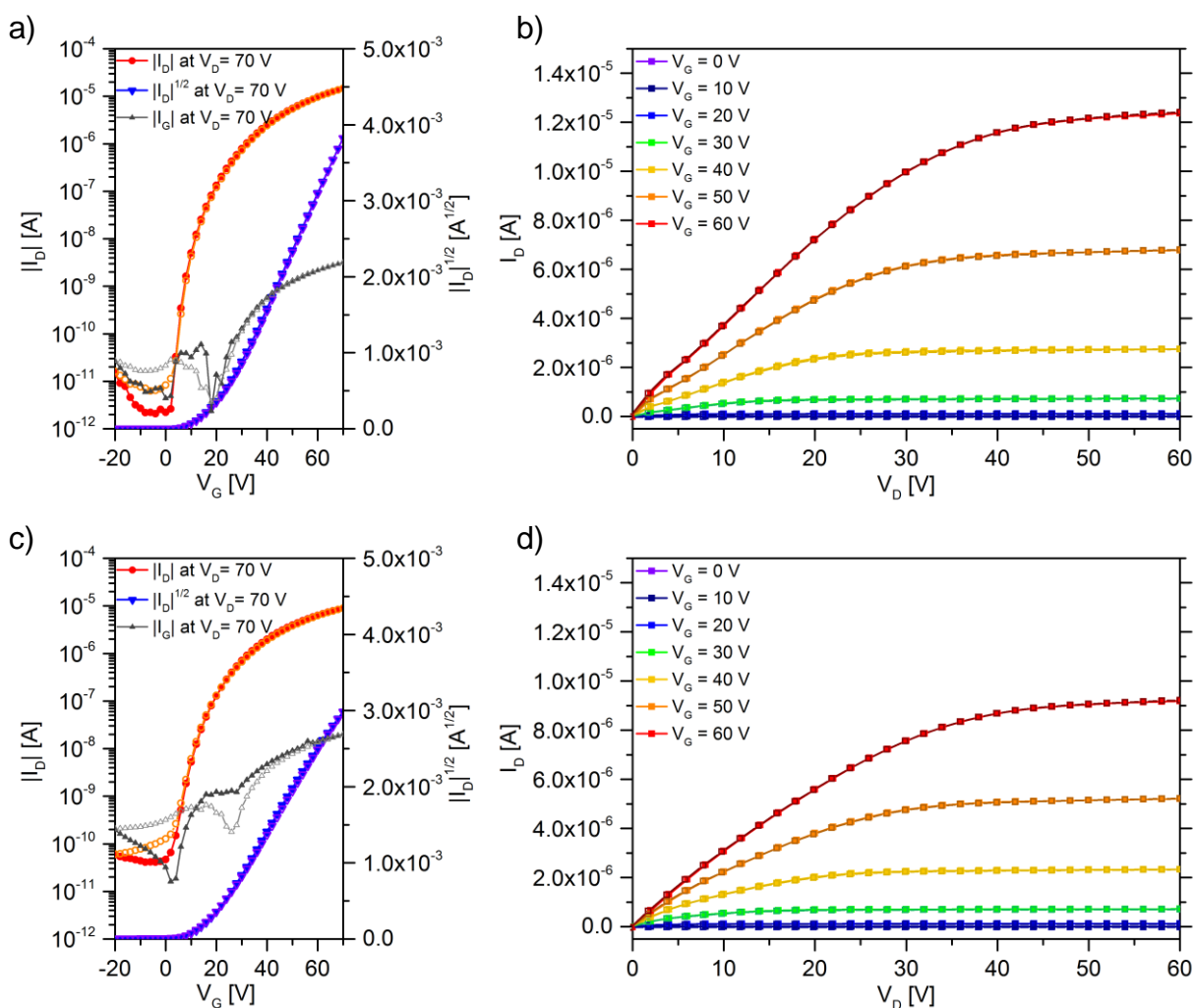
Figure 77. Field-effect transistor characteristics for phenazinothiadiazoles spin-cast from chlorobenzene (W = 10,000 μm, L = 50 μm). (a) Transfer and (b) output I-V curves for **Cl₄-Phen**; (c) transfer and (d) output characteristics for **F₄-Phen**.

Similarly to the observations made for the domain sizes by optical microscopy, the impact of chlorobenzene on the charge transport is not as pronounced for the chlorinated compound compared to **F₄-Phen**. Devices from **Cl₄-Phen** showed for both solvents the highest electron mobility values. Thin film transistors with **Cl₄-Phen** always exhibited an average electron mobility of about 0.1 cm²/Vs and reached up to 0.36 cm²/Vs. These values, which are higher than the corresponding electron mobilities for **TIPS-TAP** found in spin-coated films, demonstrate the efficacy of structural design of the phenazinothiadiazoles, the strong π-π-interaction and perfect orientation for a 2-D lateral charge transport. All devices exhibited a linear injection behaviour, indicating an excellent contact and a low injection barrier for electrons from gold electrodes into the deep LUMO of **Cl₄-Phen** and **F₄-Phen** (**Figure 77**).

7.4.   Zone-casting of Cl₄-Phen and thin film transistors

The promising charge transport properties and the relatively high electron mobilities for polycrystalline films of **Cl₄-Phen** lead to an attempt fabricating ordered films with **Cl₄-Phen** through zone-casting for high

performing transistors. Due to the formation of highly aligned and highly crystalline **Cl₄-Phen** films and the reduced concentration of grain boundaries one expects an improvement of the transistor performance. First attempts to employ the zone-casting deposition technique for **Cl₄-Phen** utilised polyimide coated glass substrates and through double layer photography patterned source-drain contacts perpendicular to the zone-cast direction. Toluene (3 mg/mL) was used for deposition due to the high solubility of **Cl₄-Phen** and the good wetting properties on the substrate. Zone-casting at different substrate temperatures at a substrate speed of 150 µm/s resulted in highly crystalline films (**Figure 78**).

Cl₄-Phen zone-cast from toluene on polyimide
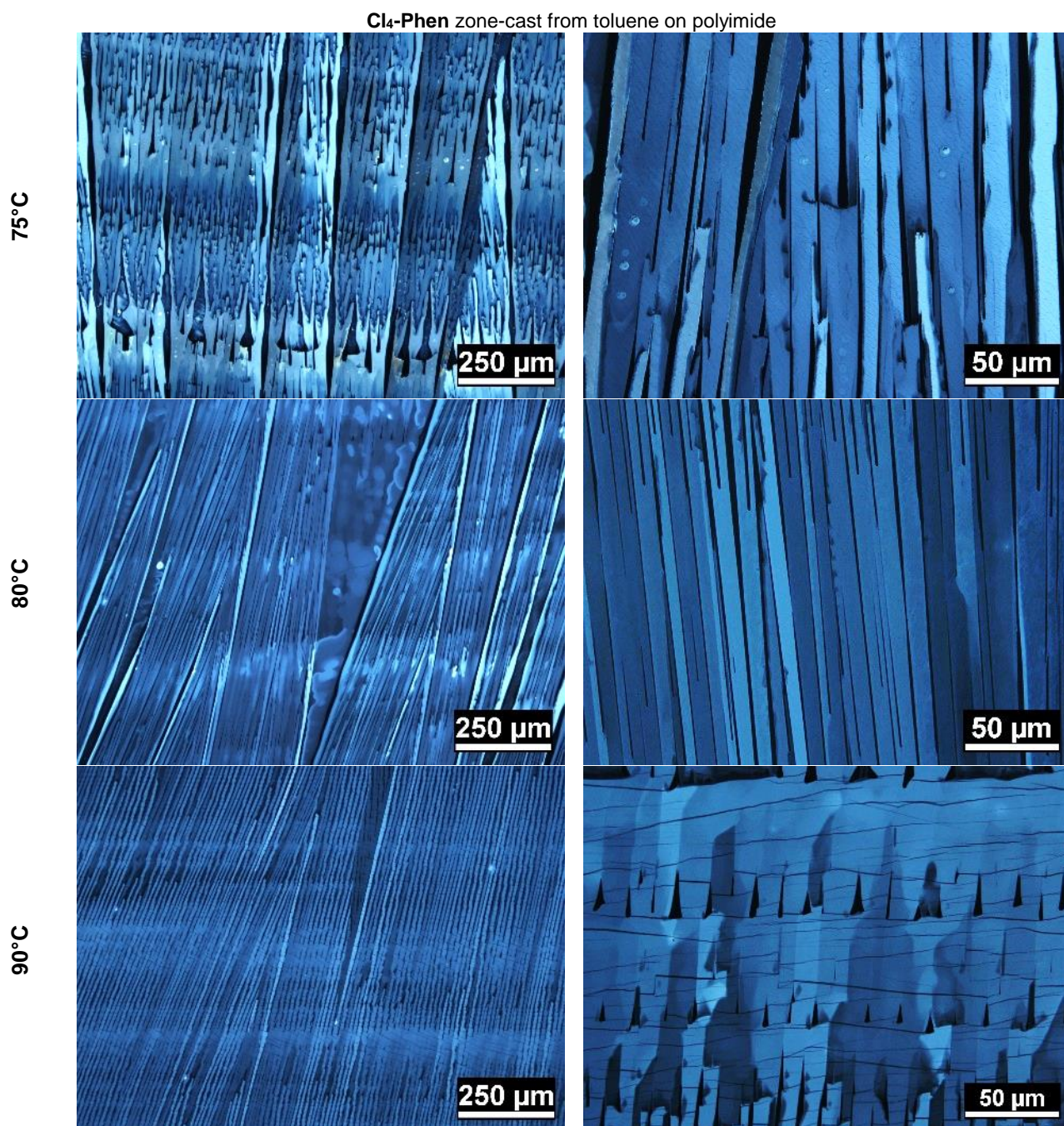
Figure 78. Optical microscopy images (crossed polarisers) of the zone-cast films of **Cl₄-Phen** on polyimide coated substrates at different substrate temperatures and different magnifications.

At 75 °C the films exhibited irregularities and the crystal growth was not uniform, resulting in poorly aligned crystalline strands of various lengths and thicknesses. At 80 °C the growth was more aligned and regularly, resulting in parallel crystalline structures. The uniform colour of each crystal strand under the crossed polarisers of the polarised microscope indicates their single crystalline character. Choosing a higher temperature for deposition during zone-casting from toluene resulted in crystal strands that were partially interconnected. Furthermore, the films exhibit a significant amount of cracks in various orientations - probably due to thermal stress or different thermal expansion coefficients of the material and substrate. The deposition at 80 °C from toluene was chosen for the fabrication of transistors. Unfortunately, these zone-cast **Cl$_4$-Phen** bottom-contact/ top-gate transistors exhibited a non-linear injection behaviour, indicating a large contact resistance (**Figure 79**). This effect has been previously observed for zone-cast **TIPS-TAP** transistors in the same architecture (see **Chapter 5**). The formation of the crystalline ribbons occurs at the gas/liquid interface of the meniscus[177], so that the crystal strands were essentially laminated onto the source drain electrodes, resulting in a completely different nature in the contact between gold and the organic compared to spin-coated devices. Furthermore, the improved in crystallinity and the strong (001)-orientation of **Cl$_4$-Phen** might have affected the efficacy of the electron injection into the aromatic core of the phenazinothiadiazole and contributed to the observed injection limitation. The threshold voltage for these devices was therefore significantly higher compared to spin-coated transistors (**Table 14**). The average electron mobility extracted in the saturation regime was slightly lower than those of the polycrystalline films and might be an effect of the contact limitations (see **Table 13** for comparison).
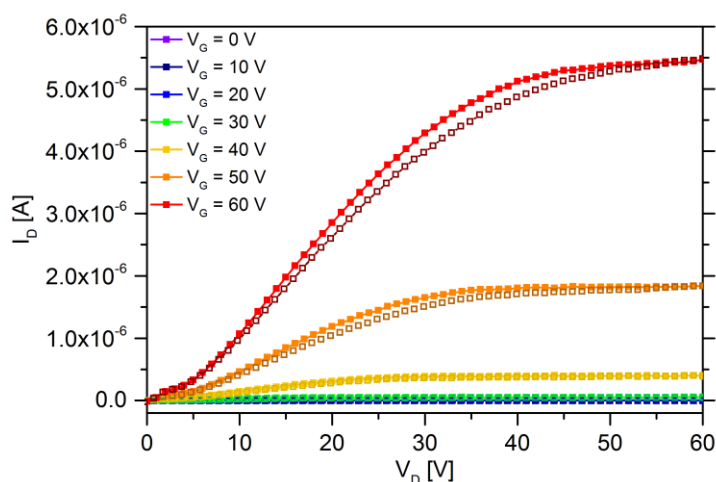
Figure 79. Representative output characteristics of a zone-cast bottom-contact/ top-gate **Cl$_4$-Phen** transistor (W = 1,000 μm; L = 20 μm) with non-ideal injection behaviour.

To compensate the injection issues and to improve the interface of the zone-cast organic film with the gold electrodes zone-casting of **Cl$_4$-Phen** on BCB was performed and top-contacts were thermally evaporated. Toluene as solvent could not be used for this architecture as the films suffered from a poor wettability with
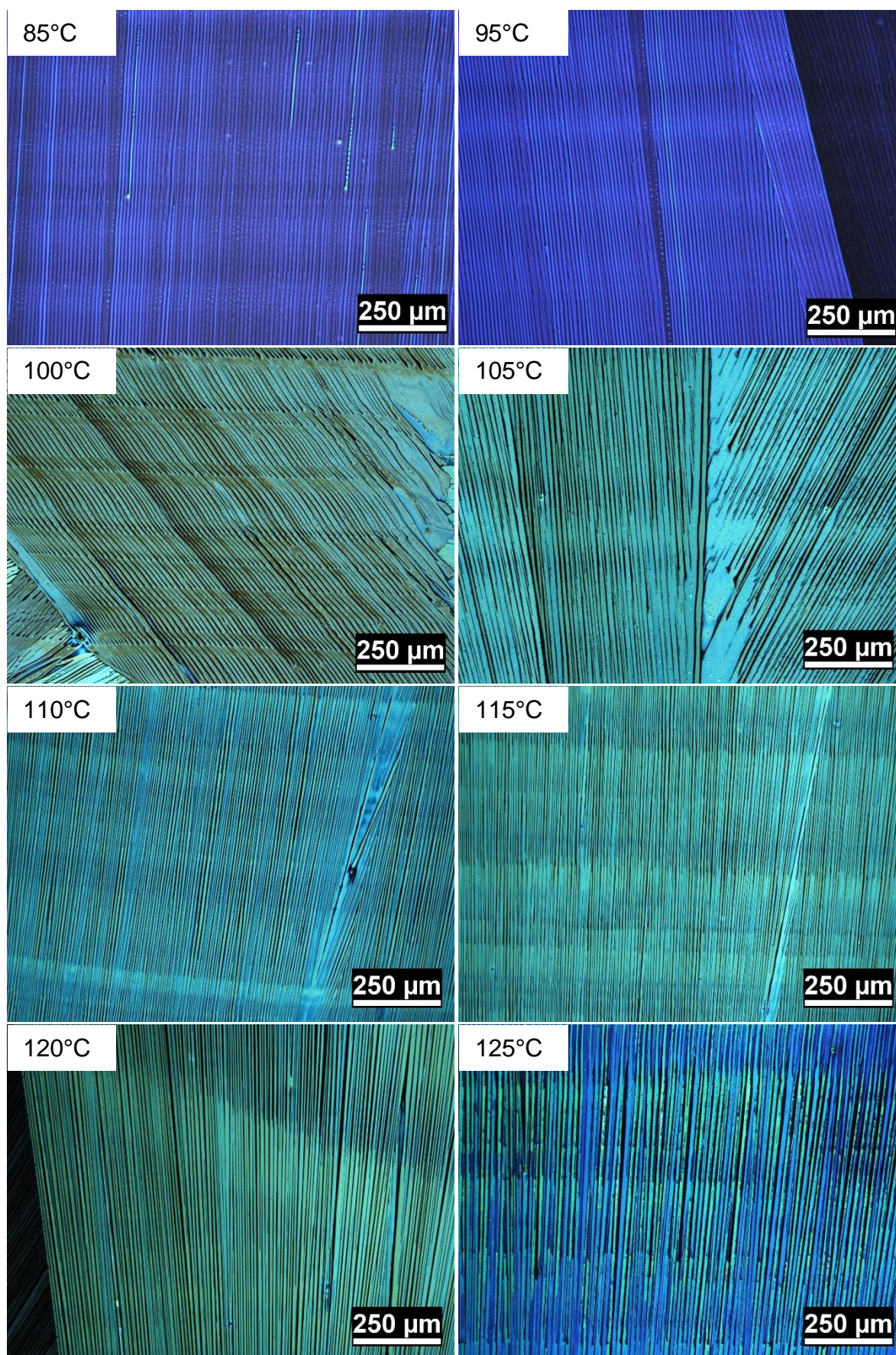
Figure 80. Optical microscopy images (crossed polarisers) of zone-cast films of **Cl₄-Phen** at different substrate temperatures on BCB.

the solution and inhomogeneous films resulted. The deposition from mesitylene solution allowed not only a wider temperature range for the deposition but also yielded highly ordered **Cl$_4$-Phen** films on BCB (**Figure 80**). Films cast at 85 °C and 95 °C were incredible thin and larger areas of different oriented domains grew into each other. A substrate temperature of 100 °C resulted a crystallisation that could only partially follow the zone-casting direction, and islands of larger crystalline plates within the crystal strands were observed. A similar film structure was found for 105 °C. Temperatures higher than 110 °C degrees resulted in predominantly parallel grown crystalline strands of uniform thickness and with constant widths (**Figure 80**). However, the optical microscope images show that the height of the crystal strands for a substrate temperature of 125 °C no longer remained uniform and that the thickness variation became broader. Source-Drain electrodes for top-contact field effect-transistors were structured through a shadow mask onto the zone-cast structures, but due to fabrication process of this mask, longer channel lengths than the bottom-contact structures had to be chosen. The injection behaviour of zone-cast transistors of **Cl$_4$-Phen** on BCB/SiO$_2$/Si was significantly improved, resulting in an ohmic contact and small threshold voltages (**Figure 81**). Despite this desired behaviour, the observed performance of these devices was rather disappointing (**Table 14**). The extracted electron mobility of **Cl$_4$-Phen** was two to three orders below that, obtained from spin-coated transistors. The average electron mobility scaled with increasing substrate temperature and the highest obtained mobility in zone-cast top-contact transistors of **Cl$_4$-Phen** on BCB was only $2.30 \cdot 10^{-3}$ cm^2/Vs (**Table 14**).

Table 14. Summarised electrical parameters for zone-cast transistors with **Cl$_4$-Phen**. Average values and standard deviation are given.

| compound	solvent / substrate temperature	FET architecture	$\mu_{electron}$ best [cm²/Vs]	μ_{hole} average [cm²/Vs]	threshold voltage average V$_{th}$ [V]	on/off ratios range
	toluene/80°C	BC/TG	0.11	0.063±0.032	30.7±2.7	10^4-10^6
	mesitylene / 110°C	BG/TC	$0.57 \cdot 10^{-3}$	$(0.58 \pm 0.29) \cdot 10^{-3}$	6.1±0.7	10^2-10^4
Cl$_4$-Phen	mesitylene / 115°C	BG/TC	$1.08 \cdot 10^{-3}$	$(1.02 \pm 0.35) \cdot 10^{-3}$	5.5±1.4	10^2-10^4
	mesitylene / 120°C	BG/TC	$1.39 \cdot 10^{-3}$	$(1.23 \pm 0.64) \cdot 10^{-3}$	6.5±1.2	10^2-10^4
	mesitylene / 125°C	BG/TC	$2.30 \cdot 10^{-3}$	$(1.54 \pm 0.73) \cdot 10^{-3}$	6.5±1.4	10^2-10^4
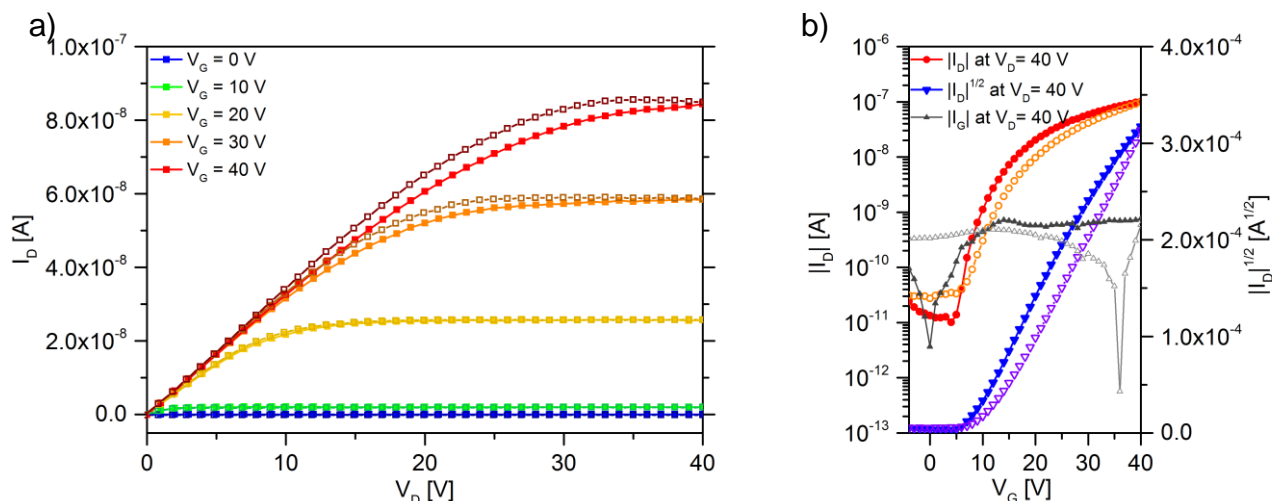
Figure 81. (a) Output characteristics and (b) transfer characteristics of a zone-cast bottom-gate/top-contact field-effect transistor (W = 1,500 µm; L = 180 µm) with **Cl$_4$-Phen**.

7.5.   Morphological properties of zone-cast Cl$_4$-Phen films

These results lead to the investigation of the origin for the reduced transistor performance. X-ray diffraction on these the zone-cast films were performed for different substrate temperatures to monitor possible changes in the molecular orientation of the chlorinated phenazinothiadiazole upon zone-casting deposition. The zone-cast films each exhibited a series of Bragg reflections at identical position compared to spin-coated films (**Figure 82**). The relative intensities are higher for the zone-cast films and even Bragg reflections at higher diffraction angles were visible, representing the highly ordered structure and crystallinity in the zone-cast samples. However, the XRD measurements clearly reveal that **Cl$_4$-Phen** exhibits the same solid state packing and orientation in zone-cast as in spin-coated films. A different polymorph or molecular orientation towards the substrate's surface could not be identified and further investigations were necessary, to reveal the origin of the reduced FET performance.

a)
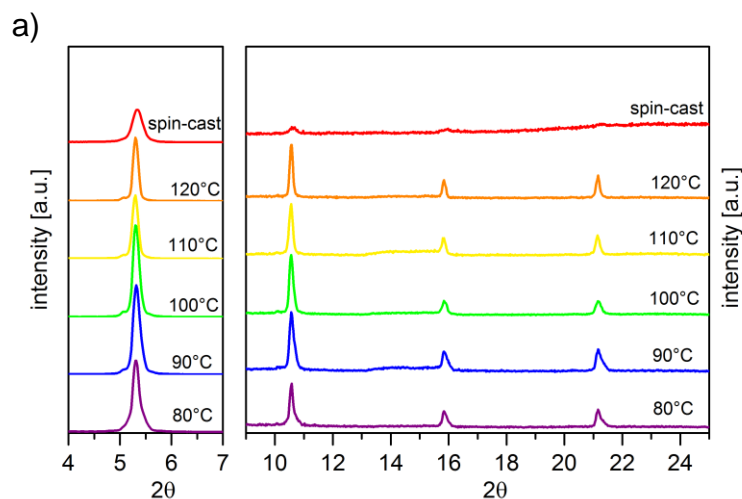
Figure 82. (a) Comparison of the X-ray diffraction pattern of **Cl₄-Phen** films deposited by zone-casting at different substrate temperatures from mesitylene on BCB and spin-coating from chlorobenzene (see also **Figure 74a**).
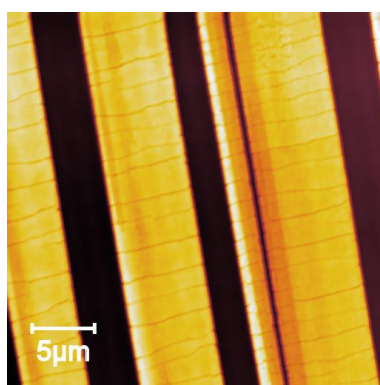
Figure 83. AFM height images of zone-cast films with **Cl₄-Phen**. The crystal strands are heavily affected by perpendicular cracks along the growth direction (20x20 μm²; deposited at 115°C).

Atomic force microscopy on the zone-cast crystal strands of **Cl₄-Phen** uncovered the cause for the low transistor performance of the long channel top-contact FETs on BCB (**Figure 83**). The height image of a zone-cast film deposited at 115 °C showed a high concentration of micro fractures along the crystal ribbon. All films exhibited these structural cracks along the crystalline strands of **Cl₄-Phen**, while for higher temperatures the density of cracks was slightly reduced. Optical microscopy at 100x magnification under dark-field illumination also visualised this feature of zone cast **Cl₄-Phen** films (**Figure 84**). Even the thin and partially irregular films of **Cl₄-Phen** at the lowest substrate temperature chosen exhibited these fractures (**Figure 84**). The low transistor performance was a direct result of the high density of these micro fractures within the long transistor channel, acting as grain boundaries and limiting the charge transport along these crystals. The top-contact devices with their long channel lengths were more affected by this effect than the bottom-contact transistors with significantly shorter channels, even though it is still to prove that also the zone-cast films at 80 °C from toluene on polyimide exhibited this structural damage.
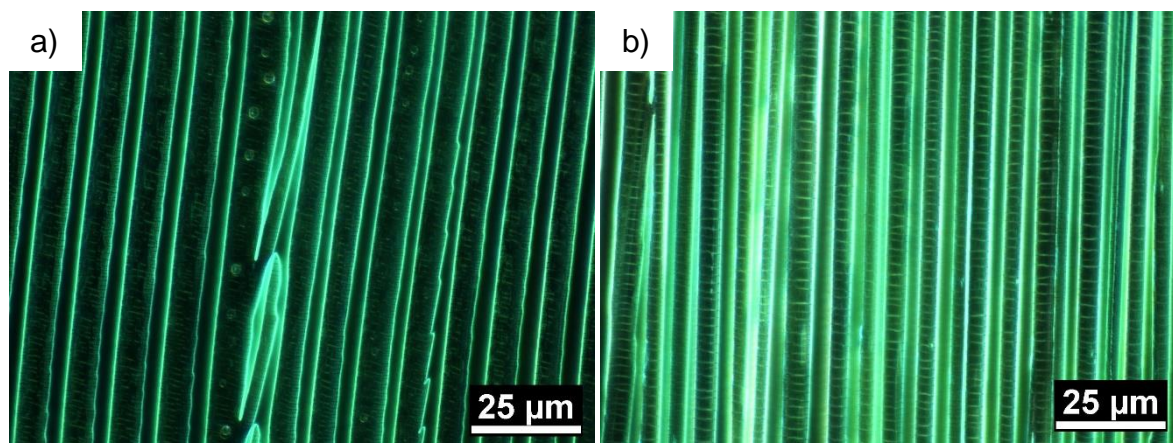
Figure 84. Dark-Field-images taken with a 100x objective from zone-cast films of **Cl₄-Phen** cast at (a) 85°C and (b) 115°C.

Unfortunately, no improvement resulted from the zone-casting of **Cl₄-Phen** due to the induced micro fractures for the deposition from mesitylene and the non-linear contact effects in bottom-contact transistors cast from toluene.

7.6.   Conclusion

The study of the tetra-halogenated phenazinothiadiazoles **Cl₄-Phen** and **F₄-Phen** shows, that these small molecules with their four-ring system can be attractive electron transporting materials with mobilities of up to 0.36 cm²/Vs in polycrystalline transistors deposited by spin-coating. The excellent FET properties are not only attributed to the very deep LUMO levels of these materials, but also originate from the supramolecular interaction in the solid state and the resulting edge-on orientation of the molecular systems in thin films ideal for a lateral charge transport. That the morphology of **Cl₄-Phen** could not be efficiently improved upon zone-casting indicates that further studies for an optimised film formation during zone-cast deposition are required for these molecules.

Chapter 8

Side-chain Modification through Norbornadienyl Substitution

The modification with a norbornadienyl substitution at the silyl ethynyl group of **TIPS-PEN** and **TIPS-TAP** is discussed in this chapter. The introduction of a bulky substituent at the side chain modifies the solid state packing of the aromatic systems changing the transfer integrals for charge transport, while the optical and electronic properties remain unaffected. The spin-coated polycrystalline films of **Nor-PEN** and **Nor-TAP** are investigated and the performance in thin film transistors is compared to their parent TIPS-derivative. For **Nor-PEN** the substitution with norbornadienyl resulted in an improvement of the film forming properties and transistor performance, reaching hole mobilities of up to 1.2 cm^2/Vs. The results of this chapter are reported in Ref. [178]: *F. Paulus, M. Porz, M. Schaffroth, F. Rominger, A. Leineweber, Y. Vaynzof, U. H. F. Bunz, „Side-Group Engineering: The Influence of Norbornadienyl Substituents on the Properties of Ethynylated Pentacene and Tetraazapentacene ", accepted manuscript, 2016, Organic Electronics*

8.1.   Motivation

The high transistor performance of **TIPS-PEN** and **TIPS-TAP** in organic field-effect transistors is a direct consequence of the crystal packing that is determined by the bulky ethynyl side chains.[21,77,82,130] Structural modifications on this part of **TIPS-PEN** have been studied in numerous publication in recent years.[32,60,78] A change in the volume of the silyl groups affects the geometrical overlap of the aromatic π-systems, the π-stacking distance, and the electronic coupling of the frontier molecular orbitals.[16,23] Small changes can heavily affect the charge transport properties, as the transfer integrals are very sensitive to the molecular orientation. While this effect has been studied for pentacene derivatives, no studies for the corresponding electron conducting tetraazapentacene has been reported.

The introduction of norbornadienyl substituents to the side chains of **TIPS-PEN** and **TIPS-TAP** was originally intended to access a new class of non-conjugated pentacene-based polymers through ROMP polymerisation, as described in **Chapter 4**.[147] However, the simple and efficient synthesis of **Nor-PEN** and **Nor-TAP**, their great stability, and the solid state packing of these compounds lead to an investigation of these materials as small molecule semiconductors in thin film transistors (**Figure 85**).

|		
TIPS-PEN	**X = CH**	**Nor-PEN**
TIPS-TAP	**X = N**	**Nor-TAP**
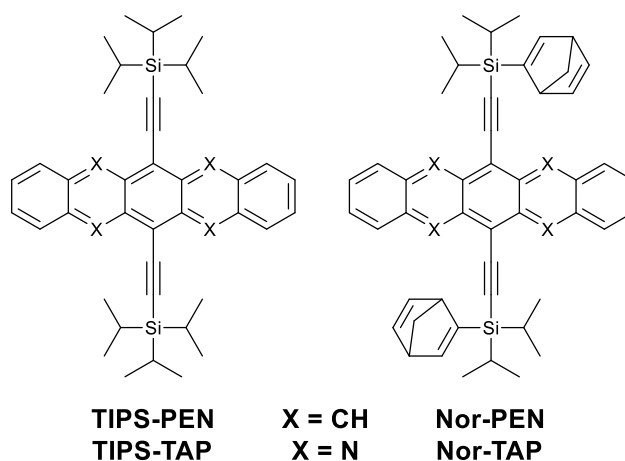
Figure 85. Molecular structure of the norbornadienyl substituted pentacene and tetraazapentacene (right) and their parent **TIPS-PEN** and **TIPS-TAP** (left).

8.2.   Solid State Properties of Nor-PEN and Nor-TAP

TIPS-PEN and **TIPS-TAP** exhibit a 2-D-brickwork arrangement that allows an efficient charge transport and a good film formation upon solution processing-techniques.[77,130] The bulky character of the norbornadienyl substituent does not dramatically change the crystal packing so that **Nor-PEN** and **Nor-TAP** also exhibit a brickwork arrangement, with a good geometrical overlap along the long axes of the molecules and only small offsets along the short axes of the aromatic bodies (**Figure 86** and **Figure 87**). In the solid state packing the norbornadienyl groups are strictly oriented antiparallel along the acene core, regularly occupying the volume between the stacked aromatic systems. Due to the use of a racemic mixture of the norbornadienyl-silyl

compound the X-ray crystal structure showed a disordered, bulky side group. However, this feature does not affect the regularity of the packing of the acene cores. The average π-π-stacking distance in **Nor-PEN** is 3.38 Å, which is slightly closer than **TIPS-PEN** (3.41 Å) (**Figure 86**).[77] The **Nor-TAP** exhibits an even closer average π-π distance of 3.29 Å which is almost identically to that of the distance in **TIPS-TAP**.[130] A table with the summarised cell parameters for all four compounds can be found in the Appendix.

a)

b)
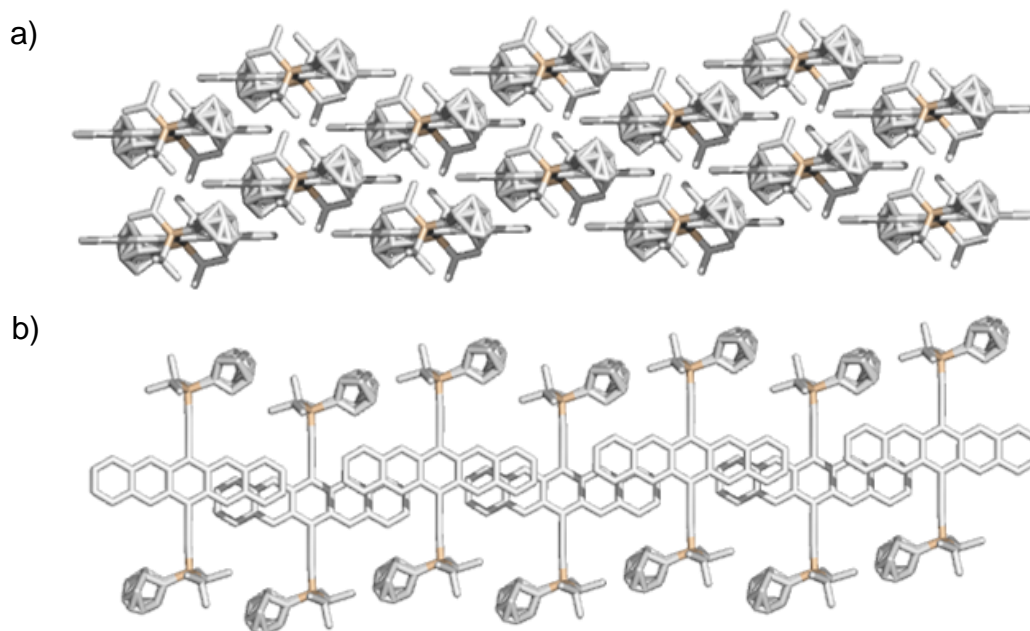
Figure 86. Crystal packing of **Nor-PEN**; (a) side view along the molecular plane and (b) top view onto the molecular π-system to visualise the brickwork packing.

a)

b)
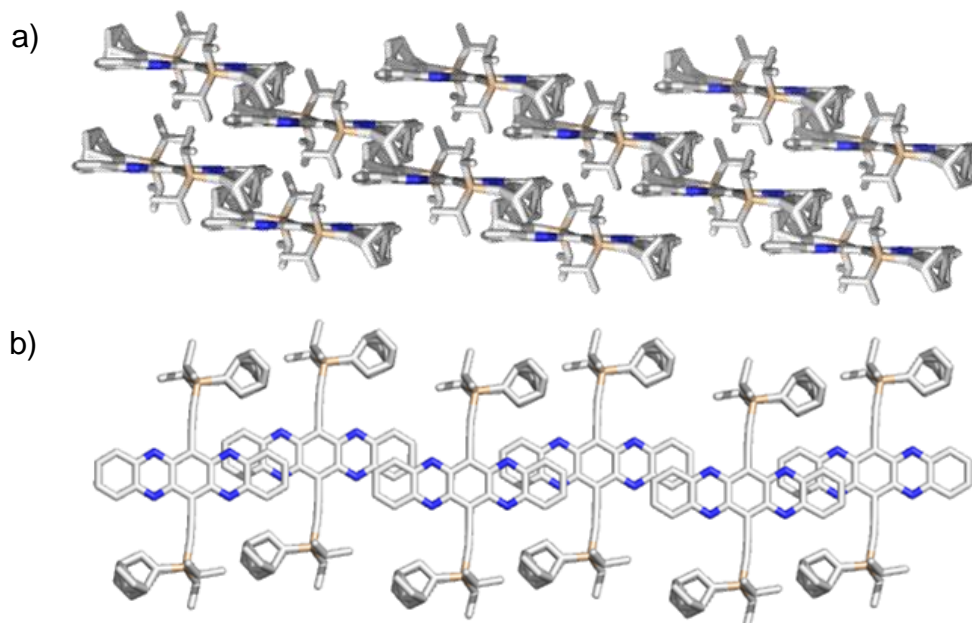
Figure 87. Solid State packing of **Nor-TAP**; (a) side view along the aromatic systems and (b) top view onto the molecular plane.

The energetic strain of the solid state packing is reflected in the deflection angle of the ethynyl side chains, which are bent out of the plane of the aromatic pentacene body. For **Nor-TAP** a deflection angle of 7.9° was

found, which is larger than in the parent **TIPS-TAP** (7.0°) (**Figure 88b**).[130] **Nor-PEN**, on the other hand, exhibits an almost planar molecular structure and the silyl ethynyl group is only bend out of the molecular plane by 3.2°, which is smaller than the deflection angle found in **TIPS-PEN** (6.0°) (**Figure 88a**).[77] The energetic strain and large deflection angles empirically affect the film formation and domain size upon deposition of the materials from solution.
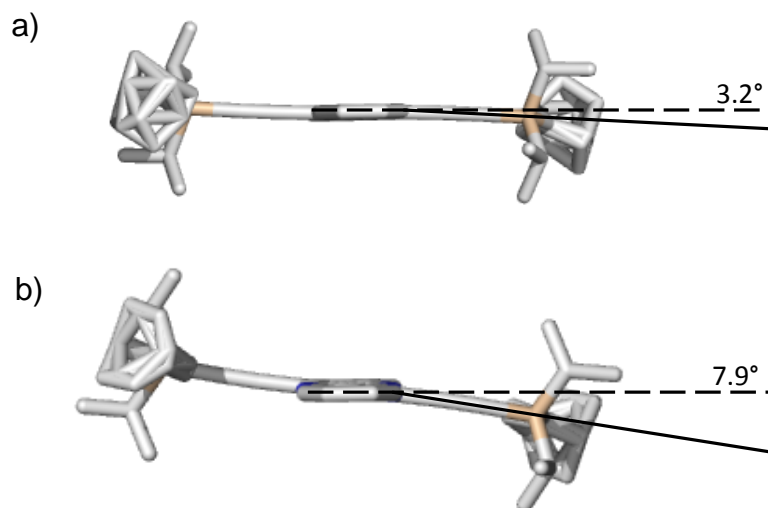

Figure 88. View along the molecule's π-systems representing the deflection angle of the ethynyl side groups out of the molecular plane for (a) **Nor-PEN** and (b) **Nor-TAP**.

The modified arrangement and relative orientation of the acene cores in the solid state will affect the charge transport properties of **Nor-PEN** and **Nor-TAP** in comparison to their parent TIPS ethynyl derivative. The transfer integrals for each molecular packing were calculated by Manuel Schaffroth and are presented in **Table 15**.[165] The quantum chemical calculations in the gas phase showed that the introduction of the norbornadienyl substituent into the side group of the acene body does not affect the position of the highest occupied and lowest unoccupied molecular orbital for the isolated molecule (**Table 15**). In addition, the calculations showed that the size of the optical gap remained unaffected. The calculations of the transfer integrals for the HOMO-HOMO and LUMO-LUMO couplings take into account that the symmetry of the crystals structure exhibits two interactions of the π-systems to neighbouring molecules which are schematically highlighted in **Figure 89**. The theoretical calculations showed that the introduction of the norbornadienyl substituents resulted in a significant improvement of the HOMO-HOMO transfer integrals for pentacene, while in parallel the transfer integrals for the LUMO-LUMO interaction are reduced as compared to the parent **TIPS-PEN**. In case of the tetraazapentacene derivative the dominating LUMO-LUMO is reduced for **Nor-TAP**, suggesting, that the electron transport is less efficient as compared to **TIPS-TAP** (**Table 15**).

Table 15. Summarised molecular orbital energies and calculated transfer integrals for **Nor-PEN**, **Nor-TAP** and **TIPS-PEN** and **TIPS-TAP**. [Table adopted with permission from Ref. [165] and Ref. [178], Copyright 2016, Elsevier]

| compound | HOMO DFT [eV] | LUMO DFT [eV] | opt. gap DFT [eV] | transfer integrals[a] | | | |
| | | | | HOMO-HOMO | | LUMO-LUMO | |
				large overlap [meV]	small overlap [meV]	large overlap [meV]	small overlap [meV]
TIPS-PEN[b]	-4.92	-3.02	1.9	38.0	0.4	223.3	105.2
Nor-PEN	-4.94	-3.04	1.9	76.3	6.7	67.5	51.3
TIPS-TAP[c]	-5.61	-3.78	1.83	13.2	3.1	184.4	62.6
Nor-TAP	-5.64	-3.82	1.83	50.2	3.9	106.0	13.0

[a] see Ref. [165] and Ref. [178] for method [b] based on crystal structure from *Anthony et al.*[77] [c] based on crystal structure from S. Miao *et al.*[130]
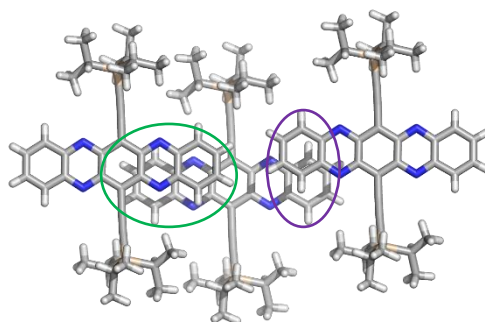
Figure 89. Molecular overlap of a **TIPS-TAP** molecule (centre) to its neighbouring molecules. The green circle highlights the large overlap and violet the small overlap of the aromatic systems, respectively. [Figure adopted with permission from Ref. [165] and Ref. [178], Copyright 2016, Elsevier]

8.3.   Optical and Electronic Properties in the Solid State

To further confirm that the substitution with norbornadienyl at the silyl group does not affect the electronic properties of the pentacene and tetraazapentacene core in thin films ultra-violet photoemission spectroscopy was performed. The long wavelength absorption edge of **Nor-PEN** and **Nor-TAP** in thin films was used to calculate the accurate position of the LUMO in the solid state. The findings were correlated to the optical properties and the results obtained from cyclic voltammetry measurements in solution. The position of the absorption maximum and the vibrionic structure of the pentacene and tetraazapentacene core in solution was not affected by the introduction of the norbornadienyl modification as can be seen in **Table 16** and **Figure 90**. Once applied in thin films, the absorption spectra of the TIPS derivatives **TIPS-PEN** and **TIPS-TAP** are broadened and red shifted, while in the case of **Nor-PEN** and **Nor-TAP** a similar red shift and only a mild broadening is observed (**Figure 90**). For both **Nor-PEN** and **Nor-TAP** the optical gap in thin films is approximately 0.1 eV larger, compared to their corresponding TIPS-derivative (**Table 16**). These observations indicate that **Nor-PEN** and **Nor-TAP** exhibit a slightly weaker interaction of the π-systems in the solid state.

Table 16. Optical and electronic properties of the norbornadienyl substituted pentacene and tetraazapentacene and **TIPS-PEN** and **TIPS-TAP** for comparison. [Table adopted with permission from Ref. [178], Copyright 2016, Elsevier]

compound	absorption λ_{max} solution [nm]	emission λ_{max} solution [nm]	Stokes shift [cm^{-1}]	absorption λ_{onset} film opt. gap [nm] / [eV]	HOMO CV [eV]	LUMO CV [eV]	HOMO film UPS [eV]	LUMO Film [eV]
TIPS-PEN	642[179]	651[179]	215	750 / 1.65[a]	-5.1[179]	-3.4[179]	**-5.05**	3.4[c]
Nor-PEN	643	654	262	725 / 1.71[a]	-5.2[b]	-3.3[b]	**-5.05**	-3.3[c]
TIPS-TAP	679	-	-	770 / 1.61[a]	-5.75[21]	-4.0[21]	-6.05	**-4.45[c]**
Nor-TAP	678	-	-	725 / 1.71[a]	-	-4.4[b]	-6.1	**-4.4[c]**

[a] optical gap film calculated from the onset of the absorption (see **Figure 90**) [b] in DCM, Au electrode, ferrocene (Fc) as external reference with a reference potential of Fc/Fc+ = 5.1 eV[180] [c] LUMO energy calculated based on the HOMO measured by UPS + optical gap film.
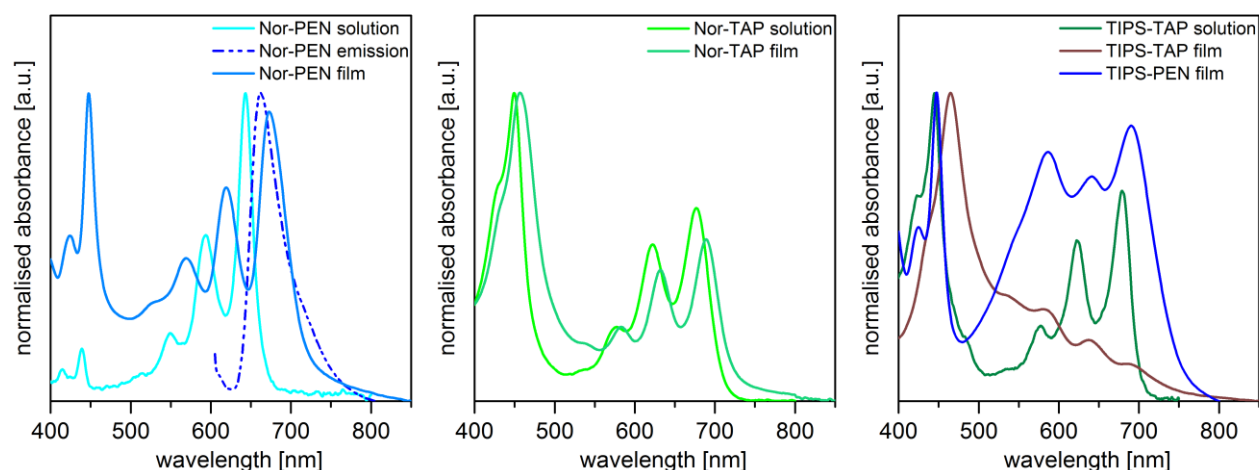
Figure 90. Absorption, emission and film absorption spectra of **Nor-PEN** (left), **Nor-TAP** (middle), **TIPS-TAP** and **TIPS-PEN** (right). (Spectra for **Nor-PEN**, **Nor-TAP** adopted from Ref. [147]).

The determination of the HOMO and LUMO level from thin film spectra of all four derivatives shows the expected effect (**Figure 91**): the energetic position of the highest occupied molecular orbital of the norbornadienyl compounds are – within the resolution of the measurement – identical to the ones of the corresponding TIPS-substituted compound. However, the position of the HOMO and LUMO level for the tetraazapentacenes was found to be significantly deeper than expected from the cyclic voltammetry experiment, due to intermolecular interactions in thin films. The UPS results highlight the low injection barrier for the injection of electrons from gold into the tetraazapentacenes due to a deep LUMO of 4.4 eV and a good hole injection into the HOMO of **TIPS-PEN** and **Nor-PEN**.
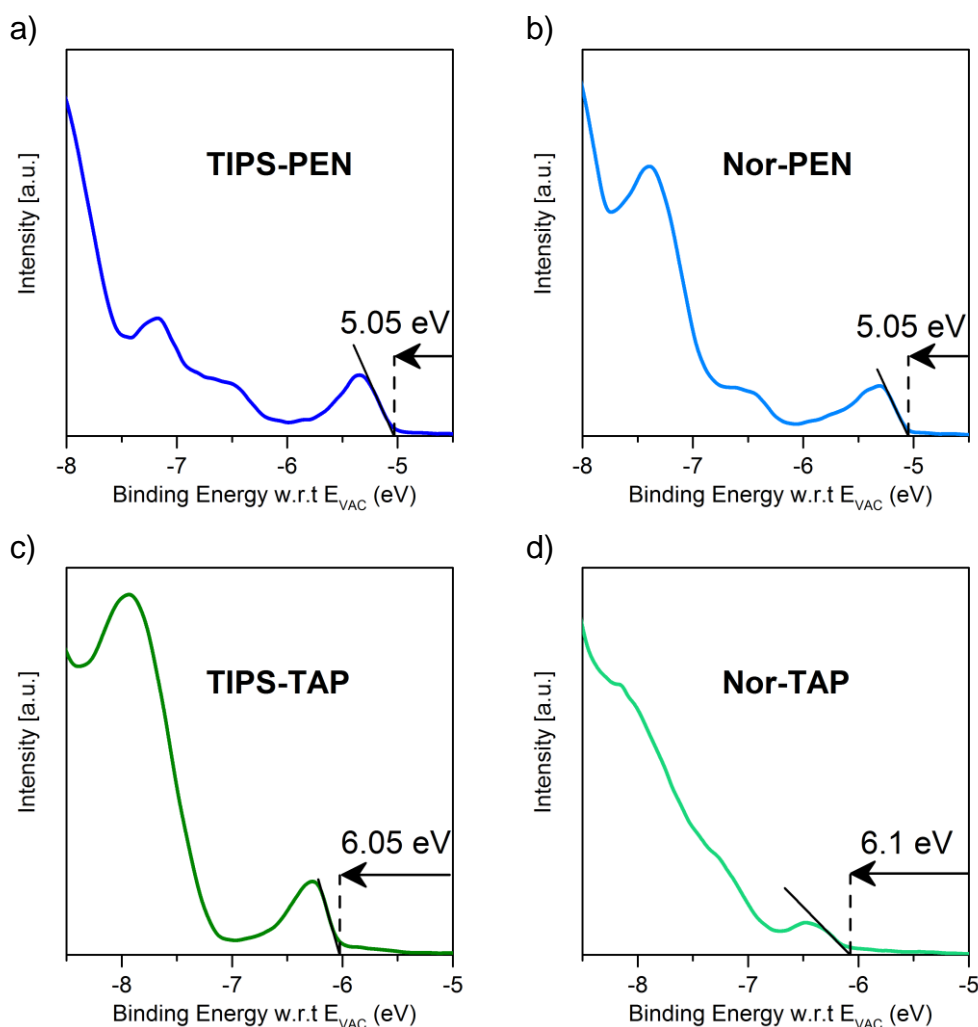
Figure 91. Ultra violet photoemission spectra of the low binding energy edge of thin films of (a) **TIPS-PEN**; (b) **Nor-PEN**, (c) **TIPS-TAP** and (d) **Nor-TAP**. [adopted with permission from Ref. [178], Copyright 2016, Elsevier]

8.4.   Morphology and Microstructure of Nor-PEN and Nor-TAP films

The microstructure of the norbornadienyl compounds was investigated by optical and atomic force microscopy and the molecular orientation was probed by X-ray diffraction measurements. Films were deposited by spin-coating from toluene on polyimide coated substrates that provided an excellent wettability for the formation of homogeneous crystalline films. Compared to a small grain size of ca. 10 nm for **TIPS-PEN** the norbornadienyl pentacene **Nor-PEN** exhibited a larger size of the crystallites for identically prepared films. The domains reached a size between 50-60 nm and appeared feather like under the polarised microscope. The opposite effect is visible for the tetraazapentacene. While spin-coated films of **TIPS-TAP** exhibited a spherulitic growth with a spherulite diameter in the range of 20-60 nm the films of **Nor-TAP** showed a dramatically reduced grain size of only a few micrometres.
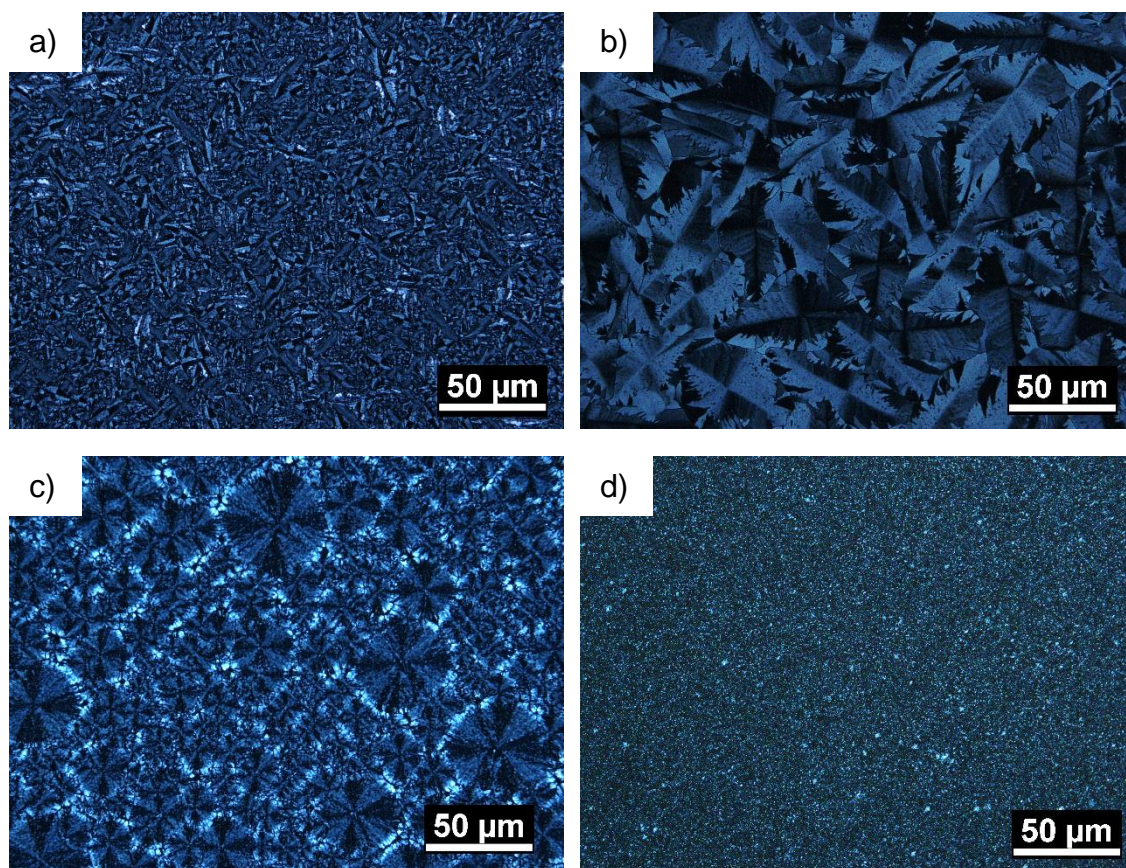
Figure 92. Optical microscope images (crossed polarisers) of the polycrystalline films of (a) **TIPS-PEN**, (b) **Nor-PEN**, (c) **TIPS-TAP** and (d) **Nor-TAP** deposited from toluene solution on polyimide coated glass substrates. [Figure reproduced with permission from Ref. [178], Copyright 2016, Elsevier]

Atomic force microscopy images reveal the small grains of **Nor-TAP**, and the homogenous size distribution and coverage. The measurement revealed for **Nor-PEN** that the feather like structures visible under the polarised microscope originate from similarly oriented grains rather than feather-shaped crystalline plates (**Figure 93**). The rms-roughness for films deposited by toluene was below 3 nm for both derivatives.
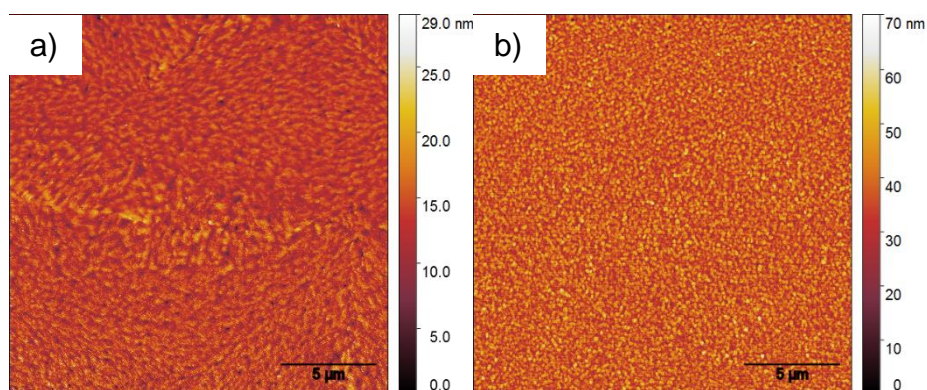
Figure 93. Atomic force microscopy (height images; 20x20 μm²) of polycrystalline films for (a) **Nor-PEN** and (b) **Nor-TAP**. [Figure reproduced with permission from Ref. [178], Copyright 2016, Elsevier]

For an efficient charge transport in thin film transistors the π-stacking should preferably occur along the substrate's surface. The XRD-patterns of the polycrystalline films of **Nor-PEN** and **Nor-TAP** are shown in **Figure**

94a. The diffraction pattern of a **Nor-TAP** film is in good agreement with the observations made by optical and atomic force microscopy. The very low intensity and broad character of the reflexes indicated a poorly organised and poorly crystalline film with small domains of **Nor-TAP**. Using the structural parameters of the **Nor-TAP** single crystal analysis, a powder diffraction pattern was calculated assuming a (001)-orientation. While the positions of the reflexes obtained from the x-ray diffraction on the films roughly coincide with the predicted diffraction angles, the relative intensities do not correlate. The disorder of the norbornadienyl group in the solid state might be responsible for the too low intensities of the diffraction measurement. Nevertheless, the similarity of the measured layer spacing of d = 16.3 Å with that resulting from the theoretical value $d_{(001)}$ = 16.6 Å obtained from the simulated powder diffraction pattern, suggests that **Nor-TAP** exhibits a (001)-orientation with respect to the substrate's surface. Further investigation of the solid state packing of **Nor-TAP** in polycrystalline films is required. Films of **Nor-PEN** exhibit two sets of higher order Bragg-reflection series (**Figure 94b**). Using the crystal structure of **Nor-PEN,** the observed diffraction pattern can be understood as a mixture of a (101)- and a (001)-orientation with calculated d-spacing values of 6.06 Å and 17.40 Å, respectively. The extracted layer distances from the XRD measurements of $d_{(101)}$= 6.07 Å and $d_{(001)}$= 17.30 Å coincide very well with the predicted values. Compared to **TIPS-PEN** and **TIPS-TAP** which show a strong (001)-orientation in spin-coated films **Nor-PEN** does not exhibit such a preferred orientation which might perturb the charge transport in these films.
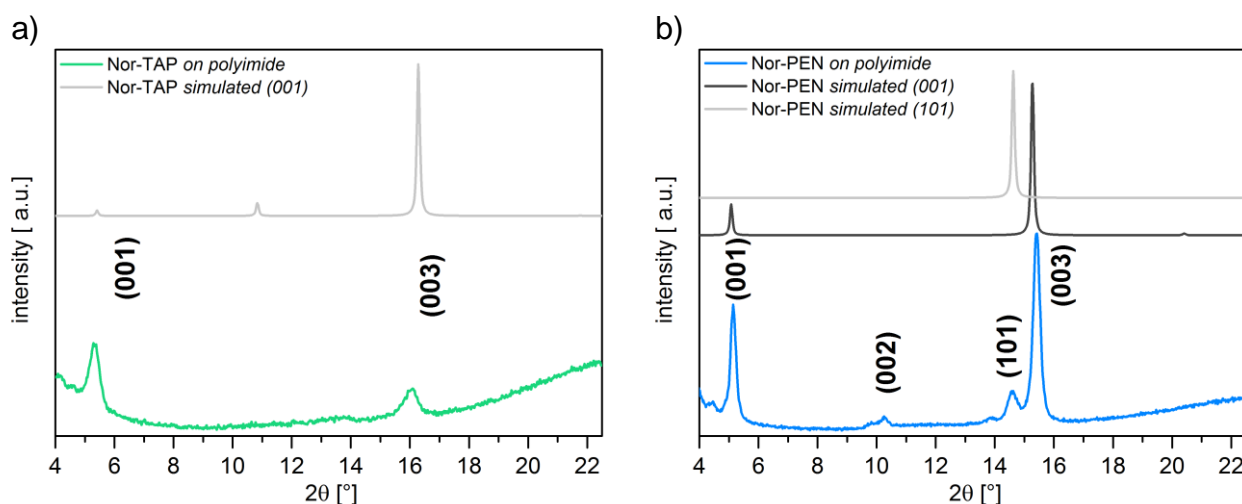

Figure 94. X-ray diffraction pattern of spin-coated films of (a) **Nor-TAP** and (b) **Nor-PEN**. [Adopted with permission from Ref. [178], Copyright 2016, Elsevier]

8.5.   Thin film transistor performance of the norbornadienyl substituted acenes

To compare and evaluate the charge transport properties of **Nor-PEN** and **Nor-TAP** thin film transistors were fabricated. The bottom-contact/ top-gate architecture was chosen and for **Nor-PEN** and **TIPS-PEN** transistors the source-drain electrodes were treated with PFBT and CYTOP™ was used as dielectric layer. **Nor-TAP**

transistors utilized PMMA as dielectric, deposited by spin-coating from acetonitrile. For all transistors the active layer was spin-coated from a toluene solution. The norbornadienyl modified materials exhibited no unexpected electrical behaviour in the transistors and are comparable to those of their parent TIPS-derivative. The injection behaviour was linear, the threshold voltages were small and the hysteresis between forward to backward sweep was negligible in all fabricated devices (**Figure 95**). The performance of **Nor-TAP** was correlated to the performance of devices from **TIPS-TAP**, described earlier in **Chapter 5**. The low LUMO of **Nor-TAP** allowed an efficient injection of electrons, and compared to **TIPS-TAP,** the output characteristics exhibited a linear behaviour at low drain voltages: probably due to the differences in film morphology. The electron mobility extracted in the saturation regime for **Nor-TAP** devices was one order of magnitude lower compared to devices from **TIPS-TAP** deposited from the same solvent (**Table 17**).
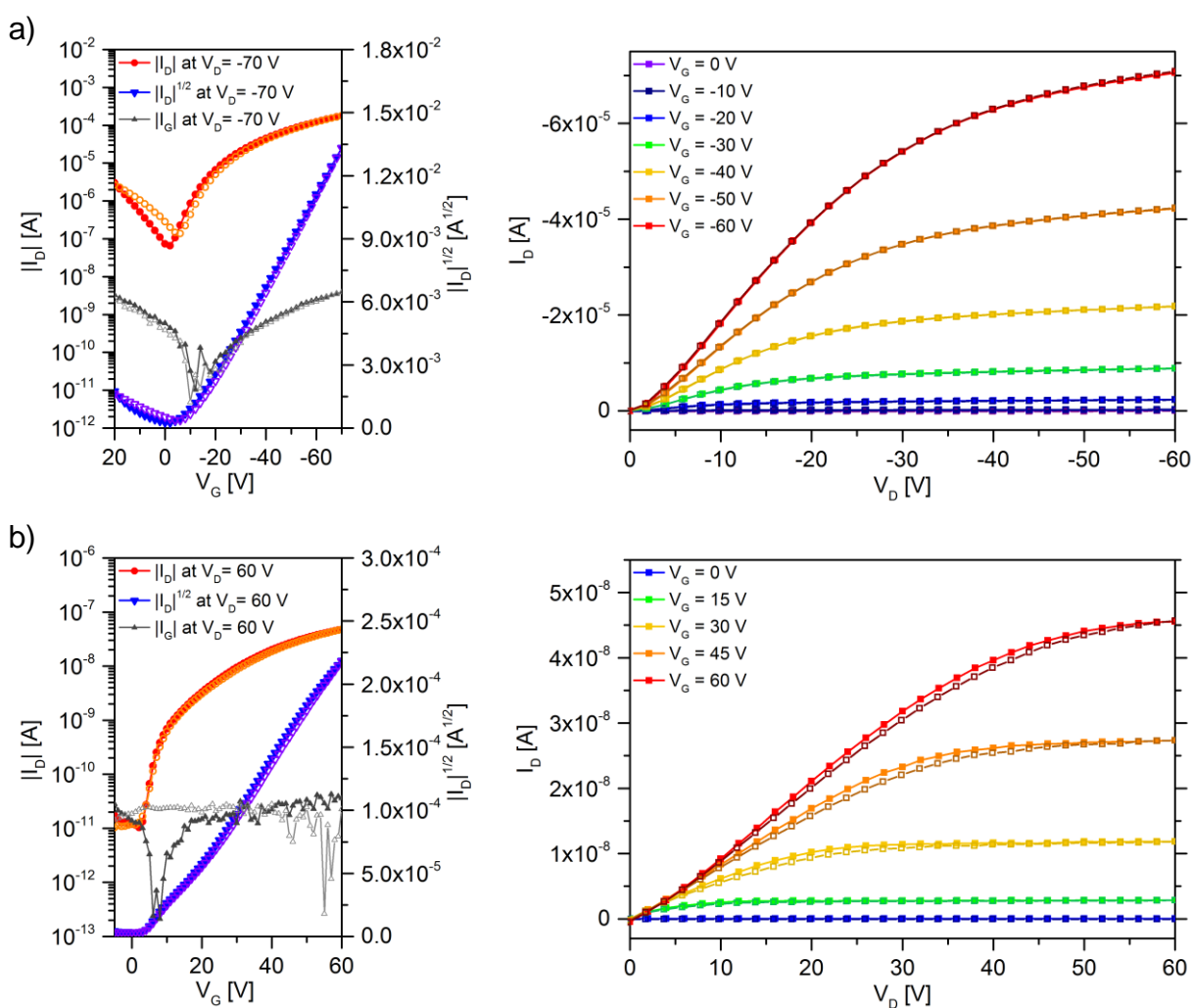

Figure 95. Field-effect transistor characteristics (transfer left; output right panel) of (a) **Nor-PEN** transistor and (b) **Nor-TAP** spun from toluene in bottom-contact/ top-gate architecture (all W = 1,000 μm; L = 20 μm). [Adopted with permission from Ref. [178], Copyright 2016, Elsevier]

The highest charge carrier mobility reached only $3.5 \cdot 10^{-4}$ cm^2/Vs, while the threshold voltages and on/off-ratios of these devices were comparable to that of **TIPS-TAP**. This lower performance might be a direct

consequence of the reduced transfer integrals for electron transport in the solid state packing of **Nor-TAP** and the poor morphology of its thin films. The combination of both effects resulted in a reduced transistor performance and lower charge carrier mobilities. Devices from **Nor-PEN** exhibit significantly higher channel currents and the extracted hole mobilities are on average higher than those found for **TIPS-PEN** when deposited from the same solvent. The threshold voltage of the **Nor-PEN** devices is slightly higher than those observed for **TIPS-PEN**. The highest hole mobility found for **Nor-PEN** in the feather like crystallisation was 0.75 cm^2/Vs. The on-off ratio in these devices was not determined as the devices exhibited a weak ambipolar behaviour (**Figure 95**). The high performance of **Nor-PEN** in thin film transistors is attributed to the improved morphology and larger domain sizes of the spin-coated films and the larger transfer integrals for holes in this material. However, it is surprising that the observed mixture of orientations for polycrystalline films of **Nor-PEN** results in such a good FET performance.

Table 17. Summarised FET-parameters for thin film transistors of **Nor-PEN**, **Nor-TAP** and their parent TIPS-derivative spin-coated from toluene in bottom-contact/ top-gate architecture. Average values and standard errors are given. For the on/off ratio the range of the fabricated devices is reported. [Adopted with permission from Ref. [178], Copyright 2016, Elsevier]

material	contact material	major charge carrier	average mobility μ_{sat} [cm^2/Vs]	best mobility μ_{sat} [cm^2/Vs]	average threshold V_{th} [V]	range on/off ratio [ ]
TIPS-PEN	Au/ PFBT	holes	0.18±0.02	0.32	4.7±1.4	10^3-10^4
Nor-PEN	Au/ PFBT	holes	0.57±0.10	0.75	-9.6±0.3	n.a.
TIPS-TAP	Au	electrons	(2.7±0.5)·10^{-3}	0.005	4.8±3.4	10^3-10^4
Nor-TAP	Au	electrons	(2.2±0.4)·10^{-4}	3.5·10^{-4}	6.1±0.6	10^3-10^4
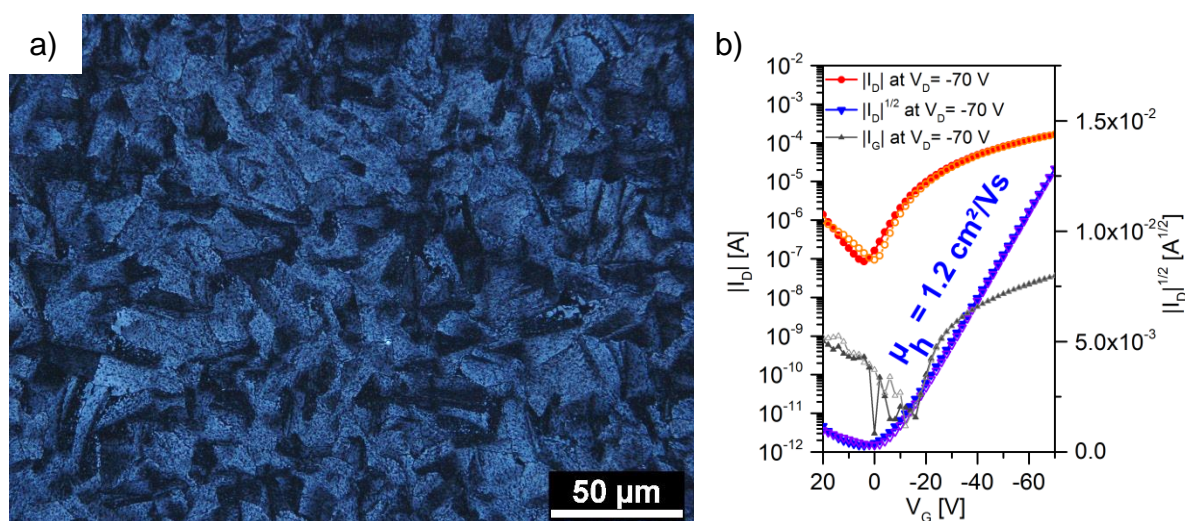
Figure 96. (a) Optical microscope image (crossed polarisers) of a **Nor-PEN** film spun from chlorobenzene solution and (b) transfer characteristic of a transistor with such an active layer.

To further boost the hole mobility in thin film transistors of **Nor-PEN** films from chlorobenzene which exhibits a slightly higher boiling point were deposited and used as the active layer (**Figure 96a**). The domains of

Nor-PEN resulting from the slower evaporating solvent were not larger, but showed rather straighter edges than the feather-like structures observed previously for the deposition from toluene (compare **Figure 92b**). The average hole mobility improved to (0.84±0.07) cm^2/Vs and a low average threshold voltage of -(5.9±0.3) V was found, identical to the one observed for toluene. The maximal hole mobility for **Nor-PEN** spin-coated from chlorobenzene reached up to 1.22 cm^2/Vs and is comparable to high-performance devices of polycrystalline **TIPS-PEN** that were fabricated by drop-casting or from tetralin solution (**Figure 96b**).[29,82,155]

8.6.   Conclusion

These results demonstrate that the substitution with norbornadienyl at the side chain of the aromatic system does not affect the optical and electronic properties of pentacene and the corresponding tetraazapentacene. However, the charge transport properties and resulting microstructures in thin films are affected upon modification of the side chain. The azaacene **Nor-TAP** exhibits an identical low LUMO of -4.4 eV to that of **TIPS-TAP** and acts as electron transporting semiconductor in thin films transistors. The lower performance with electron mobilities in the range of 10^{-4} cm^2/Vs can be attributed to the reduced transfer integrals for an electron transport in the solid state of **Nor-TAP** and its reduced grain size in thin films. Film formation by spin-coating results in poorly organised and semi crystalline films with small domain sizes that do not allow an efficient charge transport. The **Nor-PEN** molecules are less strained in the solid state packing and the polycrystalline films exhibit a larger domain size compared to identically prepared **TIPS-PEN** films. Furthermore, the slightly better molecular overlap in the packed state results in higher transfer integrals for the hole transport and an improved performance of **Nor-PEN** in organic field-effect transistors with an average mobility of 0.57 cm^2/Vs as compared to **TIPS-PEN**. This study shows that the fine-tuning and engineering of side chains can lead to higher transistor performances and better film morphologies, creating a large potential for further improvement of electron transporting N-heteroacenes.

Chapter 9

Summary and Outlook

This chapter summarises the most important results obtained in this work. Future directions for investigation are proposed as the most promising and interesting routes to continue this field of research.

9.1.   Summary

The key goal of this work was to investigate the charge transport properties of novel acene based small molecules and non-conjugated pentacene-based polymers. The rational design of these compounds and the powerful synthetic tools developed in the recent years, such as palladium cross-coupling reactions allowed the creation of these N-heteroacenes with the desired optical, electronic and solid state properties. In this work, both hole and electron charge transport properties in acene structures were investigated in order to demonstrate the versatility of these materials and to derive structure function relationships to serve as guidelines for future synthesis of N-heteroacenes. The synthetic flexibility of this family of compounds allows tailoring of their optoelectronic and morphological properties for future applications.

Hole charge transport was investigated in two different approaches for synthesis of acene-based semiconductors. First, charge transport in non-conjugated polymers, incorporating 6,13-substituted pentacene units was studied. Five differently structured polymers were characterised to understand their structural and electronic properties in relation to their performance in field-effect transistors (FETs). The polymers offer an ease of processibility, which is unavailable to pentacene-based small molecules. Four out of five polymers resulted in functioning FETs (**Figure 97**).
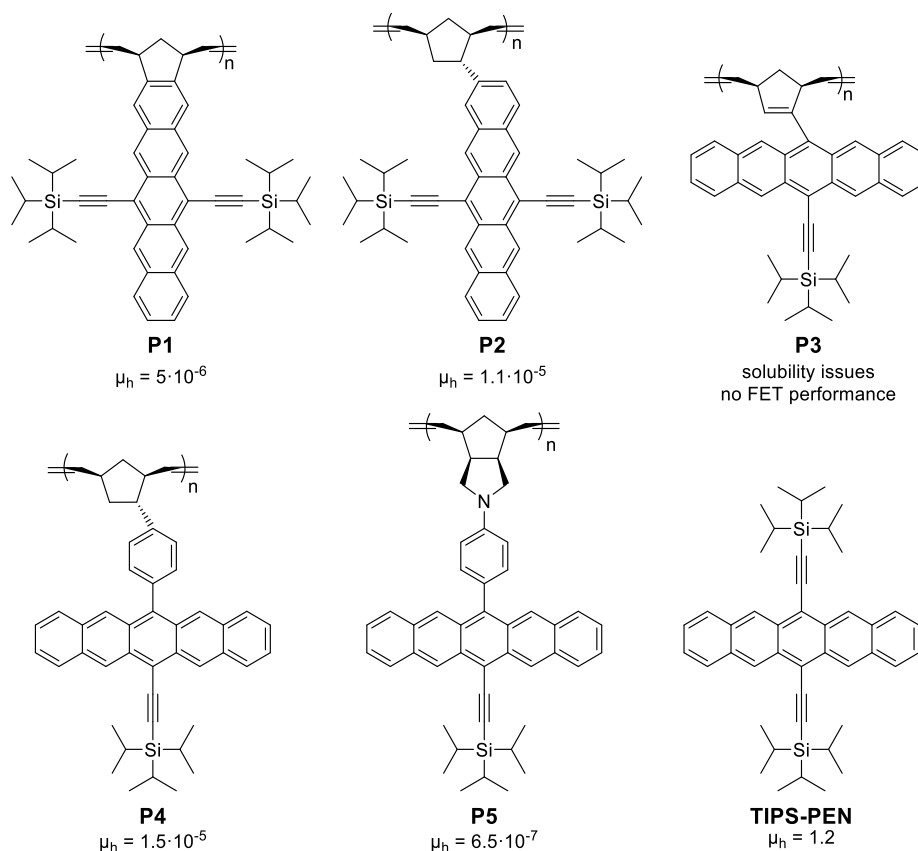
Figure 97. Molecular structures of the investigated non-conjugated pentacene-based polymers **P1**-**P5** and **TIPS-PEN** with the corresponding hole mobilities obatined in this study.

Disappointingly, the extracted hole mobilities were significantly lower than that of **TIPS-PEN**, but comparable to previously reported conjugated pentacene-based polymers. The inferior performance of these polymers is related to their amorphous nature and the lack of solid state interactions of the acene cores.

Hole conduction was also investigated in three consanguine *N,N'*-Dihydrotetraazapentacene (DHTA) compounds. Processing conditions, such as the choice of solvent, had a pronounced effect on the performance of these materials in field-effect transistors. The changes in performance was correlated to changes in film microstructure, as summarised in **Figure 98**. A wide range of mobilities was observed, depending on the molecular functionalization and the film microstructure, with a maximum hole mobility of 0.11 cm^2/Vs measured for the **DHTA-Cl$_2$** derivative, exhibiting an almost solvent independent transistor performance.
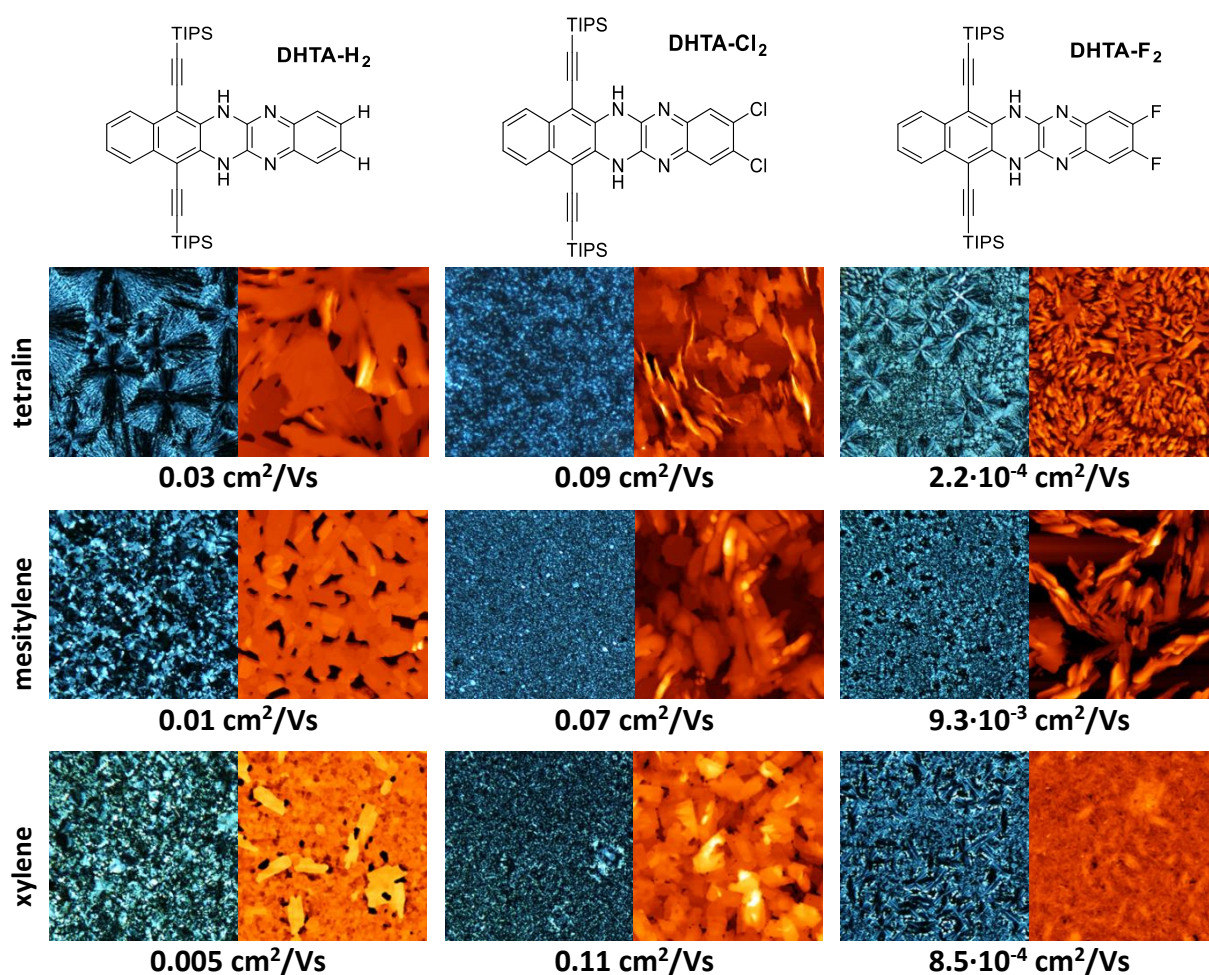
Figure 98. Microstructure of DHTA compounds (POM and AFM micrographs) based on the choice of deposition solvent and best hole mobilities are given for each material/solvent combination. [Based on Ref [169] - Reproduced by permission of The Royal Society of Chemistry].

Hole transport was also observed for larger *N,N'*-Dihydroazaacenes such as **NH-Hex** and **NH-Hep** and the hole mobilities reached 10^{-3} and 10^{-2} cm^2/Vs, respectively but are still lower to those observed for the *N,N'*-dihydroazapentacene derivatives.

Another key observation in the case of DHTA compounds was the appearance of polymorphism upon deposition on polyimide coated glass substrates. In all three compounds, a different solid state packing was formed during spin coating, **DHTA-F$_2$** exhibited a mixture of two different solid state phases in thin films. The thin phase and packing of **DHTA-H$_2$** could be elucidated through dissection of carefully grown crystals on polyimide. These findings illustrate that interpreting charge transport properties based on crystal structure obtained from single crystal x-ray diffraction measurements is not always possible and can be misleading.

While hole transport in N-heteroacenes demonstrates their applicability for p-channel organic field-effect transistors, it is more interesting to investigate the electron transport in these nitrogen-containing materials. As a main example for this, electron transport was investigated in depth for the **TIPS-TAP** molecule. Again the deposition procedures as well as the transistor architecture played a major role in determining the transistor performance. The charge transport properties of polycrystalline films of TIPS-TAP deposited by spin-coating were investigated and correlated to the film microstructure. The electron mobility could be enhanced from 0.005 cm^2/Vs for deposition from low boiling point solvent and small domain sizes, to the highest value of 0.31 cm^2/Vs achieved for tetralin with films exhibiting textbook spherulitic growth of millimetre size. With optimised conditions for zone casting, uniaxially aligned ribbons were obtained and resulted in a mobility of 0.42 cm^2/Vs (Figure 3).
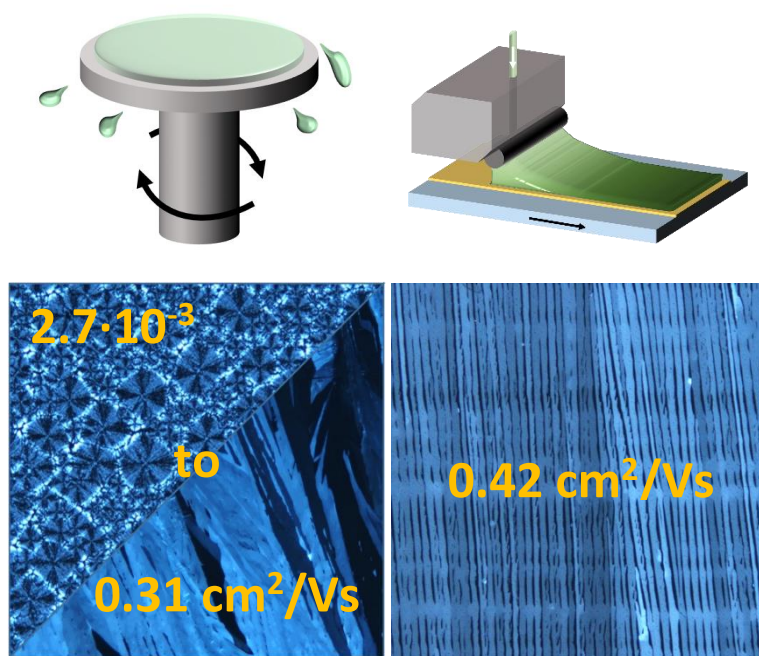

Figure 99. Illustration of **TIPS-TAP** microstructures obtained from spin-coating (left) and zone-casting (right) and the corresponding electron mobilities in BC/TG OFETs. [Partially reproduced from Ref [163] - Reproduced by permission of The Royal Society of Chemistry]

XRD and GIWAXS measurements on polycrystalline and highly aligned films of **TIPS-TAP** confirmed that the acene molecules follow a preferred (00*l*)-orientation in spin-coated films and zone-cast films independent of the choice of substrate. The gracing incidence measurements showed that the slowly deposited **TIPS-TAP**

ribbons grow along the (100)-crystal face, in agreement with observations made for the parent **TIPS-PEN**.[166,177]

The effect of bias stressing for >100 hours under various environmental conditions on charge transport of polycrystalline **TIPS-TAP** films was also investigated. As can be seen in **Figure 100**, upon 900 minutes of bias stressing in nitrogen, the extracted threshold voltage shifted to higher values due to the filling of deep traps while in parallel the extracted electron mobility increased. The process of continuous trap filling is also exemplified by the decrease in the relative hysteresis of the device.
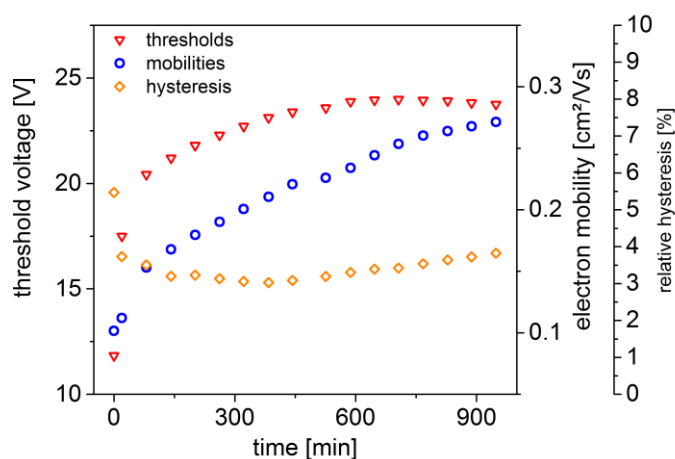
Figure 100. Evolution of the threshold voltage, electron mobility and relative hysteresis of a BG/TC **TIPS-TAP** transistor. [Reproduced from Ref [163] - Reproduced by permission of The Royal Society of Chemistry]

Altering the environmental conditions to include also oxygen and water revealed that the **TIPS-TAP** transistor is relatively stable upon exposure to oxygen, however degrades fairly quickly when the device is exposed and stressed in a water containing environment. These studies demonstrate the importance of characterising the device performance under various conditions to develop appropriate synthetic routes to resolve the environmental instability of the material.

Efficient electron transport was also observed for two halogenated phenazinothiadiazoles **Cl$_4$-Phen** and **F$_4$-Phen** shown in **Figure 101a**. The thiadiazole moiety provided the formation of supramolecular dimers that formed a brickwall-like solid state packing and resulted in high electron mobilities.
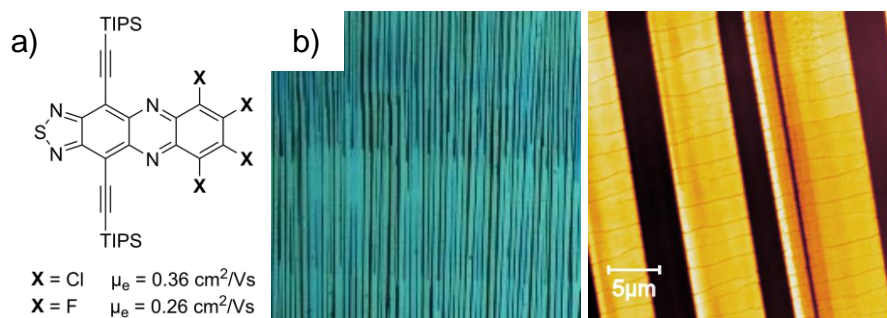
Figure 101. (a) Molecular structure of the halogenated phanazinothiadiazoles and (b) POM and AFM images of zone-cast **Cl$_4$-Phen** films.

In spin-coated transistors deposited from chlorobenzene, the chlorinated and fluorinated derivative exhibited electron mobilities of up to 0.36 and 0.26 cm^2/Vs, respectively. Although the application of the zone casting technique for **Cl$_4$-Phen** resulted in highly aligned crystalline films, further improvements in electron mobility were not observed, most likely due to the formation of micro fractures in the crystalline ribbons, hindering charge transport in long channels (**Figure 101b**). Finally, the effect of varying the side chains of **TIPS-PEN** and **TIPS-TAP** was investigated as a route to enhance the mobilities in these compounds. A substitution with norbornadienyl at the silyl atom of the side chain resulted in an altered solid state packing, while the optical and electronic properties of the π-systems of the pentacene and tetraaza pentacene remained unaffected. Interestingly, **Nor-PEN** exhibited a superior transistor performance to that of devices prepared in identical fashion from **TIPS-PEN**, while **Nor-TAP** showed a significantly poorer charge transport as compared to **TIPS-TAP** (**Figure 102**).
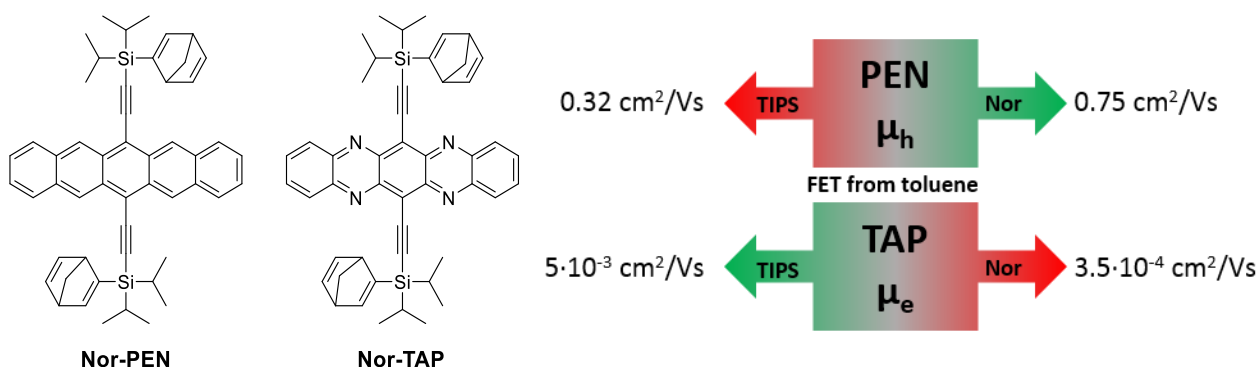

Figure 102. (a) Molecular structure of norbornadienyl substituted pentacene derivatives (b) Development of charge carrier mobility upon norbornadienyl substitution.

The enhanced hole mobility observed for **Nor-PEN** originates from the closer π-π-distance of 3.38 Å as compared to **TIPS-PEN** and the reduced energetic strain of the ethynyl group in the solid state. Furthermore, the transfer integral for holes was significantly increased. The introduction of norbornadienyl at the tetraazapentacene lowered the transfer integral for electrons and resulted in an increased energetic strain in the molecular packing and therefore a much poorer film formation with smaller domain sizes. The extracted

electron mobility values for **Nor-TAP** were consequently lower as compared to those from similarly prepared **TIPS-TAP** devices.

For all the materials investigated as part of this work, the optical and electronic properties have been measured in the solid state. These results are summarised in **Figure 103**. The electronic structure (HOMO and LUMO positions) of the material determines the injection energy barriers and is crucial for the understanding of the transistor behaviour. While the determination of energy levels is significantly easier using cyclic voltammetry (CV) or DFT calculations, the obtained values do not represent the energy levels in thin films. Looking at the LUMO level position of **TIPS-TAP** as an example, DFT calculations place it at -3.43 eV[130], CV measurements at -4.01 eV[21], while the LUMO position in thin films is actually -4.45 eV.[163]
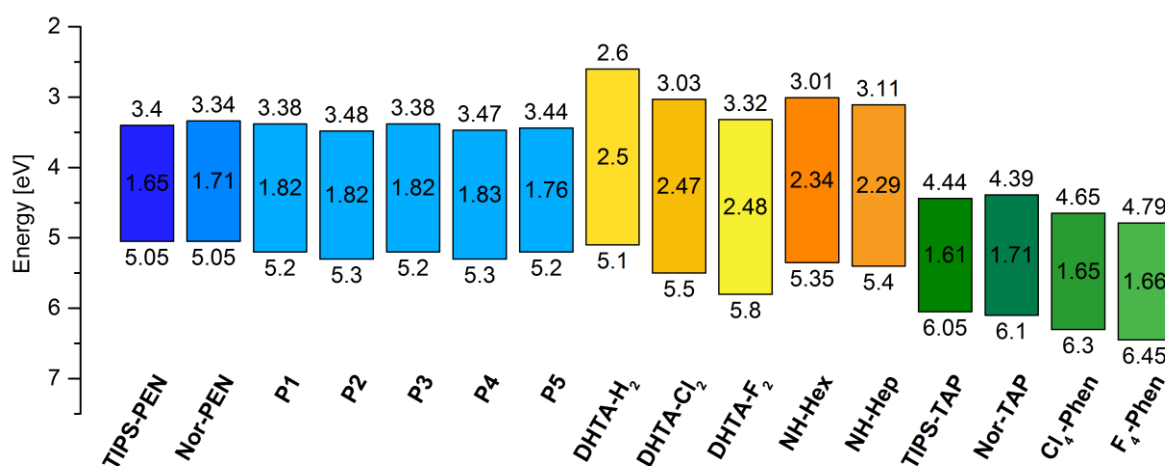
Figure 103. Summarised ionisation potentials, optical bandgaps and electron affinities in [eV] for the investigated materials in thin films as determined by UPS and UV-vis spectroscopy.
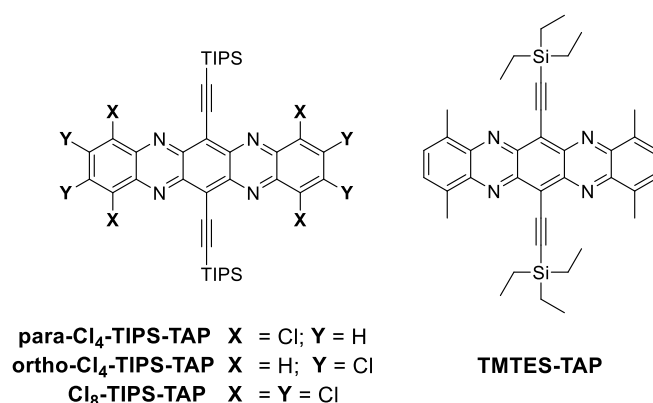
Structural characterisation of N-heteroacenes is of equal importance. All small molecules studied in this thesis were investigated using X-ray diffraction (XRD) to elucidate the molecular orientation in thin films. All ethynyl substituted pentacene derivatives and halogenated phenazinothiadiazoles provided a sharp Bragg reflex at a small diffraction angle 2θ at approximately 5-6°, which corresponds to a d_0-spacing value of 16-18 Å (**Figure 104**). Such a large value is explained by an 'edge-on' orientation of these small molecules. Most commonly the molecules exhibit a strongly preferred (00*l*)-orientation in films, independent of substrate and processing conditions, suggesting that, irrespectively of their molecular structure, the aromatic π-systems are always positioned standing on the substrate's surface. This suggests that while N-heteroacenes are suitable for efficient charge transport in the lateral direction, such as in thin film transistors, they are unlike to be of use in structures that require a vertical charge transport, such as light-emitting diodes or photovoltaic devices.
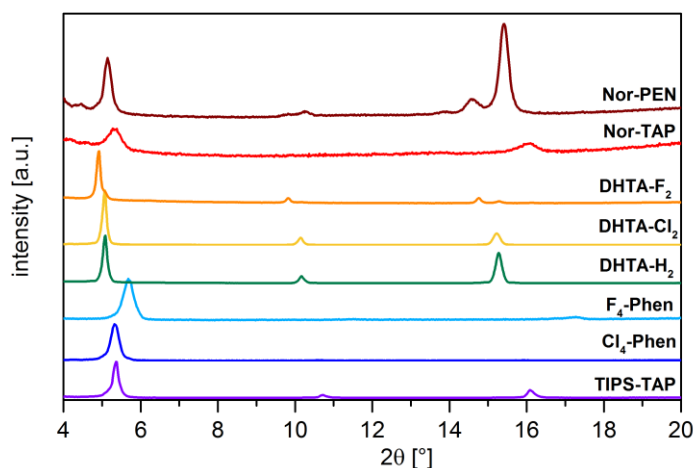
Figure 104. Representative XRD patterns of the polycrystalline films fabricated by spin-coating (from various solvents) of the investigated molecular compounds.

9.2.   Outlook

Undoubtedly N-heteroacenes are of great interest for application in field-effect transistors. Based on the studies described in this thesis, several molecular structures are particularly promising for future investigating. The film forming behaviour and charge transport properties of 2-D packed molecules is superior to other solid state packing motifs. Especially symmetrically substituted azaacenes exhibit this favourable feature as has been demonstrated by this work and recent publications on **TIPS-TAP**. The future research of N-heteroacenes should focus on the synthesis and investigation of this structural motif as suggested in **Figure 105**.

para-**Cl₄-TIPS-TAP**   X = Cl; **Y** = H
ortho-**Cl₄-TIPS-TAP** X = H; **Y** = Cl
          Cl₈-TIPS-TAP   X = **Y** = Cl   **TMTES-TAP**

Figure 105. Suggested molecular structures for future investigations of electron transport in field-effect transistors.

It should be possible to tune the optoelectronic and solid state properties in these compounds by adapting structural alterations that have been successfully implemented for **TIPS-PEN** by Anthony and others. This approach is likely to result in efficient charge transport and thus, high electron mobilities for these materials. Other synthetic directions should include further attempts of side chain engineering to enhance the LUMO-LUMO coupling of N-heteroacenes, similarly to the favourable results of norbornadienyl modified side chains

on the performance of the pentacene derivatives or the recently reported substitution with germanium in the side chain of functionalised acenes.[99,100]

Another important direction of future work is the effect of material purity on the FET performance. The reported FET performance for **TIPS-TAP** parallel to this work by Miao and co-workers significantly differs from the results reported here. It should be investigated whether low purity or unintentional doping of **TIPS-TAP** results in similar performances and is the origin of the discrepancy.

This is particularly important for electron transporting N-heteroacenes that are obtained through oxidation of the corresponding *N,N'*-dihydro compound. An incomplete oxidation or impurities will not only serve as trapping centres for charge transport, but also result in a poorer film microstructure, as they act as nucleation sites that prevent large, pure crystalline domains from forming. A subsequent reduction of N-heteroacenes has already been observed in acidic environment, even during storage of these materials in a standard lab environment and should be further investigated as the main disadvantage of N-heteroacene. In this context the environmental degradation of N-heteroacene field-effect transistors should be investigated in detail in order to develop synthetic design rules that would improve the stability of these compounds. These issues must be resolved as the first step for the integration of these compounds in any industrial applications.
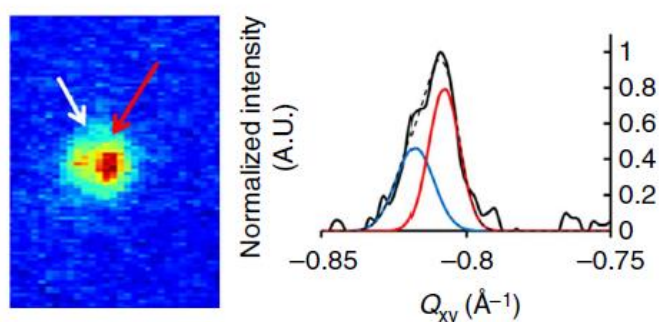
Figure 106. (left) GIWAXS diffraction map of the (0-11) Bragg reflex of sheared **TIPS-PEN** from the metastable (red arrow) and equilibrium (red arrow) solid state phases. (right) Fitted integrated peak intensity with a Gaussian contribution of the metastable (red curve) and equilibrium (blue curve) polymorph. (Adopted from Ref [177] - Copyright 2014, Nature Publishing Group.)

This work has demonstrated that the utilisation of the zone-casting deposition technique results in highly ordered and aligned crystalline films of **TIPS-TAP**. Zone-casting employed in this work focused on a slow deposition and low casting speeds to lower induced lattice strain in the deposited materials. Since polymorphism is a widely observed feature for small molecules and has been demonstrated in case of the **DHTA** compounds, future research and investigation on N-heteroacenes should focus on the solid state properties of the zone-cast films. Higher deposition speeds and temperatures, different organic solvents and substrates or shear forces during the zone-casting process might result in altered solid state packings and provide enhanced charge transport properties, as it has been reported for **TIPS-PEN**.[20,95,177] In situ GIWAXS or near-edge X-ray absorption fine-structure (NEXAFS) measurements are an appropriate tool to study these

phenomena and should be employed to reveal the molecular interaction and ordering in different solid state and metastable phases of N-heteroacenes and correlated to the performance and charge transport anisotropy in electronic devices.

Appendix

Supplementary Material

A 1 – Systemic names of structures used in this work

compound (abbreviation)	systematic name
TIPS-PEN	6,13-Bis[(tripropan-2-ylsilyl)ethynyl]pentacene
TIPS-TAP	6,13-Bis[(tripropan-2-ylsilyl)ethynyl]quinoxalino[2,3-b] phenazine
NH-Hex	7,14-Bis[(tripropan-2-ylsilyl)ethynyl]-5a,6,15,15a-tetrahydrobenzo[b]naphtho[2,3-i] phenazine
NH-Hep	6,17-Bis[(tributan-2-ylsilyl)ethynyl]-7,16-dihydrodinaphtho[2,3-b:2',3'-i] phenazine
DHTA-H$_2$	7,12-Bis(3,3-dimethylbut-1-yn-1-yl)-6,13-dihydrobenzo[g]quinoxalino[2,3-b] quinoxaline
DHTA-Cl$_2$	2,3-Dichloro-7,12-bis{[tri(propan-2-yl)silyl]ethynyl}-6,13-dihydrobenzo[g]quinoxalino [2,3-b] quinoxaline
DHTA-F$_2$	2,3-Difluoro-7,12-bis{[tri(propan-2-yl)silyl]ethynyl}-6,13-dihydrobenzo[g]quinoxalino [2,3-b] quinoxaline
Cl$_4$-Phen	6,7,8,9-Tetrachloro-4,11-bis[(tripropan-2-ylsilyl)ethynyl][1,2,5]thiadiazolo[3,4-b] phenazine
F$_4$-Phen	6,7,8,9-Tetrafluoro-4,11-bis[(tripropan-2-ylsilyl)ethynyl][1,2,5]thiadiazolo[3,4-b] phenazine
Nor-PEN	(Pentacene-6,13-diyldiethyne-2,1-diyl)bis[bicyclo[2.2.1]hepta-2,5-dien-2-yl- (dipropan-2-yl) silane]
Nor-TAP	6,13-bis{[bicyclo[2.2.1]hepta-2,5-dien-2-yl(dipropan-2-yl)silyl]ethynyl}- quinoxalino[2,3-b] phenazine

A 2 – Additional Optical microscope images

Figure 107. Optical microscopy image (almost crossed-polarisers) of a spin-cast film of **TIPS-PEN** from tetralin solution on polyimide coated glass FET-substrates with pre-structured bottom-contacts, Cytop™ dielectric and gate electrode.
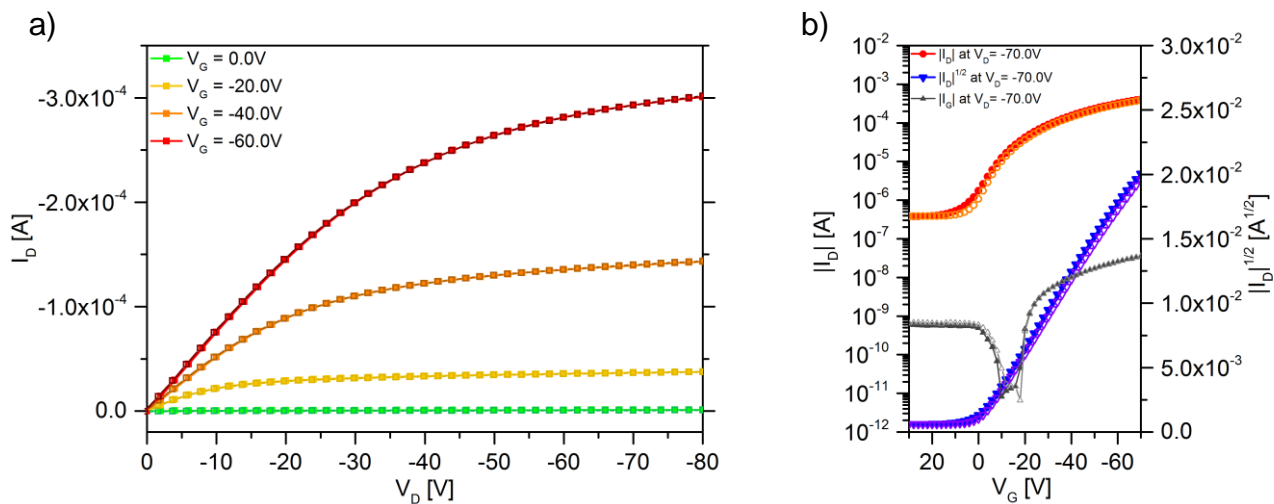

**Figure 108**. Film of **P1** under crossed-polarisers.
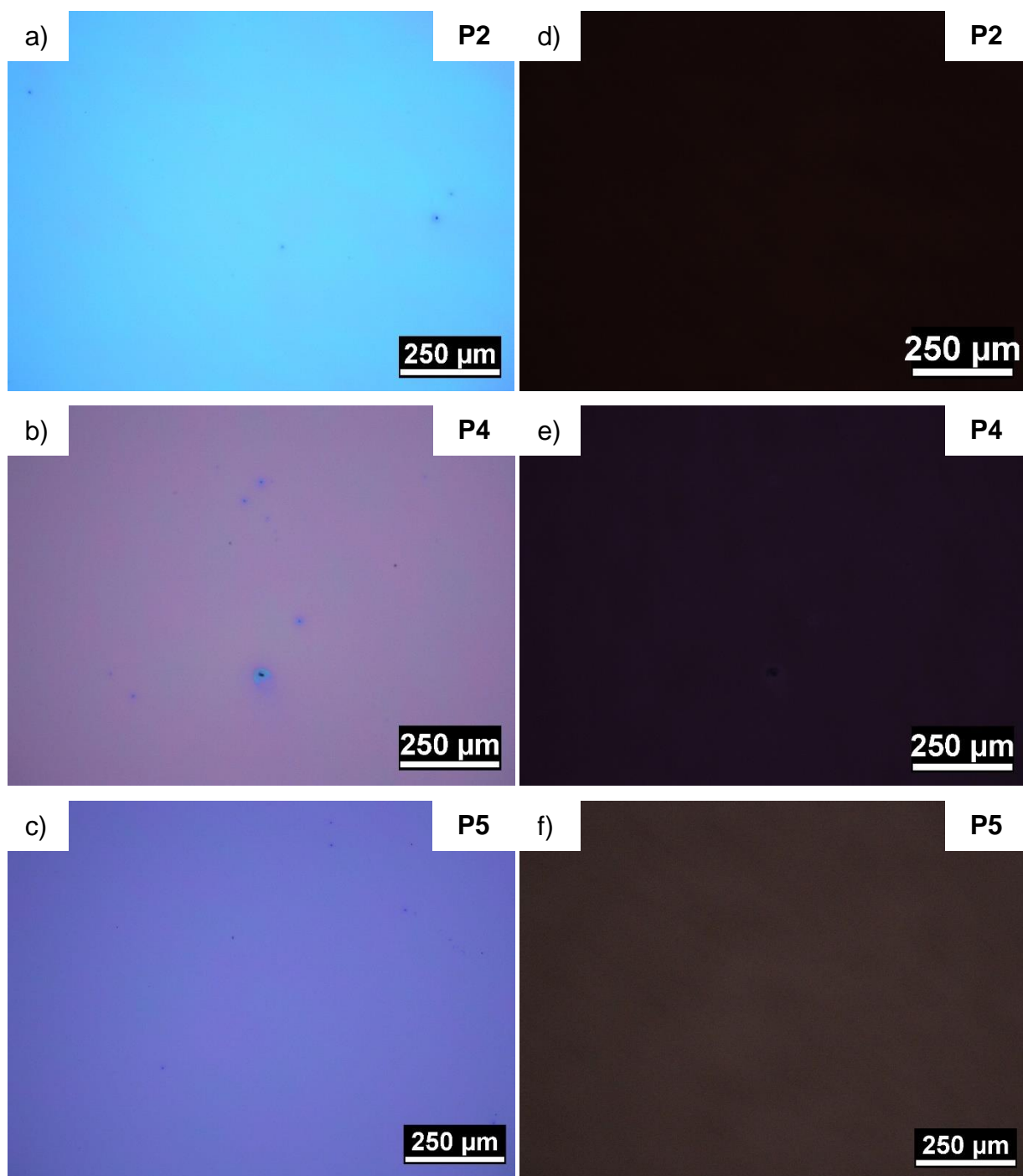
Figure 109. Optical microscope images of films of **P2**, **P4** and **P5**: (a)-(c) Bright field images and (d)-(f) under crossed polarisers.

A 2 – Additional I-V characteristics

a)

b)

Figure 110. (a) Output and (b) transfer characteristic of a **TIPS-PEN** transistor (active layer spun from tetralin) fabricated by using Cytop™ dielectric (W = 1,000 µm; L = 20 µm).

a)

b)

c)
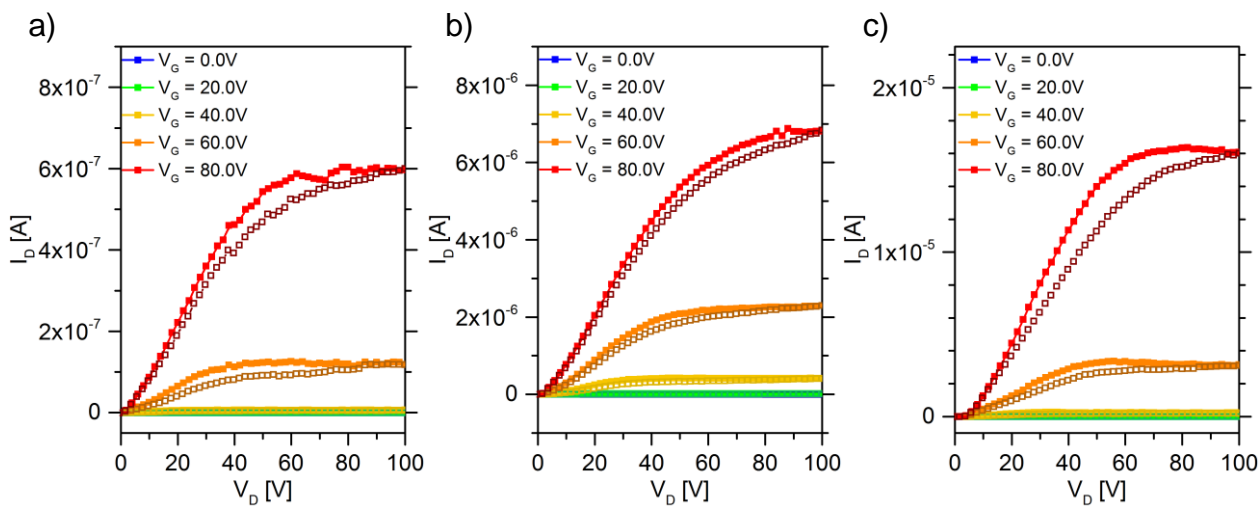
Figure 111. Output characteristics for zone-cast **TIPS-TAP** (mesitylene solution) on pre-structured bottom-contacts at (a) 80°C; (b) 100°C; (c) 120°C substrate temperature (250 µm/s) showing a non-linear contact behaviour in every case (W = 1,000 µm; L = 10 µm for (a) and 20 µm for (b)+(c)).
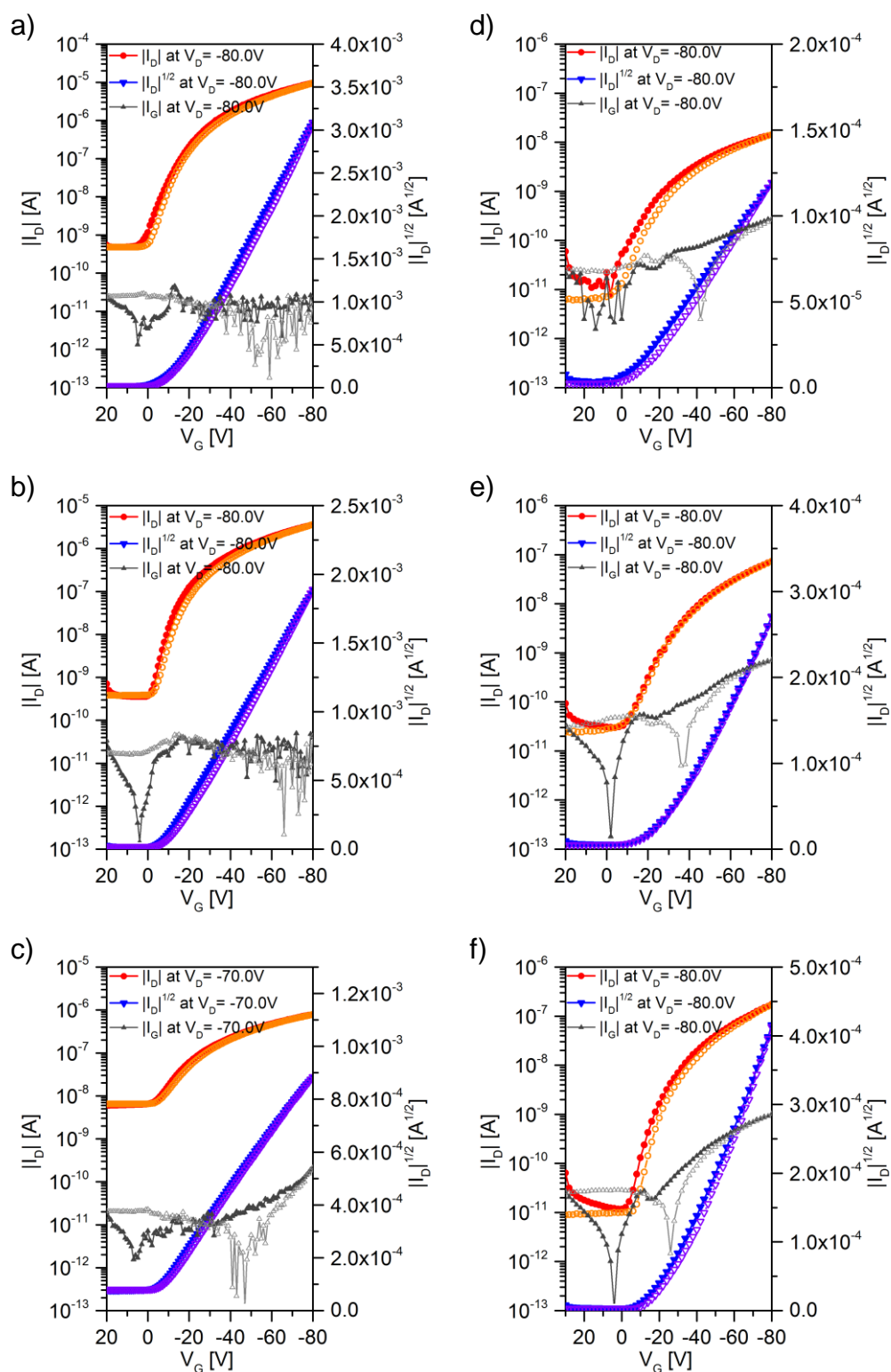
Figure 112. Representative transfer characteristics of (a)-(c) **DHTA-H₂** and (d)-(f) **DHTA-F₂** transistors with an active layers deposited from (a)+(d) tetralin, (b)+(e) mesitylene and (c)+(f) xylene.

A 3 – Assignment of (*hkl*) indices for GIWAXS measurement of TIPS-TAP films

GIWAXS Measurements were performed on a zone-cast film of **TIPS-TAP** on BCB coated Si/SiO$_2$ substrates. Casting speed was 150 µm/s and substrate temperature 120°C. **TIPS-TAP** was deposited from a mesitylene solution. Incident direction of the X-ray beam parallel (**Figure 113**) and orthogonal (**Figure 114**) to the casting direction.
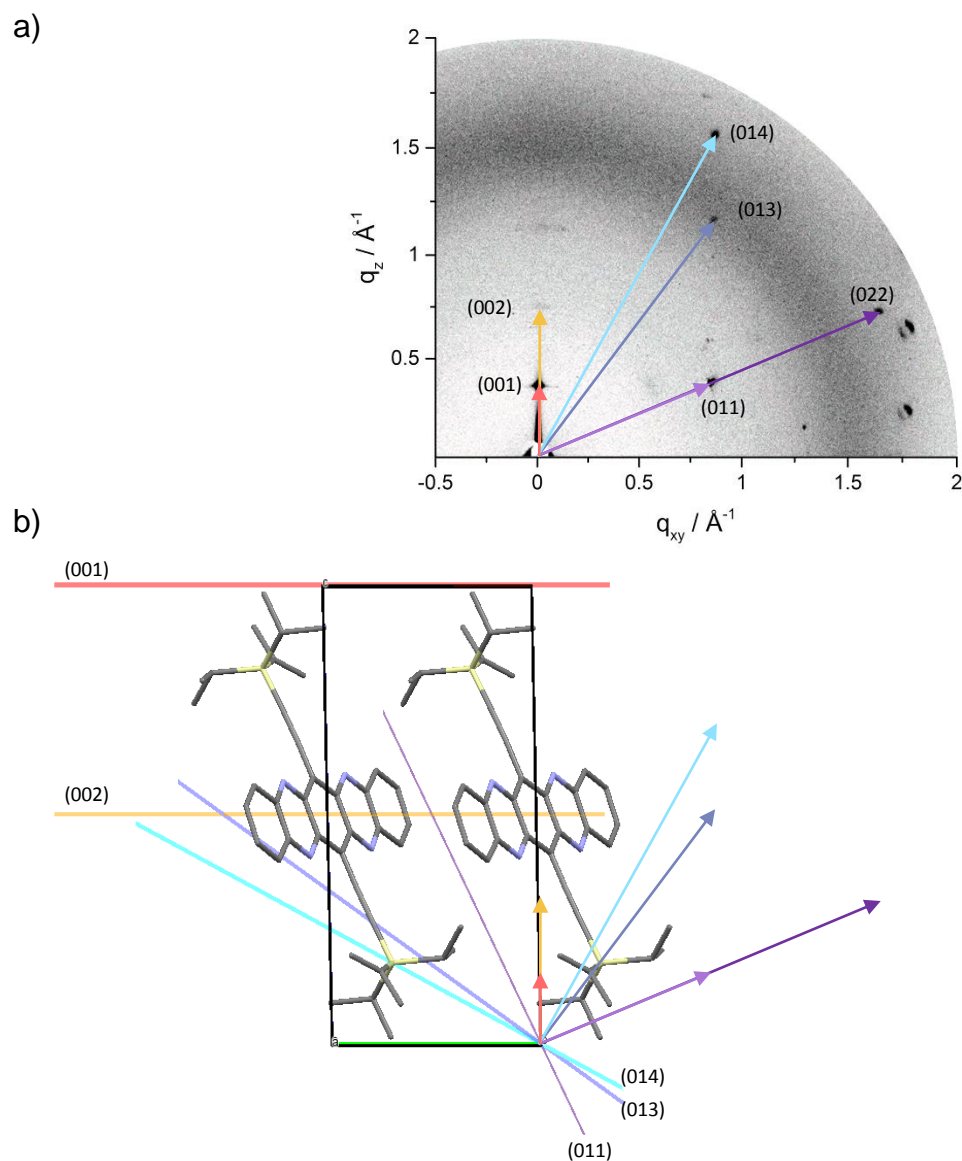
Figure 113. (a) GIWAXS diffraction map (for X-ray beam parallel to the zone-cast direction) and selected scattering vectors (coloured arrows) for selected reflections. (b) Single crystal unit cell of **TIPS-TAP** (view along a-axis) with coloured (*hkl*) Miller planes and the projected scattering vectors from (a). It is obvious that the scattering vectors are perpendicular to the indicated Miller planes. (Crystal structure based on S.Miao *et al.* from Ref. [130].)

a)

b)
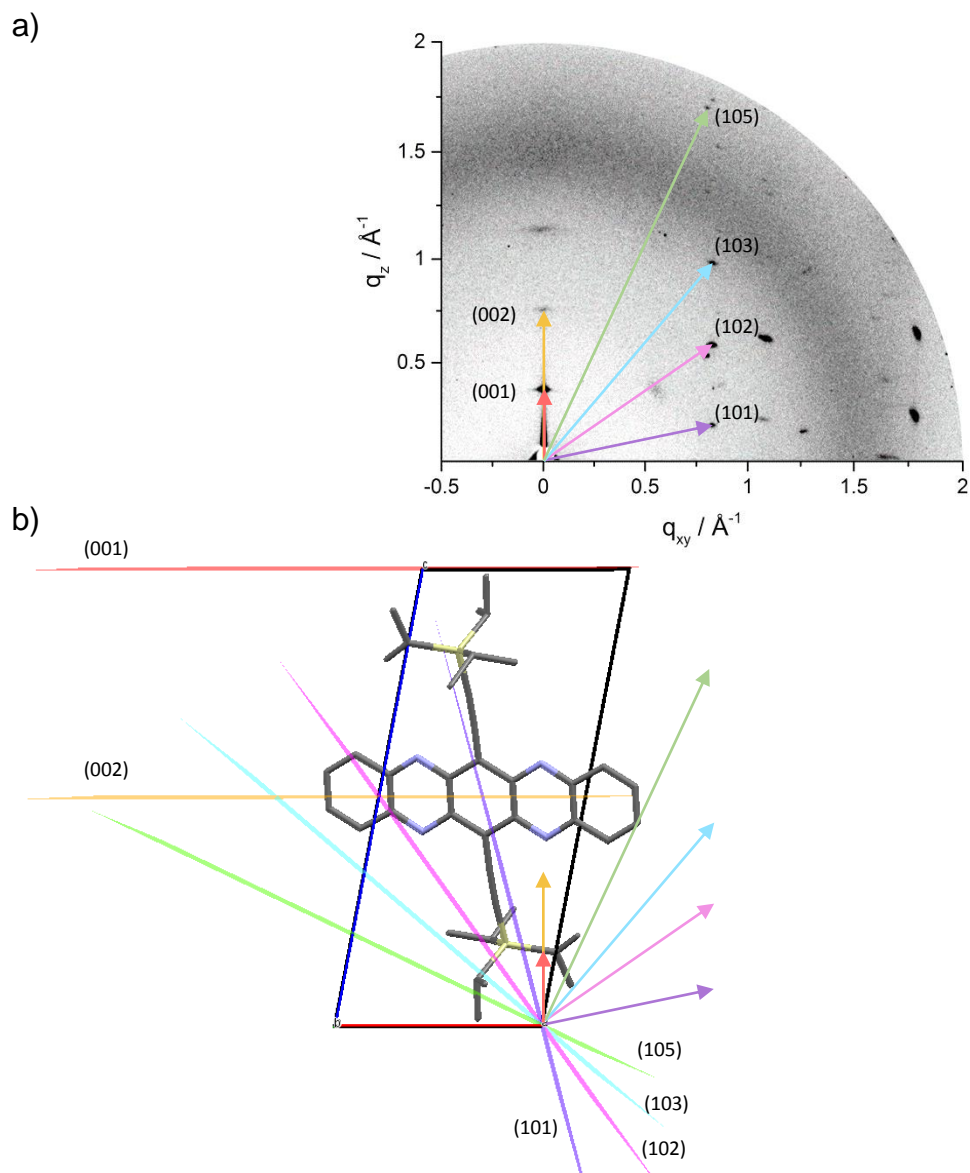
Figure 114. (a) 2-D diffraction pattern from the GIWAXS measurement with incidence perpendicular to the zone-cast direction of the **TIPS-TAP** film cast at 120°C. Coloured vectors for selected reflections are given. (b) Projection of these coloured vectors on the unit cell of **TIPS-TAP** (oriented with view along b axis). The vectors are normal vectors to the corresponding (*hkl*) Miller planes. (Crystal structure based on S.Miao *et al.* from Ref. [130].)

A 4 – I-V characteristics of TIPS-TAP OFETs during bias-stressing

All **TIPS-TAP** devices presented here are BG/TC devices (W = 1,500 µm); gold as contact material; BCB passivation; organic active layer deposited by spin-coating from mesitylene solution and patterned as described in Chapter 3. I-V characteristics of representative devices shown in this section.
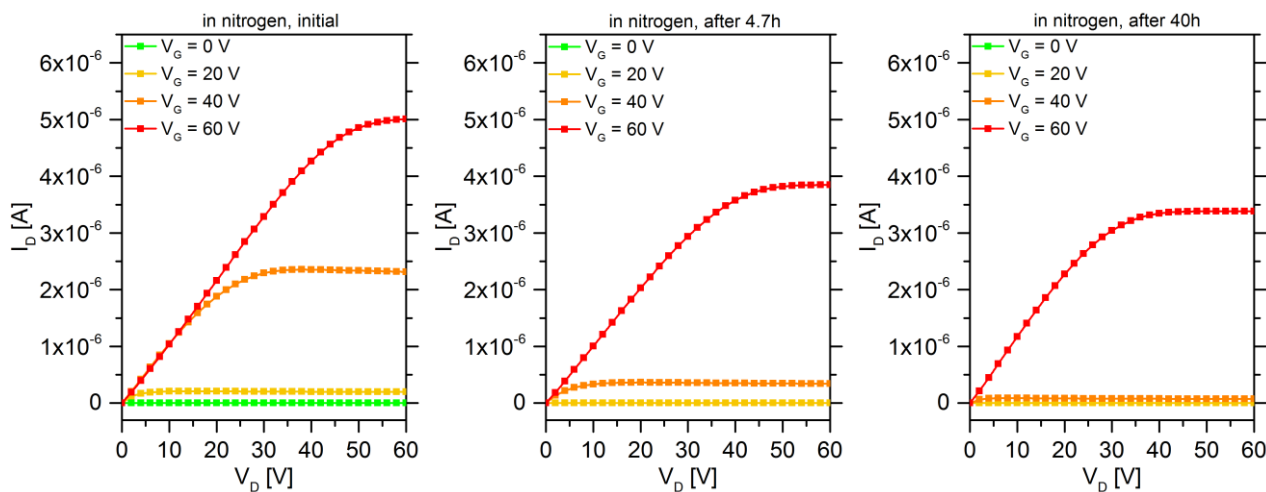
A 4.1. Bias-stressing in nitrogen
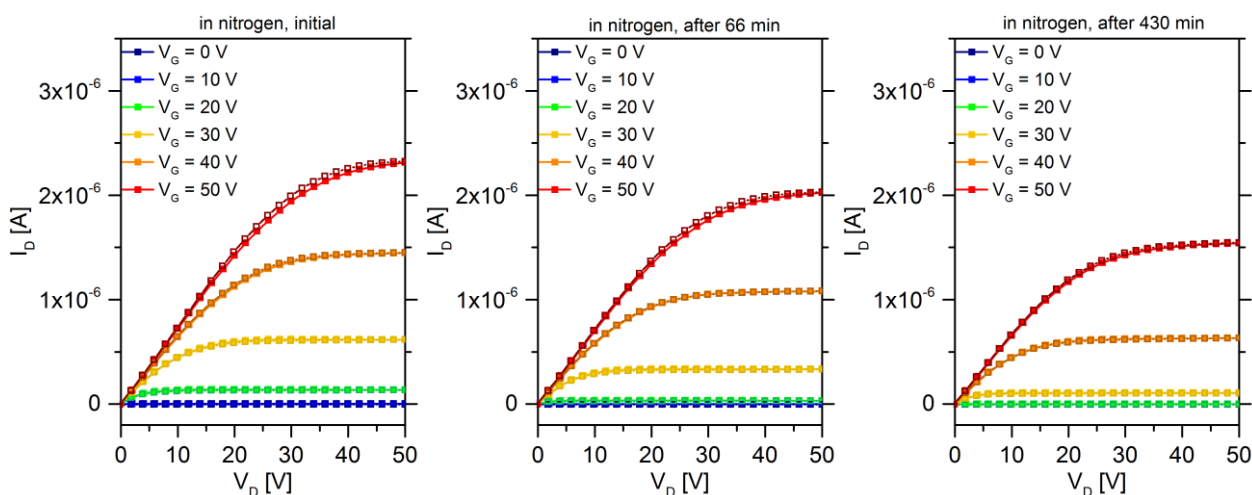
Figure 115. Output characteristics at different times of a **TIPS-TAP** BG/TC FET (L = 67 µm) bias-stressed in pure nitrogen atmosphere.
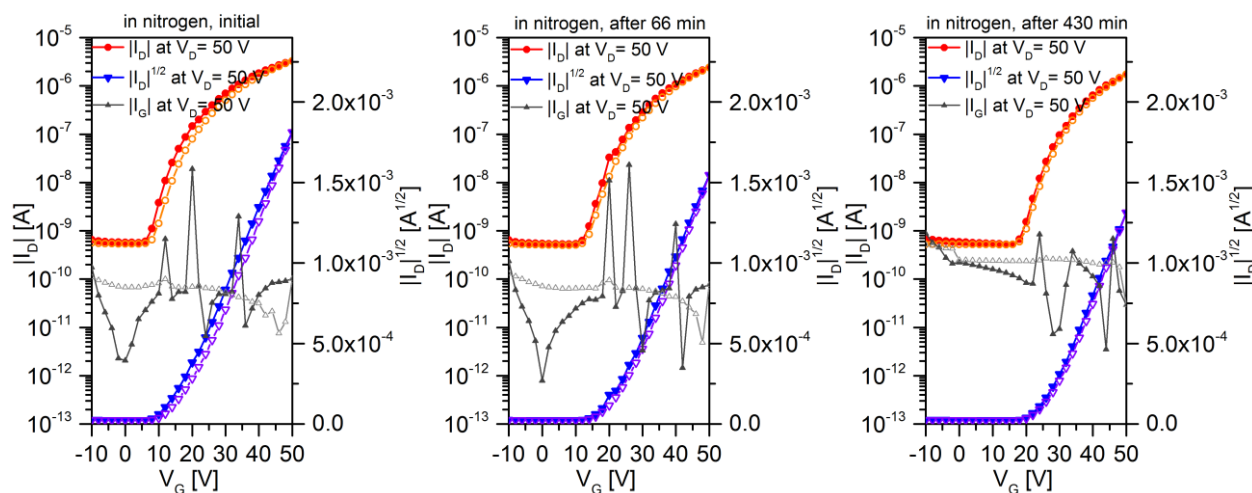
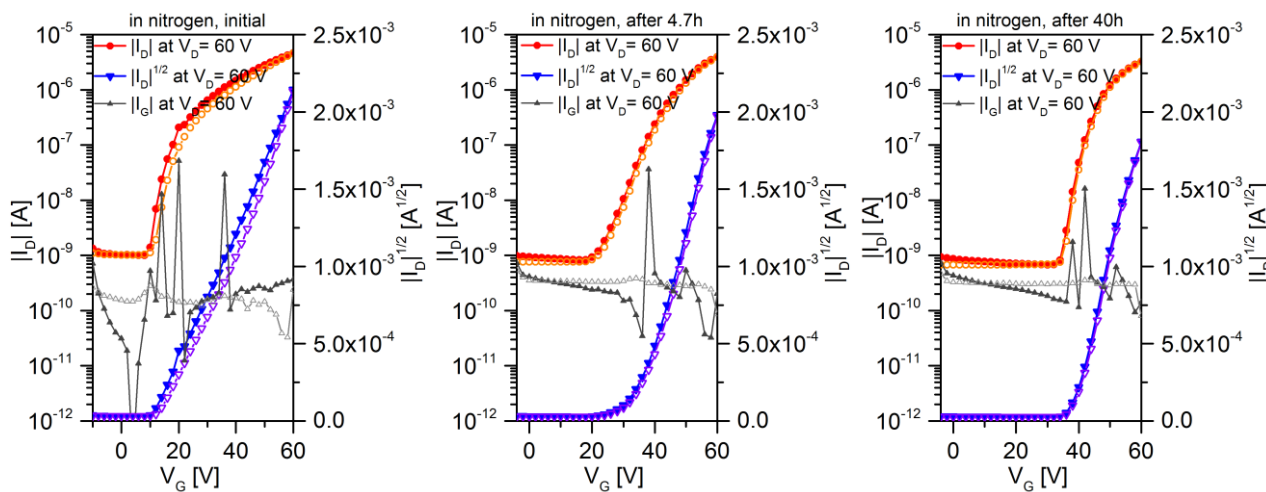**Figure 116.** Transfer characteristics at different times of a **TIPS-TAP** BG/TC FET (L = 67 µm) bias-stressed in pure nitrogen.

A 4.2. Bias-stressing in nitrogen (with resting periods/pauses)

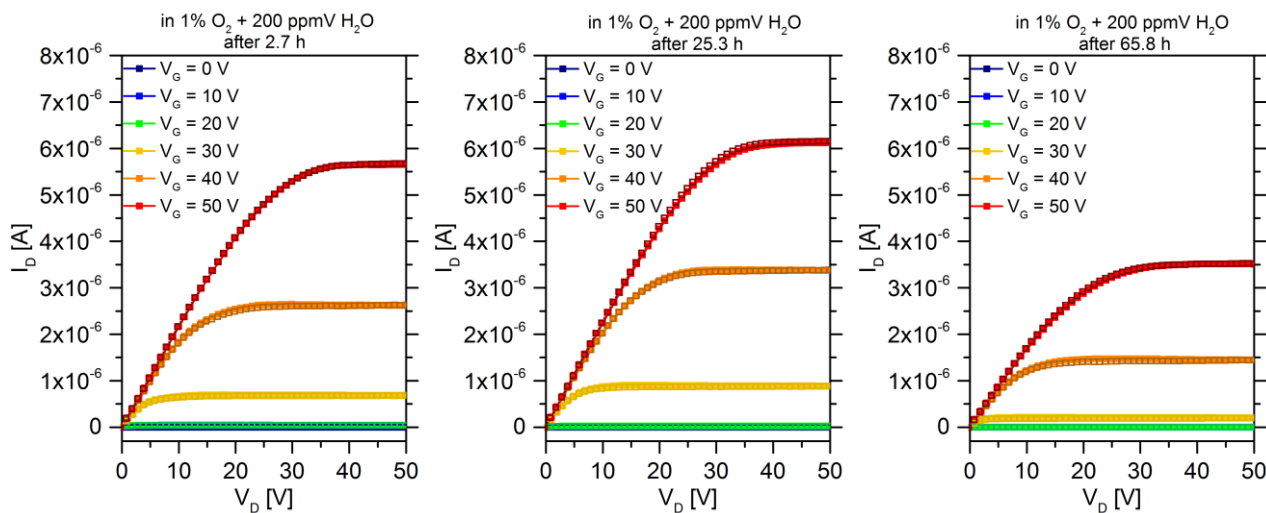**Figure 117.** Output characteristics at different times of a **TIPS-TAP** FET (L = 117 µm) bias-stressed in pure nitrogen with resting periods after each stress cycle.
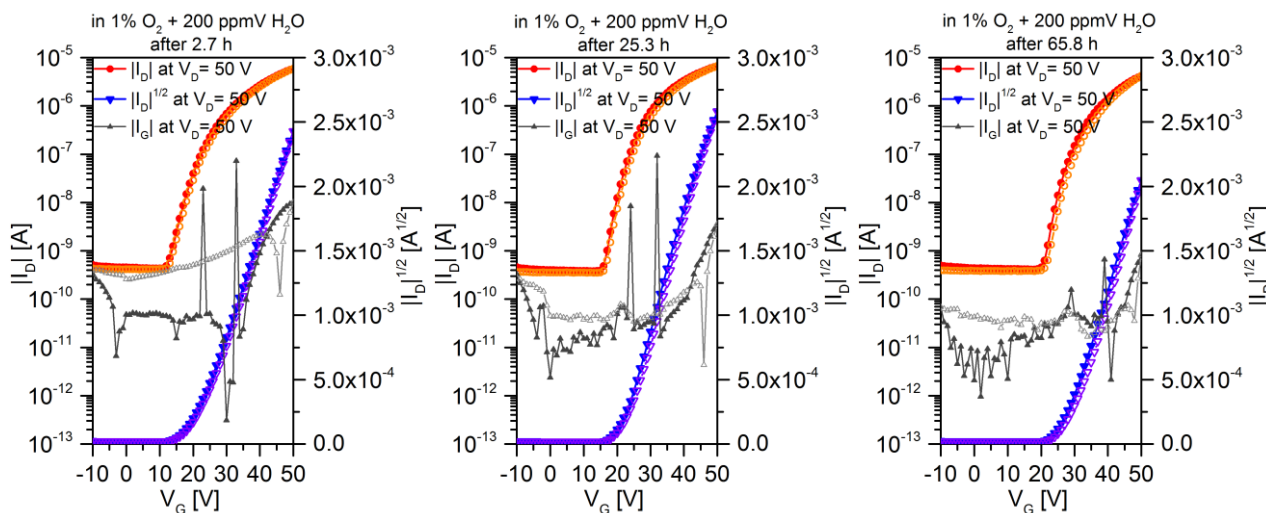

Figure 118. Transfer characteristics at different times of a **TIPS-TAP** FET (L = 117 µm) bias-stressed in pure nitrogen with resting periods after each stress cycle.

A 4.3 Bias-stressing in 1.5% oxygen

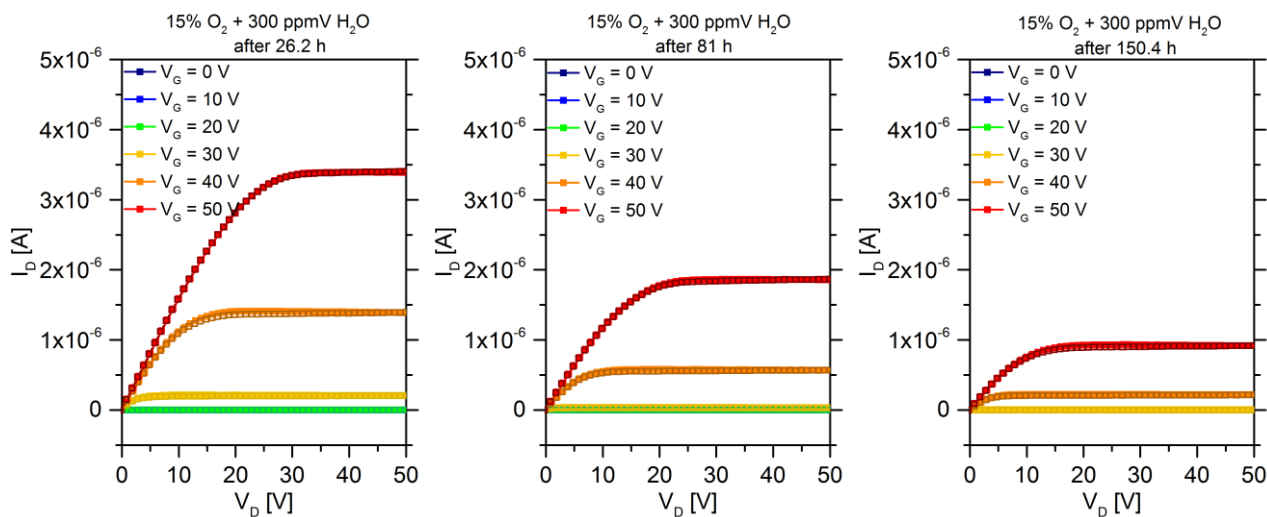**Figure 119.** Output characteristics of a BG/TC **TIPS-TAP** FET (L = 115 µm) at different times during the bias-stress experiment in 1% oxygen atmosphere.
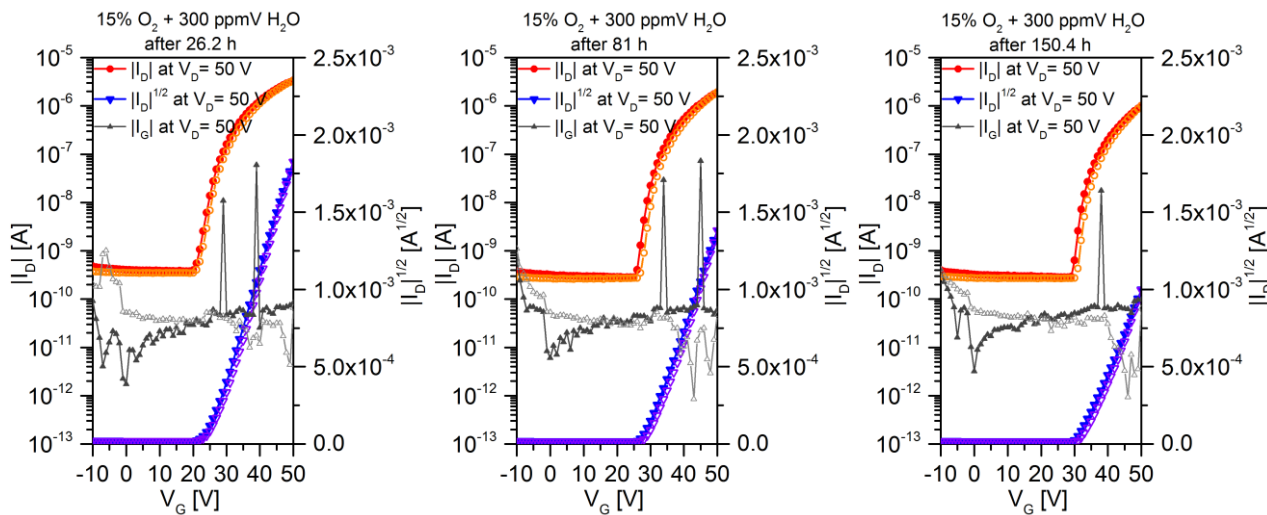

Figure 120. Transfer characteristics of a BG/TC **TIPS-TAP** FET (L = 115 µm) at different times during the bias-stress experiment in 1% oxygen atmosphere.

A 4.4 Bias-stressing in 15% oxygen

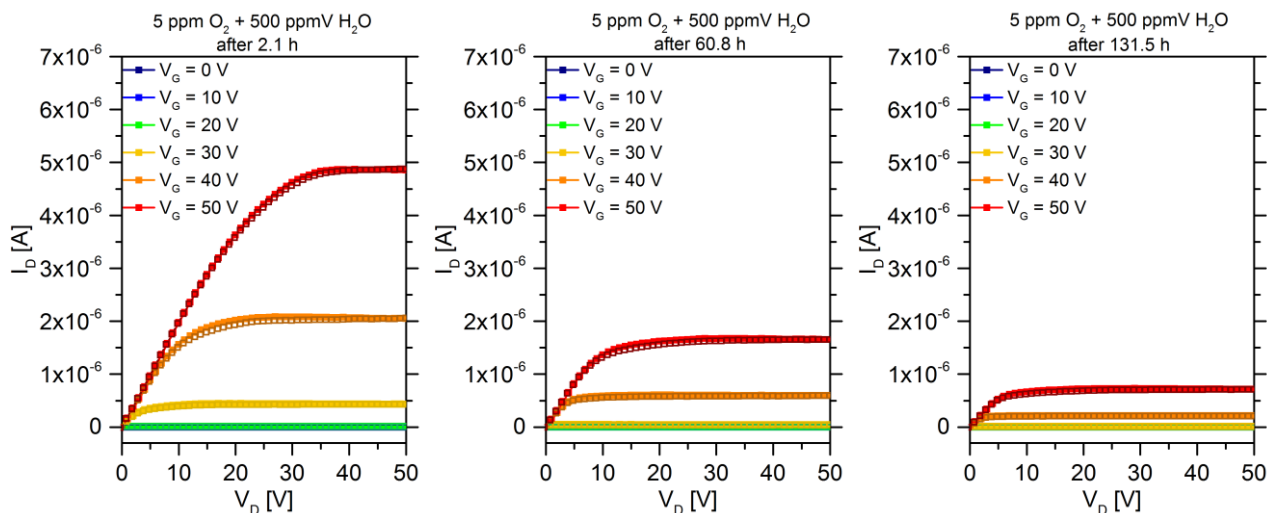
Figure 121. Output characteristics of a **TIPS-TAP** transistor in bottom-gate/ top-contact architecture (L = 85 μm) during bias-stress in 15% oxygen atmosphere.

Figure 122. Transfer characteristics of a **TIPS-TAP** transistor in bottom-gate/ top-contact architecture (L = 85 μm) during bias-stress in 15% oxygen atmosphere.

A 4.5 Bias-stressing with 5 ppm oxygen and 500 ppmV water

Figure 123. Output characteristics of a BG/TC **TIPS-TAP** FET (L = 125 μm) during the bias-stress experiment in an environment without oxygen and higher humidity level of 500 ppmV.
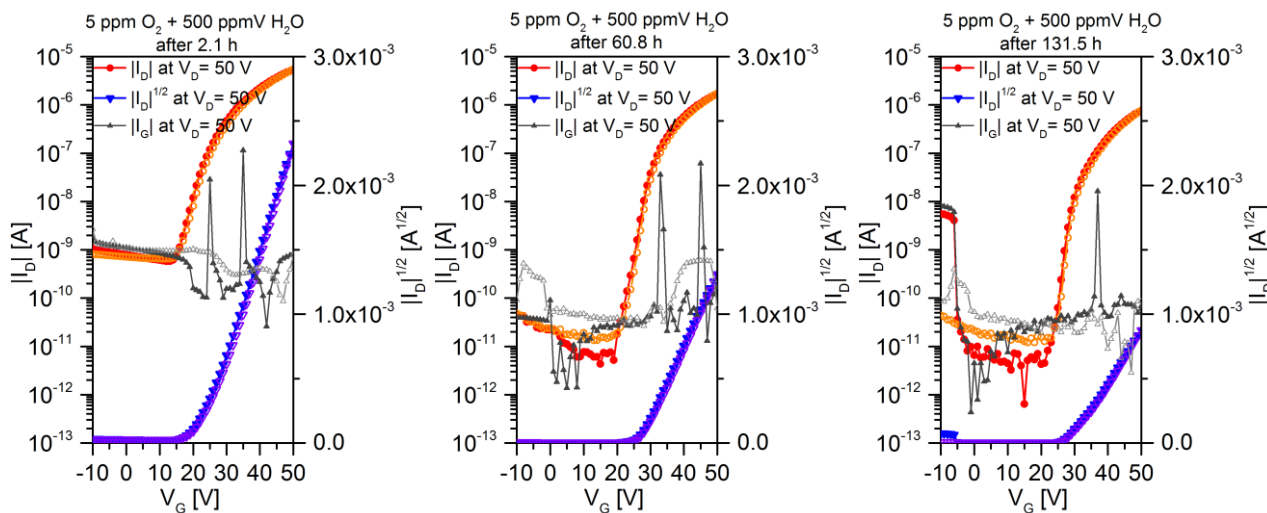
Figure 124. Transfer characteristics of a BG/TC **TIPS-TAP** FET (L = 125 μm) during the bias-stress experiment in an environment without oxygen and higher humidity level of 500 ppmV.

A 4.6. Bias-stressing in ambient condition (air; 20.9 % O_2, 4500 ppmV H_2O)

TIPS-TAP device tested after fabrication:
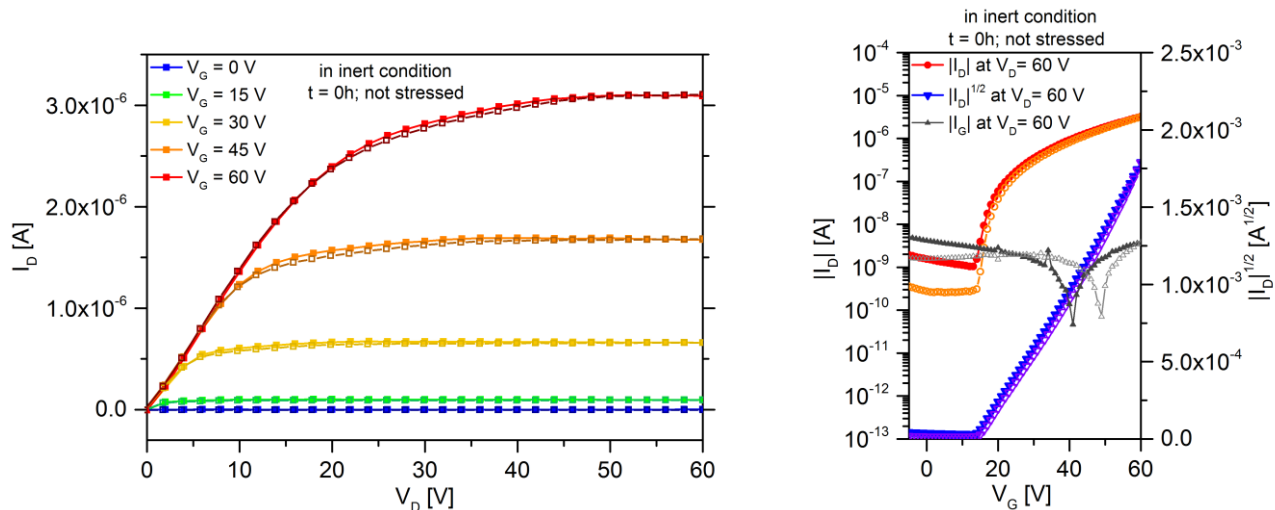
The same device in the environmental sample holder, purged with air
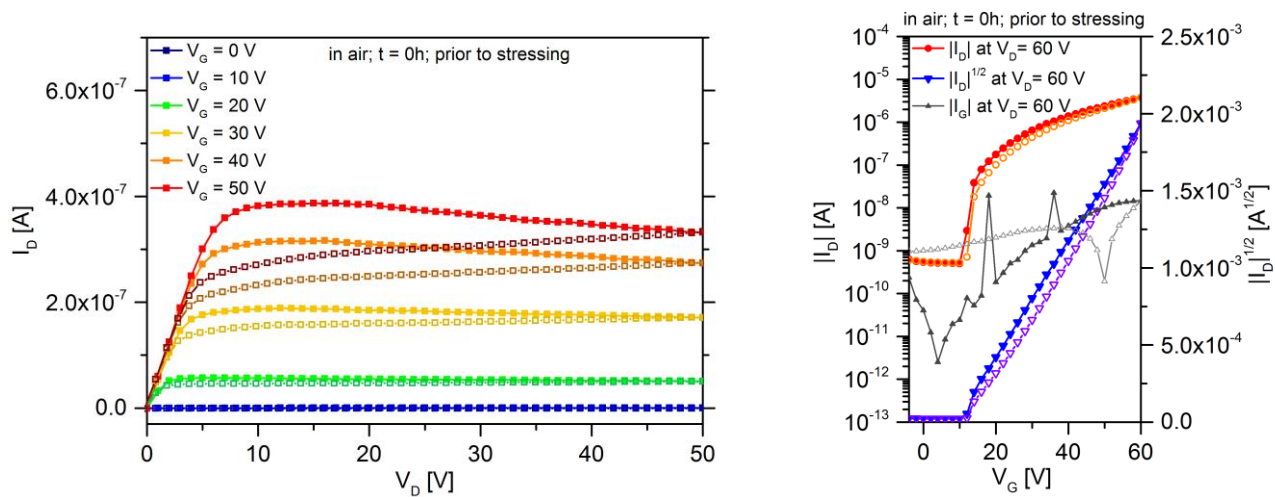
Bias-stressing in air – evolution over the first few hours

Figure 125. I-V characteristics of a representative **TIPS-TAP** transistor tested and bias-stressed in air at different times of the experiment. (left column - output characteristics, right column - transfer characteristic; L = 118 µm)

A 5 – Environmental Control Setup

Figure 126. (a) Environmental sample holder with central sample chamber for four samples, contact pins and cover plate & glass. (b) Gas mixing board for humidity and oxygen control. (Both images kindly provided by Prof Dr Y. Vaynzof and Dr P. E. Hopkinson)

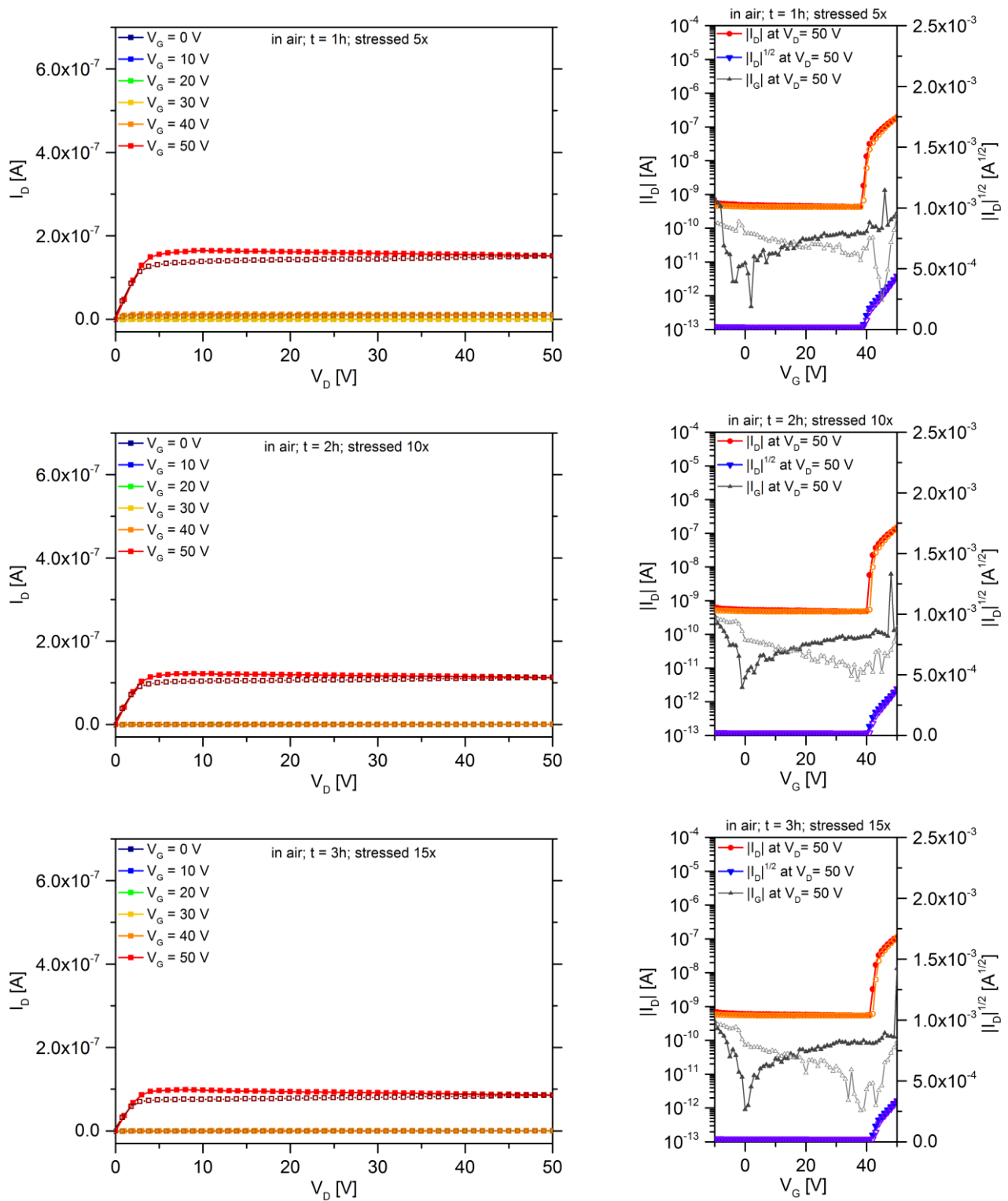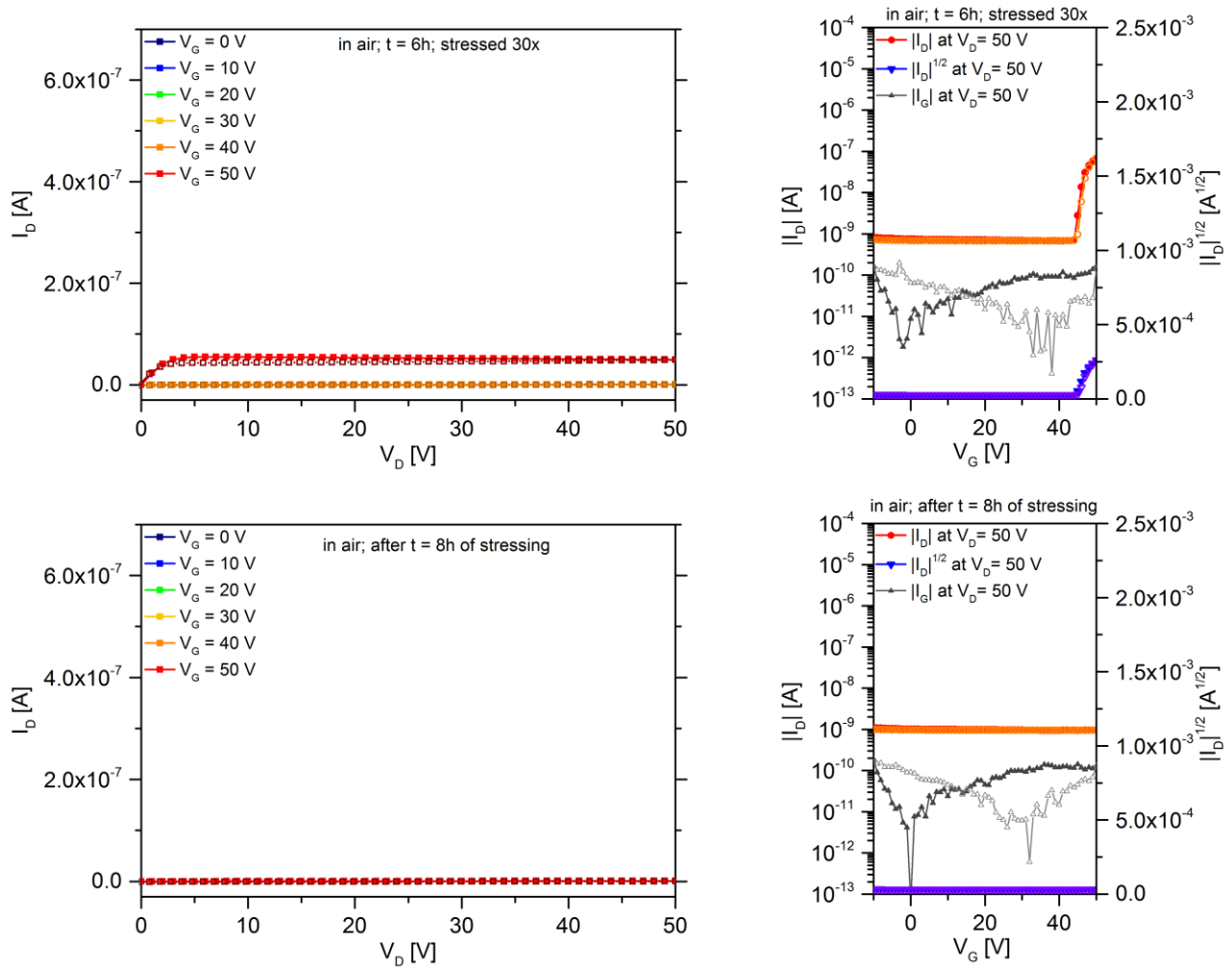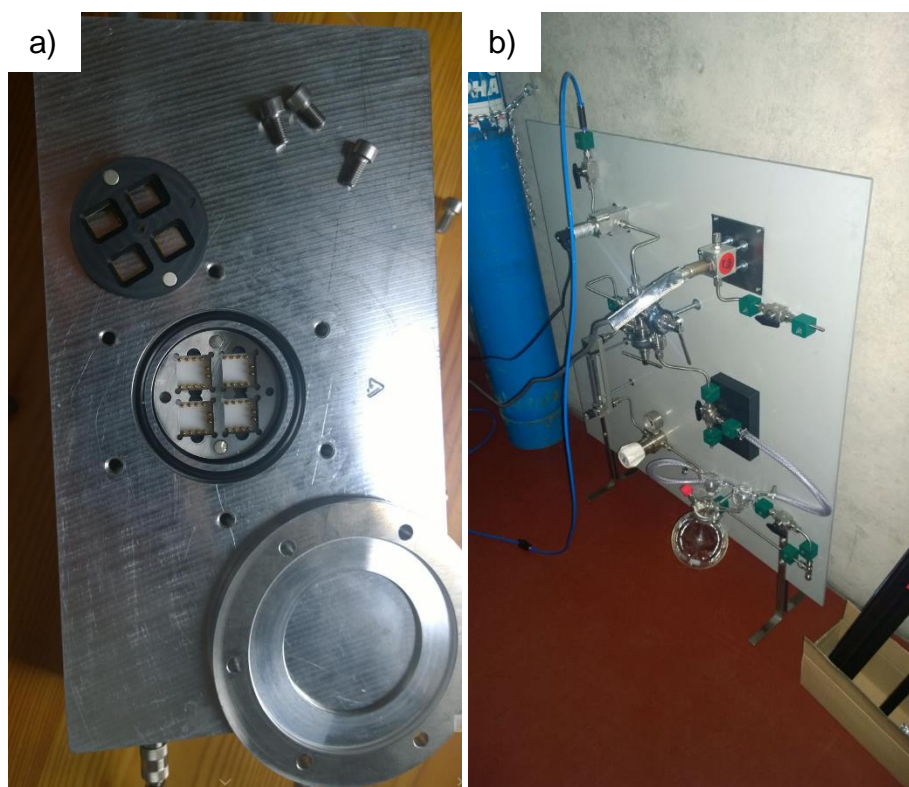## A 6 – Crystal structures and additional parameters

Table 18. Summarised unit cell parameters and CCDC numbers for crystal structure of DHTA-derivatives.

compound	a [Å]	b [Å]	c [Å]	α [°]	β [°]	γ [°]	CCDC	space group	Ref.
DHTA-H_2 single crystal	7.5919(18)	13.551(3)	18.320(4)	89.808(6)	87.902(6)	81.114(6)	803806	P$\bar{1}$	[139]
DHTA-H_2 film phase	7.7626(9)	29.865(4)	34.922(5)	90	95.412(3)	90	1021651	P2_1/c	[169]
DHTA-F_2 single crystal (RT)	18.845(2)	13.5519(13)	16.4737(18)	90	107.673(3)	90	1021650	P2_1/c	[169]
DHTA-F_2 @ -73 K	16.4266(17)	39.893(4)	36.045(4)	90	99.223(3)	90	1021652	P2_1/c	[169]
DHTA-Cl_2 single crystal	14.8777(2)	19.1070(1)	14.2470(2)	90	98.460(1)	90	803808	P2_1/c	[139]
DHTA-Cl_2 polymorph	7.8827(18)	17.964(4)	14.838(3)	90	103.640(7)	90	-	P2_1	-

Table 19. Summarised structural data for **Nor-PEN** and **Nor-TAP** and comparison to the TIPS derivatives.

compound	a [Å]	b [Å]	c [Å]	α [°]	β [°]	γ [°]	CCDC	space group	Ref.
Nor-PEN	7.4483(16)	8.8759(18)	17.631(4)	95.929(4)	94.048(4)	113.779(3)	1428813	$P\bar{1}$	[147]
Nor-TAP	7.4460(8)	8.7331(10)	16.5225(19)	81.188(3)	88.469(3)	78.898(3)	1428814	$P\bar{1}$	[147]
TIPS-PEN	7.5650(15)	7.7500(15)	16.835(3)	89.15(3)	78.42(3)	83.63(3)	172476	$P\bar{1}$	[77]
TIPS-TAP	7.5325(19)	7.5698(18)	16.802(3)	89.740(11)	79.117(12)	82.487(11)	-	$P\bar{1}$	[130]
TIPS-TAP	7.5841(4)	7.6120(3)	16.8363(8)	78.981(4)	89.541(4)	81.900(4)	800375	$P\bar{1}$	[21]

Table 20. Crystal data and structure refinement for **DHTA-H$_2$** in thin films.

Identification code	**fap1**
Empirical formula	$C_{40}H_{52}N_4Si_2$
Formula weight	645.03
Temperature	294(2) K
Wavelength	0.71073 Å
Crystal system	monoclinic
Space group	$P2_1/n$
Z	8
Unit cell dimensions	a = 7.7626(9) Å α = 90 deg.
	b = 29.864(4) Å β = 95.412(3) deg.
	c = 34.922(5) Å γ = 90 deg.
Volume	8059.8(17) Å^3
Density (calculated)	1.06 g/cm^3
Absorption coefficient	0.12 mm^{-1}
Crystal shape	plate
Crystal size	0.100 x 0.100 x 0.040 mm^3
Crystal colour	yellow
Theta range for data collection	0.9 to 15.9 deg.
Index ranges	$-5 \leq h \leq 5$, $-22 \leq k \leq 22$, $-26 \leq l \leq 26$
Reflections collected	19416
Independent reflections	3813 (R(int) = 0.0982)
Observed reflections	1887 (I > 2σ(I))
Absorption correction	Semi-empirical from equivalents
Max. and min. transmission	0.96 and 0.82
Refinement method	Full-matrix least-squares on F^2
Data/restraints/parameters	3813 / 1038 / 389
Goodness-of-fit on F^2	2.06
Final R indices (I>2sigma(I))	R1 = 0.153, wR2 = 0.373
Largest diff. peak and hole	0.54 and -0.37 eÅ^{-3}

Table 21. Crystal data and structure refinement for **DHTA-Cl$_2$** 2nd polymorph.

Identification code	**fap2**
Empirical formula	$C_{40}H_{50}Cl_2N_4Si_2$
Formula weight	713.92
Temperature	296(2) K
Wavelength	0.71073 Å
Crystal system	monoclinic
Space group	$P2_1$
Z	2
Unit cell dimensions	a = 7.8827(18) Å α = 90 deg.
	b = 17.964(4) Å β =103.640(7) deg.
	c = 14.838(3) Å γ = 90 deg.
Volume	2041.9(8) Å^3
Density (calculated)	1.16 g/cm^3
Absorption coefficient	0.25 mm^{-1}
Crystal shape	needle
Crystal size	0.270 x 0.090 x 0.060 mm^3
Crystal colour	yellow
Theta range for data collection	2.3 to 19.8 deg.
Index ranges	-7≤h≤7, -17≤k≤17, -14≤l≤14
Reflections collected	10810
Independent reflections	3693 (R(int) = 0.0783)
Observed reflections	2355 (I > 2σ(I))
Absorption correction	Semi-empirical from equivalents
Max. and min. transmission	0.96 and 0.79
Refinement method	Full-matrix least-squares on F^2
Data/restraints/parameters	3693 / 628 / 445
Goodness-of-fit on F^2	1.03
Final R indices (I>2sigma(I))	R1 = 0.076, wR2 = 0.170
Absolute structure parameter	0.22(9)
Largest diff. peak and hole	0.26 and -0.24 eÅ^{-3}

Table 22. Crystal data and structure refinement for **DHTA-F$_2$** @ -73°C

Identification code	**fap3**
Empirical formula	$C_{40}H_{50}F_2N_4Si_2$
Formula weight	681.02
Temperature	200(2) K
Wavelength	0.71073 Å
Crystal system	monoclinic
Space group	P2$_1$/c
Z	24
Unit cell dimensions	a = 16.4266(17) Å α = 90 deg.
	b = 39.893(4) Å β = 99.223(3) deg.
	c = 36.045(4) Å γ = 90 deg.
Volume	23315(4) Å^3
Density (calculated)	1.16 g/cm^3
Absorption coefficient	0.13 mm^{-1}
Crystal shape	plate
Crystal size	0.210 x 0.170 x 0.060 mm^3
Crystal colour	yellow
Theta range for data collection	0.8 to 18.0 deg.
Index ranges	-14≤h≤14, -34≤k≤34, -31≤l≤31
Reflections collected	94768
Independent reflections	16054 (R(int) = 0.1515)
Observed reflections	7700 (I > 2σ(I))
Absorption correction	Semi-empirical from equivalents
Max. and min. transmission	0.96 and 0.87
Refinement method	Full-matrix least-squares on F^2
Data/restraints/parameters	16054 / 12672 / 2593
Goodness-of-fit on F^2	1.01
Final R indices (I>2sigma(I))	R1 = 0.082, wR2 = 0.178
Largest diff. peak and hole	0.50 and -0.29 eÅ^{-3}

Bibliography

[1] C. K. Chiang, M. A. Druy, S. C. Gau, A. J. Heeger, E. J. Louis, A. G. Macdiarmid, Y. W. Park, H. Shirakawa, *J. Am. Chem. Soc.* **1978**, 1013–1015.

[2] H. Shirakawa, E. J. Louis, A. G. MacDiarmid, C. K. Chiang, A. J. Heeger, *J. Chem. Soc. Chem. Commun.* **1977**, 578.

[3] "The Nobel Prize in Chemistry 2000," Nobelprize.org, "Nobel Media AB 2014", *<<http://www.nobelprize.org/nobel_prizes/chemistry/laureates/2000/>>* **2016**, *18th march*, at 12:33 am.

[4] M. Mas-Torrent, C. Rovira, *Chem. Rev.* **2011**, *111*, 4833–4856.

[5] A. Tsumura, H. Koezuka, T. Ando, *Appl. Phys. Lett.* **1986**, *49*, 1210–1212.

[6] H. Sirringhaus, *Adv. Mater.* **2014**, *26*, 1319–35.

[7] S. M. Sze, K. K. Ng, *Physics of Semiconductor Devices*, John Wiley & Sons, Inc., Hoboken, NJ, USA, **2006**.

[8] J. E. Lilienfeld, *Method and Apparatus for Controlling Electric Currents (U. S. Patent No. 1,745,175)*, **1930**.

[9] W. Shockley, *IEEE Trans. Electron Devices* **1976**, *23*, 597–620.

[10] "The Nobel Prize in Physics 1956," Nobelprize.org, "Nobel Media AB 2014", *<<http://www.nobelprize.org/nobel_prizes/physics/laureates/1956/>>* **2016**, *18th march*, at 12:35 am.

[11] A. Facchetti, *Mater. Today* **2007**, *10*, 28–37.

[12] Y. Shirota, H. Kageyama, *Chem. Rev.* **2007**, *107*, 953–1010.

[13] C. Wang, H. Dong, W. Hu, Y. Liu, D. Zhu, *Chem. Rev.* **2012**, *112*, 2208–67.

[14] H. Klauk, *Chem. Soc. Rev.* **2010**, *39*, 2643–66.

[15] J. Zaumseil, H. Sirringhaus, *Chem. Rev.* **2007**, *107*, 1296–1323.

[16] C. R. Newman, C. D. Frisbie, D. A. da Silva Filho, J.-L. Brédas, P. C. Ewbank, K. R. Mann, *Chem. Mater.* **2004**, *16*, 4436–4451.

[17] Y. Wen, Y. Liu, Y. Guo, G. Yu, W. Hu, *Chem. Rev.* **2011**, *111*, 3358–3406.

[18] G. Horowitz, *Adv. Polym. Sci.* **2010**, *223*, 113–153.

[19] T. Uemura, C. Rolin, T.-H. Ke, P. Fesenko, J. Genoe, P. Heremans, J. Takeya, *Adv. Mater.* **2016**, *28*, 151–155.

[20] G. Giri, E. Verploegen, S. C. B. Mannsfeld, S. Atahan-Evrenk, D. H. Kim, S. Y. Lee, H. a. Becerril, A. Aspuru-Guzik, M. F. Toney, Z. Bao, *Nature* **2011**, *480*, 504–508.

[21] Z. Liang, Q. Tang, J. Xu, Q. Miao, *Adv. Mater.* **2011**, *23*, 1535–9.

[22] H. Sirringhaus, *Adv. Mater.* **2009**, *21*, 3859–3873.

[23] V. Coropceanu, J. Cornil, D. A. da Silva Filho, Y. Olivier, R. Silbey, J.-L. Brédas, *Chem. Rev.* **2007**, *107*, 926–52.

[24] M. C. J. M. Vissenberg, M. Matters, **1998**, *57*, 13.

[25] O. D. Jurchescu, J. Baas, T. T. M. Palstra, *Appl. Phys. Lett.* **2004**, *84*, 3061–3063.

[26] H. Bässler, A. Köhler, in *Top. Curr. Chem.*, **2011**, pp. 1–65.

[27] H. Sirringhaus, *Adv. Mater.* **2005**, *17*, 2411–2425.

[28] M. E. Gershenson, V. Podzorov, A. F. Morpurgo, *Rev. Mod. Phys.* **2006**, *78*, 973–989.

[29] T. Sakanoue, H. Sirringhaus, *Nat. Mater.* **2010**, *9*, 736–40.

[30] H. Bässler, *Phys. Status. Solidi. B, Basic Res.* **1993**, *175*.

[31] J. L. Bredas, J. P. Calbert, D. a da Silva Filho, J. Cornil, *Proc. Natl. Acad. Sci.* **2002**, *99*, 5804–5809.

[32] J. E. Anthony, D. L. Eaton, S. R. Parkin, *Org. Lett.* **2002**, *4*, 15–18.

[33] B. Grimm, C. Risko, J. D. Azoulay, J.-L. Brédas, G. C. Bazan, *Chem. Sci.* **2013**, *4*, 1807.

[34] A. Salleo, *Mater. Today* **2007**, *10*, 38–45.

[35] H. Sirringhaus, P. J. Brown, R. H. Friend, M. M. Nielsen, K. Bechgaard, B. M. W. Langeveld-Voss, A. J. H. Spiering, R. A. J. Janssen, E. W. Meijer, P. Herwig, et al., *Nature* **1999**, *401*, 685–688.

[36] Z. Bao, a Dodabalapur, a J. Lovinger, *Appl Phys Lett* **1996**, *69*, 4108–4110.

[37] J. Rivnay, A. Salleo, S. Mannsfeld, C. Miller, M. Toney, *Chem. Rev.* **2012**, *112*, 5488–5519.

[38] C. Liu, Y. Xu, Y.-Y. Noh, *Mater. Today* **2015**, *18*, 79–96.

[39] G. Heimel, L. Romaner, E. Zojer, J.-L. Bredas, *Acc. Chem. Res.* **2008**, *41*, 721–9.

[40] C. D. Dimitrakopoulos, P. R. L. Malenfant, *Adv. Mater.* **2002**, *14*, 99–117.

[41] Y. Wu, Y. Li, B. S. Ong, *J. Am. Chem. Soc.* **2006**, *128*, 4202–4203.

[42] W. Osikowicz, M. P. De Jong, S. Braun, C. Tengstedt, M. Fahlman, W. R. Salaneck, *Appl. Phys. Lett.* **2006**, *88*, 19–22.

[43] Y. Shirai, J. M. Guerrero, T. Sasaki, T. He, H. Ding, G. Vives, B.-C. Yu, L. Cheng, A. K. Flatt, P. G. Taylor, et al., *J. Org. Chem.* **2009**, *74*, 7885–97.

[44] A. Facchetti, M.-H. Yoon, T. J. Marks, *Adv. Mater.* **2005**, *17*, 1705–1725.

[45] L. Chua, J. Zaumseil, J. Chang, E. C.-W. Ou, P. K.-H. Ho, H. Sirringhaus, R. H. Friend, *Nature* **2005**, *434*, 194–9.

[46] J. Veres, S. D. Ogier, S. W. Leeming, D. C. Cupertino, S. Mohialdin Khaffaf, *Adv. Funct. Mater.* **2003**, *13*, 199–204.

[47] T. Richards, M. Bird, H. Sirringhaus, *J. Chem. Phys.* **2008**, *128*, 234905.

[48] M. Halik, A. Hirsch, *Adv. Mater.* **2011**, *23*, 2689–2695.

[49] K.-J. Baeg, A. Facchetti, Y.-Y. Noh, *J. Mater. Chem.* **2012**, *22*, 21138.

[50] T. N. Ng, M. L. Chabinyc, R. A. Street, A. Salleo, *2007 Ieee Int. Reliab. Phys. Symp. Proc. - 45th Annu.* **2007**, 243–247\r749.

[51] D. Knipp, R. A. Street, A. Völkel, J. Ho, *J. Appl. Phys.* **2003**, *93*, 347–355.

[52] A. Salleo, F. Endicott, R. A. Street, *Appl. Phys. Lett.* **2005**, *86*, 1–3.

[53] A. Salleo, R. A. Street, *J. Appl. Phys.* **2003**, *94*, 471–479.

[54] W. L. Kalb, T. Mathis, S. Haas, A. F. Stassen, B. Batlogg, *Appl. Phys. Lett.* **2007**, *90*, 88–91.

[55]   T. Umeda, D. Kumaki, S. Tokito, *Org. Electron. physics, Mater. Appl.* **2008**, *9*, 545–549.

[56]   K. Takagi, T. Nagase, T. Kobayashi, H. Naito, *Org. Electron.* **2016**, *32*, 65–69.

[57]   S. Trasatti, *Pure Appl. Chem.* **1986**, *58*, 955–966.

[58]   Y. Chang, M. Kuo, C. Chen, H. Lu, I. Chao, *J. Phys. Chem. C* **2010**, *114*, 11595–11601.

[59]   B. A. Jones, A. Facchetti, M. R. Wasielewski, T. J. Marks, *J. Am. Chem. Soc.* **2007**, *129*, 15259–15278.

[60]   J. E. Anthony, *Chem. Rev.* **2006**, *106*, 5028–5048.

[61]   J. E. Anthony, *Angew. Chemie Int. Ed.* **2008**, *47*, 452–483.

[62]   C. D. Sheraw, T. N. Jackson, D. L. Eaton, J. E. Anthony, *Adv. Mater.* **2003**, *15*, 2009.

[63]   E. Menard, V. Podzorov, S. H. Hur, A. Gaur, M. E. Gershenson, J. A. Rogers, *Adv. Mater.* **2004**, *16*, 2097–2101.

[64]   V. Podzorov, E. Menard, J. A. Rogers, M. E. Gershenson, *Phys. Rev. Lett.* **2005**, *95*, 1–4.

[65]   D. Käfer, L. Ruppel, G. Witte, C. Wöll, *Phys. Rev. Lett.* **2005**, *95*, 166602.

[66]   D. Käfer, G. Witte, *Phys. Chem. Chem. Phys.* **2005**, *7*, 2850–3.

[67]   C. C. Mattheus, A. B. Dros, J. Baas, A. Meetsma, J. L. de Boer, T. T. M. Palstra, *Acta Crystallogr. Sect. C Cryst. Struct. Commun.* **2001**, *57*, 939–941.

[68]   C. C. Mattheus, G. a de Wijs, R. a de Groot, T. T. M. Palstra, *J. Am. Chem. Soc.* **2003**, *125*, 6323–30.

[69]   M. Ahles, R. Schmechel, H. Von Seggern, *Appl. Phys. Lett.* **2005**, *87*, 85–88.

[70]   M. Ahles, R. Schmechel, H. von Seggern, *Appl. Phys. Lett.* **2004**, *85*, 4499.

[71]   P. I. Djurovich, E. I. Mayo, S. R. Forrest, M. E. Thompson, *Org. Electron. physics, Mater. Appl.* **2009**, *10*, 515–520.

[72]   T. B. Singh, F. Meghdadi, S. Günes, N. Marjanovic, G. Horowitz, P. Lang, S. Bauer, N. S. Sariciftci, *Adv. Mater.* **2005**, *17*, 2315–2320.

[73]   O. D. Jurchescu, M. Popinciuc, B. J. van Wees, T. T. M. Palstra, *Adv. Mater.* **2007**, *19*, 688–692.

[74]   S. Ogawa, T. Naijo, Y. Kimura, H. Ishii, M. Niwano, *Appl. Phys. Lett.* **2005**, *86*, 252104.

[75]   a R. Reddy, M. Bendikov, *Chem. Commun.* **2006**, 1179.

[76]   R. B. Campbell, J. M. Robertson, J. Trotter, *Acta Crystallogr.* **1962**, *15*, 289.

[77]   J. E. Anthony, J. S. Brooks, D. L. Eaton, S. R. Parkin, *J. Am. Chem. Soc.* **2001**, *123*, 9482–9483.

[78]   J. Chen, S. Subramanian, S. R. Parkin, M. Siegler, K. Gallup, C. Haughn, D. C. Martin, J. E. Anthony, *J. Mater. Chem.* **2008**, *18*, 1961.

[79]   D. J. Gundlach, J. E. Royer, S. K. Park, S. Subramanian, O. D. Jurchescu, B. H. Hamadani, a J. Moad, R. J. Kline, L. C. Teague, O. Kirillov, et al., *Nat. Mater.* **2008**, *7*, 216–221.

[80]   O. Ostroverkhova, S. Shcherbyna, D. G. Cooke, R. F. Egerton, F. A. Hegmann, R. R. Tykwinski, S. R. Parkin, J. E. Anthony, *J. Appl. Phys.* **2005**, *98*, 033701.

[81]   O. Ostroverkhova, D. G. Cooke, F. A. Hegmann, R. R. Tykwinski, S. R. Parkin, J. E. Anthony, *Appl. Phys. Lett.* **2006**, *89*, 192113.

[82]   S. K. Park, T. N. Jackson, J. E. Anthony, D. a. Mourey, *Appl. Phys. Lett.* **2007**, *91*, 063514.

[83]   J. Wade, F. Steiner, D. Niedzialek, D. James, Y. Jung, D.-J. Yun, D. D. Bradley, J. Nelson, J.-S. Kim, *J. Mater. Chem. C* **2014**, *00*, 1–6.

[84]   Y.-H. Kim, Y. U. Lee, J.-I. Han, S.-M. Han, M.-K. Han, *J. Electrochem. Soc.* **2007**, *154*, H995.

[85]   A. S. Eggeman, S. Illig, A. Troisi, H. Sirringhaus, P. A. Midgley, *Nat. Mater.* **2013**, *12*, 1045–9.

[86]   S. S. Lee, S. B. Tang, D. M. Smilgies, A. R. Woll, M. A. Loth, J. M. Mativetsky, J. E. Anthony, Y. L. Loo, *Adv. Mater.* **2012**, *24*, 2692–2698.

[87]   S. S. Lee, M. a. Loth, J. E. Anthony, Y. L. Loo, *J. Am. Chem. Soc.* **2012**, *134*, 5436–5439.

[88]   C. M. Duffy, J. W. Andreasen, D. W. Breiby, M. M. Nielsen, M. Ando, T. Minakata, H. Sirringhaus, *Chem. Mater.* **2008**, *20*, 7252–7259.

[89]   D. T. James, J. M. Frost, J. Wade, J. Nelson, J. Kim, *ACS Nano* **2013**, *7*, 7983–7991.

[90]   Y. Su, X. Gao, J. Liu, R. Xing, Y. Han, *Phys. Chem. Chem. Phys.* **2013**, *15*, 14396.

[91]   A. Tracz, T. Pakula, J. K. Jeszka, *Mater. Sci.* **2004**, *22*, 415–421.

[92]   W. Pisula, A. Menon, M. Stepputat, I. Lieberwirth, U. Kolb, A. Tracz, H. Sirringhaus, T. Pakula, K. Müllen, *Adv. Mater.* **2005**, *17*, 684–689.

[93]   H. Zhao, Z. Wang, G. Dong, L. Duan, *Phys. Chem. Chem. Phys.* **2015**, *17*, 6274–6279.

[94]   H. Zhao, D. Li, G. Dong, L. Duan, X. Liu, L. Wang, *Langmuir* **2014**, *30*, 12082–12088.

[95]   G. Giri, S. Park, M. Vosgueritchian, M. M. Shulaker, Z. Bao, *Adv. Mater.* **2014**, *26*, 487–93.

[96]   Y. Diao, B. C.-K. Tee, G. Giri, J. Xu, D. H. Kim, H. a Becerril, R. M. Stoltenberg, T. H. Lee, G. Xue, S. C. B. Mannsfeld, et al., *Nat. Mater.* **2013**, *12*, 665–71.

[97]   A. B. Naden, J. Loos, D. a. MacLaren, *J. Mater. Chem. C* **2014**, *2*, 245–255.

[98]   G. R. Llorente, M.-B. Dufourg-Madec, D. J. Crouch, R. G. Pritchard, S. Ogier, S. G. Yeates, *Chem. Commun.* **2009**, 3059.

[99]   Y. Mei, M. a. Loth, M. Payne, W. Zhang, J. Smith, C. S. Day, S. R. Parkin, M. Heeney, I. McCulloch, T. D. Anthopoulos, et al., *Adv. Mater.* **2013**, *25*, 4352–4357.

[100]   C.-H. Kim, H. Hlaing, M. M. Payne, K. G. Yager, Y. Bonnassieux, G. Horowitz, J. E. Anthony, I. Kymissis, *Chemphyschem* **2014**, 1–4.

[101]   D. Lehnherr, R. R. Tykwinski, *Materials (Basel).* **2010**, *3*, 2772–2800.

[102]   S. Tokito, K.-H. Weifurtner, H. Fujikawa, T. Tsutsui, Y. Taga, in *Proc. SPIE 4105, Org. Light. Mater. Devices IV, (February 2, 2001)*, pp. 69–74.

[103]   T. Okamoto, Y. Jiang, H. A. Becerril, S. Hong, M. L. Senatore, M. L. Tang, M. F. Toney, T. Siegrist, Z. Bao, *J. Mater. Chem.* **2011**, *21*, 7078.

[104]   T. Okamoto, Z. Bao, *J. Am. Chem. Soc.* **2007**, *129*, 10308–10309.

[105]   E. Kumarasamy, S. N. Sanders, A. B. Pun, S. A. Vaselabadi, J. Z. Low, M. Y. Sfeir, M. L. Steigerwald, G. E. Stein, L. M. Campos, *Macromolecules* **2016**, *49*, 1279–1285.

[106]   Y. Inoue, Y. Sakamoto, T. Suzuki, M. Kobayashi, Y. Gao, S. Tokito, *Jpn. J. Appl. Phys.* **2005**, *44*, 3663–3668.

[107]   Y. Sakamoto, T. Suzuki, M. Kobayashi, Y. Gao, Y. Fukai, Y. Inoue, F. Sato, S. Tokito, *J. Am. Chem. Soc.* **2004**, *126*, 8138–8140.

[108]   C. R. Swartz, S. R. Parkin, J. E. Bullock, J. E. Anthony, A. C. Mayer, G. G. Malliaras, *Org. Lett.* **2005**, *7*, 3163–3166.

[109]   M. L. Tang, J. H. Oh, A. D. Reichardt, Z. Bao, *J. Am. Chem. Soc.* **2009**, *131*, 3733–3740.

[110]   M. Winkler, K. N. Houk, *J. Am. Chem. Soc.* **2007**, *129*, 1805–15.

[111]   Z. Liang, Q. Tang, R. Mao, D. Liu, J. Xu, Q. Miao, *Adv. Mater.* **2011**, *23*, 5514–8.

[112]   F. Wudl, P. A. Koutentis, A. Weitz, B. Ma, T. Strassner, K. N. Houk, S. I. Khan, *Pure Appl. Chem.* **1999**, *71*, 295–302.

[113]   U. H. F. Bunz, *Pure Appl. Chem.* **2010**, *82*, 953–968.

[114]   Q. Miao, *Synlett* **2012**, *23*, 326–336.

[115]   U. H. F. Bunz, J. U. Engelhart, B. D. Lindner, M. Schaffroth, *Angew. Chemie Int. Ed.* **2013**, *52*, 3810–3821.

[116]   Q. Miao, *Adv. Mater.* **2014**, *26*, 5541–5549.

[117]   U. H. F. Bunz, *Acc. Chem. Res.* **2015**, *48*, 1676–1686.

[118]   W. Zhang, Y. Liu, G. Yu, *Adv. Mater.* **2014**, 6898–6904.

[119]   O. Fischer, E. Hepp, *Berichte der Dtsch. Chem. Gesellschaft* **1890**, *23*, 2789–2793.

[120]   O. Hinsberg, *Justus Liebig's Ann. der Chemie* **1901**, *319*, 257–286.

[121]   Q. Miao, T.-Q. Nguyen, T. Someya, G. B. Blanchet, C. Nuckolls, *J. Am. Chem. Soc.* **2003**, *125*, 10284–7.

[122]   Y. Ma, Y. Sun, Y. Liu, J. Gao, S. Chen, X. Sun, W. Qiu, G. Yu, G. Cui, W. Hu, et al., *J. Mater. Chem.* **2005**, *15*, 4894.

[123]   Q. Tang, D. Zhang, S. Wang, N. Ke, J. Xu, J. C. Yu, Q. Miao, *Chem. Mater.* **2009**, *21*, 1400–1405.

[124]   J. I. Wu, C. S. Wannere, Y. Mo, P. V. R. Schleyer, U. H. F. Bunz, *J. Org. Chem.* **2009**, *74*, 4343–9.

[125]   D. Liu, Z. Li, Z. He, J. Xu, Q. Miao, *J. Mater. Chem.* **2012**, *22*, 4396.

[126]   K. Isoda, M. Nakamura, T. Tatenuma, H. Ogata, T. Sugaya, M. Tadokoro, *Chem. Lett.* **2012**, *41*, 937–939.

[127]   Z. He, D. Liu, R. Mao, Q. Tang, Q. Miao, *Org. Lett.* **2012**, *14*, 1050–3.

[128]   Y.-Y. Liu, C.-L. Song, W.-J. Zeng, K.-G. Zhou, Z.-F. Shi, C.-B. Ma, F. Yang, H.-L. Zhang, X. Gong, *J. Am. Chem. Soc.* **2010**, *132*, 16349–51.

[129]   C.-L. Song, C.-B. Ma, F. Yang, W.-J. Zeng, H.-L. Zhang, X. Gong, *Org. Lett.* **2011**, *13*, 2880–3.

[130]   S. Miao, A. L. Appleton, N. Berger, S. Barlow, S. R. Marder, K. I. Hardcastle, U. H. F. Bunz, *Chem. - A Eur. J.* **2009**, *15*, 4990–4993.

[131]   J. U. Engelhart, Dissertation, Neue Wege Zu Großen N-Heteroacenen: Synthese, Struktur Und Reaktivität, Universität Heidelberg, **2015**.

[132]   C. Wang, Z. Liang, Y. Liu, X. Wang, N. Zhao, Q. Miao, W. Hu, J. Xu, *J. Mater. Chem.* **2011**, *21*, 15201.

[133]   D. Liu, X. Xu, Y. Su, Z. He, J. Xu, Q. Miao, *Angew. Chem. Int. Ed. Engl.* **2013**, 6222–6227.

[134]   D. Liu, Z. He, Y. Su, Y. Diao, S. C. B. Mannsfeld, Z. Bao, J. Xu, Q. Miao, *Adv. Mater.* **2014**, *26*, 7190–6.

[135] G. Xue, J. Wu, C. Fan, S. Liu, Z. Huang, Y. Liu, B. Shan, H. L. Xin, Q. Miao, H. Chen, et al., *Mater. Horiz.* **2016**, 44–46.

[136] J. Herz, T. Buckup, F. Paulus, J. Engelhart, U. H. F. Bunz, M. Motzkus, *J. Phys. Chem. Lett.* **2014**, *5*, 2425–2430.

[137] J. Herz, T. Buckup, F. Paulus, J. U. Engelhart, U. H. F. Bunz, M. Motzkus, *J. Phys. Chem. A* **2015**, *119*, 6602–6610.

[138] U. H. F. Bunz, J. U. Engelhart, B. D. Lindner, M. Schaffroth, *Angew. Chemie Int. Ed.* **2013**, *52*, 3810–3821.

[139] O. Tverskoy, F. Rominger, A. Peters, H.-J. Himmel, U. H. F. Bunz, *Angew. Chem. Int. Ed. Engl.* **2011**, *50*, 3557–60.

[140] J. U. Engelhart, B. D. Lindner, O. Tverskoy, F. Rominger, U. H. F. Bunz, *Chem. - A Eur. J.* **2013**, *19*, 15089–15092.

[141] P. Biegger, M. Schaffroth, C. Patze, O. Tverskoy, F. Rominger, U. H. F. Bunz, *Chem. - A Eur. J.* **2015**, *21*, 7048–7052.

[142] P. Biegger, S. Stolz, S. N. Intorp, Y. Zhang, J. U. Engelhart, F. Rominger, K. I. Hardcastle, U. Lemmer, X. Qian, M. Hamburger, et al., *J. Org. Chem.* **2015**, *80*, 582–589.

[143] J. U. Engelhart, O. Tverskoy, U. H. F. Bunz, *J. Am. Chem. Soc.* **2014**, *136*, 15166–15169.

[144] J. U. Engelhart, B. D. Lindner, M. Schaffroth, D. Schrempp, O. Tverskoy, U. H. F. Bunz, *Chem. - A Eur. J.* **2015**, *21*, 8121–8129.

[145] A. H. Endres, M. Schaffroth, F. Paulus, H. Reiss, H. Wadepohl, F. Rominger, R. Krämer, U. H. F. Bunz, *J. Am. Chem. Soc.* **2016**, *138*, 1792–1795.

[146] B. D. Lindner, Dissertation, Elektronenarme N-Heteroacene: Ein Weg Zu Neuen Elektronentransportmaterialien, Universität Heidelberg, **2013**.

[147] M. M. Porz, Dissertation, Nichtkonjugierte Acenhaltige Polymere Durch Ringöffnende Metathesepolymerisation, Universität Heidelberg, **2015**.

[148] H. Yan, Z. Chen, Y. Zheng, C. Newman, J. R. Quinn, F. Dötz, M. Kastler, A. Facchetti, *Nature* **2009**, *457*, 679–86.

[149] S. A. Paniagua, P. J. Hotchkiss, S. C. Jones, S. R. Marder, A. Mudalige, F. S. Marrikar, J. E. Pemberton, N. R. Armstrong, *J. Phys. Chem. C* **2008**, *112*, 7809–7817.

[150] Y. D. Park, J. A. Lim, H. S. Lee, K. Cho, *Mater. Today* **2007**, *10*, 46–54.

[151] D. L. Angst, G. W. Simmons, *Langmuir* **1991**, *7*, 2236–2242.

[152] J. Chang, J. Li, K. L. Chang, J. Zhang, J. Wu, *RSC Adv.* **2013**, *3*, 8721.

[153] A. Salleo, M. L. Chabinyc, M. S. Yang, R. a. Street, *Appl. Phys. Lett.* **2002**, *81*, 4383.

[154] M. Porz, F. Paulus, S. Höfle, T. Lutz, U. Lemmer, A. Colsmann, U. H. F. Bunz, *Macromol. Rapid Commun.* **2013**, *34*, 1611–1617.

[155] M. M. Payne, S. R. Parkin, J. E. Anthony, C. Kuo, T. N. Jackson, *J. Am. Chem. Soc.* **2005**, *127*, 4986–4987.

[156] W. Huang, K. Besar, R. Lecover, A. Mar, P. N. Breysse, H. E. Katz, B. Timmer, W. Olthuis, A. Van Den Berg, J. Yu, et al., *J. Mater. Chem. C* **2013**, *107*, 666–677.

[157] C. H. Cheung, K. K. Tsung, K. C. Kwok, S. K. So, *Appl. Phys. Lett.* **2008**, *93*, 3–5.

[158] C. Y. H. Chan, K. K. Tsung, W. H. Choi, S. K. So, *Org. Electron.* **2013**, *14*, 1351–1358.

[159] X. Yang, Ed. , *Semiconducting Polymer Composites*, Wiley VCH, Weinheim, **2012**.

[160] J. A. Bartelt, Z. M. Beiley, E. T. Hoke, W. R. Mateker, J. D. Douglas, B. A. Collins, J. R. Tumbleston, K. R. Graham, A. Amassian, H. Ade, et al., *Adv. Energy Mater.* **2013**, *3*, 364–374.

[161] Y. Qi, S. K. Mohapatra, S. Bok Kim, S. Barlow, S. R. Marder, A. Kahn, *Appl. Phys. Lett.* **2012**, *100*, 083305.

[162] Y. Jiang, S. Hong, J. H. Oh, R. Mondal, T. Okamoto, E. Verploegen, M. F. Toney, M. D. McGehee, Z. Bao, *J. Mater. Chem.* **2012**, *22*, 4356–4363.

[163] F. Paulus, J. U. Engelhart, P. E. Hopkinson, C. Schimpf, A. Leineweber, H. Sirringhaus, Y. Vaynzof, U. H. F. Bunz, *J. Mater. Chem. C* **2016**, *4*, 1194–1200.

[164] X. Xu, T. Xiao, X. Gu, X. Yang, S. V Kershaw, N. Zhao, J. Xu, Q. Miao, *ACS Appl. Mater. Interfaces* **2015**, 150417115849009.

[165] M. Schaffroth, Dissertation, N-Heteroacene: Theoretische Betrachtungen Und Neue Motive, Universität Heidelberg, **2015**.

[166] W. H. Lee, D. H. Kim, Y. Jang, J. H. Cho, M. Hwang, Y. D. Park, Y. H. Kim, J. I. Han, K. Cho, *Appl. Phys. Lett.* **2007**, *90*, 132106.

[167] J. H. Park, Y. T. Lee, H. S. Lee, J. Y. Lee, K. Lee, G. B. Lee, J. Han, T. W. Kim, S. Im, *ACS Appl. Mater. Interfaces* **2013**, *5*, 1625–1629.

[168] W. H. Lee, H. H. Choi, D. H. Kim, K. Cho, *Adv. Mater.* **2014**, *26*, 1660–1680.

[169] F. Paulus, B. D. Lindner, H. Reiß, F. Rominger, A. Leineweber, Y. Vaynzof, H. Sirringhaus, U. H. F. Bunz, *J. Mater. Chem. C* **2015**, *3*, 1604–1609.

[170] S. Miao, S. M. Brombosz, P. V. R. Schleyer, J. I. Wu, S. Barlow, S. R. Marder, K. I. Hardcastle, U. H. F. Bunz, *J. Am. Chem. Soc.* **2008**, *130*, 7339–44.

[171] J. Engelhart, Synthese Großer N-Heteroacene Mittels Nicht-Klassischer Methoden, **2011**.

[172] B. D. Lindner, F. Paulus, A. L. Appleton, M. Schaffroth, J. U. Engelhart, K. M. Schelkle, O. Tverskoy, F. Rominger, M. Hamburger, U. H. F. Bunz, *J. Mater. Chem. C* **2014**, *2*, 9609–9612.

[173] R. Schmidt, S. Göttling, D. Leusser, D. Stalke, A.-M. Krause, F. Würthner, *J. Mater. Chem.* **2006**, *16*, 3708.

[174] X. Xu, B. Shan, S. Kalytchuk, M. Xie, S. Yang, D. Liu, S. V Kershaw, Q. Miao, *Chem. Commun. (Camb).* **2014**, *50*, 12828–31.

[175] A. L. Appleton, S. Miao, S. M. Brombosz, N. J. Berger, S. Barlow, S. R. Marder, B. M. Lawrence, K. I. Hardcastle, U. H. F. Bunz, *Org. Lett.* **2009**, *11*, 5222–5225.

[176] B. D. Lindner, B. A. Coombs, M. Schaffroth, J. U. Engelhart, O. Tverskoy, F. Rominger, M. Hamburger, U. H. F. Bunz, *Org. Lett.* **2013**, *15*, 666–669.

[177] G. Giri, R. Li, D.-M. Smilgies, E. Q. Li, Y. Diao, K. M. Lenn, M. Chiu, D. W. Lin, R. Allen, J. Reinspach, et al., *Nat. Commun.* **2014**, *5*, 3573.

[178] F. Paulus, M. Porz, M. Schaffroth, F. Rominger, A. Leineweber, Y. Vaynzof, U. H. F. Bunz, *Org. Electron.* **2016**, accepted manuscript.

[179] I. Kaur, W. Jia, R. P. Kopreski, S. Selvarasah, M. R. Dokmeci, C. Pramanik, N. E. McGruer, G. P. Miller, *J. Am. Chem. Soc.* **2008**, *130*, 16274–16286.

[180]   C. M. Cardona, W. Li, A. E. Kaifer, D. Stockdale, G. C. Bazan, *Adv. Mater.* **2011**, *23*, 2367–2371.

Acknowledgments

Meinem Doktorvater Prof. Dr. Uwe H. F. Bunz sei an erster Stelle gedankt für die interessante Aufgabenstellung, die Freiheit in der Ausarbeitung des Themas und die Möglichkeit diese Arbeit in seiner Arbeitsgruppe am OCI in Heidelberg anzufertigen.

Bei Prof. Dr. Michael Mastalerz möchte ich mich für die freundliche Übernahme des Koreferats bedanken.

Ein besonderer Dank gebührt Prof. Dr. Henning Sirringhaus, der mir die Möglichkeit gegeben hat während eines Gastaufenthalts an der Universität Cambridge in seiner Gruppe die Heidelberger Materialien zu untersuchen. Ohne diese wertvollen Monate und seiner Expertise und das Wissen, das ich dort erhalten durfte, wäre diese Arbeit wahrscheinlich gar nicht möglich gewesen.

Für die finanzielle Unterstützung während der Doktorarbeit danke ich dem Promotionskolleg „Verknüpfung molekularer π-Systeme zu Funktionsmaterialien".

Ich danke Prof. Dr. Andreas Leineweber für die zahlreichen XRD Messungen in Stuttgart und in Freiberg. Die detaillierten Erklärungen, unzähligen Telefonate und Emails haben mir unglaublich viel geholfen, die Datensätze zu interpretieren und zu verstehen. Ebenso sei seinem Mitarbeiter Dr. Christian Schimpf gedankt für die Durchführung vieler Messungen.

Ich möchte mich auch bei Dr. Wojciech Pisula und Dr. Tomasz Marszalek in Mainz für die Durchführung von GIWAXS Messungen bedanken.

Prof. Motzkus möchte ich herzlich für den freien Zugang zum AFM danken. Vor allem aber für die tolle Kooperation im Bereich der Kurzzeitspektroskopie.

Ich danke auch dem Kirchhoff-Institut für Physik in Heidelberg für freien und unkomplizierten Zugang zu deren Reinraum. Herrn Wolf sei für die viele Hilfe und Unterstützung bei der Arbeit dort gedankt.

Dr. Frank Rominger und seinem Team am OCI in Heidelberg möchte ich danken für die Einkristallmessungen und Strukturanalysen und die vielen Gespräche über Polymorphie und Röntgenbeugung.

Especially, I would like to thank Prof Dr Yana Vaynzof for conducting numerous UPS measurements and the analysis of these data. I would also like to thank her Post-doc Dr Paul Hopkinson for several good ideas, trouble shooting and his helping hand. Both also have corrected major parts of this thesis!

Den Handwerkern in der Schlosserei, der Feinmechanik oder der Elektrowerkstatt muss ich besonders danken. Ohne eure permanente Hilfe und die schnelle Lösung von Problemen hätte ich in meinem Kellerlabor nichts erreicht. Auch, dass ihr immer auf meine Sonderwünsche eingegangen seid, war mehr als hilfreich!

Eidesstattliche Versicherung
gemäß § 8 der Promotionsordnung
der Naturwissenschaftlich-Mathematischen Gesamtfakultät
der Universität Heidelberg

1. Bei der eingereichten Dissertation zu dem Thema

    „N-Heteroacenes in Organic Field-Effect Transistors"

    handelt es sich um meine eigenständig erbrachte Leistung.

2. Ich habe nur die angegebenen Quellen und Hilfsmittel benutzt und mich keiner unzulässigen Hilfe Dritter bedient. Insbesondere habe ich wörtlich oder sinngemäß aus anderen Werken übernommene Inhalte als solche kenntlich gemacht.

3. Die Arbeit oder Teile davon habe ich bislang nicht an einer Hochschule des In- oder Auslands als Bestandteil einer Prüfungs- oder Qualifikationsleistung vorgelegt.

4. Die Richtigkeit der vorstehenden Erklärung bestätige ich.

5. Die Bedeutung der eidesstattlichen Versicherung und die strafrechtlichen Folgen einer unrichtigen oder unvollständigen eidesstattlichen Versicherung sind mir bekannt.

Ich versichere an Eides statt, dass ich nach bestem Wissen die reine Wahrheit erklärt und nichts verschwiegen habe

_____   _____

(Ort, Datum)   (Unterschrift)